Supramolecular Polymorphism in Homo- and Heterochiral Supramolecular Polymerizations

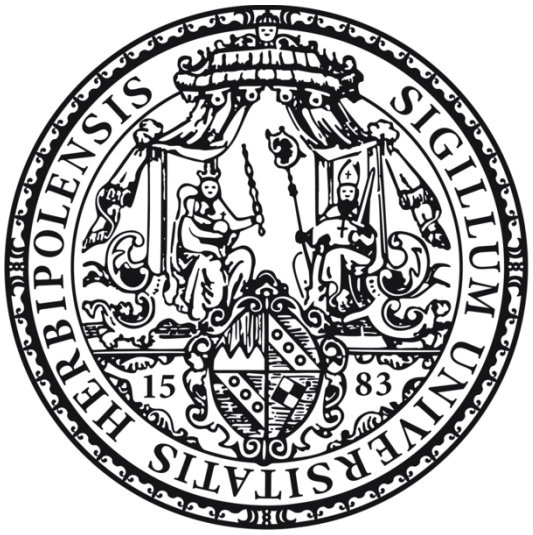

Dissertation zur Erlangung

des naturwissenschaftlichen Doktorgrades

der Julius-Maximilians-Universität Würzburg

vorgelegt von

Marius Wehner

aus Langenleiten

Würzburg 2020

Eingereicht bei der Fakultät für Chemie und Pharmazie am

_____

Gutachter der schriftlichen Arbeit:

1. Gutachter: Prof. Dr. Frank Würthner

2. Gutachter: Prof. Dr. Gustavo Fernández

Prüfer des öffentlichen Promotionskolloquiums:

1. Prüfer: Prof. Dr. Frank Würthner

2. Prüfer: Prof. Dr. Gustavo Fernández

3. Prüfer: Prof. Dr. Dr. Lorenz Meinel

4. Prüfer: Prof. Dr. Jürgen Groll

5. Prüfer: Prof. Dr. Claudia Höbartner

Datum des öffentlichen Promotionskolloquiums

10.09.2020

Doktorurkunde ausgehändigt am

_____

für meine Familie

List of Abbreviations, Variables and Physical Constants

Abbreviations

1D	one-dimensional
2D	two-dimensional
3D	three-dimensional
AFM	atomic force microscopy
A_{tr}	kinetically trapped aggregate
a.u.	arbitrary unit
BCP	block copolymer
B3LYP	Becke-3-parameter-Lee-Yang-Parr (exchange-correlation functional)
Boc	*tert*-butoxy carbonyl
BTA	benzene-1,3,5-tricarboxamide
CD	circular dichroism
CDSA	crystallization-driven self-assembly
cryo-TEM	cryogenic transmission electron microscopy
DCTB	*trans*-2-[3-(4-*tert*-butylphenyl)-2-methyl-2-propenylidene]malononitrile
DFT	density functional theory
eq.	equivalents
ESI	electrospray ionization
FESEM	field emission scanning electron microscopy
FT-IR	Fourier-transform infrared
h	hour(s)
HEWL	hen egg white lysozyme

HOPG	highly oriented pyrolytic graphite
HRMS	high-resolution mass spectrometry
i.e.	that is (latin: id est)
LD	linear dichroism
LSP	living supramolecular polymerization
MALDI	matrix-assisted laser desorption/ionization
MCH	methylcyclohexane
min	minute(s)
Mono	monomer
MOPAC	molecular orbital package
MS	mass spectrometry
M_{tr}	kinetically trapped monomer
NEB	nudged elastic band
NMR	nuclear magnetic resonance
OPV	oligo(*para*-phenylene vinylene)
PBI	perylene bisimide
PDI	polydispersity index
PIC	pseudoisocyanine chloride
ppm	parts per million
ref.	reference
RMSD	root-mean-square deviation
rpm	revolutions per minute
rt	room temperature
s	second(s)
SP	supramolecular polymer
STM	scanning tunneling microscopy
TCE	1,1,2,2-tetrachloroethane

THF	tetrahydrofuran
TLC	thin-layer chromatography
TOF	time of flight
Tol	toluene
UPy	2-ureido-4[1*H*]-pyrimidinone
UV	ultraviolet
vis	visible
VT	variable temperature

Variables

A	Absorbance
α_{Agg}	degree of aggregation
$\alpha_{\mathrm{Agg\text{-}\pi}}$	degree of aggregated π surfaces
α_{Mono}	fraction of monomers
$c_{\mathrm{Agg}}^{\mathrm{even}}$	concentration of molecules incorporated in even-sized aggregates
$c_{\mathrm{Agg}}^{\mathrm{odd}}$	concentration of molecules incorporated in odd-sized aggregates
c_{D}	concentration of molecules incorporated in dimers
c_{Mono}	monomer concentration
c_{T}	total concentration
d	path length
$\Delta\varepsilon$	molar CD absorption
ΔG^{O}	standard Gibbs free energy
ΔH	molar enthalpy release upon isodesmic aggregation
ΔH^{O}	standard molar enthalpy
ΔH_{E}	molar enthalpy release upon elongation
ΔS^{O}	standard molar entropy

ε	molar extinction coefficient
ε_{Mono}	molar extinction coefficient of the monomer
ε_{Agg}	molar extinction coefficient of the aggregate
K	association constant
K_2	association constant for dimerization
K_E	association constant for elongation
K_N	association constant for nucleation
λ	wavelength
m.p.	melting point
μ_{eg}	transition dipole moment
Φ_{fl}	fluorescence quantum yield
s	nucleus size
σ	cooperativity factor
T	temperature
t	time
T_E	critical elongation temperature
T_M	melting temperature
v/v	volumetric ratio

Physical constants

Å	ångström (10^{-10} m)
k_B	Boltzmann constant ($k_B = 1.380649 \times 10^{-23}$ J K^{-1})
R	universal gas constant ($R = 8.314462$ J mol^{-1} K^{-1})

Table of contents

Chapter 1

–

Introduction and Aim of the Thesis

After Hermann Staudinger's revolutionary proposal that polymers are high molecular weight macromolecules consisting of short monomeric repeating units in 1920,[1] polymer chemistry witnessed a great upswing. Today a world without polymers in soft materials, electronics, medical devices, coatings, households and many more sectors is unimaginable.[2-5] In classic polymers, the covalent linkage of monomers usually leads to high kinetic and thermodynamic stabilities which are on the one hand crucial for many applications but on the other hand might give rise to increasing sustainability and recycling issues as well as limited processability.[2, 6-7] In the last 30 years, however, supramolecular chemistry has developed as a powerful platform to tackle these problems resulting in novel functional materials.[8-10]

In contrast to covalently linked polymers, supramolecular polymers are polymeric arrays of monomeric units that are interconnected by reversible and directional secondary interactions such as metal-ligand coordination, hydrogen bonds, π–π stacking or combinations of them (Figure 1).[11] Accordingly, supramolecular polymers are of one-dimensional (1D) nature and typically consist of a single chain as opposed to nano- or liquid-crystalline three-dimensional (3D) materials.[12]

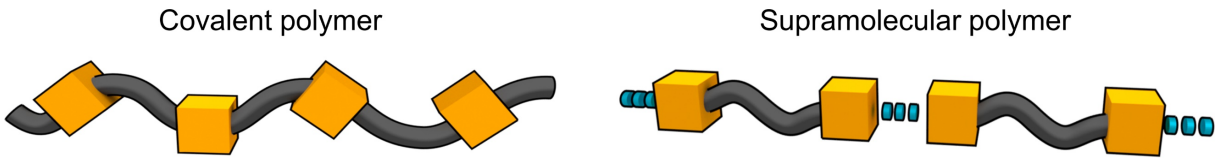

Figure 1. Comparison between covalent and supramolecular polymers. The characteristic intermolecular interactions within supramolecular polymers are indicated with blue dashes.

The strong intermolecular interactions within supramolecular polymers can not only recreate some of the key properties of covalent polymers but also lead to a strikingly dynamic nature of supramolecular polymers which enables several novel functionalities such as stimuli-

responsiveness[10, 13-15] or self-healing.[16-18] Hence, supramolecular polymers have been applied in a plethora of sophisticated materials[8] with mechanical, optical, electronic or biological functionalities.[10, 17, 19-23]

While former studies on supramolecular polymers were mainly dedicated to analyze the thermodynamics and self-assembly mechanism of those equilibrium structures by mathematical models,[11, 24-31] recent academic interest shifts toward kinetically controlled supramolecular polymerization and the generation of out-of-equilibrium species.[9, 12, 32-37]

One of the first examples of kinetically controlled aggregation processes of synthetic polymers were reported in the early 1990s by Okamoto[38] as well as Bouman and Meijer in 1995[39] who showed that the helical screw sense of optically active methacrylate polymer can be altered by the pH value or that stereomutation occurred in thin films of a chiral, 3-substituted polythiophene depending on the thermal history of the material, respectively. Similarly, supramolecular polymerization processes of organic molecules might also be governed by a complex interplay between thermodynamics and kinetics yielding different self-assembly products of the same molecule (supramolecular polymorphs) depending on the history of the sample.[32, 37, 40] Within the research field of supramolecular chemistry, this phenomenon is termed “pathway complexity” and was systematically unraveled by the seminal work of Meijer and coworkers, who provided profound mechanistic studies on the supramolecular polymerization of a chiral oligo(*para*-phenylenevinylene) (OPV) dye.[29] The precise control of supramolecular polymerization pathways laid the foundation for the establishment of the first seed-induced living supramolecular polymerization (LSP) of a zinc porphyrin derivative which was reported by Sugiyasu and Takeuchi two years later.[41] In a seeded supramolecular polymerization (SSP) or LSP, the spontaneous self-assembly of the molecular building blocks into extended supramolecular polymers is prohibited due to the formation of kinetically trapped products.[12, 41-44] Under suitable conditions, the addition of seeds or initiator molecules − which act as preformed nuclei similar as in conventional crystallization processes – induces the supramolecular polymerization of these kinetically trapped species. SSP and LSP are useful methods for the preparation of highly ordered supramolecular polymers with small polydispersity indices (PDIs)[41-42, 44] and are further discussed in *Chapter 2*.

Beyond that, supramolecular pathway control in one-dimensional (1D) self-assembly is fundamental for a better understanding of three-dimensional (3D) crystallization processes which can be regarded as “supramolecular reactions” per excellence involving specific molecular recognition events leading to the self-assembly of the molecules into the periodic

crystal lattices.[45-47] Similar to supramolecular polymerizations, the complex interplay between thermodynamics and kinetics during crystallization can lead to different crystal forms of the same molecule which is called polymorphism.[45, 48] Since the physical and chemical properties of a given compound strongly depend on its mutual packing arrangement, control of polymorphism is of utmost importance for chemical industry where crystallization is an attractive purification technique.[46, 48-49] However, it still remains challenging to accurately predict which polymorph will form during crystallization of organic molecules because energies between different polymorphs might only differ by a few kJ mol^{-1} and crystallization is usually under kinetic control and a function of experimental parameters like temperature, solvent, heating and cooling rates or other mechanical forces such as shock.[48-50] In contrast to the crystallization of enantiopure compounds due to exclusively homochiral self-association, crystallization of racemates either yields conglomerates by homochiral aggregation or racemic crystals by heterochiral aggregation.[51-53] Conglomerates are equimolar mixtures of crystals containing only a single enantiomer while racemic crystals contain both enantiomers in an ordered (racemic compound) or disordered fashion (solid solution).[51-53] Although the early stages of crystallization (nuclei formation and subsequent elongation) are decisive for polymorph and conglomerate or racemic crystal formation, they are poorly understood at the molecular level and experimentally difficult to assess.[54-61]

In order to gain deeper insights into the initial stages of polymorphism as well as conglomerate *versus* racemic crystal formation, the complexity of the self-assembly process needs to be reduced from 3D crystallization to 1D supramolecular self-assembly. For this purpose, dye molecules were designed that contain a perylene bisimide (PBI) chromophore as the central unit which serves as "intermolecular glue" due to its strong π–π stacking ability and as a sensitive probe for the packing arrangements of the monomers within the supramolecular polymorphs,[62-63] thereby allowing to monitor polymorph formation by different spectroscopic techniques such as UV/vis-absorption, circular dichroism (CD) or fluorescence spectroscopy.[27, 64] Due to their outstanding properties such as high thermal, chemical and photochemical stability,[64] PBI dyes have been extensively investigated for applications including dye lasers,[65-67] optical sensors[68-70], probes for biomacromolecules[71-72] or as color pigments or fluorescent dyes.[64, 73-74] Recently, Würthner and coworkers intensively investigated the SSP and LSP of PBI organogelators[43, 75-77] such as **PBI-1** (Figure 2)[43] and utilized kinetic polymerization conditions for the preparation of sophisticated block copolymer structures combining two different bay-substituted PBIs.[78-79] The central requirement for performing SSP and LSP was the control of the pathway complexity of these dyes and the

establishment of kinetically metastable states which was achieved by tailored molecular design, namely by introducing amide-appended side chains with C2[43, 76-79] or C4 spacers[75] to the imide positions of the central PBI moieties. It was demonstrated that amide-appended **PBI-1** can form kinetically trapped monomers and thermodynamically stable 1D nanofibers by a cooperative aggregation mechanism[43] while the introduction of two α-CH_3 groups in structurally related **PBI-2** (Figure 2) led to a single accessible anticooperative polymerization pathway and nanoparticle formation (the respective aggregation mechanisms are discussed in *Chapter 2.2*).[28] In order to achieve a rich supramolecular polymorphism, PBI derivatives **(*R*,*R*)-** and **(*S*,*S*)-PBI** were designed (Figure 2) which bear side chains that combine the different structural elements derived from **PBI-1** and **PBI-2** (outlined in grey in Figure 2) that favor either kinetic trapping and 1D nanofiber formation (amide-appended side chain with C2 spacer) or nanoparticle formation (α-CH_3 groups). This molecular design should increase the number of potentially accessible supramolecular polymorphs compared to **PBI-1** and **PBI-2**.

The aim of the first part of this thesis was to investigate **(*R*,*R*)-PBI** as a model system for polymorphism at its origin by a supramolecular approach. The pathway complexity of **(*R*,*R*)-PBI** was fine-tuned by experimental parameters such as solvent, temperature and concentration to make several supramolecular polymorphs accessible (Figure 2). Mechanistic and quantum chemical studies on the kinetics and thermodynamics of the supramolecular polymerization of **(*R*,*R*)-PBI** were conducted to shed light on the initial stages of polymorphism. The second part of this work deals with mechanistic investigations on the supramolecular polymerization of the racemic mixture of **(*R*,*R*)-** and **(*S*,*S*)-PBI** with regard to homochiral and heterochiral aggregation leading to conglomerates and racemic supramolecular polymers, respectively (Figure 2).

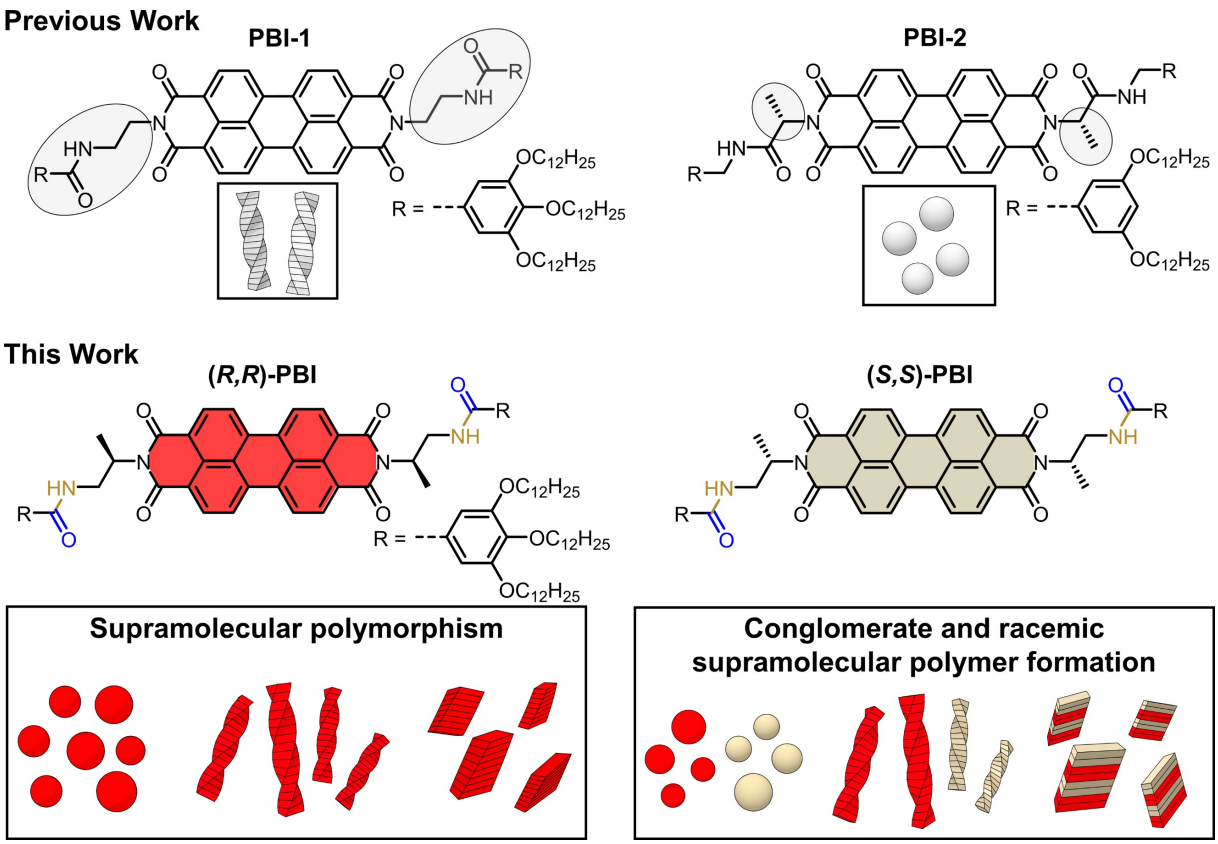

Figure 2. Chemical structures and schematic illustrations of the supramolecular nanostructures of previously investigated **PBI-1**[43, 80] and **PBI-2**[28] as well as those of the supramolecular polymorphs of **(*R*,*R*)-** and **(*S*,*S*)-PBI** and their racemic mixture studied in this thesis.

Chapter 2 gives an overview of the historical development of supramolecular polymer chemistry followed by a discussion of different thermodynamic models to analyze the self-assembly of monomeric building blocks into supramolecular nanostructures. Furthermore, kinetic control over aggregation pathways is described that ultimately led to the establishment of seeded and living supramolecular polymerization as well as supramolecular polymorphism. At the end of the chapter a literature survey about supramolecular polymerizations of racemic mixtures is provided.

Chapter 3 deals with the self-assembly of **(*R*,*R*)-PBI** into three different supramolecular polymorphs which were characterized by UV/vis, CD, fluorescence and Fourier-transform infrared (FT-IR) spectroscopy as well as atomic force microscopy (AFM) and quantum chemical calculations. The thermodynamic and kinetics features of the supramolecular polymorphism were analyzed by concentration-, time- and temperature-dependent UV/vis spectroscopy. The polymerization pathways towards different nanostructures were controlled

physically by ultrasonication and chemically − in analogy to 3D crystallization experiments – by seeding (SSP). Quantum chemical calculations provided insights into the nucleation processes of the different polymorphs at the molecular level.

Chapter 4 describes the supramolecular polymerization of a racemic mixture of **(*R*,*R*)-** and **(*S*,*S*)-PBI** which afforded two conglomerates by homochiral aggregation of the respective enantiomers under kinetic control. In contrast, under thermodynamic conditions, a racemic supramolecular polymer is formed with heterochiral contacts between **(*R*,*R*)-** and **(*S*,*S*)-PBI**. The kinetics and thermodynamics of conglomerate *versus* racemic supramolecular polymer formation were investigated in detail by UV/vis spectroscopy, AFM and quantum chemical calculations.

Chapter 5 and *Chapter 6* summarize the results of the present thesis in English and German, respectively.

Chapter 2

–

State of Knowledge

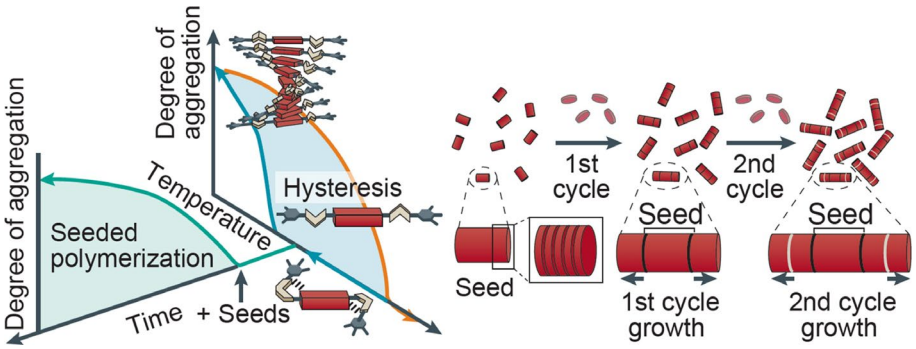

Part of this chapter was published in:

M. Wehner, F. Würthner, *Nat. Rev. Chem.* **2020**, *4*, 38−53.

(https://www.nature.com/articles/s41570-019-0153-8?proof=trueMay.).

Adapted or reprinted with permission from reference[12]. Copyright 2019 Springer Nature.

Abstract. Supramolecular polymers exhibit fascinating structures, and their properties, and thus applications, depend both on the strength and dynamics of the non-covalent bonds and on the functional properties of the monomeric building blocks. In this chapter, the progress in methods developed to control supramolecular polymerization based on physicochemical insights into the thermodynamics and kinetics of non-covalent interactions is highlighted. Prerequisites for polymer formation and stability, such as high binding strength (thermodynamics) between complementary receptor units as well as common mathematical models for the analysis of supramolecular polymerization processes are discussed, while the main focus is on the kinetic control of pathway selectivity, which in recent years has allowed seed-induced living supramolecular polymerization, chain growth-type supramolecular polymerization and the preparation of specific supramolecular polymer polymorphs. Finally, recent examples of supramolecular polymerization processes of racemic mixtures are presented.

2.1 Supramolecular Polymers

The field of supramolecular chemistry emanated from research on host-guest complexes with high association constants and selectivity for certain metal cations. Following the award of the Nobel Prize in chemistry in 1987 to Pedersen, Lehn and Cram for their pioneering work in the field,[81-84] it evolved into a much broader discipline. Lehn, in particular, broadened the perspective in the following years with his vision of 'chemistry beyond the molecule'[85] towards the self-assembly of various structures, such as zero-dimensional cages, helicates and grids right up to three-dimensional coordination polymers (metal-organic frameworks).[86] Likewise, it was Lehn who introduced the concept of supramolecular polymerization in 1990 by using molecular recognition events based on complementary triple hydrogen bonding between ditopic diacylaminopyridines and ditopic uracil derivatives to generate the first supramolecular main-chain polymer (Figure 3).[87]

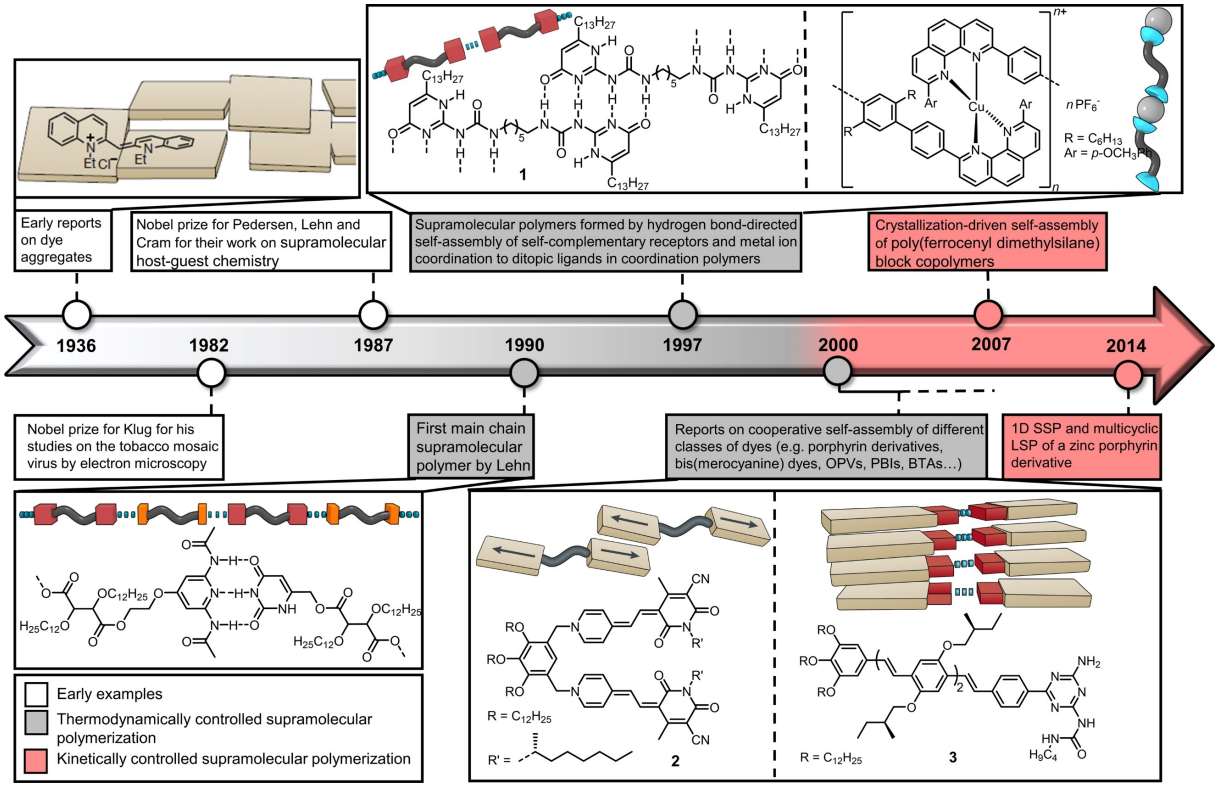

Figure 3. A timeline highlighting the milestones in the development of supramolecular polymer chemistry starting from early examples (white) of dye aggregates followed by thermodynamically (grey) and later kinetically controlled supramolecular polymerizations (red). BTA: benzene-1,3,5-tricarboxamide; OPV: oligo(*para*-phenylenevinylene); PBI: perylene bisimide.

As is often the case in science, however, this widening of the field and integration of new research topics led to the identification of earlier contributions that may be regarded as supramolecular polymers as well. A particularly striking example in this regard is the J-aggregates, which were discovered in the late 1930s by Scheibe[88-89] and Jelley[90-91] (after whom they are named). Scheibe dedicated much of his scientific career to the study of cyanine dye aggregates and published around 100 articles in the period from 1937 to 1974 from his laboratory at the Technical University of Munich. Unfortunately, his fundamental contributions were published mainly in German and in journals that no longer exist. Accordingly, although his research is well recognized in the community of physicists dedicated to research on exciton transport in dye aggregates, chemists working in the now very active fields of aggregation-induced emission[92] and supramolecular polymers are less aware of his work. It is noteworthy then that as early as his second article on J-aggregates of pseudoisocyanine chloride (PIC) dyes in 1937, Scheibe concluded that 'a special kind of polymerization' is observed upon dissolution of PIC in water and a sharp new absorption band formed upon increasing concentration, concomitant with intense fluorescence and a strong increase of the viscosity leading to gelation at concentrations above 10^{-2} M.[89] Finally, he concluded that the observed phenomena originate from the 'reversible polymerization of dye ions'. Thus, undoubtedly, Scheibe was fully aware of the phenomena nowadays described as supramolecular polymerization and aggregation-induced emission. Although the exact structure of the PIC aggregate is still a matter of debate, proposed structural models such as doublestring cables (Figure 3) and hierarchically assembled double-string cables appear quite reasonable.[93-94]

A further seminal contribution to the development of supramolecular polymerization came from Klug and coworkers who, by developing a new crystallographic electron microscopy technique, were able to study complex biomacromolecules and biological self-assembly processes such as the RNA-templated protein assembly of the tobacco mosaic virus, which follows a nucleation-growth mechanism[95-96] (see *Chapter 2.2*). Once again though, because these seminal achievements of Scheibe and Klug were devoted to rather different objectives and the building blocks of the assemblies under investigation were not the result of supramolecular design, the research field of supramolecular polymerization was not truly launched until the mid-1990s. The first challenge was to identify complementary supramolecular motifs with sufficient binding strength to direct supramolecular polymerization even in dilute solution. This was apparently not the case for Lehn's diacylaminopyridine-uracil receptor pair, where the hydrogen-bonded assembly of a 1:1 mixture of ditopic monomers prevailed only with the aid of additional non-covalent interactions in liquid-crystalline mesophases.[87] Since the mid-

1990s, however, many groups have described the formation of supramolecular polymer architectures with extended chain lengths in dilute solution.[8-11, 97-98] In all of these supramolecular polymers, the constituent monomeric units are linked by highly directional, reversible secondary interactions. The most common structures rely on hydrogen bonding,[99] metal ion coordination[100] and π–π interactions,[27] but approaches based on the antiparallel stacking of dipolar dyes (electrostatics)[101] and rotaxane-type[102-104] threading of guest molecules through macrocyclic receptors have also been widely applied. Most of these interactions show fast equilibration and as a result thermodynamically equilibrated supramolecular oligomers or polymers are formed.

Some of the most versatile and well-studied binding motifs are depicted in (Figure 3). The champion among these is the small 2-ureido-4[1*H*]-pyrimidinone, which dimerizes on the formation of self-complementary quadruple hydrogen bonds with an association constant of $6 \times 10^7\ M^{-1}$ in $CHCl_3$.[11, 105] In their seminal work, Meijer et al. showed that difunctional compound **1** forms stable 1D supramolecular polymers with long chain lengths – which would correspond to masses of up to 10^6 Da – that exhibit highly temperature- and concentration-dependent viscoelastic properties as a result of reversible hydrogen bonding. In a slightly different approach, the Rebek group created linear supramolecular polymers by guest-mediated self-assembly of ditopic urea-functionalized calix[4]arenes, resulting in polymer-like rheological behaviour with a strong concentration and temperature dependency in solution and fibres with tensile strengths on the order of 10^8 Pa in the solid state.[106-108] Whereas these examples are based on self-complementary ditopic binding sites to give [··A–A··]$_n$-type supramolecular polymers, at about the same time Rehahn introduced metallosupramolecular polymers based on the interaction of coordinating ligands with metal ions to give [··A–A··M··]$_n$-type coordination polymers (Figure 3).[109] In all these cases, high degrees of polymerization and properties similar to those of covalent polymers were demonstrated in dilute solutions.[25, 110] In the following decade, mechanistic studies were devoted to the thermodynamics of supramolecular polymerizations and brought the field to another level of understanding. Steadily increasing computational power and the development of sophisticated mathematical models facilitated the identification and mechanistic investigations of cooperative supramolecular polymerizations which already allow under highly dilute conditions the formation of elongated supramolecular nanofibres. In this regard, porphyrin derivatives,[41-42, 111-116] bis(merocyanine),[31, 101, 117-120] oligo(*para*-phenylenevinylene) (OPV)[29, 121-123] and PBI dyes[43, 64, 77, 124-126] as well as benzene-1,3,5-tricarboxamides[127-129] represent the best studied

organic molecules with regard to the thermodynamics of their cooperative supramolecular polymerizations.

2.2 Thermodynamics of Supramolecular Polymerization

Dye molecules are particularly well suited to study self-assembly mechanisms and the thermodynamics of self-assembly processes by UV/vis spectroscopy [25, 27] which is a result of the easily detectable spectral changes arising from exciton coupling of the dyes' transition dipole moments.[130] By monitoring spectral changes upon changing concentration or temperature, the concentration- or temperature-dependent degree of aggregation α_{Agg} at a certain wavelength can be calculated according to equation (1) from the apparent molar extinction coefficients ε and the molar extinction coefficients of the monomer $\varepsilon_{\mathrm{Mono}}$ and aggregate $\varepsilon_{\mathrm{Agg}}$, respectively.[31] The degree of aggregation α_{Agg} which always lies in between zero (only monomers are present) and unity (all molecules are incorporated into aggregates) is the central variable for the determination of the thermodynamic parameters of supramolecular polymerization processes.

$$\alpha_{\mathrm{Agg}} = \frac{\varepsilon_{\mathrm{Mono}} - \varepsilon}{\varepsilon_{\mathrm{Mono}} - \varepsilon_{\mathrm{Agg}}} \tag{1}$$

The simplest self-assembly process is the association of monomers into dimers. The concentration-dependent degree of aggregation α_{Agg} can be calculated by equation (2), in which K_2 is the dimerization constant and c_{T} the total concentration of molecules.[27]

$$\alpha_{\mathrm{Agg}} = \frac{4K_2c_{\mathrm{T}} + 1 - \sqrt{8K_2c_{\mathrm{T}} + 1}}{4K_2c_{\mathrm{T}}} \tag{2}$$

Although the monomer-dimer model has been successfully applied for aggregation processes of phthalocyanines or merocyanine dyes,[11, 131-134] it is oversimplified for the analysis of higher aggregate species that form if for example both dyes' π surfaces show equal reactivity.[27]

The three most common aggregation models for extended supramolecular stacks – isodesmic,[24-27, 30] cooperative[25-27, 30-31, 122, 135] and anticooperative with preferential dimer formation[28] – are illustrated in (Figure 4).

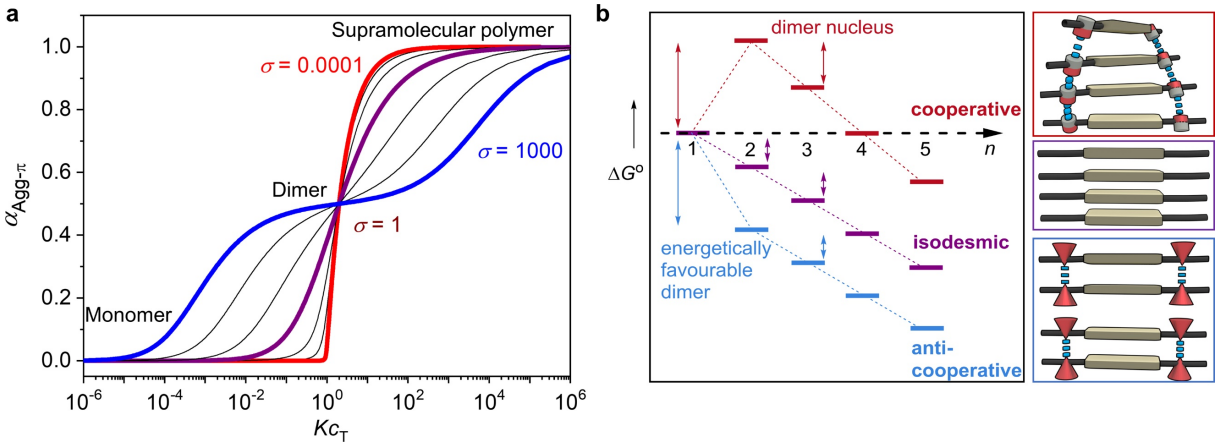

Figure 4. (**a**) The fraction of aggregated π surfaces $\alpha_{Agg-\pi}$ as a function of the normalized concentration Kc_T with different σ values and a nucleus size of two. (**b**) Qualitative energy diagram of a cooperative (red), isodesmic (purple) or anticooperative (blue) supramolecular polymerization with schematic illustrations of sections of supramolecular polymers formed by the respective aggregation mechanisms (grey cuboids, π surfaces; cylinders or cones, functional groups capable of forming two or one supramolecular contact(s) such as hydrogen bonds, which are indicated with dashed blue lines).

They can be easily understood on the basis of the concept that each addition of a monomer to the growing supramolecular polymer chain is characterized by the same binding constant (isodesmic case) or that the nucleation is disfavoured (cooperative case) or favoured (anticooperative case), which is attributed to electronic or steric peculiarities of the respective supramolecular building block (Figure 4b).[25] In an isodesmic supramolecular polymerization (cooperativity factor $\sigma = K_N/K_E = 1$; purple lines in Figure 4), the self-assembly of monomeric building blocks to 1D aggregates is described by a single binding constant K (the nucleation constant K_N equals the elongation constant K_E). This is usually the case for supramolecular systems where only a single type of non-covalent bond (for example, only π–π interactions; purple box in Figure 4b) is formed and where crowding of the solubilizing side chains does not play a role in the polymerization process. Such a situation is often found, for instance, for PBI dyes.[136] For isodesmic self-assembly processes the concentration-dependent degree of aggregation can be calculated according to equation (3):[26-27]

$$\alpha_{\mathrm{Agg}} = 1 - \frac{2Kc_{\mathrm{T}} + 1 - \sqrt{4Kc_{\mathrm{T}} + 1}}{2K^2 c_{\mathrm{T}}^2} \tag{3}$$

In contrast to concentration-dependent studies, temperature-dependent spectroscopic measurements at a fixed concentration allow to acquire a much larger data set in a single measurement and hence, several mathematical models have been developed to describe temperature-dependent self-assembly.[30-31, 122] Accordingly, the temperature-dependent degree of aggregation of an isodesmic supramolecular polymerization can be derived from equation (4), where ΔH is the molar enthalpy release upon aggregation, R the universal gas constant, T the absolute temperature and T_{M} the melting temperature, defined as the temperature where $\alpha_{\mathrm{Agg}} = 0.5$.[30-31]

$$\alpha_{\mathrm{Agg}} \cong \frac{1}{1 + \exp\left(-0.908\Delta H \frac{T - T_{\mathrm{M}}}{RT_{\mathrm{M}}^2}\right)} \tag{4}$$

In reality, however, truly isodesmic self-assembly with equal binding constants for both π surfaces appears likely to be the exception rather than the rule. The ubiquitous and quite successful application of this model might in reality be the result of a too-limited concentration range in many studies caused by poor solubility or technical limitations. With increasing awareness of this problem, several different mathematical models for the formation of 1D supramolecular polymerizations have been developed.

In contrast to isodesmic aggregation, for phthalocyanines, dimerization seems to be favoured over the further elongation process.[11] Such anticooperative supramolecular polymerizations (blue lines in Figure 4) are characterized by a nucleation that is energetically more favourable compared with further elongation ($\sigma = K_{\mathrm{N}}/K_{\mathrm{E}} > 1$). In general, anticooperative aggregation processes can be described by the Goldstein–Stryer model according to equation (5) in which s the nucleus size and c_{Mono} the monomer concentration.[31, 135]

$$K_E c_T = \sum_{n=1}^{s} n\sigma^{n-1}(K_E c_{\text{Mono}})^n + \sum_{n=s+1}^{\infty} n\sigma^{s-1}(K_E c_{\text{Mono}})^n =$$

$$= \frac{s(K_E c_{\text{Mono}})^s \sigma^{s-1}}{1 - K_E c_{\text{Mono}}} + \frac{(K_E c_{\text{Mono}})^{s+1}\sigma^{s-1}}{(1 - K_E c_{\text{Mono}})^2} + \frac{K_E c_{\text{Mono}}(s(\sigma K_E c_{\text{Mono}})^{s-1} - 1)}{\sigma K_E c_{\text{Mono}} - 1} \quad (5)$$

$$- \frac{\sigma(K_E c_{\text{Mono}})^2((\sigma K_E c_{\text{Mono}})^{s-1} - 1)}{(\sigma K_E c_{\text{Mono}} - 1)^2}$$

If exclusively dimer nuclei are formed, the Goldstein-Stryer model simplifies to the so-called K_2–K model given by equation (6).[27-28]

$$K_E c_T = (1 - \sigma) K_E c_{\text{Mono}} + \frac{\sigma K_E c_{\text{Mono}}}{(1 - K_E c_{\text{Mono}})^2} \quad (6)$$

The concentration-dependent degree of aggregation can then be calculated by using equation (5) for nuclei sizes $s > 2$ or in the case of dimer nuclei equation (6) in combination with equation (7) in which α_{Mono} is the monomer fraction.[28, 31]

$$\alpha_{\text{Agg}} = 1 - \alpha_{\text{Mono}} = 1 - \frac{K_E c_{\text{Mono}}}{K_E c_{\text{T}}} \quad (7)$$

However, for the most abundant anticooperative growth process of dye aggregates with dimer nuclei, the dominance of aggregates consisting of even numbers of monomers is not covered by the aforementioned model. Therefore, a modified K_2–K model was developed by Würthner and coworkers that accounts for the preferential formation of even-sized aggregates due to the thermodynamically favoured dimerization, which is schematically illustrated for a supramolecular polymer with multiple intermolecular contacts within a dimer unit but only single intermolecular π–π interaction between the dimers[28] (Figure 4b, blue box).

According to the anticooperative K_2–K model with preferential dimer formation, the total concentration of molecules c_{T} can be described by equation (8).[28] The second and third term

in equation (8) denote the concentration of molecules incorporated into even- and odd-sized aggregates, respectively.

$$c_{\mathrm{T}} = c_{\mathrm{Mono}} + \frac{2K_2 c_{\mathrm{Mono}}^2}{(1 - K_2 K_{\mathrm{E}} c_{\mathrm{Mono}}^2)^2} + \frac{K_2 K_{\mathrm{E}} c_{\mathrm{Mono}}^3 (3 - K_2 K_{\mathrm{E}} c_{\mathrm{Mono}}^2)}{(1 - K_2 K_{\mathrm{E}} c_{\mathrm{Mono}}^2)^2} \quad (8)$$

The concentration of molecules in dimers c_{D} and aggregates c_{Agg} can be calculated from c_{Mono} according to equation (9) and (10) in which $c_{\mathrm{Agg}}^{\mathrm{even}}$ and $c_{\mathrm{Agg}}^{\mathrm{odd}}$ are the concentrations of molecules in even and odd-sized aggregates, respectively.[28]

$$c_{\mathrm{D}} = 2K_2 c_{\mathrm{Mono}}^2 \quad (9)$$

$$c_{\mathrm{Agg}} = c_{\mathrm{Agg}}^{\mathrm{even}} + c_{\mathrm{Agg}}^{\mathrm{odd}} - c_{\mathrm{D}} = \frac{2K_2 c_{\mathrm{Mono}}^2}{(1 - K_2 K_{\mathrm{E}} c_{\mathrm{Mono}}^2)^2} + \frac{K_2 K_{\mathrm{E}} c_{\mathrm{Mono}}^3 (3 - K_2 K_{\mathrm{E}} c_{\mathrm{Mono}}^2)}{(1 - K_2 K_{\mathrm{E}} c_{\mathrm{Mono}}^2)^2} - c_{\mathrm{D}} \quad (10)$$

From this data, the concentration-dependent absorption spectra of a given compound can be reconstructed by a global fitting routine.[28] In general, anticooperative supramolecular polymerizations are to be expected for systems in which repulsive forces from steric interactions build up with increasing aggregate size,[137] or where particularly strong electrostatic interactions as given in dipolar merocyanine dyes are strongly reduced after the formation of a centrosymmetric dimer unit.[101]

With regard to the formation of extended supramolecular polymer chains, cooperative self-assembly is the most interesting case. As soon as multiple types of non-covalent interactions such as a combination of *π*–*π* interactions and hydrogen bonds (Figure 4b, red box) are involved in the self-assembly processes of organic molecules, cooperative supramolecular polymerizations (red lines in Figure 4) might occur.[110] A cooperative supramolecular polymerization following a nucleation-elongation mechanism can be separated into two steps.[25, 31] First, a nucleus of a certain size *s* is formed by a linear isodesmic polymerization with a lower association constant K_{N}. After the critical nucleus size has been reached, various cooperative effects lead to a higher association constant K_{E} for the association of additional monomers to the preformed nucleus. Further elongation may then proceed again as a linear

isodesmic supramolecular polymerization characterized by the association constant K_E. It is important to realize that in such a thermodynamic scenario neither dimers nor other small oligomers are observed in significant quantity and, instead, at the critical concentration an instantaneous growth of the supramolecular polymer chain occurs (Figure 4a, red line). The general model describing the concentration-dependent cooperative self-assembly processes is again provided by the Goldstein–Stryer model (equation (5) in combination with equation (7)).[31, 135] For the simplest nucleation–elongation process, assuming dimer nuclei, the simplified K_2–K model (equation (6)) can be applied as well.[26-27, 138] Owing to the ease of data acquisition and treatment, temperature-dependent studies are the preferred method for the analysis of cooperative self-assembly processes.[30-31, 122] Thereby, the temperature-dependent degree of aggregation α_{Agg} of the nucleation and elongation regime are treated separately. In the nucleation regime, α_{Agg} can be expressed by equation (11) where ΔH_E is the enthalpy release upon elongation and T_E the critical temperature at which elongation sets in.[31, 122]

$$\alpha_{Agg} = K_N^{1/3} \exp\left((2/3\, K_N^{-1/3} - 1) \frac{\Delta H_E}{R T_E^2} (T - T_E) \right) \tag{11}$$

The thermodynamically more favorable elongation process can be described by equation (12) in which the parameter α_{SAT} was introduced to ensure that α_{Agg} does not exceed unity.[31, 122]

$$\alpha_{Agg} = \alpha_{SAT} \left(1 - \exp\left(\frac{-\Delta H_E}{R T_E^2} (T - T_E) \right) \right) \tag{12}$$

2.3 Kinetics of Supramolecular Polymerization

In recent years, intensive efforts have been devoted to explore the kinetics of supramolecular polymerizations. If strong or multiple non-covalent interactions with cooperativity are involved, the final outcome of the self-assembly process might be dictated by kinetics rather than thermodynamics. The former (strong interactions) is the case for many coordination bonds (for example, the coordination between Ru^{2+} ions and various azaaromatic ligands)[100] and the latter (multiple non-covalent interactions) is frequently the case for π-organogelator molecules, where hydrogen bonding between amide or urea units supports the π–π stacking interactions

between the aromatic π surfaces.[139] In such situations, the supramolecular architecture corresponding to the aggregation pathway with the lowest activation barrier might form faster than the thermodynamically most stable polymer. Depending on the energy barrier $\Delta G^{\neq}$, which separates the kinetic product from the thermodynamically stable polymer, one distinguishes between a kinetically metastable state ($\Delta G^{\neq} \sim k_B T$, where k_B is the Boltzmann constant and T is the absolute temperature) and a kinetically trapped state ($\Delta G^{\neq} >> k_B T$).[32] Kinetic models to describe polymerization processes that follow a nucleation–elongation mechanism were initially reported for protein polymerizations decades ago.[135, 140-141] However, their relevance to supramolecular polymerizations was recognized only recently. Experimental studies of kinetically controlled processes are far more challenging compared with the investigation of all-equilibrated systems because in the case of kinetic assemblies the final outcome is largely dependent on the preparation method,[32, 142] ranging from temperature modulation,[29, 114, 143-145] different kinds of solvent processing[123, 146-150] and the application of external stimuli[115, 151-152] to photochemical conversion.[153] Additionally, supramolecular polymerizations can be controlled by the constant influx of energy or matter and thus maintained in far-from-equilibrium states (for example, induced gelation processes by consumption of a 'chemical fuel',[154] catalytic control over gel formation,[155] redox-mediated self-assembly[156] leading to self-oscillating supramolecular polymers[157] or enzymatic modulation of supramolecular helicity[158]).

One of the first in-depth investigations of a supramolecular polymerization controlled by underlying kinetic influences was reported by our group for the cooperative self-assembly of bis(merocyanine) dye **2** (Figure 5a).[119, 159] On addition of the poor solvent methylcyclohexane (MCH) to a solution of predominantly monomeric **2** in the good solvent tetrahydrofuran (THF) two different types of nanorod products (named '**H1** and **H2** aggregates' due to their hypsochromically shifted absorption bands) were observed and distinguished by atomic force microscopy (AFM) and their UV/vis and circular dichroism (CD) spectra (Figure 5b). At an MCH/THF volume ratio of 70:30, time-dependent UV/vis, CD and AFM studies showed the instantaneous formation of centrosymmetric dye pairs (directed by dipolar and π–π stacking interactions; Figure 5c) between the chromophores of monomeric **2** to give a random-coil supramolecular polymer (named the 'D state'). However, within about 14 min, six of these polymer chains intertwine to give extended helical nanorods (**H1**). Finally, as the time course of the supramolecular polymerization progressed, a total inversion of the CD spectrum was observed (supramolecular stereomutation) and a denser nanorod structure was formed (**H2**). When the MCH content was increased to 80% in the MCH/THF mixture, kinetically metastable

H1 was effectively trapped for days, which was explained by the strong electrostatic attraction between the dipolar merocyanine dyes in a low-polarity environment. Mechanistic studies revealed that the hierarchical self-assembly **D** → **H1** → **H2** requires the disassembly of the **H1** nanorods before the formation of **H2** (Figure 5c; **H1** is an 'off-pathway' intermediate, vide infra), which was also corroborated by majority-rules and sergeant-and-soldiers effect experiments in subsequent studies.[120, 159]

In another series of investigations, the hierarchical self-assembly of OPV **3** (Figure 5d) and its pathway complexity was investigated in great detail by the Meijer group.[29, 121-122] On injection of a monomeric solution of **3** in chloroform to an excess of the poor solvent MCH, **3** dimerized by self-complementary fourfold hydrogen bonding of its ureidotriazine units, followed by further assembly into helical π stacks. Stopped-flow measurements revealed that at 293 K and at low concentrations ($c_T \leq 9 \times 10^{-6}$ M) (*M*)-helical OPV assemblies were formed, while at higher concentrations in the initial stages of the self-assembly process, kinetically metastable (*P*)-helical aggregates appeared, which converted into the thermodynamically stable (*M*)-aggregates over time (Figure 5e).[29] A mathematical model with two competing nucleated growth pathways was introduced that accurately described the observed kinetics, revealing that metastable (*P*)-assemblies appear only in the initial stages of the self-assembly process at sufficiently high concentrations. Thus, (*P*)-nuclei are thermodynamically favored over (*M*)-nuclei, while (*M*)-aggregates are thermodynamically favored over (*P*)-aggregates. Hence, (*P*)-aggregates represent kinetically metastable off-pathway intermediates towards the formation of the thermodynamically stable (*M*)-helical polymers (on pathway; Figure 5f).

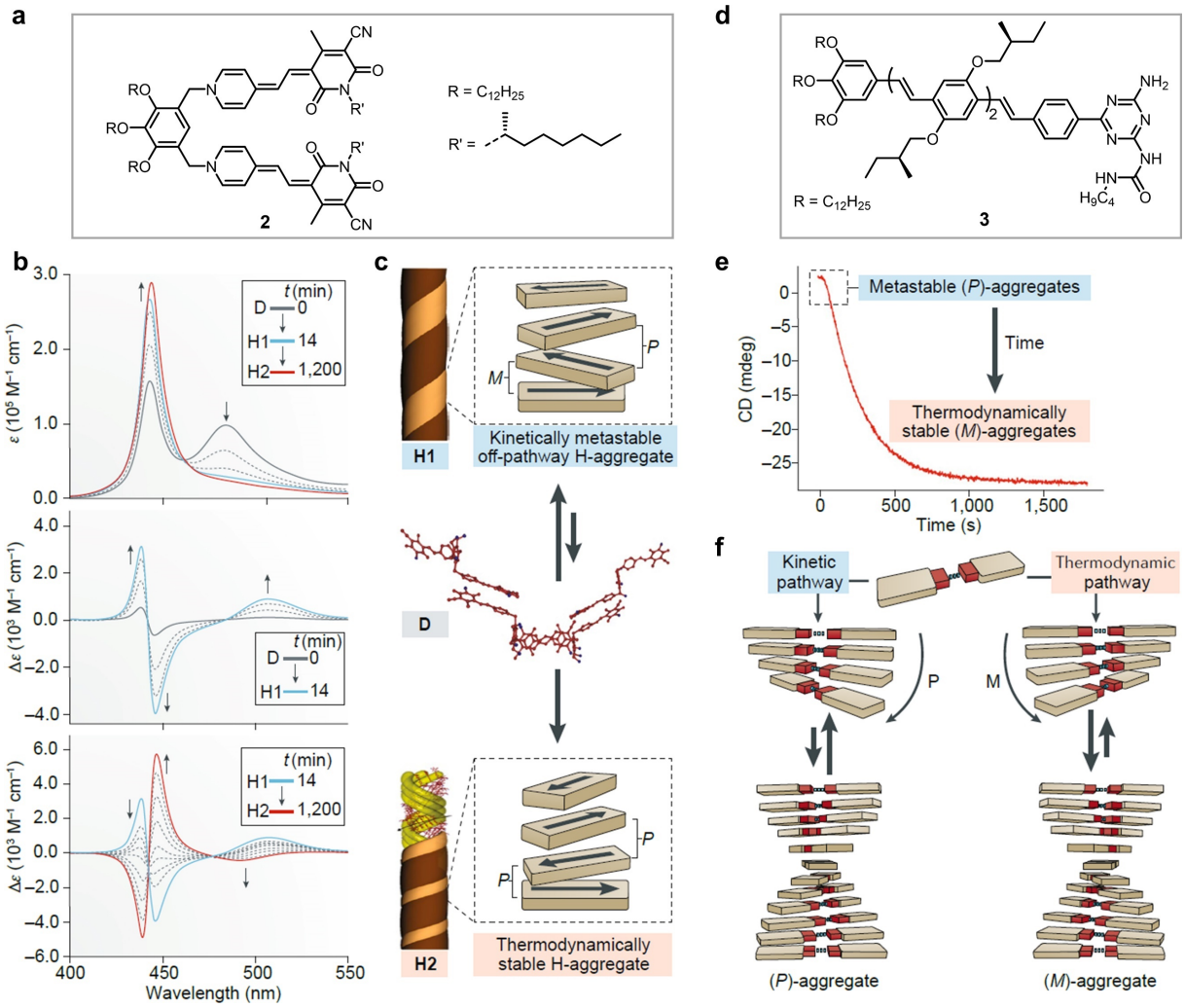

Figure 5. Chemical structures of bis(merocyanine) **2** (**a**) and OPV **3** (**d**). (**b**) Time-dependent UV/vis and circular dichroism (CD) spectra of the kinetically controlled supramolecular polymerization of dipolar bis(merocyanine) **2** into helical H-aggregates that involves a supramolecular stereomutation via a supramolecular polymer chain composed of dimer (**D**) units with negligible chiral bias. (**c**) Schematic representation of the three different supramolecular polymers that are involved in the supramolecular stereomutation of **2** shown in part **b**. (**e**) Time-dependent CD spectrum of the transformation of metastable (*P*)-helical oligo(*para*-phenylene vinylene) **3** aggregates into the thermodynamically stable state with (*M*)-helicity. (**f**) Schematic representation of the two competing cooperative aggregation pathways of OPV **3** directed by hydrogen-bonding and π–π stacking interactions.

From the mechanistic point of view, it is important to distinguish two possible situations for such supramolecular polymerizations. In the first, the initial product is an off-pathway aggregate which must disassemble before polymerization into the thermodynamically stable state. By contrast, in the second situation, the thermodynamically stable supramolecular polymer is directly built from the initial product by a rearrangement process without disassembly into monomers, and is thus called an 'on-pathway intermediate'.[160] Both of the

previously discussed examples, bis(merocyanine) **2** and OPV **3**, can be assigned to the former situation (that is, initial formation of an off-pathway aggregate). These studies demonstrate how profound knowledge of the thermodynamic characteristics together with detailed kinetic analysis paved the way for control of supramolecular polymerization pathways,[40, 160] yielding kinetic intermediates and products with distinct structural and functional properties.[161-164] By elucidation of the pathway complexity in a variety of supramolecular self-assembly processes,[112, 114, 165-166] a multitude of examples were discovered where different nanostructures (polymorphs) were formed depending on the choice of solvent, temperature and monomer concentration (*Chapter 2.5*).[47, 77, 128, 161, 167-168] In Figure 6, a selection of the most recent examples of pathway control by additives or external stimuli leading to the formation of (metastable) supramolecular polymorphs is summarized.[32, 37, 40]

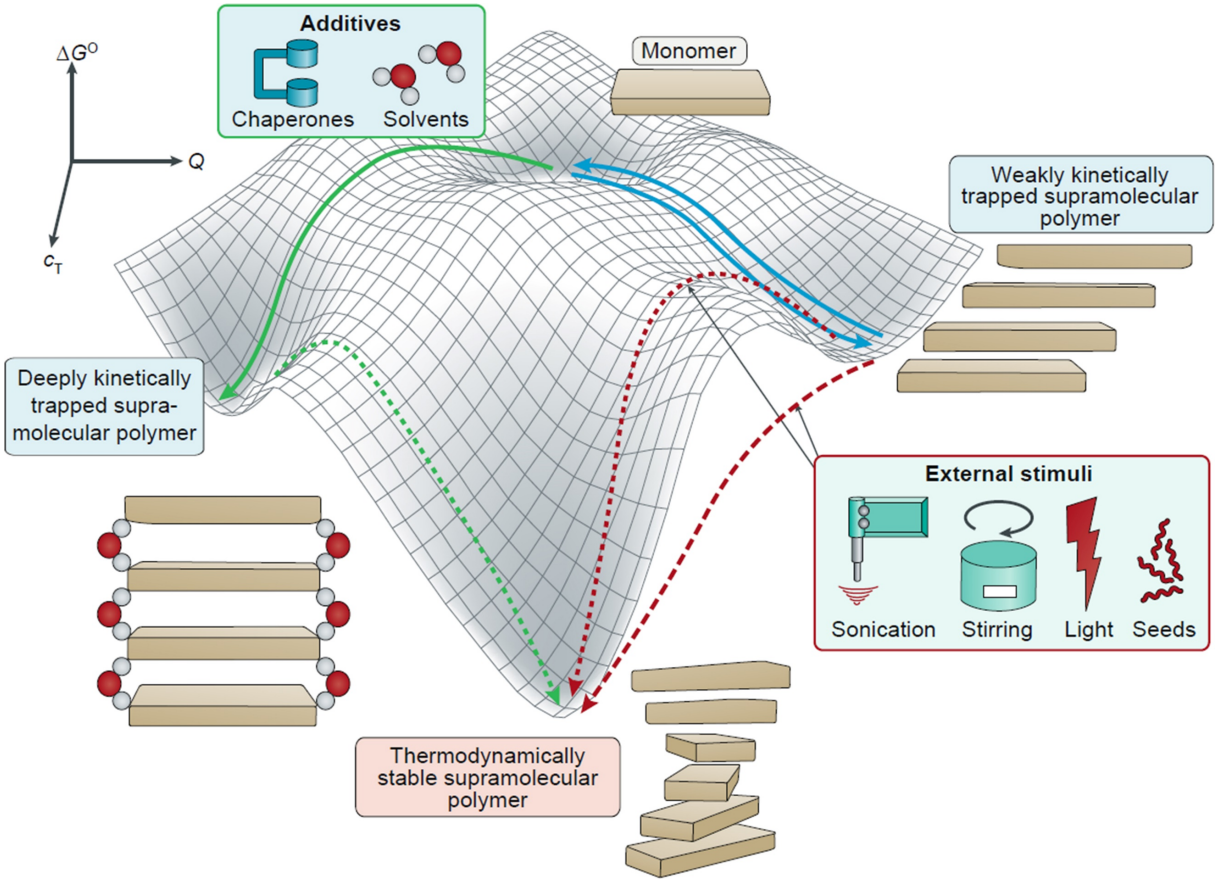

Figure 6. Qualitative energy landscape of supramolecular polymerization processes in which on increasing the concentration different kinetically trapped states or the thermodynamically stable supramolecular polymer are accessible.

In nature, protein self-assembly processes frequently occur under the control of 'additives' called 'molecular chaperones'.[169-170] Many chaperone families use energy released from the

hydrolysis of adenosine triphosphate to assist folding and unfolding or to prevent or reverse aggregation of their substrates and hence control the supramolecular pathway of protein self-assembly towards the native state.[169-171] Such additive-controlled supramolecular pathways indicated by green arrows in Figure 6 have also been reported for artificial supramolecular systems, yet in a much less sophisticated way than in nature.

In the simplest case, the addition of solvents and the order of addition serve as modulators for supramolecular polymerizations.[32, 147] The Rybtchinski group studied the profound effect of water as a cosolvent in supramolecular polymerizations and showed that a PBI-terpyridine complex in THF/water solutions with high water contents remained in a kinetically trapped state, while a higher THF amount led to rapid equilibration and the formation of the thermodynamically stable supramolecular polymer (Figure 6, dotted green arrow).[146] Recently, Meijer and coworkers reported that the aggregation pathway can be modulated by tiny amounts of water that influence the energy landscape of a tetraamide-substituted biphenyl derivative with three accessible polymorphs.[172] For low water content (8 ppm), only a single polymorph is produced in MCH on cooling, whereas with 47-ppm water, two additional polymorphs are formed in which either 0.5 or 2 equivalents of water are incorporated into the respective supramolecular structures. This group has also shown that hydrogen bond-mediated co-assembly and subsequent removal of (*S*)-dibenzoyl tartaric acid directs the supramolecular polymerization of OPV **3** (Figure 5d) towards a kinetically metastable aggregate.[29] As shown by Aida and coworkers, in the most extreme case, the typical thermal signature of enthalpy-driven supramolecular polymerization (that is, disassembly into monomers on heating) can be altered by hydrogen-bond donor solvents such as *n*-hexanol towards a thermally bisignate supramolecular polymerization with aggregates at low and high temperatures and monomers at intermediate temperatures.[113]

Furthermore, external stimuli such as ultrasonication,[42, 77] stirring,[42, 76, 173] irradiation[153, 174] and seeding (*Chapter 2.4*), have been used to either generate (Figure 6, blue arrows) or, more frequently, transform kinetically trapped species into different kinetically or thermodynamically stable supramolecular polymers (Figure 6, dotted and dashed red arrows). In this regard, stirring might be a valuable tool to select supramolecular pathways, as convincingly demonstrated by the seminal work of Ribó et al., who showed that vortex stirring on slow rotary evaporation of a solution of an achiral porphyrin led to the preferential formation of aggregates with a helicity that was dictated by the vortex direction.[173] It was also reported that stirring increases or decreases the transformation rate of kinetically trapped nanoparticles into off-pathway nanofibers or on-pathway nanosheets, respectively, which might result from

a disruption of the kinetically metastable nanoparticles.[42] External stimuli can also be applied to generate a kinetically metastable, transient product from the thermodynamically stable ribbon-like assembly as demonstrated by the De Cola group.[153] They studied a luminescent platinum(II) complex which forms a kinetic, a transient, and a thermodynamic nanocrystalline self-assembly product in water/dioxane mixture with distinct emission properties that allowed real-time visualization of the self-assembly processes. Notably, such nanocrystalline self-assembly products are strictly speaking no supramolecular polymers.[12] On irradiation of the thermodynamically stable nanocrystals with intense laser light, they are quantitatively converted into the unstable transient assemblies. Furthermore, the kinetic polymorph could be transformed into its thermodynamically stable assembly by addition of seeds (small aggregate fragments) of the thermodynamic product, which eliminates the energy barriers for the interconversion (Figure 6, dashed red line). Such seed-induced supramolecular polymerizations that usually bear characteristics of conventional living polymerizations[175] constitute a groundbreaking development in the field of supramolecular chemistry for the fabrication of highly ordered supramolecular polymers with small polydispersities (PDI) and tailored functional properties.[41, 43-44] Accordingly, the next chapter is dedicated to this exciting new research avenue of seeded (SSP) and seed-induced living supramolecular polymerization (LSP).

2.4 Seeded and Living Supramolecular Polymerization

Seed-induced LSP essentially resembles covalent living polymerization, a term coined by Szwarc in 1956.[176] A covalent living polymerization is a special case of a chain-growth polymerization in which inactivated monomers react with suitable initiators to produce chain ends that always remain active for further monomer addition, while termination or chain-transfer reactions are either slow or ideally completely absent.[175, 177]

To conceptually understand this approach for its supramolecular counterpart, LSP, we must first discuss its features in some more detail: When the initiation of a LSP is precisely controlled by the addition of seeds larger than the critical nucleus size (Figure 7a) in the presence of a sufficiently high nucleation barrier (Figure 4b), undesired spontaneous nucleation may be prevented and the supramolecular system is directly shifted into the elongation phase (Figure 7b, dark grey arrows), where a chain growth-type addition of monomers occurs from the seed termini.[41, 178]

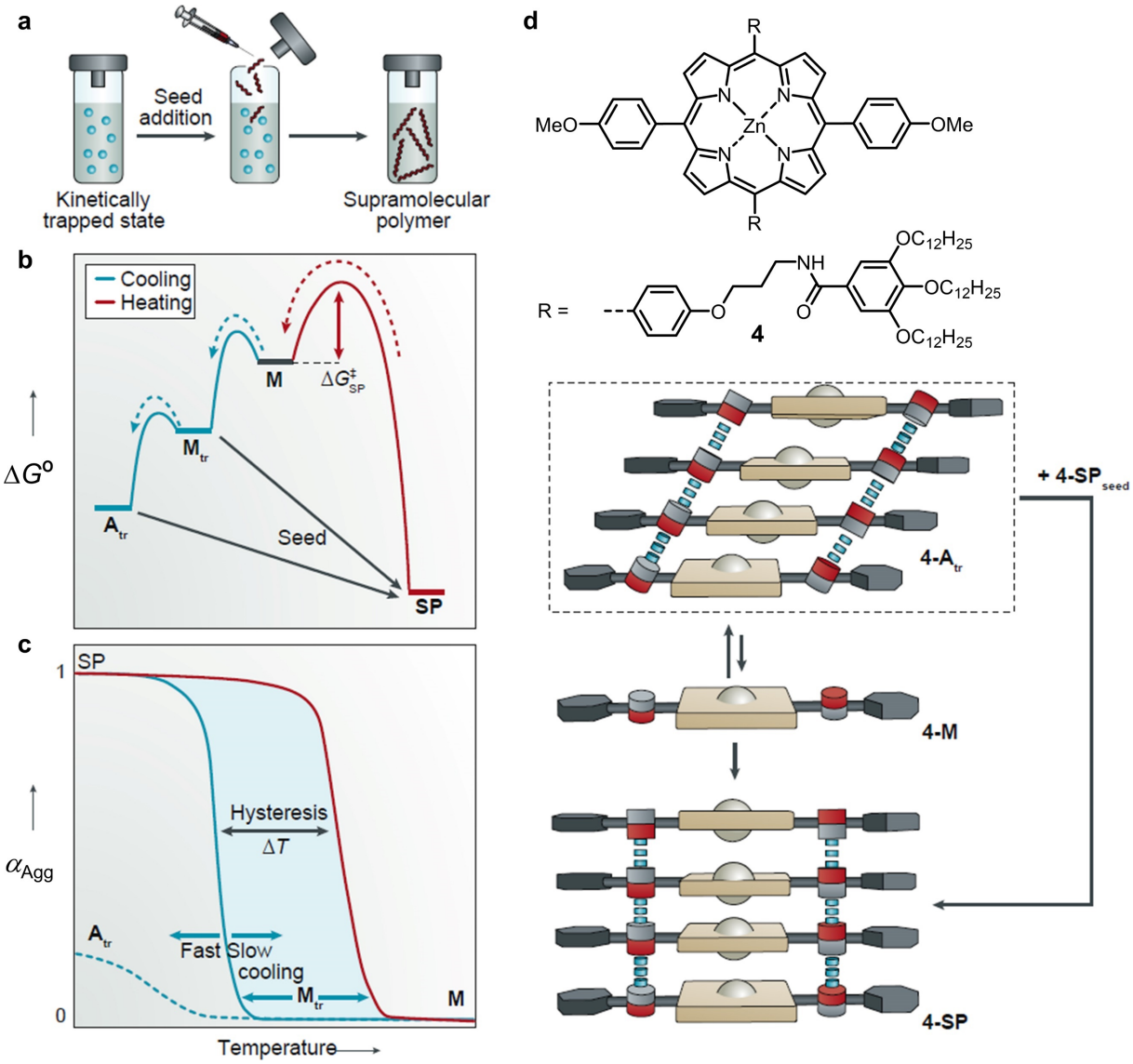

Figure 7. (**a**) Schematic illustration of a seeded supramolecular polymerization (SSP) performed by the addition of seeds (red) to a solution of a kinetically trapped state (blue). (**b**) Qualitative Gibbs free energy diagram of a supramolecular polymerization with a monomer (**M**) that can form either a kinetically trapped off-pathway monomer ($\mathbf{M_{tr}}$) or an aggregate ($\mathbf{A_{tr}}$) and the thermodynamically stable supramolecular polymer (**SP**). (**c**) Temperature-dependent degree of aggregation α_{Agg} of a kinetically controlled supramolecular polymerization in which the kinetically trapped state is generated on cooling of a monomer solution according to part **b**. α_{Agg} refers to the thermodynamically stable **SP**. (**d**) Seeded and living polymerization of zinc porphyrin derivative **4**.[41] The cartoons depict the relative arrangements of **4** within its different aggregates.

Due to the cooperative aggregation mechanism required for a seeded supramolecular polymerization (SSP), the resulting supramolecular polymer should always remain active for further monomer addition (since $K_E > K_N$), which means that most SSPs display a living character.[25-26] However, it should be emphasized that supramolecular polymerizations should be termed 'living supramolecular polymerization' only if multicycle experiments unequivocally

prove that the aggregate termini are active for further supramolecular polymerization after the first SSP cycle. The successive growth over time should be followed by both spectroscopic techniques to reveal the kinetics and microscopic techniques to prove the structural growth in a living manner. In the absence of such a proof, the supramolecular polymerization is called "seeded supramolecular polymerization". Several prerequisites have to be fulfilled to perform a seed-induced LSP of monomeric building blocks:[43] (1) supramolecular polymerization has to be kinetically controllable to retard spontaneous supramolecular polymerization, which is referred to as 'kinetic trapping' (Figure 7b,c); (2) the supramolecular polymerization must occur through a cooperative nucleation-elongation mechanism where nucleation is much slower than elongation to ensure that polymer growth by 'incorporation' of the kinetically trapped species occurs only from the seeds' termini; and (3) the seeds can be externally prepared (for example, by ultrasonication of the elongated supramolecular polymer nanofibers). To obtain supramolecular polymers with narrow dispersity that are stable for a certain time, it is furthermore crucial that chain exchange and reshuffling[129] are both slow processes. Usually, the biggest hurdle for the establishment of LSP of a building block is to have experimental conditions (solvent, temperature, processing methods and so on) that lead to a kinetically delayed supramolecular polymerization. Such a lag phase can be easily noticed by the appearance of a thermal hysteresis[41, 43, 76, 179-181] (Figure 7c) between the heating cycle and the cooling cycle during temperature-dependent measurements (in most cases UV/vis or CD spectroscopy).

While heat-induced disassembly of supramolecular polymers SP usually proceeds under thermodynamic control (Figure 7b, dashed red line), cooling with high cooling rates (more than 5 K min^{-1}) often leads to the formation of kinetically trapped states since the structural changes of the molecules required for supramolecular polymerization are too slow for such rapid temperature changes.[43, 76] Thus, instead of supramolecular polymerization, the formation of trapped monomers ($\mathbf{M_{tr}}$) or trapped aggregate species ($\mathbf{A_{tr}}$) is observed (Figure 7b, dashed blue lines). This behaviour is well known for crystallization processes where rapid cooling often leads to the formation of amorphous agglomerates instead of crystals.[46] However, for pristine supramolecular polymerizations that is, the formation of a single chain of self-assembled molecules by a small number of specific intermolecular interactions (a different situation from the larger surface areas important in crystallization), there is a conceptual difference. In this regard, several seminal articles showed that such a thermal 'hysteresis window' (Figure 7c) which provides an effective range for the performance of SSPs can be tuned by the cooling rate, solvent composition and concentration of the kinetically trapped state.[41, 43, 179, 182] Usually,

faster cooling rates lead to a more efficient kinetic trapping and to an 'opening' of the hysteresis window, while slow cooling rates favor an equilibration of the system towards the thermodynamically stable state (that is the thermal hysteresis is narrowed) (Figure 7c). Conditions that favor formation of a kinetically trapped off-pathway monomer $\mathbf{M_{tr}}$[43] (that is, low concentration) lead to a widening the hysteresis window, while the formation of kinetically trapped off-pathway aggregates $\mathbf{A_{tr}}$ is facilitated by increasing concentration.[41, 75] Such amorphous off-pathway aggregates might be kinetically stable over long periods and either do not or only slowly transform into the respective thermodynamically stable supramolecular polymer. Hence, in a plot of the degree of aggregation (α_{Agg}), referring to the thermodynamically stable supramolecular polymer, versus temperature, $\alpha_{Agg} = 1$ might not be reached (Figure 7c). The role of solvent polarity is not always obvious because the relative Gibbs free energies of the supramolecular states as well as nucleation barriers are both influenced by the solvent composition.[183-184]

Conceptually important input for the control of supramolecular polymerization processes was provided by Winnik and Manners (Figure 3), who studied the formation of cylindrical block copolymer (BCP) micelles from covalent BCPs by 'living' crystallization-driven self-assembly (CDSA),[185-186] and by Aida and coworkers, who prepared a supramolecular p–n heterojunction (BCP) by stepwise co-assembly of dispersed hexabenzocoronene derivatives.[187] Combining this knowledge with mechanistic insights into biological supramolecular polymerization processes such as amyloid fibril formation observed in prion infection[188-189] and the previously discussed research on the control of self-assembly pathways in supramolecular polymerizations under kinetic control, Sugiyasu and Takeuchi established the first seeded LSP using a rather simple dye molecule in 2014.[41] They exploited the aggregation behaviour of zinc porphyrin **4**, which forms two different aggregates – a kinetically trapped J-aggregate $\mathbf{4\text{-}A_{tr}}$ and the thermodynamically stable supramolecular polymer **4-SP** (H-aggregate) as depicted in Figure 7d. These two dye aggregates are clearly distinguishable by their different absorption maxima that are either bathochromically shifted (J-aggregate) or hypsochromically shifted (H-aggregate) with regard to the monomer absorption maximum. On rapid cooling of a hot MCH solution, **4** initially self-assembles into kinetically trapped nanoparticulate J-aggregates $\mathbf{4\text{-}A_{tr}}$ in an isodesmic fashion as a result of the lower activation barrier compared with that for the second aggregation pathway, which proceeds according to the nucleation-elongation mechanism and leads to the thermodynamically stable supramolecular polymer **4-SP**. In the absence of mechanical agitation (such as stirring), these off-pathway J-aggregates are stable for days because of a low monomer concentration that does not reach the critical concentration

needed for nucleation of **4-SP**. However, on addition of presonicated H-aggregate fragments (**4-SP$_{seed}$**), monomeric **4** (**4-M**) is 'consumed' from its equilibrium with **4-A$_{tr}$** and the transformation into **4-SP** (Figure 7b,d) is accomplished within hours depending on the amount of seed added. By this approach, highly ordered supramolecular polymers with small PDIs of about 1.1 were realized. Furthermore, in a multicycle UV/vis experiment, the transformation of **4-A$_{tr}$** to the thermodynamically stable **4-SP** was demonstrated by the plotting of the time-dependent changes in absorbance at a particular wavelength after successive addition of kinetically trapped **4-A$_{tr}$** to seeds (first cycle) or to the resulting polymer solution of **4-SP** (second to fourth cycle). After each polymerization cycle, the characteristic absorption (at a given wavelength) of **4-SP** was 'restored', concomitant with an increase of the polymer length as evidenced by dynamic light scattering and AFM studies, which clearly proved the living character of the supramolecular polymerization of **4**. Furthermore, AFM studies revealed that polymer growth of nanofibrous **4-SP** occurred from the termini of **4-SP$_{seed}$** by the incorporation of monomers that are removed from the dynamic equilibrium with **4-A$_{tr}$**.[41, 178] While the aforementioned experiments were constrained to the formation of 1D nanofibers (**4-SP**), the same group recently reported control over 1D and two-dimensional (2D) SSP for a slightly modified zinc porphyrin derivative bearing hexyloxy or heptyloxy groups instead of methoxy substituents at the phenyl rings attached to the porphyrin core.[42]

While this first example relied on ill-defined off-pathway aggregates **A$_{tr}$**, several ingenious strategies have recently been developed to encode the molecular information for kinetic trapping into out-of-equilibrium states to achieve programmable LSP (Figure 8).[43-44, 75-76, 174, 180, 190-191] In 2015, our group,[43] as well as Aida and Miyajima's groups,[44] introduced the first examples for the kinetic trapping of molecules by the formation of intramolecular hydrogen bonds instead of off-pathway aggregates (Figure 8a,b). Amide-appended **PBI-1** self-assembles according to a nucleation-elongation mechanism.[43] The structure shown in Figure 8a is that of a kinetically trapped monomer (**PBI-1-M$_{tr}$**) in which intramolecular hydrogen bonds are formed between the amide protons and the adjacent imide oxygens. The accessibility of such a structure results in a pronounced hysteresis effect (Figure 7c) between the thermodynamically controlled heat-induced disassembly and the kinetically controlled assembly process that occurs on cooling. Within the hysteresis loop, the addition of small nanofibrous seeds obtained by ultrasonication of **PBI-1-SP** instantaneously induces the transformation of **PBI-1-M$_{tr}$** into **PBI-1-SP** according to an LSP mechanism[43] (Figure 7b,c).

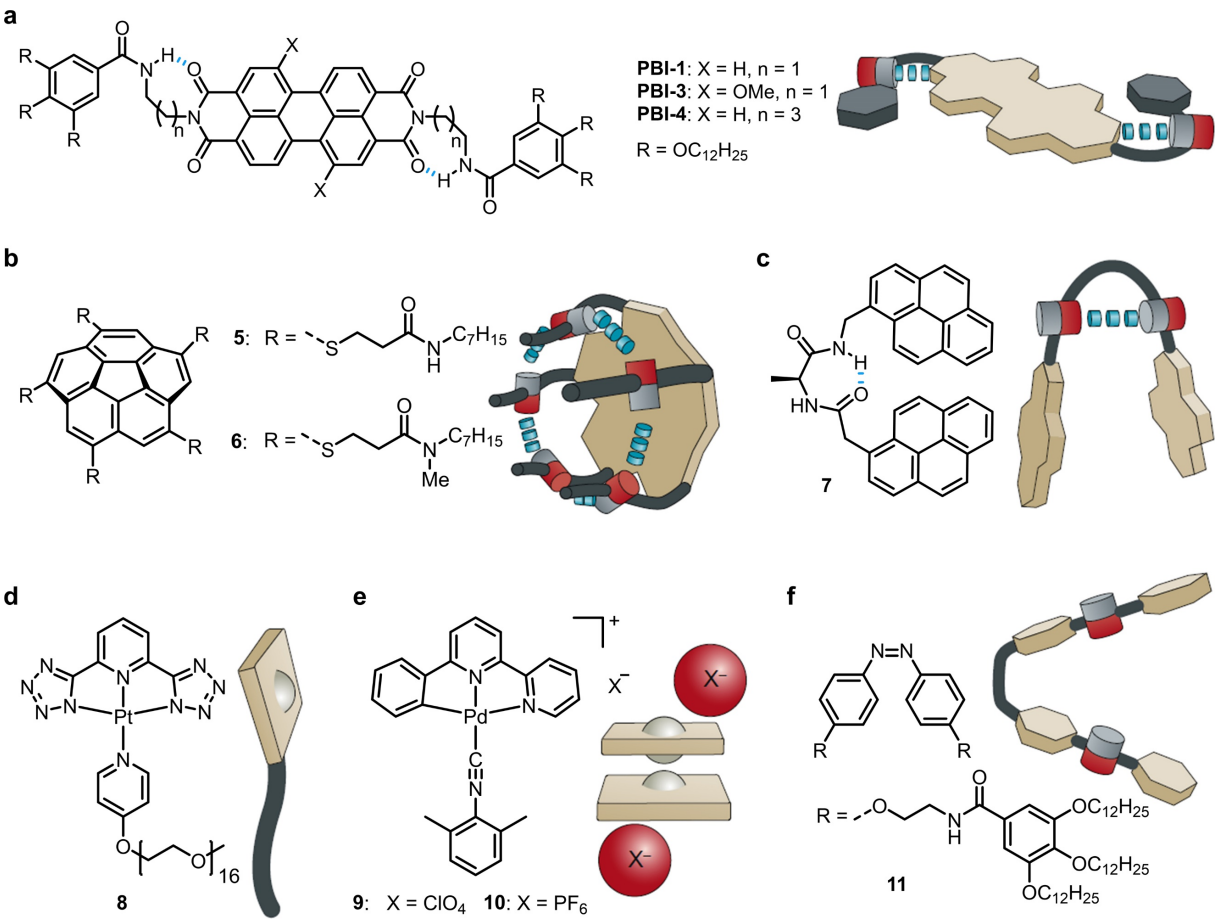

Figure 8. (**a**) Kinetic trapping of **PBI-1, PBI-3** and **PBI-4** by formation of intramolecular hydrogen bonds.[43, 75-76] **b**) Structures of deeply kinetically trapped corannulene derivative **5** on fivefold intramolecular hydrogen bonding and molecular initiator **6**.[44] (**c**) Kinetic trapping of pyrene-substituted diamide **7** by formation of an intramolecular hydrogen bond and folding.[180] (**d**) Structure of platinum complex **8** undergoing living crystallization-driven self-assembly.[190] (**e**) Counterion-modulated kinetic trapping of palladium complexes **9** and **10**.[191] (**f**) Kinetic trapping of azobenzene dye **11** regulated by photoisomerization.[174]

The greater solubility of **PBI-3** (with two methoxy groups in the bay region) allowed the kinetics of such an LSP of a PBI molecule to be analyzed by multicycle UV/vis spectroscopy. Successive additions of kinetically trapped species led to the growth of thermodynamically stable, emissive nanofibers with J-type exciton coupling.[76] In a further study, the effect of the length of the alkyl spacer between the imide and amide nitrogen atoms on the aggregation pathways of the respective (bay-unsubstituted) PBI molecules was elucidated.[75] Whereas **PBI-1** can be kinetically trapped in a monomeric state through the formation of intramolecular hydrogen bonds, monomers of the analogous butylene-tethered **PBI-4** instead self-assemble into kinetically trapped amorphous aggregates (Figure 8a).[75]

Whereas the kinetically trapped states of these PBI derivatives were found to be metastable and could only retard (but not inhibit) the spontaneous supramolecular polymerization, C_5-symmetric corannulene derivative **5** (Figure 8b) carrying amide-appended thioalkyl side chains forms a kinetically deeply trapped monomer by fivefold intramolecular hydrogen bonds between the amide groups (**5-M$_{tr}$**) in nonpolar MCH, thereby completely preventing the spontaneous supramolecular polymerization.[44, 192] With this uniquely designed corannulene derivative, Aida, Miyajima and coworkers realized the first chain-growth supramolecular polymerization using molecular initiators instead of an SSP (Figure 8b).[44] In this case, supramolecular polymerization is initiated by the addition of the *N*-methylated analogue **6**, which cannot form intramolecular hydrogen bonds. However, **6** forms intermolecular hydrogen bonds with a molecule of **5-M$_{tr}$**, which is itself then 'opened' to form further intermolecular amide-amide hydrogen bonds. Thus, **6** initiates the supramolecular polymerization of **5-M$_{tr}$** leading to the formation of 1D nanofibers (**5-SP**) with small PDIs between 1.2 and 1.3. The supramolecular polymer continuously grew when a fresh feed of **5-M$_{tr}$** was provided, which was verified by dynamic light scattering and diffusion-ordered NMR measurements, confirming the living character of the SSP. In further experiments, initiators bearing a stereogenic center proximal to the amide groups were used, allowing the optical resolution of a racemic mixture of kinetically trapped chiral derivatives of **5-M$_{tr}$**.[44]

Whilst this initiator-controlled LSP remains a unique example (in all other cases LSP was initiated by seeds rather than initiator molecules), the method of creating a kinetically metastable state either by off-pathway aggregation or by intramolecular hydrogen bonding in the cooperative self-assembly of organic dye molecules and subsequent seed-induced LSP already proved to be quite general. It has meanwhile been applied for several other compound classes, such as amide-appended *N*-annulated perylenes[181-182] and naphthalene diimides[184, 193] or pyrene-substituted amino acid-based diamide **7**, for which a new kinetic trapping concept based on a combination of an intramolecular hydrogen bond and folding was reported (Figure 8c).[180] A similar kinetic trapping strategy was applied by Ogi and Yamaguchi for an amide-functionalized diketopyrrolopyrrole dye leading to a seed-induced LSP in aqueous media.[194]

Further examples of LSP with metal-organic compounds were reported by De Cola and Manners[190, 195] for square-planar amphiphilic Pt^{II} complex **8** (Figure 8d), which polymerizes according to a 'living' CDSA mechanism and by Che et al. for pincer Pd^{II}–isocyanide complexes **9** and **10** modulated by the respective counteranions (Figure 8e).[191] In the latter case, ClO_4^- counteranions delay the supramolecular polymerization of the positively charged Pd entities into thermodynamically stable 1D chains with short Pd^{II}–Pd^{II} distances owing to the

formation of counteranion-blocked cation pairs (kinetically trapped state). By changing the counteranion to PF_6^-, a fast supramolecular polymerization to the thermodynamically stable 1D chain polymer was observed, which then served as a seed for the elongation of the kinetically trapped Pd^{II}–ClO_4 complex into its respective polymer. Another strategy for establishing an LSP was provided by Yagai, Sugiyasu and Takeuchi, who coupled the photoisomerization of azobenzene chromophore **11** with its supramolecular polymerization (Figure 8f).[174] The dye is kinetically trapped as a monomer in its *cis* conformation. On irradiation with visible light, the *trans* form is generated and is prone to LSP.

The LSP approach is not restricted to processes in solution. Besenius, Ravoo and coworkers demonstrated the production of surface-anchored peptide-based supramolecular polymers by stepwise addition of oppositely charged peptide-based comonomers (that is, by charge regulation of the active chain ends).[196] Later, Besenius, Hermans and coworkers described that the hydrogelation of a benzene-1,3,5-tricarboxamide–peptide conjugate could be initiated at the solid-liquid interface of an acidified poly(dimethylsiloxane) (PDMS) surface.[197] Further recent advancements in the field of LSP were described by Balasubramanian, George and coworkers, who demonstrated that transient self-assembly and seed-mediated LSP of phosphate receptor-functionalized monomers can be controlled biomimetically by the consumption of the chemical fuel ATP.[198] Vemula, George and coworkers later showed that the living growth of a charge-transfer amphiphile constructed from a potassium coronene salt donor and a methyl viologen-derived acceptor could be modulated by the addition of several amines.[199]

2.5 Polymorphism in Supramolecular Polymerization

The phenomenon of polymorphism – defined as the ability of a chemical compound to exist in more than one crystalline form – was recognized almost 200 years ago by Mitscherlich,[200] who discovered different crystal forms of the same compound in a number of phosphate and arsenate salts.[46, 48, 201] Ten years later, Liebig and Wöhler reported the first example of a polymorphic organic compound, that is benzamide.[202-203] Up until now, knowledge on polymorphism has tremendously increased and many aspects like conformational,[204] disappearing[205] and concomitant polymorphs[206] or polymorphism in the context of crystal engineering[47, 54] have been addressed.[201, 207]

Notably, polymorphism is not restricted to the crystallization of inorganic and organic small molecules but can also be observed during the supramolecular assembly of nascent polypeptide chains into biologically active proteins.[171, 208] An important class of naturally occurring

polymorphic proteins are amyloid fibrils which are involved in several diseases including Alzheimer's or Parkinson's disease.[171, 209-210] In this regard, detailed studies on the fibrillation of hen egg white lysozyme (HEWL) which is homologous to human lysozyme revealed a rich polymorphism.[211-212] Upon incubation at 90 °C at a pH = 2, HEWL amyloid-aggregation first yielded amyloid-like filaments which assemble laterally into twisted ribbons and further into helical ribbons. These helical ribbons progressively close into nanotubes.[211-212] Further examples of supramolecular polymorphism in biological systems include the diverse assembly of tubulin, the main protein component of microtubules,[213] or the pH- or ionic-strength-dependent transformations between tubular polymers of the tobacco mosaic virus as demonstrated by seminal work of Klug (Figure 3).[214-215]

In recent years, kinetic pathway control of supramolecular polymerizations paved the way for the identification of a variety of artificial supramolecular systems displaying morphological transitions due to changes in experimental parameters such as solvent, temperature or concentration or in response to external stimuli (*Chapter 2.3*).[12-13, 15, 32, 37, 40] From these studies, two recently published examples were extracted where supramolecular polymorphism was investigated in great detail.[128, 167] Inspired by polymorphism in biological systems, Palmans, Lin, Meijer and coworkers designed carboxylic-acid functionalized water-soluble BTA **12** which shows reversible temperature-dependent supramolecular polymorphism in water (Figure 9).[128]

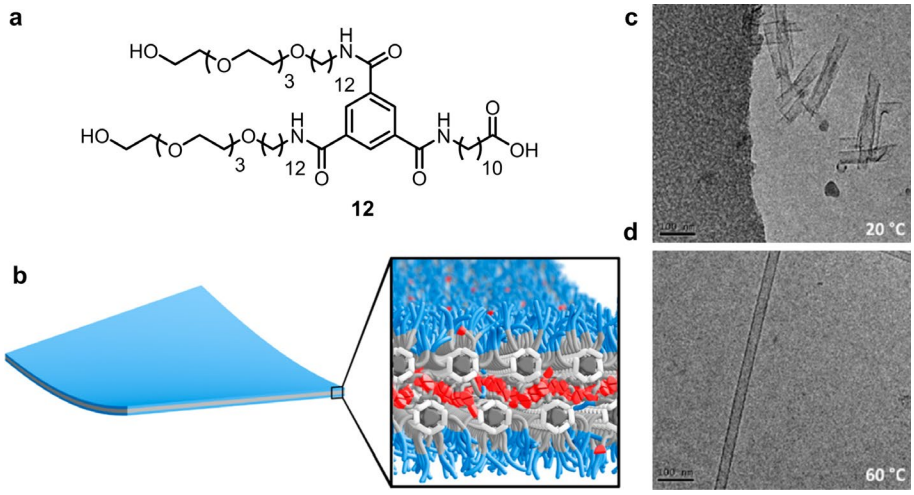

Figure 9. (**a**) Chemical structure and (**b**) hypothesized packing model of BTA-derivative **12**. Cryo-TEM images of a centrifuged sample of **12** at 293 K (**c**) and a sample heated to 333 K (**d**) in water, respectively. Adapted with permission from reference[128] (https://pubs.acs.org/doi/abs/10.1021/jacs.8b07697). Copyright 2018 American Chemical Society.

The self-assembly of BTA **12** into ribbons, membranes and hollow nanotubes is governed by a maximization of hydrophobic interactions between the aliphatic spacer units providing a local environment where pairwise hydrogen-bond formation between the BTA's carboxylic acid groups as well as triple hydrogen-bonding of the amide moieties can be realized (Figure 9b). A combination of different experimental techniques such as small angle X-Ray scattering, cryogenic transmission electron microscopy (Cryo-TEM, Figure 9c,d) and UV/vis spectroscopy revealed that **12** forms a mixture of membranes and tubes at room temperature (Figure 9c) while heating to 333 K resulted in a structural transition into perfectly straight hollow nanotubes (Figure 9d). Hydrogen-deuterium exchange mass spectrometry studies indicated that the overall packing of the BTA strands within the membranes and nanotubes becomes more flexible and accessible to solvent exchange at higher temperatures. This ultimately resulted in an ordering of ill-defined species into straight nanotubes upon heating which was attributed to the alleviation of some strain energy in the assemblies.[128] Notably, a tailored molecular design was the crucial prerequisite for achieving supramolecular polymorphism and slight modifications of the aliphatic carboxylic acid chain, namely shortening or introduction of water-soluble oligo(ethylene glycol) units, resulted in strikingly different self-assembly behaviors without such pronounced supramolecular polymorphism.[128]

Another elaborate study on supramolecular polymorphism was recently provided by Sánchez and Fernández who studied the self-assembly behavior of oligo(phenylene ethynylene)-based dichloro(bis)pyridyl-Pt^{II} complex **13** (Figure 10).[167] Pt-complex **13** polymerizes in MCH into two different metallosupramolecular polymers, namely a slipped state A which is stabilized by unconventional N−H···Cl−Pt interactions and a pseudoparallel state B with N−H···O_{alkyl} interactions (Figure 10a) as evidenced by FT-IR and NMR spectroscopy as well as quantum chemical calculations.[167] AFM revealed flexible nanofibers for state A (Figure 10b) while state B shows longer, thicker and more rigid fibers with a strong bundling tendency (Figure 10c). Furthermore, the authors were able to control the supramolecular pathways towards state A and B by fine-tuning the temperature, concentration and cooling rate which allowed them to construct a phase diagram of the investigated system (Figure 10d). While low concentrations ($c_T \leq 5.0 \times 10^{-5}$ M) and fast cooling rates (2 K min^{-1}) favor the formation of the slipped polymorph A, higher concentrations ($c_T > 5.0 \times 10^{-5}$ M) and slow cooling rates (0.1 K min^{-1}) stabilize the pseudo-parallel polymorph B.

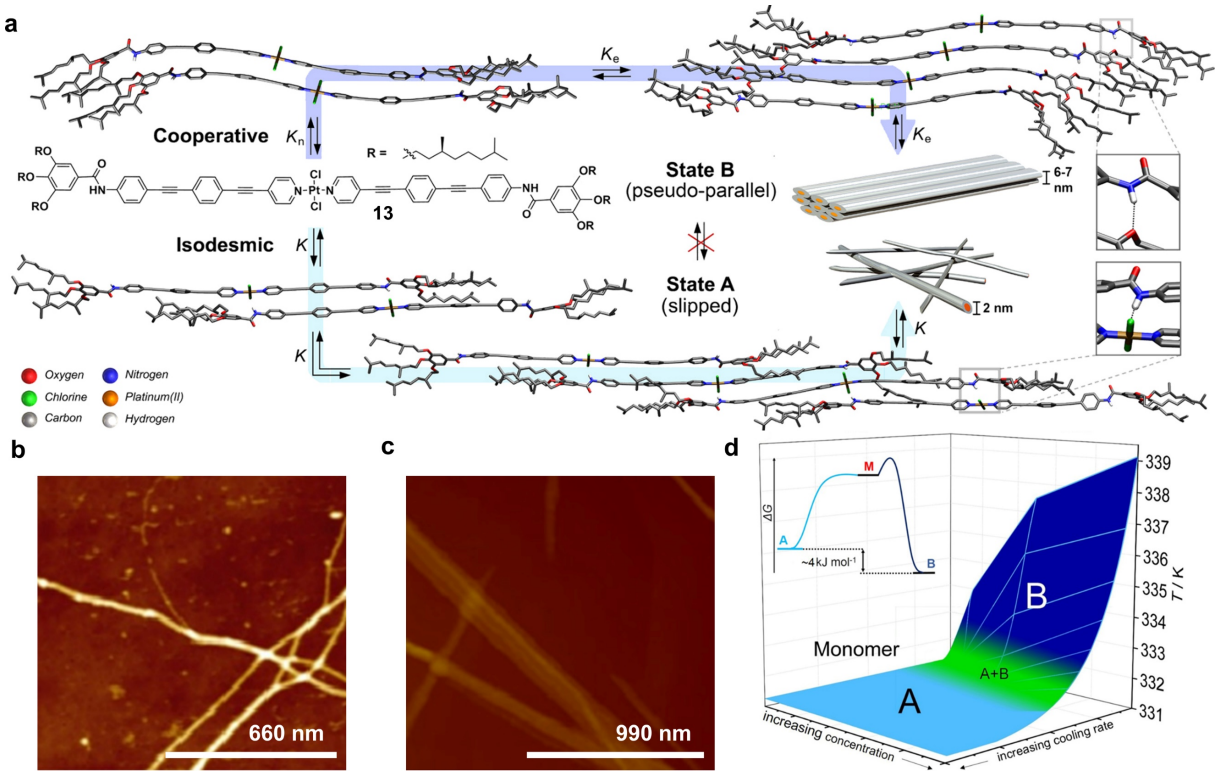

Figure 10. (**a**) Chemical structure of Pt complex **13** and calculated packing models of **13** (slipped state A vs. pseudoparallel state B). AFM height images of species A (**b**) and B (**c**) as well as a phase diagram (**d**) illustrating the self-assembly behavior of **13**. Adapted with permission from reference[167] (https://pubs.acs.org/doi/abs/10.1021/jacs.8b11011). Copyright 2019 American Chemical Society.

Most interestingly, at an intermediate concentration of $c_T = 5.0 \times 10^{-5}$ M and cooling rate of 0.5 K min^{-1}, both supramolecular polymerization pathways are accessible resulting in the concomitant appearance of both polymorphs A and B which are kinetically stable for weeks. Only upon annealing, polymorph A slowly transforms into the thermodynamically more stable supramolecular polymer B.[167]

These studies demonstrate that with tailored molecular building blocks valuable insights into polymorphism can be obtained by a supramolecular approach. While the aforementioned studies were devoted to achiral systems, control of the supramolecular polymorphism of chiral compounds and successive investigations of the self-assembly of racemic mixtures would be highly desirable for mechanistic studies of the crystallization of racemates at a lower level of hierarchy, namely 1D supramolecular self-assembly (*Chapter 2.6*).

2.6 Supramolecular Polymerization of Racemic Mixtures

Due to the recent advancements in the control of supramolecular polymerization pathways (*Chapter 2.3*) and characterization of supramolecular polymers,[25, 216] it seems likely that racemic mixtures of chiral building blocks showing different supramolecular polymorphs are well-suited to study the solid-state phenomena of conglomerate and racemic crystal formation at their origin. In general, crystallization of organic racemates affords in over 90% of all cases racemic crystals which can be further classified either as racemic compounds or solid solutions with a regular or random packing of the *R*- and *S*-enantiomers within the same crystal, respectively (Figure 11).[52, 217-218] However, in rare cases (< 10%) conglomerates are formed which are defined as mixtures of homochiral crystals containing only one of the two enantiomers present in a racemate (Figure 11).[219]

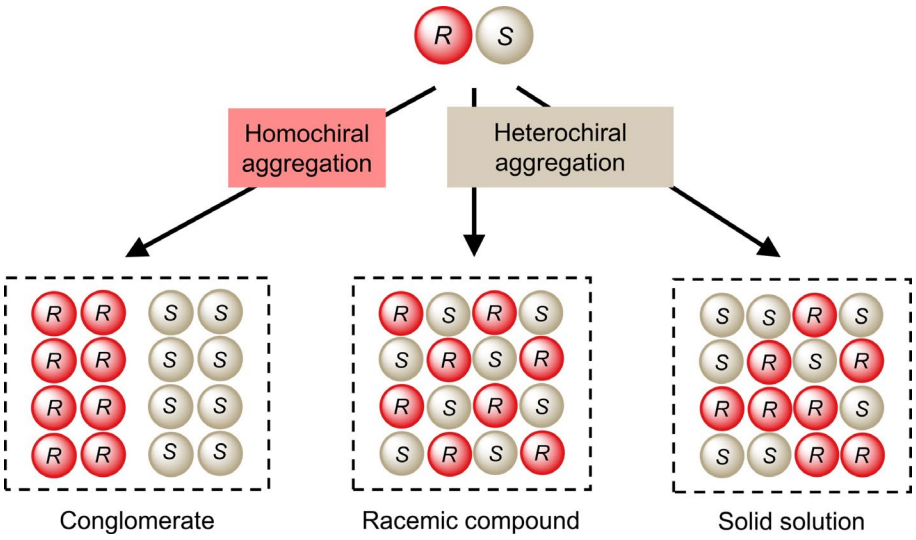

Figure 11. Schematic illustration of possible packing arrangements of *R*- and *S*-chiral molecules within crystals obtained by crystallization of racemates.

Comparing 3D crystallization with 1D supramolecular polymerization, conglomerate formation by homochiral aggregation is analogous to narcissistic self-sorting whereas racemic crystal formation is comparable to social self-sorting induced by heterochiral aggregation.[220-221]

Due to the paramount importance of 3D conglomerate and racemic compound formation for the purification of racemates in chemical industry,[222-225] considerable efforts were devoted to mechanistic investigations on the thermodynamics and kinetics of these phenomena.[226-230] However, these studies demonstrate that it still remains a major scientific challenge to understand nucleation well enough to predict whether a conglomerate or racemic crystal will

form.[227, 229] In this regard, reducing the complexity of 3D crystallization to 2D self-assembly on surfaces or 1D supramolecular polymerization might serve as a viable approach to gain deeper mechanistic insights into conglomerate and racemic crystal formation at the molecular level. For 2D conglomerate and racemic compound formation on surfaces,[218, 231] elaborate studies have been reported including homodimer formation of racemic cysteine on Au (110) surface[231-232] or the assembly of racemic heptahelicene on a Cu (111)[233] or Ag (100) surface.[234] A particularly interesting example at the intersection between 2D and 1D conglomerate vs. racemic compound formation was provided by De Feyter and Schenning.[235] The authors studied the self-assembly behavior of a racemic mixture consisting of OPV-phenylglycinamide derivatives **(*R*)-** and **(*S*)-14** (Figure 12) at the interface between 1-phenyloctane and highly oriented pyrolytic graphite (HOPG) by scanning tunneling microscopy (STM) and demonstrated a length-scale dependent formation of conglomerates and racemic compounds (Figure 12b,c).

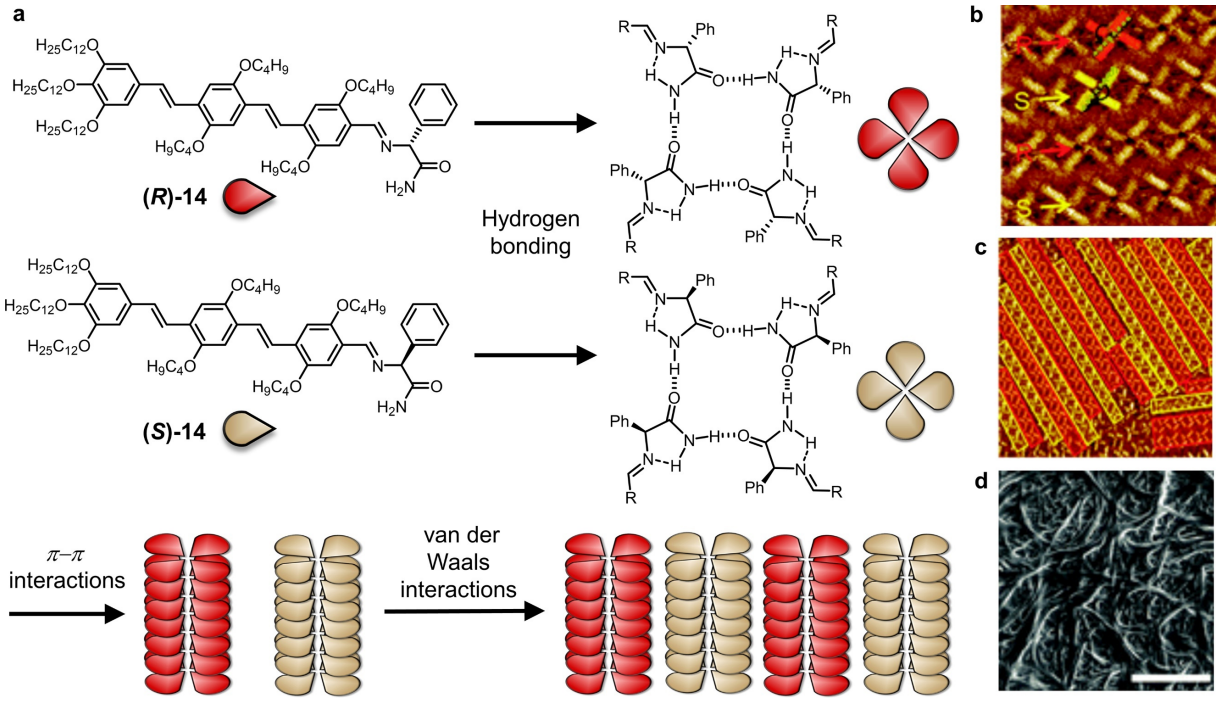

Figure 12. (**a**) Chemical structures and self-assembly behavior of OPV derivatives **(*R*)-** and **(*S*)-14**. STM images of the **(*R*)-** and **(*S*)-14** racemate at the 1-phenyloctane-HOPG interface showing tetramers (**b**) that further assemble into lamellar structures (**c**). Red and yellow rectangles indicate the lamellae formed by **(*R*)-** and **(*S*)-14**, respectively. (**d**) FESEM image of a dried gel of the racemate in octane. Adapted with permission from reference[235] (https://pubs.rsc.org/en/Content/ArticleLanding/CC/2013/C3CC45806G#!divAbstract). Copyright 2013 The Royal Society of Chemistry.

When the racemic mixture of **(*R*)-** and **(*S*)-14** is deposited on a HOPG surface, intermolecular hydrogen-bonding between the amide moieties of **(*R*)-** and **(*S*)-14** leads to the formation of homochiral counter-clockwise and clockwise twisted tetramers, respectively, which further polymerize due to $\pi-\pi$ interactions into enantiopure lamellae (Figure 12a−c). The enantiopure strands further aggregate into racemate bundles by heterochiral aggregation (Figure 12a,c). Hence, at the tetramer level, conglomerates are observed while at the lamellar level enantiopure nanofibers of **(*R*)-14** are surrounded by those of **(*S*)-14** suggesting a racemic compound.[235] Additionally, the self-assembly of the racemic mixture was studied in octane solution where gelation was observed at a concentration of $c_T = 5.0 \times 10^{-3}$ M resulting in an entangled fibrillar network as revealed by field emission scanning electron microscopy (FESEM, Figure 12d). Combining these studies with further AFM and temperature-dependent UV/vis results, the authors hypothesized that the racemic mixture shows in solution the same aggregation behavior as in the solid state.[235]

In contrast to conglomerate and racemic compound formation in two and three dimensions, knowledge on these phenomena in 1D supramolecular polymerization is mainly restricted to systems where either homochiral or heterochiral aggregates prevail and, hence, conglomerate and racemic supramolecular polymer formation within the same racemic mixture is rarely observed.[220-221, 236] One particularly profound mechanistic study on supramolecular conglomerate formation was reported by Percec and coworkes who elucidated the 1D and 3D assembly of a racemic mixture of dendronized cyclotriveratrylenes (CTVs) **(*R*)-** and **(*S*)-15** (Figure 13).[237]

In dodecane or *n*-butanol solution the racemic mixture polymerizes according to a nucleation-elongation mechanism into an 1:1 mixture of single-handed columns. 1D supramolecular conglomerate formation was indicated by temperature-dependent UV/vis spectroscopy revealing similar elongation temperatures of the racemic mixture and a half as concentrated solution of the enantiopure compounds. Further evidence was obtained by majority-rules experiments[238] that show an almost linear increase of the net helicity with increasing enantiomeric excess (*ee*) meaning that heterochiral aggregation is disfavored.[237] However, deeper structural and mechanistic insights into supramolecular conglomerate formation were drawn from a multitude of different experiments on solid samples of the racemic mixture of **(*R*)-** and **(*S*)-15**.[237] X-Ray diffraction (XRD) studies revealed that the racemic mixture packs into columns with approximate triple 12_1 helix conformation in the bulk.

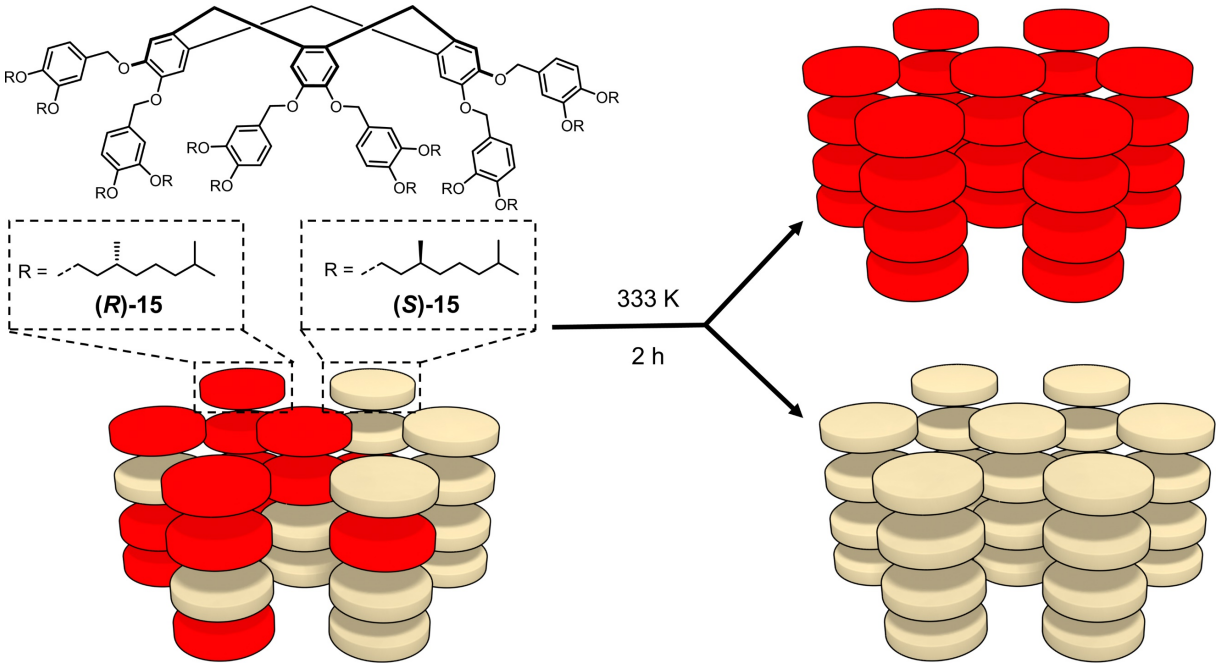

Figure 13. Chemical structures of **(*R*)-** and **(*S*)-15** and schematic illustration of the self-assembly of their racemic mixture comprising a deracemization of a solid-solution like columnar hexagonal lattice into an ordered conglomerate upon annealing.[237]

The same packing model was assumed for the supramolecular polymers of the racemic mixture in solution based on almost identical CD spectra of the enantiopure compounds in solution and thin film (note that the racemic mixture does not exhibit any CD signal). Most notably, the authors monitored a transition from a less ordered racemic crystal with a columnar hexagonal lattice into a more ordered crystalline conglomerate upon annealing at 60 °C for 2 h by differential scanning calorimetry, solid-state NMR spectroscopy and XRD measurements. From these studies it can be concluded that **(*R*)-** and **(*S*)-15** show a pronounced tendency for homochiral aggregation which is further facilitated by fast motions, either in solution[129] or by annealing in the bulk, leading to 1D and 3D conglomerates.

Chapter 3

–

Supramolecular Polymorphism in One-Dimensional Self-Assembly by Kinetic Pathway Control

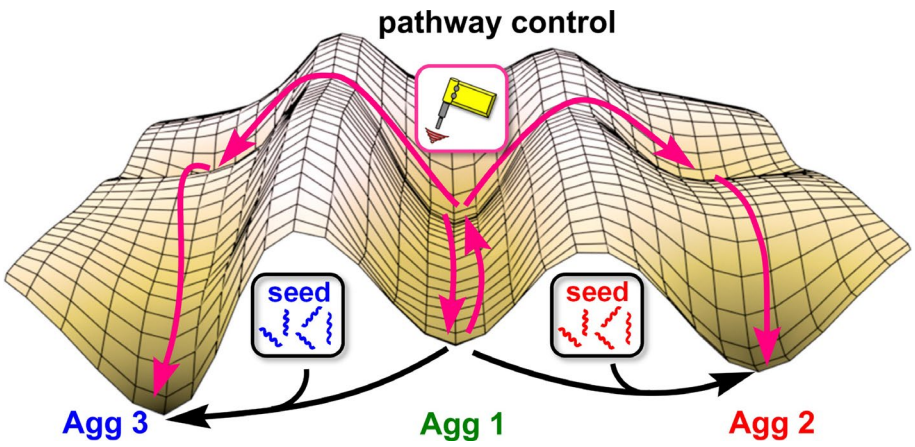

This chapter and the corresponding supporting information (*Chapter 7*.1) were published in:

M. Wehner, M. I. S. Röhr, M. Bühler, V. Stepanenko, W. Wagner, F. Würthner, *J. Am. Chem. Soc.* **2019**, *141*, 6092−6107.
(https://pubs.acs.org/doi/10.1021/jacs.9b02046).

Abstract. Controlling polymorphism in molecular solids is of great interest since the properties and performances of molecular materials depend on the molecules' mutual packing arrangements. Herein, we describe a perylene bisimide (PBI) organogelator molecule **(*R*,*R*)-**

PBI that self-assembles into three different one-dimensional supramolecular polymorphs (**Agg 1−3**) in the same solvent and at the same concentration at room temperature. The three supramolecular polymorphs were characterized by UV/vis, CD, fluorescence and FT-IR spectroscopy, atomic force microscopy (AFM), and theoretical calculations, revealing that their packing arrangements are governed by distinct $\pi-\pi$ stacking modes and unique hydrogen-bonding patterns. Nudged elastic band (NEB) calculations for the nucleation processes toward **Agg 2** and **Agg 3** indicate that nucleation starts from a central kinetically trapped state **Agg 1** and involves the reorganization of **Agg 1** dimers. Time-, concentration-, and temperature-dependent UV/vis experiments provided insights into the thermodynamic stability of the supramolecular polymorphs of **(*R*,*R*)-PBI** and the kinetics for their interconversion. On the basis of this information the production of a certain polymorph could be accomplished either physically by ultrasonication or chemically by seeding. This work contributes to the understanding of polymorphism at the lowest level of hierarchy that is the generation of self-assembled 1D aggregate structures.

3.1 Introduction

Polymorphism, defined as the occurrence of more than one crystalline phase resulting from different packing arrangements of the same compound in the solid state, is a ubiquitous phenomenon which is of great importance not only for academia but also to chemical industry where crystallization is an attractive purification technique.[46, 48, 81] In polymorphs, the mutual arrangement of molecules, atoms, or ions differ, which can have substantial implications on their physical and chemical properties, such as morphologies, solubilities, electric conductivities, or varying processabilities.[46, 48, 81] This is dramatically illustrated in pharmaceutical industry where inadvertent production of undesired drug polymorphs can lead to dosage forms that are either toxic or ineffective because the bioavailability of the respective drug is dependent on the solubility of the polymorph.[49] Further industry-relevant examples of polymorph-dependent properties are pigment colors,[239] detonation sensitivities of explosives,[240] or performances of waxes, soaps, or petroleum products.[46, 49, 240] For instance, for the most important class of color pigments based on copper phthalocyanines, ten different polymorphs are known whose color range is from the greenish cyan β-polymorph up to the reddish blue ε-polymorph.[241] Therefore, it is highly desirable to control the polymorphism of organic compounds which is practically difficult to address since polymorphism arises due to the complex interplay between thermodynamics and kinetics within the crystallization process.[48] Thermodynamic considerations deal with the stability of the respective polymorphs which usually differ only by a few kJ mol^{-1},[45, 49] while kinetic pathways determine how fast a certain polymorph is formed which depends on their activation barriers for nucleation.[48] Comparable to most chemical reactions wherein covalent bonds are built or broken, the formation of a certain polymorph is usually under kinetic control and therefore a complex function of experimental variables such as solvent, temperature, and heating and cooling rates.[48] From the molecular point of view, crystallization of a certain polymorph can be regarded as a supramolecular reaction involving the initial self-assembly of the molecules into energetically suitable aggregates (nuclei) due to noncovalent intermolecular interactions followed by translation into a three-dimensional (3D) structure.[46-48] To gain mechanistic insights into polymorphism, the thermodynamics and kinetics as well as the initial nucleation event and transformations between certain polymorphs need to be addressed which are often either too rapid or too slow to be studied adequately.[48, 54]

Supramolecular chemistry provides a powerful tool to tackle these issues because experimental parameters such as solvent composition, concentration, temperature, or mechanical forces can

be fine-tuned (*Chapter 2.3*) to study self-assembly and polymorph-transformations in an appropriate timescale and therefore polymorphism at its origin. Here a most suitable simplification arises if the self-assembly is not of three-dimensional character as in above-discussed crystallization phenomena but of one-dimensional character as given in supramolecular polymerizations. Interestingly, this field dealt for many years with the thermodynamics,[8, 25, 242] that is, the generation of equilibrium structures, and only recently academic interest shifted toward the kinetic control[9-10, 32, 159] of self-assembly processes and the establishment of out-of-equilibrium species.[147, 154, 157, 243] Key to the exploitation of the potential of kinetics for the production of supramolecular polymorphs (aggregates) is to understand the pathway complexity[40, 160] leading to kinetically trapped off-pathway[29, 153, 179] or on-pathway[42, 146, 168, 244] products. Inspired by research on crystallization-driven block copolymer self-assembly from crystal facets by Manners,[185, 245] the concept of kinetic trapping was utilized for the supramolecular counter-part of seed-induced crystal growth of a variety of dyes by "living" supramolecular polymerization, supported by $\pi-\pi$ stacking and intramolecular hydrogen-bonding,[41, 43-44, 75, 180, 193] charge regulation on the active chain end,[196] or photoisomerization.[174] All these concepts have in common that kinetic trapping leads to a retarded supramolecular polymerization, which can be initiated by seeding, a process commonly used in crystal engineering to produce different polymorphs from super-saturated solutions.[46, 48, 81] The seeding method constitutes a beautiful example of how three-dimensional self-assembly processes leading to different solid-state polymorphs can be mimicked at lower complexity, that is, the seed-induced formation of 1D helical fibers or 2D networks such as organogels[139] by a supramolecular approach.

Herein, we report to the best of our knowledge the first example of a molecule, **(*R*,*R*)-PBI**, that forms three different one-dimensional supramolecular polymorphs (Figure 14) in the same solvent at the same concentration, which is exceptional, since three or more different packing motifs are often only achieved by changing the solvent,[97, 148, 246] the sequence of solvent addition,[147] combination of solvent processing and photochemical conversion,[153] or by concentration[247-250] or temperature changes.[128] **(*R*,*R*)-PBI** is also distinct from structurally related **PBI-1, PBI-2,** and **PBI-5** of our previous research whose self-assembly always afforded a single polymorph (Figure 14). For **PBI-1** and **PBI-5**, these were one-dimensional helical nanofibers with H-type (**PBI-1**)[80] and J-type (**PBI-5**)[251-252] exciton couplings formed by cooperative nucleation-elongation growth, while for **PBI-2** hydrogen-bonded dimers were formed which in an anticooperative growth process further self-assembled into smaller-sized oligomers.[28]

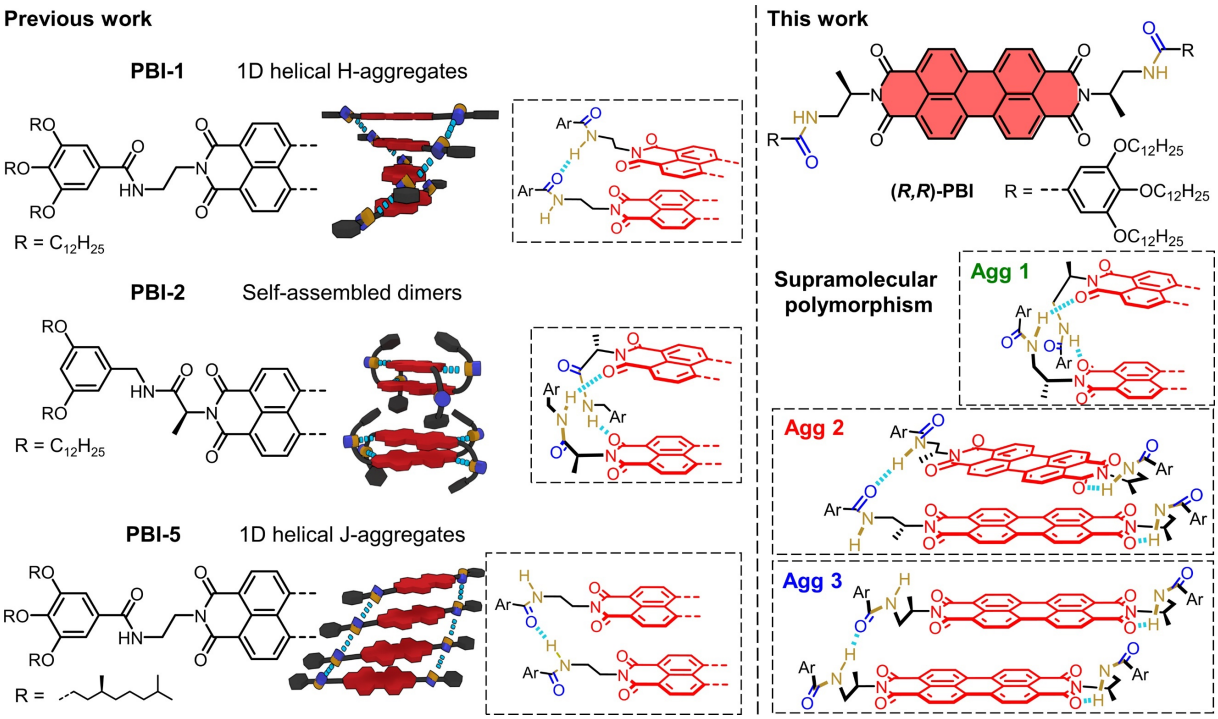

Figure 14. Chemical structures of **PBI-1**, **PBI-2**, **PBI-5** and **(*R*,*R*)-PBI**. For **PBI-1**, **PBI-2** and **PBI-5**, only one-half of the symmetric molecules are shown and their aggregate structure together with the hydrogen-bonding pattern within the different aggregates is schematically depicted next to the respective molecule. **(*R*,*R*)-PBI** exhibits supramolecular polymorphism, and the unique hydrogen-bonding patterns within the three polymorphs **(*R*,*R*)-PBI Agg 1−3** (for simplicity denoted as **Agg 1−3** within *Chapter 3*) are depicted. Note that for **Agg 1**, only one-half of the PBI molecules are shown. Ar denotes in all cases the aromatic side chain shown in the respective chemical structure.

Compared to **PBI-1, PBI-2,** and **PBI-5**, the energy landscape of **(*R*,*R*)-PBI** is, however, more complex and enables the formation of a variety of supramolecular polymer structures by proper control of the self-assembly conditions. All polymorphs were kinetically stable at room temperature in solution over weeks which was exploited to prepare the same polymorphs in the solid state. With this model system, we studied supramolecular polymorphism at its infancy and gained kinetic and thermodynamic insights into the first stages of polymorphism, namely polymorph formation and transformation.

3.2 Results

3.2.1 Synthesis of (*R,R*)-PBI

Following literature known methods,[75, 80, 253] **(*R,R*)-PBI** was synthesized through imidization of perylene-3,4:9,10-tetracarboxylic acid bisanhydride (**20**) with (*R*)-*N*-(2-aminopropyl)-3,4,5-tris(dodecyloxy)benzamide (**(*R*)-19**) in imidazole and isolated as a red solid in a yield of 61% (Scheme 1). The benzamide precursor was prepared from 3,4,5-tris-(dodecyloxy)benzoic acid (**16**)[254] by amidization with (*R*)-*tert*-butyl (1-aminopropan-2-yl)carbamate (**(*R*)-17**)[75, 255-256] and successive cleavage of the *tert*-butyloxycarbonyl (Boc) protecting group with trifluoroacetic acid. The synthetic details and characterization data of the compounds are provided in *Chapter 7.1*.

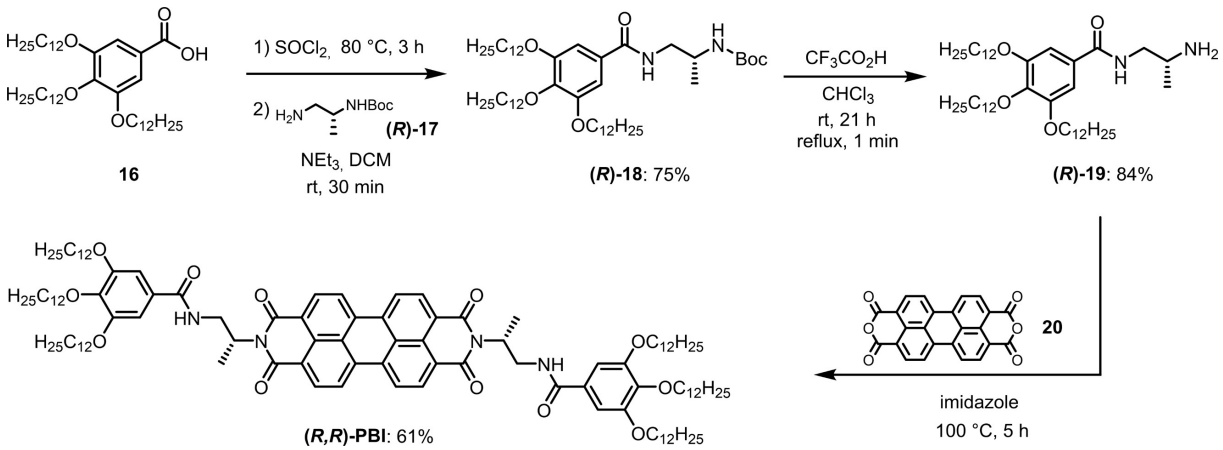

Scheme 1. Synthesis of **(*R,R*)-PBI** starting from literature known 3,4,5-trisdodecylbenzoic acid (**16**). The synthesis of **(*R,R*)-PBI** was reported in reference[253].

3.2.2 Supramolecular Synthesis and Characterization of Three 1D Polymorphs

To get access to different supramolecular polymorphs, the Gibbs free energy surface of the supramolecular system has to show minima which can be reached while the activation barriers between different polymorph states have to be low enough to be overcome over time or by applying "physical stress" such as mechanical agitation. After first time-dependent UV/vis absorption spectroscopy studies of **(*R,R*)-PBI** in different solvents and solvent mixtures, we found that a mixture of methylcyclohexane (MCH) and toluene (Tol) with a volume ratio of MCH/Tol = 5:4 was suitable to study the supramolecular polymorphism of **(*R,R*)-PBI**. In this particular solvent mixture, **(*R,R*)-PBI** can self-assemble driven by $\pi-\pi$ stacking and hydrogen-

bonding to give initially polymorph **Agg 1** which transforms into polymorph **Agg 2** within two weeks according to time-dependent UV/vis studies (for simplicity, the enantiopure supramolecular polymorphs **(*R,R*)-Agg 1–3** will be abbreviated as **Agg 1–3** within *Chapter 3*). Unfortunately, precipitation of **Agg 2** hampered an accurate evaluation of these initial studies. Since precipitation in amide-functionalized PBI organogelators usually results from the bundling of the nanofibers,[43, 80] we next applied ultrasonication (for experimental details see *Chapter 7.1*) for several reasons:[257-262] (i) precipitation can be avoided due to scission of (bundled) nanofibers and (ii) ultrasonication provides energy to overcome activation barriers between different polymorphs. Although it is not fully understood how ultrasound can direct self-assembly pathways, it is hypothesized that ultrasound helps the nucleation process by modifying supersaturation conditions through the mechanism of cavitation accompanied by collapsing bubbles leading to local spots of extreme conditions (e.g., high concentrations or rapid cooling rates).[257-262] Therefore, ultrasound provides the ideal tool to access different aggregation pathways yielding distinct polymorphs by modifying the nucleation conditions. Indeed, three different supramolecular polymorphs of **(*R,R*)-PBI**, termed as **Agg 1** to **Agg 3**, could be obtained by this ultrasonication-assisted supramolecular polymerization: **Agg 1** formed directly by dissolving **(*R,R*)-PBI** in MCH/Tol (5:4, v/v) at a total concentration of $c_T = 3.0 \times 10^{-4}$ M, and **Agg 2** and **Agg 3** were prepared by ultrasonication (for experimental details see the *Chapter 7.1*) of **Agg 1** solutions at 293 − 298 K for 45 min or at 308 K for 180 min, respectively (Figure 15). Notably, all polymorphs were prepared at the same concentration ($c_T = 3.0 \times 10^{-4}$ M) in the same solvent mixture MCH/Tol (5:4, v/v) and are kinetically stable (day to months, depending on c_T) at room temperature.

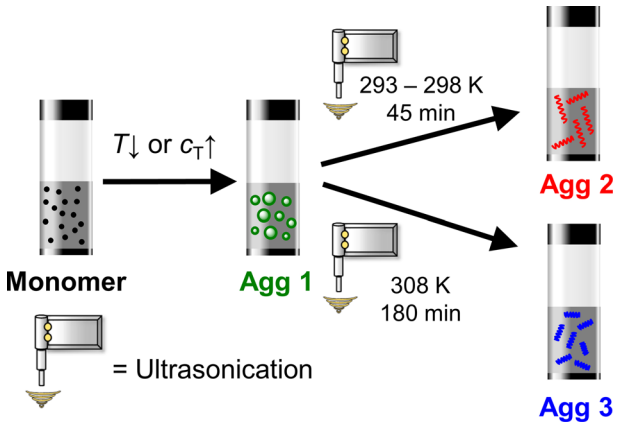

Figure 15. Supramolecular polymerization of three different 1D polymorphs of **(*R,R*)-PBI**, which are designated as **Agg 1** to **Agg 3**.

Spectroscopic techniques such as UV/vis absorption, circular dichroism (CD), and steady-state fluorescence spectroscopy (Figure 16a,b) were applied to elucidate the relative arrangement of the chromophores (insets in Figure 16c–e) within the supramolecular polymorphs. AFM was used to investigate the structures of the polymorphs (Figure 16c–e and *Chapter 7.1*, Figure 34) and FT-IR spectroscopy to clarify the hydrogen-bonding pattern within the polymorphs (Figure 17).

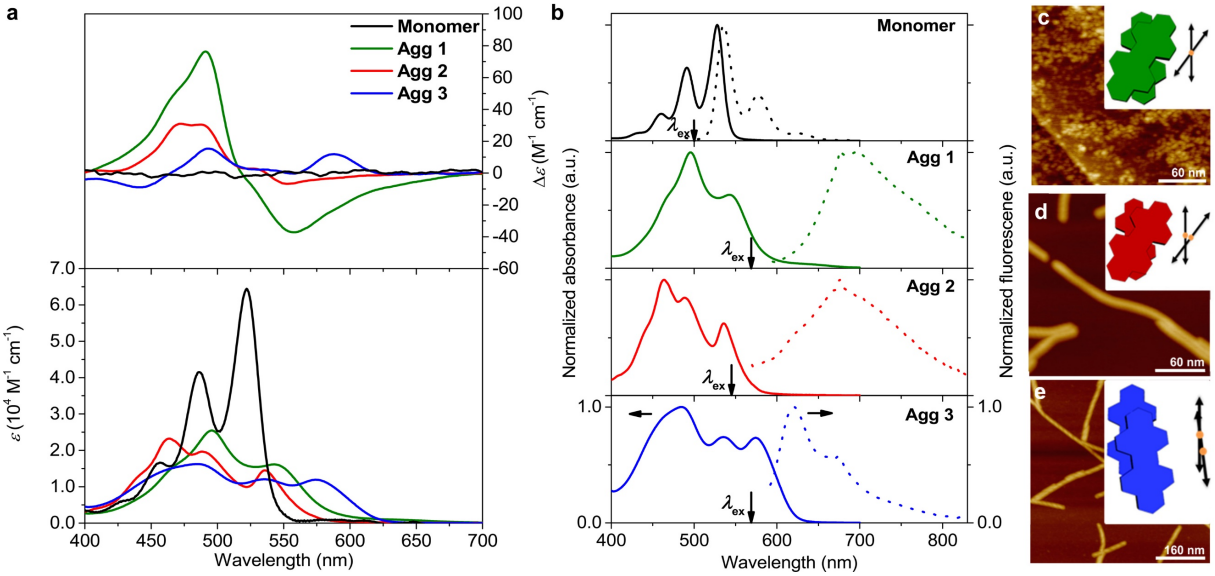

Figure 16. (**a**) UV/vis-absorption and CD spectra of monomeric ($c_T = 2.0 \times 10^{-6}$ M, 357 K) **(*R,R*)-PBI** and its three polymorphs ($c_T = 3.0 \times 10^{-4}$ M, 298 K) in MCH/Tol (5:4, v/v). (**b**) Normalized absorbance (solid lines) and fluorescence spectra (dashed lines) of monomeric **(*R,R*)-PBI** in $CHCl_3$ and of its three polymorphs **Agg 1**–**3** in MCH/Tol (5:4, v/v). The respective excitation wavelengths are indicated in the spectra. AFM height images of **Agg 1** (**c**), **Agg 2** (**d**), and **Agg 3** (**e**) spin-coated (10000 rpm) on HOPG from MCH/Tol (5:4, v/v). Z scale is 3 nm (**c**), 11 nm (**d**), and 14 nm (**e**).* For more details, see *Chapter 7.1*, Figure 34. Insets in (**c**–**e**): Schematic depiction of the arrangement of the PBI molecules and their transition dipole moments μ_{eg} (shown as double arrows) within the three polymorphs derived from UV/vis and CD spectra as well as theoretical calculations. The centers of the respective PBI molecules are illustrated as orange points.

Monomeric **(*R,R*)-PBI** shows the typical vibronic progressions of the $S_0 \rightarrow S_1$ electronic transition of bay-unsubstituted PBIs[64] with an absorption maximum at $\lambda = 522$ nm and is CD silent (Figure 16a).[263] The fluorescence spectrum of monomeric **(*R,R*)-PBI** shows a maximum at $\lambda = 536$ nm and resembles a mirror image of the absorption spectrum (Figure 16b).

* AFM measurements were performed by V. Stepanenko.

Upon cooling to 298 K and increasing the concentration to $c_T = 3.0 \times 10^{-4}$ M, the absorption maximum of monomeric **(*R,R*)-PBI** was hypsochromically shifted to $\lambda = 496$ nm with a loss of vibronic fine structure and the concomitant appearance of a weaker band at $\lambda = 543$ nm (**Agg 1**, Figure 16a). These spectral features are commonly found in rotationally displaced π stacked PBI H-aggregates such as **PBI-2**.[28, 252, 264] The rotational displacement of the PBIs is further supported by a strong CD signal with positive and negative maxima at $\lambda = 490$ and 557 nm corresponding to the two absorption maxima in the UV/vis spectrum of **Agg 1**. The fluorescence spectrum of **Agg 1** shows a strongly red-shifted broad emission profile characteristic for the formation of a PBI excimer (Figure 16b).[264-266] AFM studies (Figure 16c and *Chapter 7.1*, Figure 34a,b) revealed a nanoparticle-like morphology with a diameter of 3.8 ± 0.3 nm which corresponds to small 1D helical oligomers of up to 12 molecules under the assumption of an interplanar $\pi-\pi$ distance of 3.6 Å (taken from the calculated dimer structure of **Agg 1**, *Chapter 3.2.3*).

The shape of the absorption spectrum of **Agg 2** (Figure 16a) between $\lambda = 450$ and 520 nm resembles that of **Agg 1**, although its absorption maximum is blue-shifted by 31 nm to $\lambda = 463$ nm compared to **Agg 1**.[267-268] Additionally, several maxima/shoulders are observable, and a particularly defined band shows up at $\lambda = 536$ nm, which may be attributed to the J-type excitonic transition upon rotational displacement of the PBI chromophores relative to each other.[252, 264, 269] A similar absorption spectrum was observed for **PBI-1** and attributed to an aggregate structure with tripodal contacts formed by two amide-amide hydrogen bonds at a hydrogen-bonding distance of ~2 Å and PBI aggregation at a $\pi-\pi$ stacking distance of ~ 3.5 Å (Figure 14).[43, 64, 80] In the CD spectrum of **Agg 2**, two maxima at $\lambda = 472$ and 488 nm and one minimum at $\lambda = 553$ nm are observed corresponding to the respective absorption bands in the UV/vis spectrum (Figure 16a). Similar to **Agg 1**, also **Agg 2** shows an excimer emission profile in the fluorescence spectrum (Figure 16b), while its morphology, that is highly defined 1D helical nanofibers with a unimolecular width of 4.7 ± 0.2 nm, lengths between 50 − 600 nm and a helical pitch of 5.5 ± 0.3 nm, differs significantly from that of **Agg 1** as revealed by AFM (Figure 16d and *Chapter 7.1*, Figure 34c−e).

In sharp contrast to the other supramolecular polymorphs, **Agg 3** shows a broad and unstructured absorption profile (Figure 16a) with a huge exciton bandwidth from $\lambda \approx 420$ nm to > 600 nm. The most striking spectral feature of **Agg 3** is the bathochromically shifted absorption band at $\lambda = 575$ nm, which results according to theoretical calculations from longitudinally and transversally displaced PBI molecules with a small rotational offset (*Chapter 3.2.3*). According to recent theoretical studies for such a slipped packing arrangement of PBIs,

a rather strong coupling between Frenkel and charge transfer mediated excitons is expected which may account for the large bandwidth of the absorption band.[63] Similar UV/vis spectra were reported for **PBI-5** aggregates[251-252] and different PBI-based pigments.[270] In the CD spectrum of **Agg 3** pronounced changes were detectable, namely a reduced CD signal intensity compared to **Agg 1** and **Agg 2** and an altered band shape with a minimum at $\lambda = 442$ nm and two maxima at $\lambda = 493$ and 588 nm (Figure 16a). **Agg 3** shows a more defined fluorescence spectrum with a maximum at $\lambda = 621$ nm and no bathochromically shifted excimer emission was observed (Figure 16b). AFM measurements reveal a 1D nanofiber morphology of **Agg 3** (Figure 16e and *Chapter 7.1*, Figure 34f–h). Compared to **Agg 2**, the nanofibers of **Agg 3** show a unimolecular width (4.6 ± 0.2 nm) but are more rigid and shorter (45 − 450 nm) and have an about three times larger helical pitch of 16 ± 2 nm.

From these studies in combination with theoretical calculations (*Chapter 3.2.3*), the relative orientation of the transition dipole moments of the $S_0 \rightarrow S_1$ electronic transition (pointing along the long molecular axes of the PBI chromophores)[64] within the polymorphs were deduced and schematically depicted in the insets of Figure 16c–e.

Further characterization of the **(*R*,*R*)-PBI** polymorphs by FT-IR spectroscopy revealed distinct differences for all three polymorphs, indicative of specific hydrogen-bonding patterns (Figure 17). In our previous studies on amide-functionalized PBI organogelators, we carefully examined the different hydrogen-bonding patterns by FT-IR spectroscopy and showed that N–H stretching frequencies of non-hydrogen-bonded N–H groups appear around 3470 − 3430 cm^{-1}, while those of intramolecularly hydrogen-bonded $N{-}H_{amide}\cdots O{=}C_{imide}$ groups are shifted to lower energies of around 3420 − 3395 cm^{-1}.[43, 75-76] A second IR band of interest arises from the C=O stretching frequency whose characteristic band for intramolecularly hydrogen-bonded amide carbonyl groups (amide I band) appears around 1656 cm^{-1}.[43, 271] The formation of intermolecular hydrogen bonds, either between amide protons and imide oxygens[28] or between amide protons and amide oxygens,[76, 80, 251, 272] leads to a further shift of the C=O and N–H stretching frequencies to lower wavenumbers of about 1652 − 1620 cm^{-1} and 3380 − 3220 cm^{-1}, respectively. Notably, intermolecular hydrogen bonds between amide groups are found to be stronger (lower wavenumbers of the respective stretching frequencies) than intermolecular hydrogen bonds between amide protons and imide oxygens of the adjacent chromophore. For **PBI-1**, the C=O and N–H stretching frequencies of intramolecularly hydrogen-bonded amide groups ($N{-}H_{amide}\cdots O{=}C_{imide}$) were reported to be 1654 and 3409 cm^{-1} and those of intermolecular amide-amide hydrogen bonds were 1653 and 3271 cm^{-1}, respectively.[43, 80]

In $CHCl_3$ solution at 323 K, **(*R*,*R*)-PBI** has a monomer-like band shape in the UV/vis spectrum (*Chapter 7.1*, Figure 35a), and intramolecular hydrogen bonds between amide protons and imide oxygens were observed showing the characteristic C=O stretching frequency of intramolecularly bound amide carbonyl groups at 1656 cm^{-1} and the corresponding N−H stretching frequency at 3406 cm^{-1} (Figure 17, for enlarged spectra see *Chapter 7.1*, Figure 35b,c).

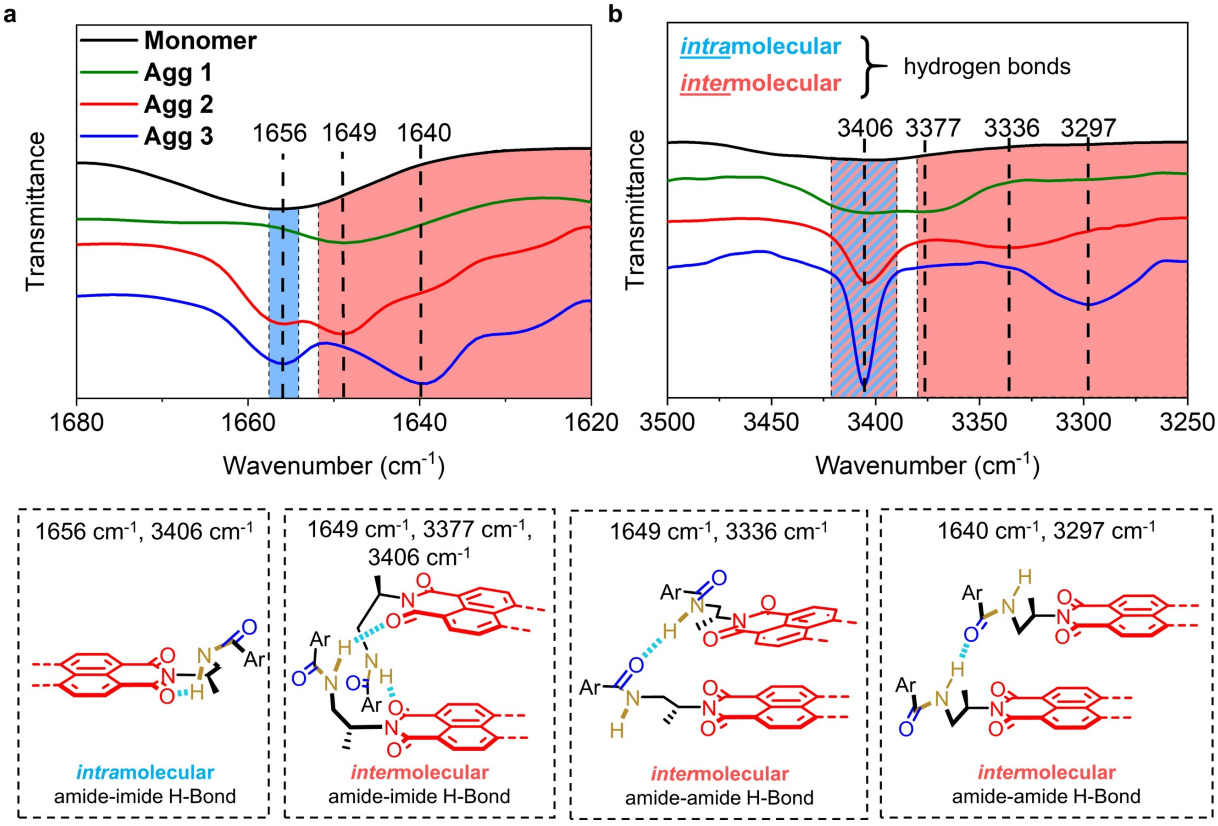

Figure 17. FT-IR spectra of the C=O (**a**) and N−H (**b**) stretching vibration of mostly (~ 85%) monomeric **(*R*,*R*)-PBI** (c_T = 4.0 × 10^{-4} M, $CHCl_3$, 323 K) and of its three supramolecular polymorphs (c_T = 5.0 × 10^{-4} M, MCH/Tol (5:4, v/v), 298 K). The approximate spectral regions corresponding to the stretching vibrations of intramolecularly (blue) and intermolecularly hydrogen-bonded (red) C=O and N−H groups are indicated based on literature known amide-functionalized PBI-organogelators.[28, 43, 75-76, 80, 251] The respective hydrogen-bonding patterns are illustrated under the spectra. Note that between 3420 − 3390 cm^{-1} both intra- and weakly intermolecularly hydrogen-bonded N−H stretching frequencies can be observed.

In the FT-IR spectrum of **Agg 1**, the aforementioned characteristic band at 1656 cm^{-1} is missing (Figure 17a). Instead, its C=O stretching vibration is shifted to 1649 cm^{-1} indicative of the formation of intermolecular hydrogen bonds, which is further corroborated by the appearance of a band at 3377 cm^{-1} in the N−H stretching region which is characteristic for intermolecular

hydrogen bonds between amide protons and imide oxygens of the neighboring PBI molecule within a dimer (Figure 17b).[28] We note that **Agg 1** shows also a minimum at 3406 cm^{-1}, which is in this case also attributed to a weaker intermolecular $N{-}H_{amide}\cdots O{=}C_{imide}$ hydrogen bond (same type as before) and not to an intramolecular hydrogen bond since the characteristic peak at 1656 cm^{-1} is not observed.

Agg 2 and **Agg 3** both show a C=O stretching vibration at 1656 cm^{-1} and a N−H stretching vibration at 3406 cm^{-1} attributable to intramolecular hydrogen bonds between an amide proton and imide oxygen (Figure 17). Additionally, a second type of hydrogen bonds with C=O and N−H stretching frequencies at 1649 and 3336 cm^{-1} (**Agg 2**) and 1640 and 3297 cm^{-1} (**Agg 3**), respectively, can be observed, which are characteristic for the formation of intermolecular hydrogen bonds between the amide groups of the spacer units.[76, 80, 251, 272] The N−H frequencies are shifted to lower wavenumbers compared to those of **Agg 1**, meaning that the intermolecular hydrogen bonds within **Agg 2** and **Agg 3** are stronger, as is the case for intermolecular amide-amide hydrogen bonds.

Considering the calculated dimer structures of **Agg 2** and **Agg 3** (Figure 18), the occurrence of two different types of hydrogen bonds can be explained by the rotational displacement of longitudinally and transversally shifted adjacent PBI chromophores within the aggregates creating a long and short side with respect to the distances between the amide nitrogens of adjacent PBI molecules (*Chapter 7.1*, Figure 36, the long and short side are in the following designated as “peripheral” and “inner” side, respectively). On the inner side with shorter distances between the amide nitrogens of 5.1 and 4.6 Å in calculated dimers of **Agg 2** and **Agg 3**, respectively, strong intermolecular hydrogen bonds are formed (Figure 17), while on the peripheral side the respective distances are 0.6 and 0.4 Å larger which disfavors the formation of intermolecular hydrogen bonds. Instead, the system adjusts with the formation of an intramolecular hydrogen bond between an amide proton and imide oxygen leading to a minimization of the Gibbs free energy of the system by 15.3 kJ mol^{-1} compared to non-hydrogen-bonded open form as calculated for an individual molecule within **Agg 2**. Summing up, **Agg 1** shows two slightly different intermolecular $N{-}H_{amide}\cdots O{=}C_{imide}$ hydrogen bonds between neighboring chromophores, while both **Agg 2** and **Agg 3** have one intramolecular $N{-}H_{amide}\cdots O{=}C_{imide}$ hydrogen bond on the long side and one intermolecular hydrogen bond between the spacer unit amide groups on the short side, which is stronger for **Agg 3** compared to **Agg 2**.

Additionally, the same three supramolecular polymorphs were also "synthesized" and characterized in the solid state by UV/vis and FT-IR spectroscopy (for experimental details see *Chaper 7.1* and Figure 37). In contrast to the FT-IR spectrum of **Agg 1** in MCH/Tol (5:4, v/v), in the N−H stretching region of the solid-state FT-IR spectrum of **Agg 1** only one broad band occurs at 3339 cm^{-1}, which further corroborates the picture of having a single type of hydrogen bond in **Agg 1**. Apart from that, all UV/vis and FT-IR results of the solid-state polymorphs resembled those obtained in solution. Together with the fact that all supramolecular polymorphs were prepared at the same concentration in the same solvent and are kinetically stable at room temperature, the designation as true "supramolecular polymorphs" is justified.

3.2.3 Theoretical Calculations on Dimers and the Energy Landscape

On the basis of our detailed information from optical and infrared spectroscopy for the different polymorphs, we sought to get further insight on the packing arrangement of the individual PBI molecules within the polymorphs by quantum chemical calculations.* Therefore, we constructed dimer systems for **Agg 1**, **Agg 2**, and **Agg 3** by taking into account all structure information obtained from the experiments. The subsequent optimization with PM6-D3H4[273-275] as implemented in MOPAC[276] and subsequent validation by additional DFT-calculations (B3LYP/def2-SVP)[275, 277-278] gave rise to relaxed structures that are presented in Figure 18.

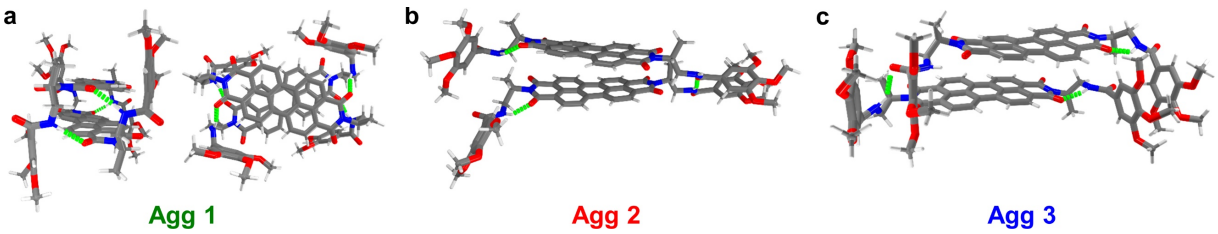

Figure 18. Geometry-optimized dimer structures obtained from DFT calculations (CAM-B3LYP/def2-SVP) of **Agg 1** (**a**), **Agg 2** (**b**), and **Agg 3** (**c**).* Dodecyloxy groups are replaced by methoxy groups for simplicity. The dashed green lines represent hydrogen bonds.

* Quantum chemical calculations were performed by M. I. S. Röhr and M. Bühler.

For **Agg 1**, the geometry-optimized dimer structure appears as an almost centrosymmetric stack of two crossed PBI cores (rotational twist: 41°) with an interplanar distance of 3.6 Å interconnected on both sides by intermolecular hydrogen bonds between the amide protons and the imide oxygens of the adjacent PBI chromophore. All methyl groups point in an outward direction and direct the phenyl residues of the individual molecules to clasp the neighbor molecule. Notably, this dimer structure is very similar to the one observed for **PBI-2** in our previous work (Figure 14) which described the first example for an anticooperative supramolecular polymerization with preferential formation of even-sized aggregates due to the very high stability of the hydrogen-bonded dimer species.[28]

In **Agg 2**, the PBI molecules show a small longitudinal and transversal displacement of 0.2 and 0.4 Å, respectively, a rotational twist of 29°, a $\pi-\pi$ distance of 3.7 Å, and all α-CH_3 groups point into the same direction (in the shown case upward). Notably, this geometry is very similar to the energy minimum found for the PBI dimer aggregates in the absence of additional hydrogen-bonding units (i.e., pure $\pi-\pi$ stacking interaction).[279] Owing to the additional hydrogen-bonding interactions, the PBI dimer of **Agg 2** is, however, not centrosymmetric anymore. Only the amide units on one side involve in the hydrogen-bond directed supramolecular polymerization, while those on the other side are intramolecularly connected to the adjacent imide carbonyl groups. In sharp contrast to **Agg 1** and **Agg 2**, the dye molecules in **Agg 3** show a significantly larger longitudinal displacement of 3.7 Å, a transversal displacement of 0.3 Å, the smallest rotational twist of only 5°, and a $\pi-\pi$ distance of 3.7 Å. The α-methyl groups in **Agg 3** all point in one direction on one side and in the opposite direction on the other side. Similar as for **Agg 2**, intermolecular $N-H_{amide}\cdots O=C_{amide}$ hydrogen bonds are found between the adjacent chromophores in **Agg 3** on one side and intramolecular $N-H_{amide}\cdots O=C_{imide}$ hydrogen bonds on the other side (Figure 17).

These geometry-optimized dimer structures of **Agg 1**, **Agg 2**, and **Agg 3** constitute three energy minima on an energy landscape. Such energy landscapes are well-known from biology (e.g., polymorphism in protein folding and self-assembly),[171, 280] where they encode the relative thermodynamic stabilities of the different unfolded, folded, or self-assembled states as well as the kinetic barriers separating them. Inspired by such energy landscapes of complex biomolecular self-assembly processes,[281] we sought to construct a quantitative potential energy surface diagram for the dimeric polymorphs of **(*R,R*)-PBI** (for details, see *Chapter 7.1*), accounting for the complex interplay between thermodynamics and kinetics resulting in the supramolecular polymorphism of **(*R,R*)-PBI**. This allows the elucidation of the transformation

pathways between the polymorphs **Agg 1** and **Agg 2** or **Agg 1** and **Agg 3** on a microscopic, molecular level.

It should be emphasized that the limitation to dimeric species strongly favors **Agg 1**, which is the only self-consistent aggregate species with four internal hydrogen bonds. In contrast, for the dimers of **Agg 2** and **Agg 3** upon addition of adjacent PBI molecules, further $\pi-\pi$ stacking and hydrogen-bonding provide additional stabilization. Accordingly, **Agg 2** and **Agg 3** dimers may be considered as the still high-energy and disfavored nuclei from which a cooperative self-assembly process is initiated. For this purpose, we have employed the nudged elastic band (NEB) method[282-283] along with the PM6-D3H4 correction to simulate the nucleation pathways starting from the optimized structures of **Agg 1**, **Agg 2**, and **Agg 3** dimers. Since linear interpolation cannot be used for the generation of initial pathways for NEB calculations of such complex transitions, we have generated them by an advanced interpolation scheme based on a root-mean-square deviation (RMSD)-driven biased molecular dynamics (for details, see *Chapter 7.1*).[284] Subsequently, structures have been sampled from the molecular dynamics trajectory and further optimized employing the NEB method using the full spring force implementation of the atomic simulation environment.[283, 285] These simulations cover all possible transformation mechanisms of **Agg 1** into either **Agg 2** or **Agg 3** (i.e., rearrangement processes of the molecules within **Agg 1** dimers as well as disassembly of these dimers into monomers followed by reassembly into a specific polymorph). This allows a distinction for whether **Agg 1** is an off- or on-pathway product for the supramolecular polymorphs **Agg 2** or **Agg 3**.[160] In an off-pathway self-assembly process, dimers of **Agg 1** would first disassemble into monomers which would then polymerize to **Agg 2** or **Agg 3**, respectively. In contrast, in an on-pathway self-assembly process, rearrangements of the PBI molecules within **Agg 1** dimers would lead to the formation of either **Agg 2** or **Agg 3** without the involvement of monomers.

The optimized NEB pathways (Figure 19a) give rise to a set of structures and their electronic energies along the "minimal energy pathway" of the rearrangement of the dimer structures. The energies of dimeric **Agg 2** (111 kJ mol^{-1}) and **Agg 3** (58 kJ mol^{-1}) are reported relative to that of an **Agg 1** dimer which was set to 0 kJ mol^{-1}. Notably, both nucleation pathways (**Agg 1** → **Agg 2** and **Agg 1** → **Agg 3**) take place without disassembly of **Agg 1** dimers into monomers, meaning that **Agg 1** is an on-pathway product for both **Agg 2** and **Agg 3**. The transformation pathways are characterized by several kinetic barriers that correspond to distinct structural reorganization events which are described in the following on the example of the transformation of **Agg 1** into **Agg 2** (Figure 19b).

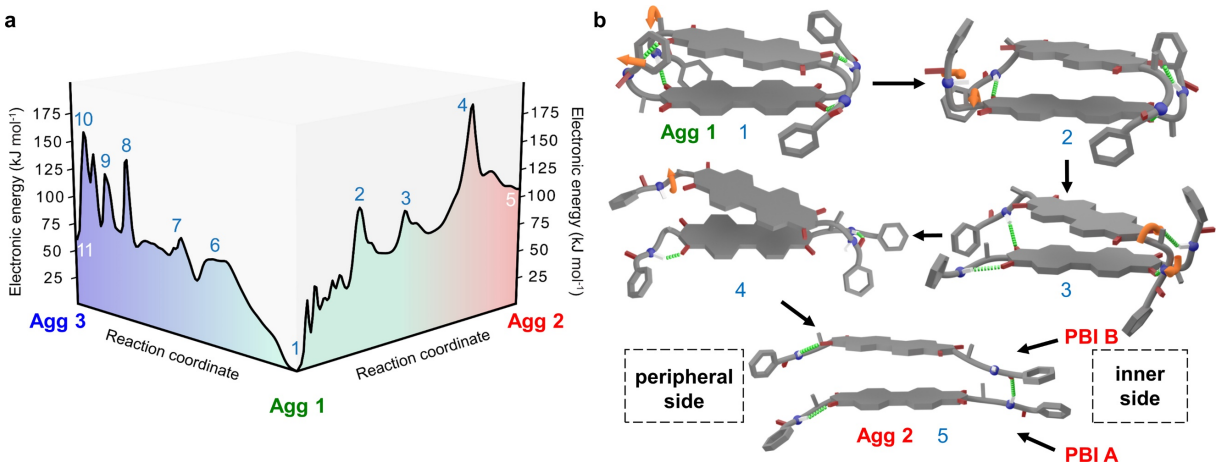

Figure 19. (**a**) Calculated quantitative potential energy landscape of the supramolecular polymorphism of **(*R*,*R*)-PBI**, illustrating the nucleation pathways of dimeric **Agg 2** or **Agg 3** starting from **Agg 1**. (**b**) Schematic illustration of the transformation of **Agg 1** into **Agg 2**. The numbered structures correspond to the respective transition states in (**a**). PBI A and PBI B denote the lower and upper PBI molecule within the dimer, respectively, and orange arrows indicate the molecular rearrangement processes. The peripheral and inner side always refer to the left and right side of the dimer, respectively.

The terminology of inner and peripheral side refers to the sites of **Agg 2** and **Agg 3** shown in Figure 19b and Figure 36 (*Chapter 7.1*). In the first step of the transition of **Agg 1** (**#1**) into **Agg 2** (**#5**), a rotation around the N_{imide}–C_{spacer} bond on the peripheral side of PBI A brings the outward pointing α-CH_3 group inward, accompanied by a breakage of the respective intermolecular hydrogen bond between the amide proton of PBI A and the imide oxygen of PBI B on the peripheral side (**#2**). Next, an outward rotation of the tris(dodecyloxy)phenyl side chain on the peripheral side of PBI A leads to the formation of a new intramolecular $N{-}H_{amide}\cdots O{=}C_{imide}$ hydrogen bond on the peripheral side of PBI A, while on the inner side, the intermolecular hydrogen bond between the amide proton of PBI A and the imide oxygen of PBI B elongates (**#3**). In the next, rate-determining step, the side chain of the inner side of PBI B rotates outward and all remaining intermolecular amide to imide hydrogen bonds are broken. A new intermolecular amide to amide hydrogen bond between PBI A and B is formed on the inner side (**#4**). In the last step, an intramolecular $N{-}H_{amide}\cdots O{=}C_{imide}$ hydrogen bond is formed on the peripheral side of PBI B and the dimer relaxes into **Agg 2** (**#5**) with all α-CH_3 groups pointing in the same direction (here upward) as required to initiate a one-dimensional fiber growth by subsequent addition of PBI molecules at both the upper and the lower PBI of the dimer unit. A detailed illustration of the transformation of dimeric **Agg 1** into **Agg 3** is provided in Figure 38 (*Chapter 7.1*).

By calculating the thermodynamic functions for the three aggregates and the transition states highest in separating them using standard statistical mechanics expressions, accounting for the contribution of translational, rotational, and vibrational energy, we can roughly estimate the energetics of the individual dimeric polymorphs and bring these results in correlation with experimental data.[286-289] For this purpose, vibrational frequency calculations have been performed for all species, and the vibrational contribution to the enthalpy, entropy, and free energy have been calculated in the harmonic approximation, including the zero-point energy contributions.[286-289] The obtained energies result in an energetic ordering with **Agg 1** being most stable set to zero, **Agg 3** with 58 kJ mol^{-1} and **Agg 2** with 111 kJ mol^{-1} and give a barrier of 193 kJ mol^{-1} for the transition from **Agg 1** to **Agg 2** and 144 kJ mol^{-1} for the transition from **Agg 1** to **Agg 3**. While these quantities overestimate the initial nucleation barrier between **Agg 1** and **Agg 2** dimers which might be a result of simplifications made during the simulations (i.e., lack of the surrounding solvent), the trends in the thermodynamic polymorph stabilities are well-reproduced (*Chapter 3.3*). It should be emphasized that the relative energies as well as the energetic barriers between the polymorphs depend on the aggregate size and therefore on the concentration of **(*R*,*R*)-PBI** (*Chapter 3.3*). Accordingly, for larger aggregates **Agg 1** becomes the least and **Agg 3** the most stable polymorph.

These model studies on dimeric polymorphs clearly show that the kinetic barriers which are a prerequisite for the supramolecular polymorphism encountered in **(*R*,*R*)-PBI** result from the aforementioned rearrangements on the molecular level, mainly from rearrangement processes of the methyl groups alpha to the imide nitrogen atoms and from changes in the hydrogen-bonding pattern. While solvation effects will for sure reduce the respective activation energies, we like to point out that our chosen solvent system toluene/methylcyclohexane ensures a high strength of hydrogen bonds.[43, 290] Because these calculations are to the best of our knowledge the first examples illustrating the initial steps of nucleation processes within one-dimensional supramolecular polymers on the molecular level explaining the pathway-complexity with a central on-pathway intermediate (**Agg 1**), we like to emphasize their still only tentative character.

3.2.4 Elucidation of the Thermodynamics of the Supramolecular Polymorphism of (*R*,*R*)-PBI

On the basis of our calculations for **(*R*,*R*)-PBI** dimer species, we assume cooperative nucleation-elongation supramolecular polymerization processes for **Agg 2** and **Agg 3** and an

anticooperative supramolecular polymerization process for **Agg 1**. Further, our calculations suggested that **Agg 1** is an on-pathway product for both, **Agg 2** and **Agg 3** (i.e., that no disassembly of **Agg 1** into monomers is needed to initiate the supramolecular polymerization into **Agg 2** and **Agg 3**).[160] In the following, this theoretical picture will be confirmed by experiments.

To gain insights into the thermodynamic properties of the polymorphs encountered in ***(R,R)*-PBI**, concentration- and temperature-dependent UV/vis experiments were performed (Figure 20).

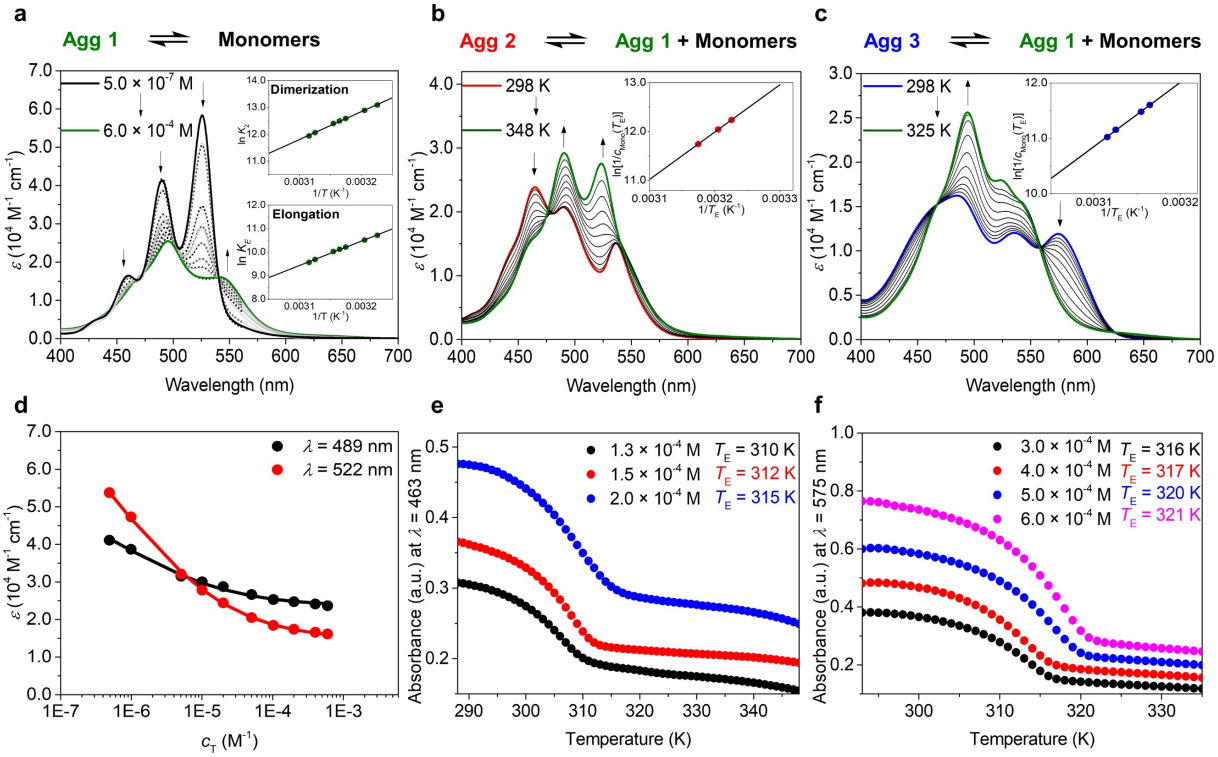

Figure 20. (**a**) Concentration-dependent UV/vis-absorption spectra of ***(R,R)*-PBI Agg 1** (solid lines) in MCH/Tol (5:4, v/v) at 310 K globally analyzed by the K_2–K model[26-27, 135] (black dots) and (**d**) comparison between fit and the extinction coefficients at λ = 522 and 489 nm (fit: solid lines, ε-values: symbols). Inset (**a**): Van't Hoff analysis of the thermodynamic parameters of the dimerization and elongation of **Agg 1**. Temperature-dependent UV/vis-absorption spectra of **Agg 2** ($c_T = 2.0 \times 10^{-4}$ M, T = 298 → 348 K, heating rate: 5 K min^{-1}) (**b**) and **Agg 3** ($c_T = 4.0 \times 10^{-4}$ M, T = 298 → 325 K, heating rate: 1 K min^{-1}) (**c**) upon heating as well as plot of the absorbances at λ = 463 nm (**e**) and λ = 575 nm (**f**) as a function of temperature and concentration for **Agg 2** and **Agg 3**, respectively. Insets: Van't Hoff analysis of the thermodynamic parameters of the elongation of **Agg 2** (**b**) and **Agg 3** (**c**). The analyzed equilibria between the different supramolecular polymorphs are shown on the top.

Next, by analyzing the concentration- and temperature-dependent UV/vis data with different mathematical models,[25-27, 135] the aggregation mechanism and thermodynamic parameters for

supramolecular self-assembly processes can be clarified. Upon increasing concentration, monomeric **(*R*,*R*)-PBI** self-assembles into **Agg 1** in MCH/Tol (5:4, v/v) characterized by a pronounced decrease of the extinction coefficient and a blue-shift (30 nm) of the absorption maximum (Figure 20a). The concentration-dependent UV/vis spectra (Figure 20a, solid lines) could be accurately globally fitted (Figure 20a, black dots) with the anticooperative K_2–K model,[27, 135] and the experimentally determined concentration-dependent extinction coefficients at λ = 489 and 522 nm (dots) matched perfectly with the globally fitted data (solid lines) (Figure 20d).

From this analysis, the dimerization constant $K_2 = 2.0 \times 10^6$ M^{-1}, the association constant for further elongation of the dimer $K_E = 1.8 \times 10^5$ M^{-1}, and the anticooperativity factor $\sigma = K_2/K_E = 10.8$ at 298 K were determined (Table 1). Upon increasing temperature, K_2 decreases with a linear relationship in the van't Hoff plot (Figure 20a, upper inset), from which the standard enthalpy $\Delta H° = -86.0$ kJ mol^{-1}, standard entropy $\Delta S° = -168$ J mol^{-1} K^{-1}, and standard Gibbs free enthalpy at 298 K upon dimerization were estimated to be $\Delta G° = -35.9$ kJ mol^{-1} (Table 1). The thermodynamic parameters of the elongation step were calculated from the respective van't Hoff plot (Figure 20a, lower inset) to be $\Delta H° = -86.0$ kJ mol^{-1}, $\Delta S° = -188$ J mol^{-1} K^{-1}, and $\Delta G°(298\ K) = -30.0$ kJ mol^{-1} (Table 1). Thus, **Agg 1** is formed in a weakly anticooperative[25] (σ = 10.8) manner with a preferential formation of dimers.[28] These dimers further elongate with a reduced aggregation tendency into small-sized oligomers appearing as nanoparticles (see AFMs in Figure 16c and *Chapter 7.1*, Figure 34a,b) similarly as previously observed for **PBI-2**.[28]

Table 1. Thermodynamic parameters K_2, K_E, $\Delta H°$, $\Delta S°$ and $\Delta G°$ obtained for the supramolecular polymerization processes of the three polymorphs **Agg 1** to **Agg 3** in MCH/Tol (5:4, v/v).

	Agg 1		**Agg 2**	**Agg 3**
	Dimerization	Elongation		
K_2 (298 K) (M^{-1})	2.0×10^6			
K_E (298 K) (M^{-1})		1.8×10^5	7.5×10^5	1.0×10^6
$\Delta H°$ (kJ mol^{-1})	−86.0	−86.0	−80.3	−96.3
$\Delta S°$ (J mol^{-1} K^{-1})	−168	−188	−157	−208
$\Delta G°$ (298 K) (kJ mol^{-1})	−35.9	−30.0	−33.5	−34.3

The formation of the dimer species can be followed by variable temperature NMR (VT-NMR) spectroscopy in deuterated toluene at a concentration of $c_T = 4.0 \times 10^{-4}$ M (*Chapter 7.1*, Figure 39). Upon decreasing temperature from 365 to 262 K, monomeric **(*R,R*)-PBI** (2 doublets for the inner and outer perylene protons) self-assembles into dimers which are characterized by a defined ^{1}H NMR spectrum. This dimerization induces a splitting of the perylene protons into four doublets indicating that the perylene protons are not chemically equivalent within a dimer while they are in monomeric **(*R,R*)-PBI**. Upon dimer formation, the signals corresponding to the N−H protons also split, which might be due to the formation of two slightly different types of intermolecular $N{-}H_{amide}\cdots O{=}C_{imide}$ hydrogen bonds (Figure 17b). Further evidence for the preferential formation of dimers can be drawn from matrix-assisted laser desorption/ionization (MALDI) mass spectrometry, where in addition to the peak corresponding to the Na^+ adduct of the monomer at *m/z* = 1841, an apparent signal at *m/z* = 3660 corresponding to Na^+ adduct of a **(*R,R*)-PBI** dimer is observed (*Chapter 7.1*, Figure 40). Notably, no signal at higher *m/z* values is observed, demonstrating the enhanced thermodynamic stability of dimers compared to larger oligomers that probably disassemble into monomers and dimers upon ionization.

While the transition from monomeric **(*R,R*)-PBI** to **Agg 1** can be fully covered and analyzed by concentration-dependent UV/vis spectroscopy in MCH/Tol (5:4, v/v) solution, **Agg 2** and **Agg 3** were accessible by supramolecular synthesis only at higher concentrations ($c_T \geq 1.0 \times 10^{-4}$ M). Thus, while the thermodynamics of the formation process cannot be monitored, the respective dissociation processes of the polymorphs **Agg 2** and **Agg 3** are accessible by temperature-dependent UV/vis spectroscopy to gain insights into their respective aggregation mechanisms. Upon increasing the temperature from 298 to 348 K, the absorption maximum of an **Agg 2** solution at $\lambda = 463$ nm disappears concomitant with the appearance of two bands at $\lambda = 489$ and 522 nm, which are indicative for the formation of a mixture of monomers and **Agg 1** (Figure 20b). The lack of defined isosbestic points further confirms the three species equilibrium between **Agg 2**, **Agg 1**, and monomers during disassembly of **Agg 2**. From a plot of the concentration-dependent absorbance at the absorption maximum of **Agg 2** at $\lambda = 463$ nm (characteristic for the disassembly of **Agg 2**, *Chapter 7.1*, Figure 41) against the temperature, the cooperative[25-27] nature of **Agg 2** formation is clearly visible (Figure 20e). From the latter graph, the critical temperatures T_E can be estimated which increase from 310 to 315 K with increasing concentration from $c_T = 1.3 \times 10^{-4}$ M to 2.0×10^{-4} M. To obtain the thermodynamic parameters, we modified a routine reported by Sugiyasu and Takeuchi[41-42] that accounts for three species in equilibrium with the assumption that during the disassembly of **Agg 2** the emerging monomers preferably form even-sized **Agg 1** oligomers[28] due to the

enhanced stability of the dimers (for details, see *Chapter 7.1*). From this analysis the elongation constants K_E at the respective critical temperatures T_E were extracted and a van't Hoff plot was prepared (inset Figure 20b) giving $\Delta H° = -80.3$ kJ mol^{-1}, $\Delta S° = -157$ J mol^{-1} K^{-1}, and $\Delta G°$ (298 K) = −33.5 kJ mol^{-1} for the elongation process of **Agg 2** (Table 1). Similarly, the disassembly of **Agg 3** was monitored by temperature-dependent UV/vis spectroscopy. Upon increasing the temperature from 298 to 325 K, the characteristic lowest energy absorption band at $\lambda = 575$ nm disappears and the broad absorption spectrum of **Agg 3** converts into an absorption spectrum resembling a mixture of **Agg 3**, **Agg 1**, and monomers (Figure 20c). As for **Agg 2**, a plot of the concentration-dependent absorbances at $\lambda = 575$ nm (characteristic for the disassembly of **Agg 3**, *Chapter 7.1*, Figure 42) reveals a cooperative aggregation mechanism with increasing critical temperatures T_E upon increasing concentration (Figure 20f). Performing the same analysis as for **Agg 2** (for details, see *Chapter 7.1*) yields $\Delta H° = -96.3$ kJ mol^{-1}, $\Delta S° = -208$ J mol^{-1} K^{-1}, and $\Delta G°$ (298 K) = −34.3 kJ mol^{-1} for the elongation process from the van't Hoff plot (inset Figure 20c and Table 1).

From the thermodynamic analysis, it becomes obvious that the thermodynamic stabilities of the three polymorphs are all in the same range and furthermore depend on the aggregate size (Figure 21, discussion in *Chapter 3.3*).

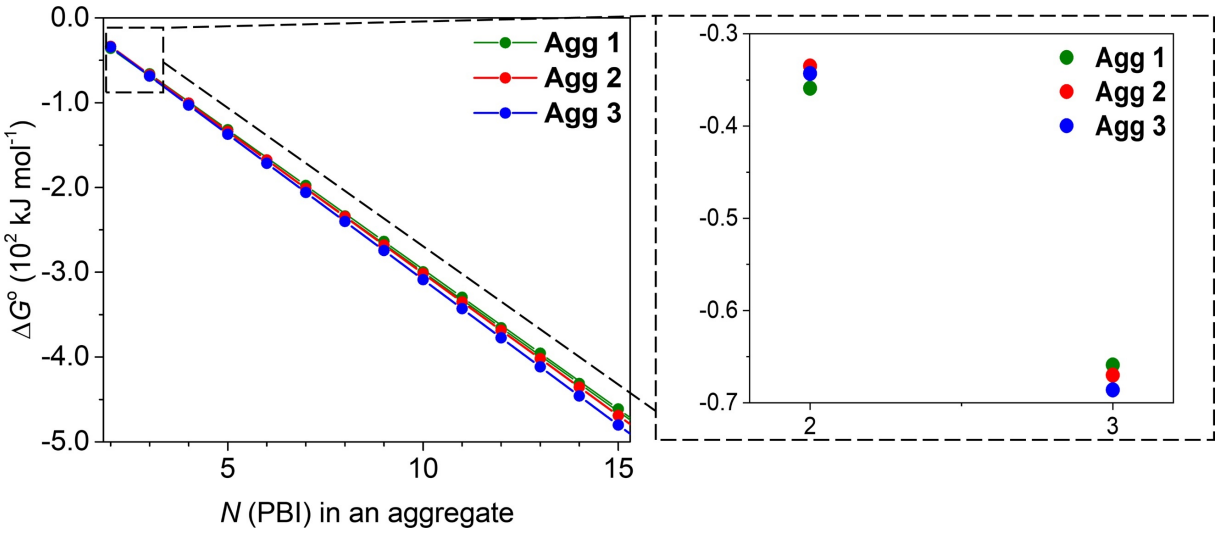

Figure 21. Change in the standard Gibbs free energy of sections of **(*R*,*R*)-PBI** polymorph stacks consisting of *N* PBI molecules at 298 K. Zoom: Standard Gibbs free energy for *N* = 2 and 3. For the sake of clarity solid lines are omitted in the insets.

3.2.5 Elucidation of the Kinetics and Pathway Control of the Supramolecular Polymorphism of (*R,R*)-PBI

In addition to the thermodynamic characterization of the three spectroscopically and microscopically distinct **(*R,R*)-PBI** polymorphs, kinetic studies were conducted to investigate the transformations between different polymorphic states, as well as the possibility of using seeds to induce the formation of a certain polymorph. As described above, ultrasonication (for experimental details see *Chapter 7.1*) was used to induce the transformation of **Agg 1** into **Agg 2** or **Agg 3** in MCH/Tol (5:4, v/v) solution (Figure 22).

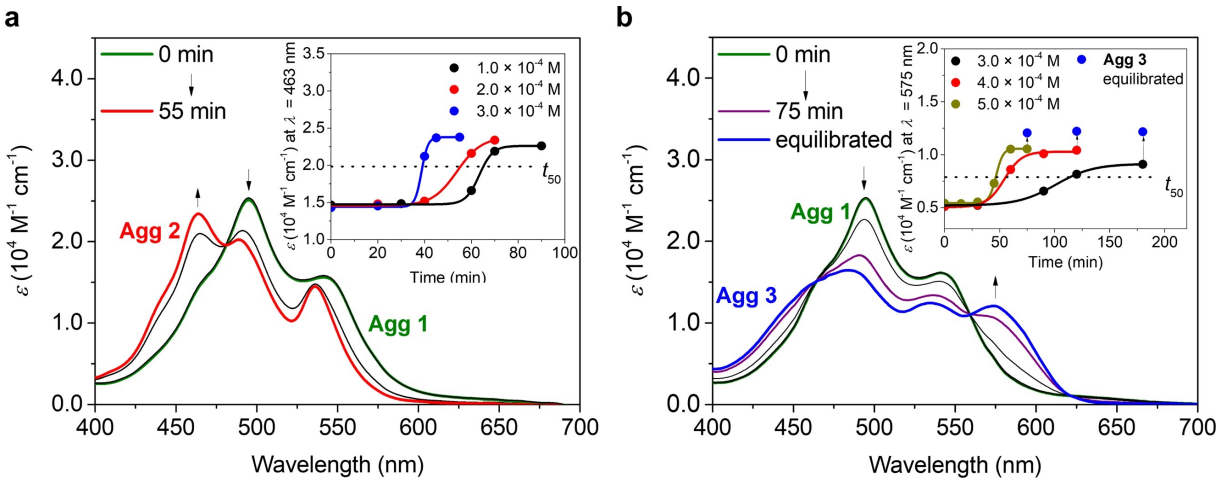

Figure 22. UV/vis-absorption spectra of the transformations of **Agg 1** → **Agg 2** (c_T = 3.0 × 10^{-4} M, 298 K) (**a**) and **Agg 1** → **Agg 3** (c_T = 5.0 × 10^{-4} M, 308 K) (**b**) in MCH/Tol (5:4, v/v) depending on the sonication period. Fully equilibrated solutions of **Agg 3** were obtained after cooling the respective solution from 308 K (purple line) to 298 K (blue line) after complete transformation. Insets: Plots of the ε values at λ = 463 nm (**a**) and λ = 575 nm (**b**) derived from the absorption spectra at different concentrations as a function of the sonication period for the transformations **Agg 1** → **Agg 2** (**a**) and **Agg 1** → **Agg 3** (**b**), respectively. Lines are set to guide the eye.

The transformation of **Agg 1** to **Agg 2** was performed at 293 − 298 K. The respective UV/vis spectra (Figure 22a) and plots of ε values at λ = 463 nm show a gradual transformation of **Agg 1** into **Agg 2** after a certain induction period that increases with decreasing concentration (inset Figure 22a). The nonlinear sigmoidal kinetics is characteristic for an autocatalytic process[120] in accordance with the cooperative aggregation mechanism of **Agg 2**.[25, 41, 43] The lag time t_{50}, defined as the time at which the transformation is 50% completed, decreases with increasing concentration (inset Figure 22a). This result is in accordance with our theoretical studies which suggested that **Agg 1** is an on-pathway intermediate[42, 146, 168, 244] to the formation of **Agg 2**, meaning that **Agg 2** is directly formed from **Agg 1** without the involvement of monomers as

intermediates. Notably, clear isosbestic points can be observed in the UV/vis spectra as well as in the corresponding CD spectra (*Chapter 7.1*, Figure 43), indicating that exactly two species, namely **Agg 1** and **Agg 2** (no **Agg 3**), are present during the transformation process.

The transformation of **Agg 1** into **Agg 3** in MCH/Tol (5:4, v/v) was achieved with the same experimental setup as the transformation of **Agg 1** into **Agg 2**. Since **Agg 3** is thermodynamically more stable than **Agg 2** upon increasing aggregate size (Table 1 and Figure 21), the concentration of the **Agg 1** solution was increased to $c_T \geq 3.0 \times 10^{-4}$ M. Simultaneously, the transformation temperature was increased to 308 K to favor the disassembly of potentially occurring **Agg 2** to form **Agg 3** exclusively. After complete transformation, the solutions were cooled from 308 K (purple line, Figure 22b) to 298 K (blue line, Figure 22b), and the characteristic absorption spectrum (for comparison see Figure 16a) of **Agg 3** was obtained. Again, isosbestic points in the UV/vis and CD spectra (*Chapter 7.1*, Figure 44) evidence the existence of only two species, namely **Agg 1** and **Agg 3**, during the transformation process, and therefore the occurrence of **Agg 2** can be excluded. A plot of the ε values at $\lambda = 575$ nm (inset Figure 22b) reveals the sigmoidal kinetics of the transformation characteristic for an autocatalytic aggregation process which is in accordance with a cooperative supramolecular polymerization process of **Agg 3**. Again, the lag time t_{50} for the transformation of **Agg 1** into **Agg 3** decreases upon increasing concentration (inset Figure 22b), indicating that **Agg 1** is an on-pathway intermediate to **Agg 3**.

From these studies, it becomes obvious that the supramolecular polymorphism of **(*R*,*R*)-PBI** can be controlled physically with **Agg 1** acting as the central kinetically trapped species from which **Agg 2** and **Agg 3** can be independently obtained by ultrasonication. This notion prompted us to perform seeded supramolecular polymerization experiments to produce **Agg 2** (Figure 23a) and **Agg 3** (Figure 23c) from **Agg 1** to control the supramolecular polymorphism in a similar way as done in conventional crystallizations by addition of crystal seeds.

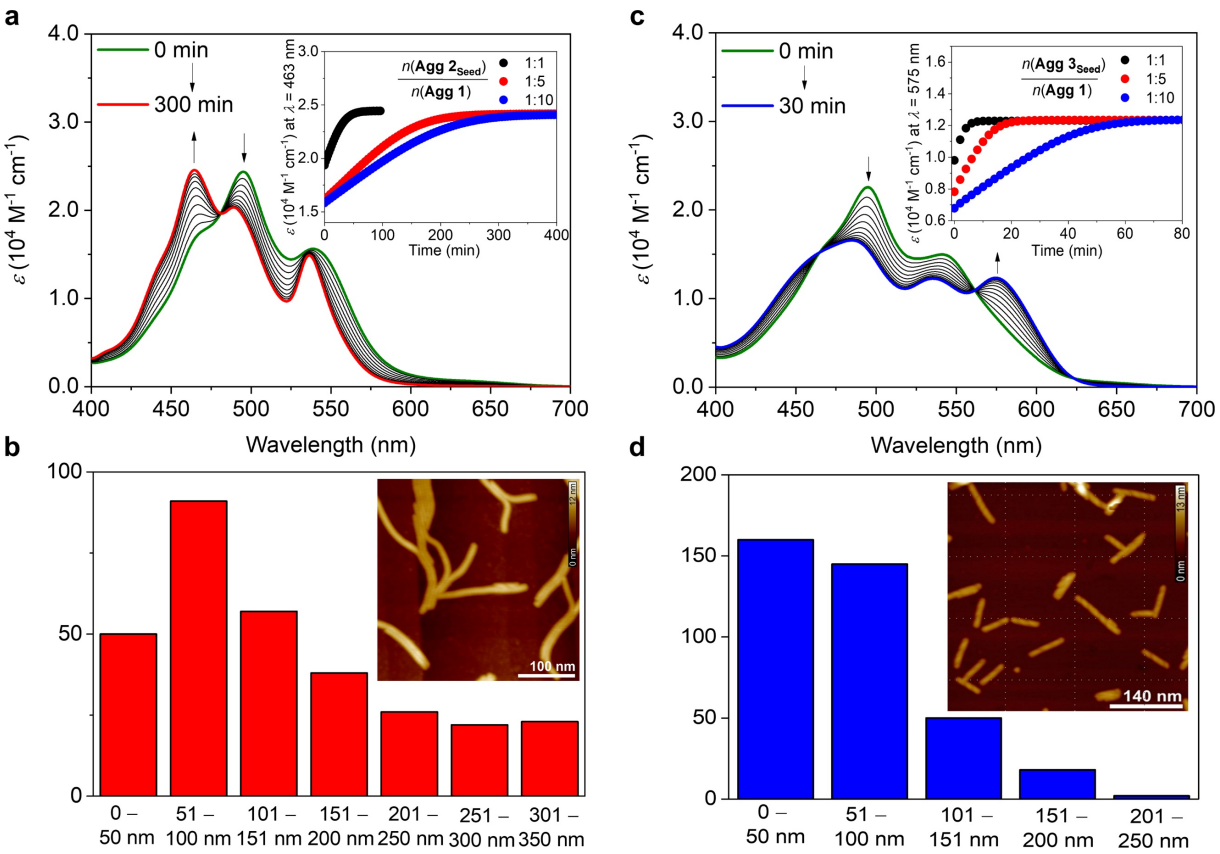

Figure 23. UV/vis-absorption spectra (n(**Agg 2**$_{seed}$)/n(**Agg 1**) = 1:5 (**a**) or n(**Agg 3**$_{seed}$)/n(**Agg 1**) = 1:5 (**c**)) and time course of the change in ε at λ = 463 nm (**a**) or λ = 575 nm (**c**) of the seeded supramolecular polymerization initiated by the addition of **Agg 2**$_{seed}$ (**a**) or **Agg 3**$_{seed}$ (**c**) to a solution of **Agg 1** (insets: n(**Agg 2**$_{seed}$)/n(**Agg 1**) (**a**) or n(**Agg 3**$_{seed}$)/n(**Agg 1**) (**c**) of 1:1 (black), 1:5 (red), and 1:10 (blue); the mixtures were prepared with stock solutions of [**Agg 1**] = [**Agg 2**$_{seed}$] = [**Agg 3**$_{seed}$] = 4.0×10^{-4} M in MCH/Tol (5:4, v/v), 298 K). Histograms of the length distributions of **Agg 2**$_{seed}$ (**b**) and **Agg 3**$_{seed}$ (**d**) as well as AFM height images of **Agg 2**$_{seed}$ (inset (**b**), Z scale is 12 nm) and **Agg 3**$_{seed}$ (inset (**d**), Z scale is 13 nm) prepared by spin-coating (10000 rpm) of the respective seed solution onto HOPG.*

Seeds of **Agg 2** (Figure 23b) and **Agg 3** (Figure 23d) were produced by treating the respective solutions ($c_T = 4.0 \times 10^{-4}$ M, MCH/Tol (5:4, v/v)) for 10 or 5 min in an ultrasonic bath, respectively. The lengths of **Agg 2**$_{seed}$ were 25 − 350 nm; those of **Agg 3**$_{seed}$, 15 − 250 nm. The morphology of the seeds (i.e., 1D nanofibers) as well as the respective UV/vis and CD spectra were identical to those of the respective polymorphs **Agg 2** and **Agg 3**.

* AFM measurements were performed by V. Stepanenko.

Seeded supramolecular polymerization was conducted by adding **Agg 2$_{seed}$** (Figure 23a,c) or **Agg 3$_{seed}$** (Figure 23b,d) solutions to a solution of kinetically trapped **Agg 1** (c_T = 4.0 × 10^{-4} M, MCH/Tol (5:4, v/v)) at molar ratios of 1:1, 1:5, and 1:10, and the induced transformations were followed by UV/vis spectroscopy. As shown in the insets of Figure 23a and b, seed addition completely eliminated the lag time resulting from the energy barrier for nucleation and directed metastable **Agg 1** into either **Agg 2** or **Agg 3** depending on the respective seeds. The seed-induced transformations are significantly faster than the spontaneous aggregation of **Agg 1** to **Agg 2** which did not occur within several days, while spontaneous transformation of **Agg 1** into **Agg 3** was never observed over time in the absence of ultrasonication. As expected, higher amounts of seeds led to faster transformation of **Agg 1** into the respective polymorph. Notably, propagation from the termini of the seeds occurred linearly as a function of time which clearly reflects the one-dimensional character of the respective nanofiber seeds (1D seeded supramolecular polymerization).[41-42]

3.3 Discussion

Crystallization is a result of a complex interplay of thermodynamics and kinetics and often accompanied by the occurrence of different solid state polymorphs. Despite the paramount importance of polymorphism in pharmaceutical and color pigment industries, mechanistic insights remain scarce[128, 146, 291] and the desired polymorphs are obtained more by empirically optimized procedures than based on mechanistic insights. In order to study polymorphism at its origin, that is, the initial self-assembly processes of molecular building blocks, here we have elucidated the simpler one-dimensional supramolecular polymerization for the model compound **(*R*,*R*)-PBI**. Our combined experimental and theoretical results are summarized in a qualitative energy landscape that covers the behavior of this system at different concentrations (Figure 24) and illustrates the pathway control of supramolecular polymorphism either physically by ultrasonication (magenta arrows) or chemically by seeding (black arrows). Upon increasing concentration, at infinite dilution stable monomeric **(*R*,*R*)-PBI** first self-assembles into **Agg 1** dimers as shown in the middle of Figure 24 (grey arrow). Upon further increase of concentration, **Agg 1** elongates into small-sized nanoparticulate oligomers following an anticooperative supramolecular polymerization.

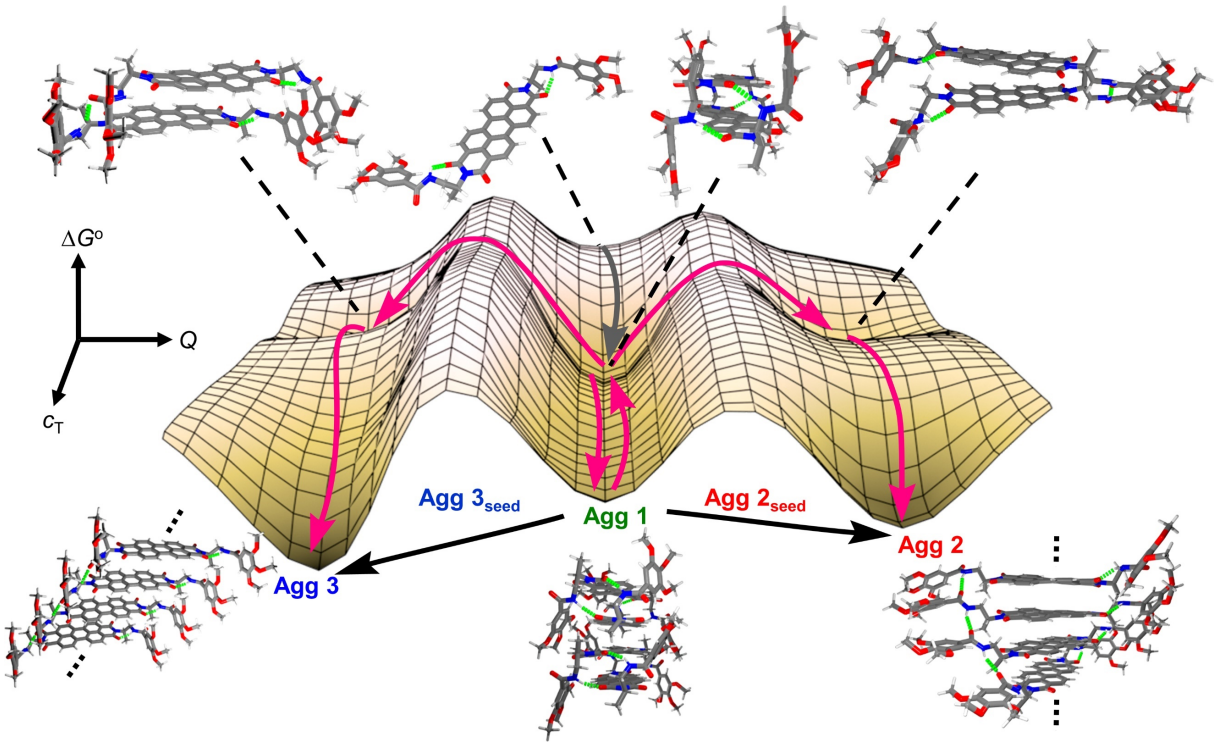

Figure 24. Qualitative energy landscape of the supramolecular polymerization of **(*R*,*R*)-PBI** dimers into its three polymorphs **Agg 1**–**3** upon increasing concentration c_T. The aggregate structures are schematically illustrated on PBI stacks generated using structural parameters obtained from PM6-D3H4 dimer calculations.* Q denotes the coordinate for the lowest-energy reaction pathway between the aggregate species at a given concentration c_T.

Already this anticooperativity points at the fact that this process is not associated with a significant gain in free enthalpy and that dimers of **Agg 1** are the predominant species within **Agg 1** oligomers due to their exceptionally high Gibbs Free energy (compared to further elongation of the dimers, Table 1) caused by 4-fold intermolecular N–H_{amide}···O=C_{imide} hydrogen-bonding between adjacent chromophores within a dimer. In contrast, the thermodynamic stability of **Agg 2** and **Agg 3** structures that was at low concentrations not sufficient to initiate nucleation now at higher concentration provides sufficient driving force to enable upon ultrasonication the nucleation and growth process of nanofibers of **Agg 2** and **Agg 3** polymorphs. Accordingly, after reaching a concentration greater than $c_T \geq 1.0 \times 10^{-4}$ M, **Agg 2** and **Agg 3** can be produced from **Agg 1** at room temperature according to the nucleation-elongation mechanism[25] as commonly observed for classical crystallization processes.

* Quantum chemical calculations were performed by M. I. S. Röhr and M. Bühler.

We note that the exact critical concentrations for the transformations **Agg 1** → **Agg 2** and **Agg 1** → **Agg 3** cannot be determined accurately, since the transformations have to be initiated and accelerated by ultrasonication to ensure a transformation in a reproducible time window of ~3 h. As predicted by our simulations on the initial step of the nucleation process of dimeric **Agg 1** into either **Agg 2** or **Agg 3**, the ultrasound-induced transformation processes proceed in an on-pathway fashion, meaning that the initial nucleation toward **Agg 2** or **Agg 3** nuclei is initiated by rearrangement processes of the individual molecules within **Agg 1** rather than disassembly into monomers (*Chapter 3.2.3* and *3.2.5*). Hence, oligomeric **Agg 1** solution is not only the central kinetically trapped state from which **Agg 2** and **Agg 3** can be produced, but it can be considered as a supersaturated solution according to classical crystallization theory.[46] In the physically controlled pathway, ultrasonication induces the rearrangement of hydrogen-bonded dimers that are in dynamic equilibrium with **Agg 1** oligomers (indicated in the middle of Figure 24) into either **Agg 2** (sonication at 293 − 298 K) or **Agg 3** dimers (sonication at 308 K) (rear magenta arrows in Figure 24). At high concentrations, these initially formed **Agg 2** or **Agg 3** dimers further self-assemble to the respective nuclei whose elongation provides the polymeric nanofibers of **Agg 2** or **Agg 3** (magenta arrows on the left- and right-hand side in Figure 24).

To understand why the supramolecular polymorphism of **(*R,R*)-PBI** arises at rather high concentrations ($c_T \geq 1.0 \times 10^{-4}$ M), the complex interplay between thermodynamics and kinetics has to be considered. Although the combination of the unique asymmetric hydrogen-bonding pattern and $\pi-\pi$ interactions within the polymorphs leads to similar Gibbs free energy releases upon formation of the intermolecular contacts between the chromophores within the polymorphs (Table 1), the formation of a certain polymorph is size-dependent which has thermodynamic (Table 1 and Figure 21) and kinetic reasons: in the qualitative free energy landscape illustrating the concentration-dependent behavior of the supramolecular system **(*R,R*)-PBI**, the dimeric structures constitute local energy minima based on our theoretical calculations (Figure 24). For small numbers of PBI chromophores N (e.g., $N = 2$), **Agg 1** is the most thermodynamically stable polymorph ($\Delta G°$ (**Agg 2**) > $\Delta G°$ (**Agg 3**) > $\Delta G°$ (**Agg 1**)) at 298 K owing to the exceptionally high stability of 4-fold hydrogen-bonded dimeric **Agg 1** which is by 2.4 kJ mol^{-1} or 1.6 kJ mol^{-1} more stable than **Agg 2** or **Agg 3** dimers (referring to our experimental data for dimer formation of **Agg 2** or **Agg 3**). While energy barriers between dimeric and enlarged **Agg 2** and **Agg 3** stemming from the cooperative character of the supramolecular polymerizations of **Agg 2** and **Agg 3** account for the thermodynamically unfavorable nucleation processes (Figure 20e,f),[25] no such energy barrier is given for the

anticooperative polymerization of **Agg 1** (Figure 24). However, as calculated from the experimentally determined $\Delta G°$ values of the supramolecular polymerization processes of **Agg 1**−**3** (Table 1 and Figure 21), the standard Gibbs free energies of larger species with $N \geq 7$ follow the trend $\Delta G°$ (**Agg 1**) > $\Delta G°$ (**Agg 2**) > $\Delta G°$ (**Agg 3**). These results are consistent with the observation that **Agg 2** and **Agg 3** form at high concentrations ($c_T \geq 1.0 \times 10^{-4}$ M) where **Agg 2** and **Agg 3** gain in stability compared to initially formed **Agg 1**, whereas at lower concentrations ($c_T \leq 2.0 \times 10^{-5}$ M) only **Agg 1** is observed.

The preferential formation of either **Agg 2** or **Agg 3** at higher concentrations has most likely also a kinetic reason: in one-dimensional helical supramolecular polymers, such as **Agg 2** and **Agg 3**, the nucleus size typically corresponds to one helical turn.[25] Considering the helical pitches of about 5.5 and 16 nm as obtained by AFM (Figure 16d,e and *Chapter 7.1*, Figure 34c−h) for **Agg 2** and **Agg 3**, respectively, and the calculated $\pi-\pi$ distance of the chromophores of 3.7 Å (Figure 18), the nucleus sizes of **Agg 2** and **Agg 3** would be about 15 and 43 molecules, respectively. Hence, at low concentrations, nucleation of **Agg 2** or **Agg 3** is less probable because of a high loss of translational entropy upon immobilization of the initially produced **Agg 2** and **Agg 3** dimers that need to further self-assemble to the whole nucleus. As indicated in Figure 24, these nucleation barriers between **Agg 1** and either **Agg 2** or **Agg 3** decrease upon increasing concentration. At concentrations above $c_T \geq 3.0 \times 10^{-4}$ M, the nucleation barrier of **Agg 2** becomes low enough that spontaneous transformation of **Agg 1** into **Agg 2** occurred even without ultrasonication, while the spontaneous transformation of **Agg 1** into **Agg 3** was never observed, meaning that the nucleation barrier between **Agg 1** and **Agg 3** is considerably higher than between **Agg 1** and **Agg 2**, which is consistent with a three-times larger nucleus size of **Agg 3** (Figure 24). This is also the reason why the ultrasound-induced transformation of **Agg 1** into **Agg 3** at a total concentration of $c_T = 3.0 \times 10^{-4}$ M has to be conducted at a higher temperature (308 K) compared to the transformation of **Agg 1** into **Agg 2** (293 − 298 K). The increased temperature further facilitates the disassembly of potentially forming **Agg 2** because of its lower thermodynamic stability compared to **Agg 3** (Table 1). Thus, the occurrence of **Agg 2** during the ultrasound-induced transformation of **Agg 1** into **Agg 3** was effectively eliminated at 308 K.

In analogy to conventional crystallization processes initiated by addition of small seed crystals, the same approach was applied as a chemical tool to control the pathway complexity of the supramolecular polymorphism of **(*R,R*)-PBI**. Seed addition almost completely eliminated the energy barriers between **Agg 1** and **Agg 2** or **Agg 1** and **Agg 3**, originating from thermodynamically unfavorable nucleation (pathways indicated with black arrows in Figure

24). Furthermore, these experiments show that **Agg 2** and **Agg 3** are thermodynamically more stable than **Agg 1** at $c_T = 4.0 \times 10^{-4}$ M, clearly reflecting the observed size-dependency of polymorph stability. Interestingly, a spontaneous back transformation to another polymorph was never observed for **Agg 2** and **Agg 3** due to their high kinetic stabilities which allows the preparation of all three polymorphs in solution followed by isolation in the solid state.

In sharp contrast to **(*R*,*R*)-PBI**, our previously studied organogelator systems **PBI-1**[43, 80] and **PBI-5**[252] each self-assemble under the investigated experimental conditions into a single thermodynamically stable supramolecular polymorph due to a perfect match of $\pi-\pi$ stacking interactions and intermolecular hydrogen bonds between the amide moieties on both sides of the respective molecule. Obviously, the additional sterical constraints imposed by the methyl substituents in close vicinity to the imide groups disfavors such a triple contact noncovalent binding motif which was never observed for **(*R*,*R*)-PBI** within our elaborate solvent-, concentration-, and temperature-dependent studies. Summing up, the similar but size-dependent aggregate stabilities due to the unique hydrogen-bonding pattern and packing motifs caused by the introduction of two α-CH_3 groups leads to a delicate trade-off between thermodynamics and kinetics, preventing the system from relaxing into a single strongly thermodynamically favored global energy minimum from which it cannot "escape" into another local energy minimum (another polymorph). This enables the supramolecular polymorphism of **(*R*,*R*)-PBI** in MCH/Tol 5:4 which was not observed for **PBI-1**, **PBI-2** or **PBI-5**.[28, 43, 80, 251-252]

At the current state of this novel field of research, it is not clear if **(*R*,*R*)-PBI** with its three polymorphs is a rare example or if for other π scaffold-based organogelators[139] conditions for the formation of different polymorphs were just not discovered. Nevertheless, taking into consideration that three-dimensional packing in crystals offers by far more possible variations than one-dimensional supramolecular polymerization, it is likely that smaller numbers of polymorphs are to be expected for the latter. Accordingly, **(*R*,*R*)-PBI** appears as a beautiful showcase, in particular due to its structural similarity to **PBI-1**, **PBI-2** and **PBI-5** for which no supramolecular polymorphism has been observed.

3.4 Conclusion

Polymorphism is a ubiquitous phenomenon in all research areas involving solid substances. Understanding and controlling the polymorphism of chemical compounds represents a major

challenge not only from an academic but also from an industrial point of view since the properties of a given material are determined by its packing arrangement.

Herein, in the context of our research on π organogelators and supramolecular polymerization, we discovered a unique example of supramolecular polymorphism which could be elucidated at the lowest level of hierarchy (i.e., the formation of 1D nanostructures). Accordingly, **(*R,R*)-PBI** shows three different one-dimensional supramolecular polymorphs that were isolable and stable over weeks in the same solvent and at the same concentration at room temperature. All three polymorphs show different packing arrangements with regard to their $\pi-\pi$ stacking modes, their orientations of the α-CH_3 groups, and hydrogen-bonding patterns, leading to similar but size-dependent thermodynamic stabilities of the three polymorphs. Kinetic investigations revealed that the polymorphism of **(*R,R*)-PBI** is not only caused by similar and size-dependent thermodynamic stabilities of the different polymorphs but also by specific energetic barriers between the respective polymorphs which are high enough to allow their isolation but low enough that they can be overcome by ultrasonication or the addition of seeds. Thus, we utilized ultrasonication as a physical tool and seeding as a chemical tool to control the pathway complexity of the supramolecular system **(*R,R*)-PBI**.

To conclude, this study elucidated by experimental and theoretical methods how supramolecular polymorphs can be properly characterized in terms of structure and thermodynamics as well as how they can be interconverted by ultrasonication or the addition of seeds. The here outlined approach should further provoke chemists to consider a supramolecular approach for the production of different ensembles of a given compound with distinct functional properties. Taking up McCrone's impactful quote that the "number of forms known for a given compound is proportional to the time and money spent in research on that compound" from 1965,[47, 292] the same holds true for supramolecular systems where we would expect that many more supramolecular structures might be accessible if sufficient efforts in fine-tuning parameters like the solvent, temperature, and concentration are spent or mechanical forces such as ultrasonication are exploited in detail and optimized.

Chapter 4

–

Control of Self-Assembly Pathways toward Conglomerate and Racemic Supramolecular Polymers

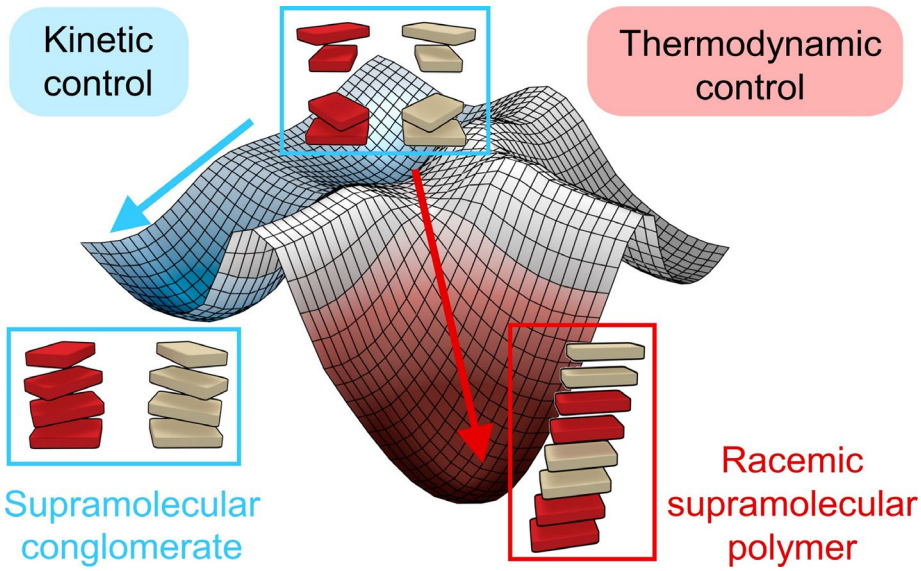

This chapter and the corresponding supporting information (*Chapter 7.2*) were submitted for publication:

M. Wehner, M. I. S. Röhr, V. Stepanenko, F. Würthner, *submitted for publication*, **2020**.

Abstract. Homo- and heterochiral aggregation during crystallization of organic molecules has significance both for fundamental questions related to the origin of life as well as for the separation of homochiral compounds from their racemates in industrial processes. Herein, we analyze these phenomena at the lowest level of hierarchy – that is the self-assembly of a racemic

mixture of **(*R*,*R*)-** and **(*S*,*S*)-PBI** into 1D supramolecular polymers. By a combination of UV/vis and NMR spectroscopy as well as atomic force microscopy, we demonstrate that homochiral aggregation of the racemic mixture leads to the formation of two types of supramolecular conglomerates under kinetic control, while under thermodynamic control heterochiral aggregation is preferred, affording a racemic supramolecular polymer. FT-IR spectroscopy and quantum chemical calculations reveal unique packing arrangements and hydrogen-bonding patterns within these supramolecular polymers. Time-, concentration- and temperature-dependent UV/vis experiments provided further insights into the kinetic and thermodynamic control of the conglomerate and racemic supramolecular polymer formation.

4.1 Introduction

Homo- and heterochiral aggregation during crystallization of organic racemates have not only been discussed in the context of the origin of homochirality on earth,[217] but are also of paramount importance for the separation and purification of racemic mixtures in pharmaceutical and agricultural industry or biotechnology.[225, 229] In general, crystallization of racemic mixtures affords in over 90% of all cases racemic crystals containing both enantiomers within the same crystal, while far less frequently, conglomerates are formed which are equimolar mixtures of homochiral crystals[51, 226] as first reported in the seminal work of L. Pasteur.[293] However, until now, the outcome of racemate crystallization processes can still not be accurately predicted due to the complex interplay between thermodynamic and kinetic factors governing nucleation and crystal growth.[226-228] Hence, a reduction of the complexity from 3D crystallization to 1D supramolecular self-assembly processes offers an appealing alternative to acquire deeper mechanistic insight on conglomerate and racemic crystal formation at its origin.

Indeed, within the last 20 years, research on self-assembly advanced significantly towards structures of increasing size including one- and two-dimensional supramolecular polymers.[8, 294] While this research relied for many years on thermodynamic control,[25-27, 242] i.e. the generation of equilibrium structures, only recently an advancement toward kinetically controlled supramolecular polymerization processes[12, 32, 35, 37, 196-197] and the smart utilization of out-of-equilibrium species took place.[154, 157, 198] Thus, combining knowledge on the thermodynamics together with detailed kinetic analysis enabled the control of supramolecular polymerization pathways towards certain supramolecular architectures.[29, 160, 295] Especially experimental parameters like the solvent,[146, 172, 183] temperature[143, 145] or external stimuli such as irradiation,[153, 174] stirring[76, 173] and seeding[41-44, 180-181, 184] proved as viable tools to control the pathway complexity of supramolecular polymerizations that led to the discovery of a multitude of examples where different supramolecular polymorphs were formed.[77, 128, 167]

An interesting example of supramolecular polymorphism has been described in the preceding *Chapter 3*. Thus, for enantiomerically pure perylene bisimide (PBI) dye **(*R*,*R*)-PBI** three polymorphic supramolecular polymers (**(*R*,*R*)-Agg 1−3**) could be produced at the same concentration in the same solvent by a proper choice of ultrasound conditions.[77] Accordingly, we were wondering if racemic mixtures of **(*R*,*R*)-PBI** with its enantiomer **(*S*,*S*)-PBI** would follow the same kinetic self-assembly pathways to give conglomerates or if a new racemic supramolecular polymer could form under properly chosen self-assembly conditions.

While thermodynamic and kinetic characteristics of conglomerate and racemic compound formation have been studied in 3D crystallization processes[226-228] or two-dimensional (2D) self-assembly processes on surfaces,[218, 231] herein the first detailed mechanistic study on conglomerate *versus* racemic compound formation in the 1D supramolecular polymerization of a racemic mixture of **(*R*,*R*)-** and **(*S*,*S*)-PBI** is provided. It is demonstrated that conglomerate helical supramolecular polymer formation proceeds under kinetic control leading to two different conglomerates **Con-Agg 1** and **Con-Agg 2** while under thermodynamic control racemic supramolecular nanorod (**Rac-Agg 4**) formation by heterochiral aggregation of **(*R*,*R*)-** and **(*S*,*S*)-PBI** is preferred.

4.2 Results

4.2.1 Synthesis of (*S*,*S*)-PBI

(*S*,*S*)-PBI was synthesized as described for **(*R*,*R*)-PBI**[253] from 3,4,5-tris-(dodecyloxy)benzoic acid (**16**)[254] according to literature known methods.[75, 77, 80, 253, 255-256, 296] Therefore, **16** was converted with thionyl chloride into the corresponding acyl chloride followed by amidization with **(*S*)-17**[255-256] which gave compound **(*S*)-18** in a yield of 84% over two steps.[75] Afterwards, the Boc protecting group of **(*S*)-18** was cleaved with trifluoroacetic acid and the resulting benzamide precursor was reacted with perylene-3,4:9,10-tetracarboxylic acid bisanhydride (**20**) in imidazole to the target compound **(*S*,*S*)-PBI** which was isolated as a red solid in a yield of 68% (Scheme 2). The synthetic details and characterization data are provided in *Chapter 7.2*.

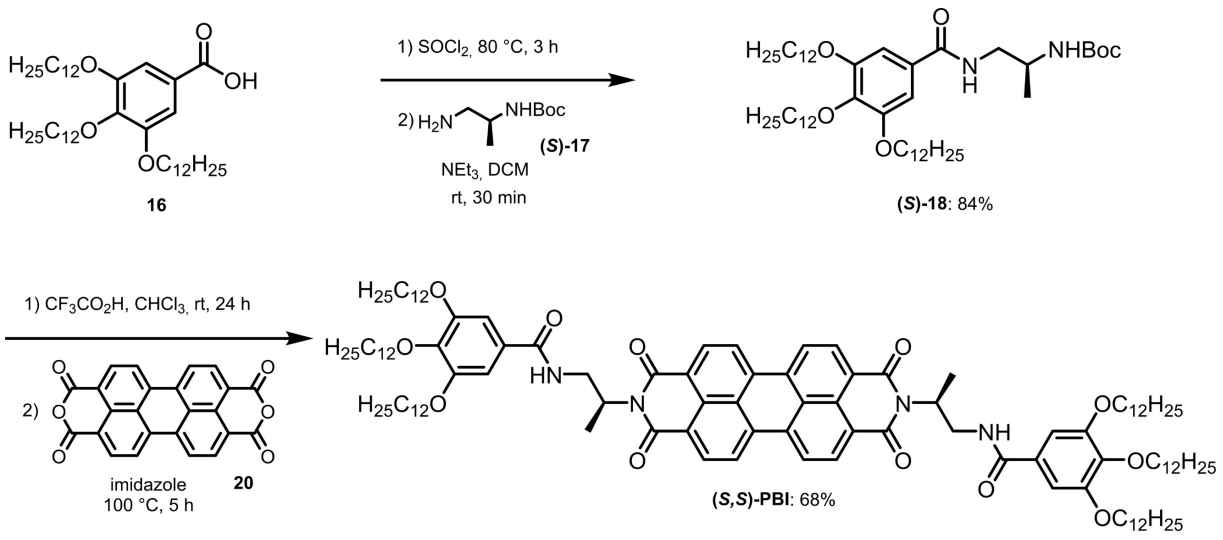

Scheme 2. Synthesis of **(*S*,*S*)-PBI** starting from literature known 3,4,5-trisdodecylbenzoic acid (**16**). The synthesis of **(*S*,*S*)-PBI** was reported in reference[253].

4.2.2 Supramolecular Synthesis and Spectroscopic Studies

Before studying the self-assembly behavior of the racemic mixture of **(*R*,*R*)-** and **(*S*,*S*)-PBI** (Figure 25a), the supramolecular polymerization of enantiopure **(*S*,*S*)-PBI** was compared to that of **(*R*,*R*)-PBI**. It should be noted that for simplicity, the supramolecular polymorphs of **(*R*,*R*)-PBI** were termed as **Agg 1**–**3** without a stereo descriptor in *Chapter 3*, while the same polymorphs will be termed as **(*R*,*R*)-Agg 1**–**3** in *Chapter 4*–*6* to distinguish them from those of **(*S*,*S*)-PBI** which are termed as **(*S*,*S*)-Agg 1**–**3**.

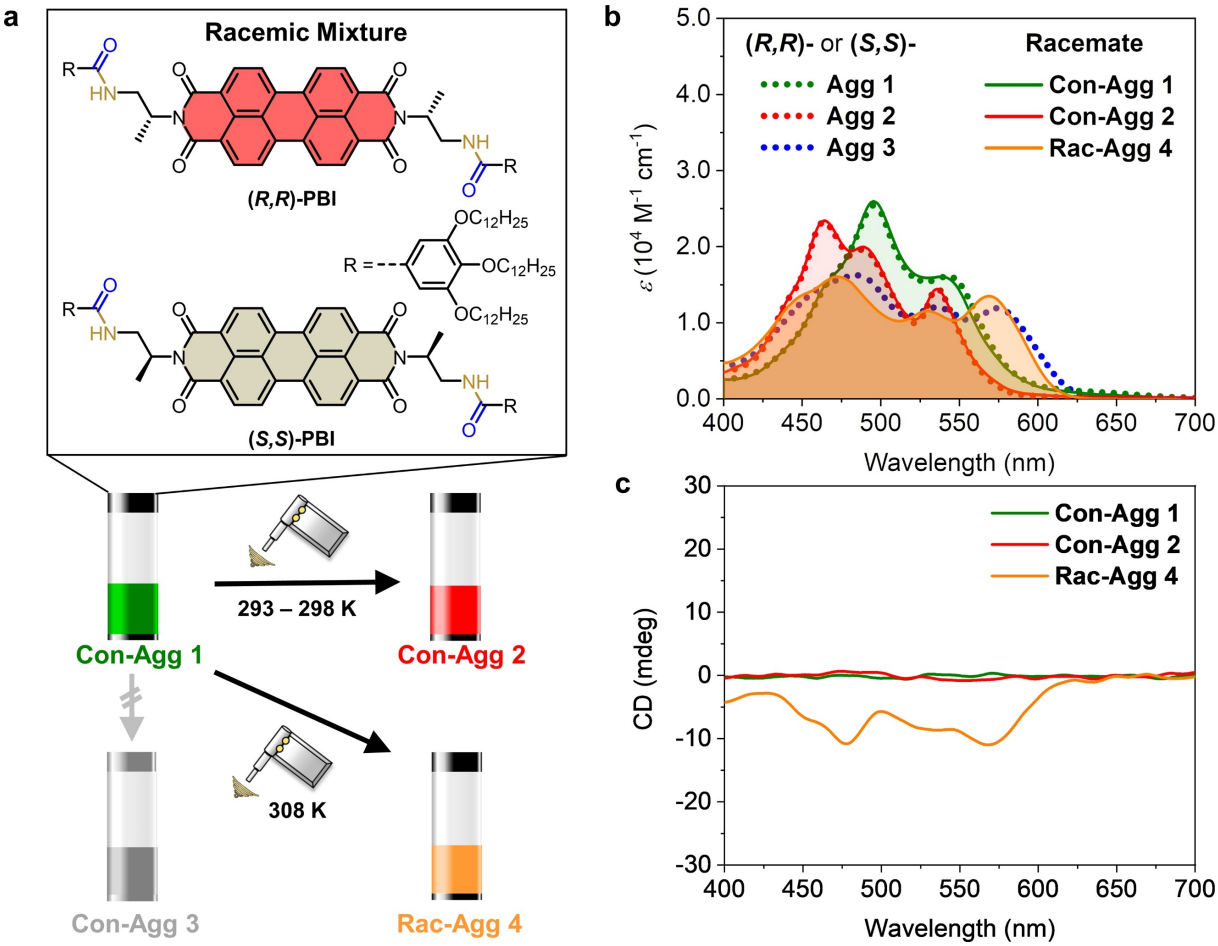

Figure 25. (**a**) Chemical structures of **(*R*,*R*)-** and **(*S*,*S*)-PBI** and schematic depiction of the ultrasound-induced supramolecular polymerization of the racemic mixture of **(*R*,*R*)-** and **(*S*,*S*)-PBI** into the conglomerates **Con-Agg 1** and **Con-Agg 2** and racemic supramolecular polymer **Rac-Agg 4**. (**b**) UV/vis-absorption and (**c**) CD spectra of the three different supramolecular polymorphs of the racemic mixture of **(*R*,*R*)-** and **(*S*,*S*)-PBI** (solid lines; $c_T = 3.0 \times 10^{-4}$ M for **Con-Agg 1** and **Con-Agg 2**; $c_T = 4.0 \times 10^{-4}$ M for **Rac-Agg 4**; 298 K) in MCH/Tol (5:4, v/v). For comparison, the absorption spectra of **(*R*,*R*)-Agg 1**–**3** (dotted lines) have been included in (**b**). It should be noted that the observed CD spectrum of **Rac-Agg 4** is a LD artefact[297] (for details, see *Chapter 7.2*).

According to UV/vis absorption spectroscopy (Figure 25b, dotted lines and *Chapter 7.2*, Figure 51), self-assembly of **(*S*,*S*)-PBI** under ultrasonication in a solvent mixture of methylcyclohexane (MCH) and toluene (Tol) at a volume ratio of 5:4 ($c_T \geq 3.0 \times 10^{-4}$ M) follows the same kinetic and thermodynamic pathways as reported for **(*R*,*R*)-PBI** (*Chapter 3.2*),[77] thereby providing the supramolecular polymorphs **(*S*,*S*)-Agg 1**−**3**. However, the 1D supramolecular polymorphs **(*S*,*S*)-Agg 1**−**3** exhibit opposite helicities than their respective enantiomeric polymorphs as evidenced by mirror image circular dichroism (CD) spectra (*Chapter 7.2*, Figure 52).

For the investigation of conglomerate *versus* racemic compound formation (Figure 25a), racemic mixtures of **(*R*,*R*)-** and **(*S*,*S*)-PBI** in MCH/Tol (5:4 v/v) were prepared as described in *Chapter 7.2*. First insights whether a supramolecular conglomerate or a racemic supramolecular polymer is formed, can be gained by UV/vis absorption spectroscopy: If the racemic mixture forms a supramolecular conglomerate, that is an equal mixture of enantiomeric supramolecular polymorphs of **(*R*,*R*)-** and **(*S*,*S*)-PBI** formed by homochiral aggregation of the individual enantiomers, the absorption spectrum of the conglomerate must be identical to those obtained for the enantiopure polymorphs. In contrast, formation of hetero-contacts between the π scaffolds within a racemic supramolecular polymer should lead to different electronic couplings[63] between the PBI chromophores and, hence, an absorption spectrum that differs from those observed for the enantiopure compounds.

We first investigated the racemic mixture under the identical conditions ($c_T = 3.0 \times 10^{-4}$ M in MCH/Tol (5:4 v/v) at 298 K) where **(*R*,*R*)-PBI** formed its three supramolecular polymorphs **(*R*,*R*)-Agg 1**−**3** (*Chapter 3.2.2*).[77] Upon cooling of the hot ($T \geq 363$ K) racemic mixture ($c_T = 3.0 \times 10^{-4}$ M) to 298 K, conglomerate **Con-Agg 1** is formed instantaneously which is composed of **(*R*,*R*)-Agg 1** and **(*S*,*S*)-Agg 1** in a 1:1 ratio resulting in the same absorption spectra of **Con-Agg 1** and **(*R*,*R*)-Agg 1** (Figure 25b). **Con-Agg 1** has an absorption maximum located at $\lambda = 496$ nm which is 26 nm hypsochromically shifted with regard to its constituting monomers (*Chapter 7.2*, Figure 53) and shows another weaker band at longer wavelengths. Such an absorption profile is typically observed for PBI H-aggregates[63] with rotationally displaced PBI molecules.[28, 252] As expected for a racemic mixture, **Con-Agg 1** does not show any CD signal (Figure 25c). Atomic force microscopy (AFM) studies reveal the same nanoparticle-like morphology of **Con-Agg 1** as observed for **(*R*,*R*)-** and **(*S*,*S*)-Agg 1** (Figure 26a,d,g and *Chapter 7.2*, Table 3) with a diameter of 3.8 ± 0.3 nm, corresponding to small 1D helical oligomers composed of hydrogen-bonded dimer pairs with an interplanar π–π distance of 3.6 Å as reported previously for **(*R*,*R*)-Agg 1** (*Chapter 3.2.3*).[77]

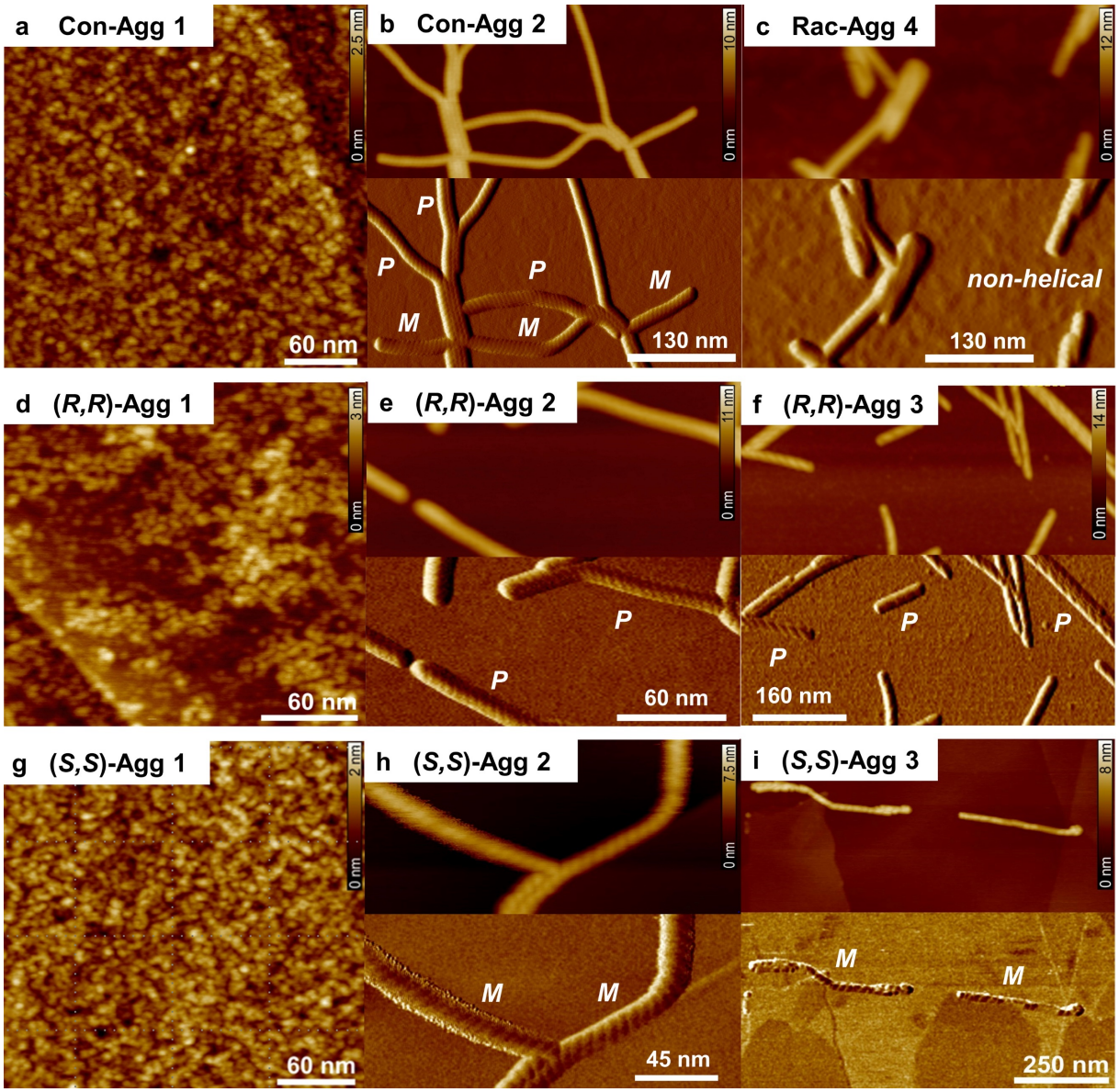

Figure 26. AFM images of **Con-Agg 1** (**a**), **Con-Agg 2** (**b**), **Rac-Agg 4** (**c**), **(*R*,*R*)-Agg 1**–**3** (**d-f**) and **(*S*,*S*)-Agg 1**–**3** (**g-i**) spin-coated on HOPG from MCH/Tol (5:4, v/v). Z scales are 2.5 (**a**), 10 (**b**), 12 (**c**), 3 (**d**), 11 (**e**), 14 (**f**), 2 (**g**), 7.5 (**h**) and 8 nm (**i**), respectively.* For **Con-Agg 1**, **(*R*,*R*)-** and **(*S*,*S*)-Agg 1** only the height images are shown whilst for the other species both height and phase images are provided. The helicities of the nanofibers of **Con-Agg 2** as well as of **(*R*,*R*)-** and **(*S*,*S*)-Agg 2** and **-Agg 3** are indicated in the respective phase images.

* AFM measurements were performed by V. Stepanenko.

Further evidence for conglomerate formation can be obtained from VT-NMR spectroscopy in deuterated toluene where the dimerization process of the respective monomers into **(*R,R*)-** and **(*S,S*)-Agg 1** leading to **Con-Agg 1** dimers upon cooling from 365 K to 262 K can be followed (*Chapter 7.2*, Figure 54). Interestingly, the VT-^{1}H NMR spectra of the dimerization of **Con-Agg 1** look identical to that of **(*R,R*)-PBI** into **(*R,R*)-Agg 1** dimers at all investigated temperatures. This proves that **Con-Agg 1** consists of homochiral **(*R,R*)-** and **(*S,S*)-Agg 1** since hetero-contact formation would result in differently arranged dimers with both, different temperature-dependent NMR spectra and absorption characteristics than enantiopure **(*R,R*)-Agg 1**.

To test if the racemic mixture follows the same self-assembly pathways as the enantiopure PBIs, **Con-Agg 1** was first sonicated under "kinetic conditions" at 293 – 298 K (Figure 25a) which are the conditions for the ultrasound-induced transformation of **(*R,R*)-Agg 1** into the kinetic polymorph **(*R,R*)-Agg 2** (*Chapter 3.2.2*).[77] Indeed, **Con-Agg 1** was successfully transformed into the supramolecular conglomerate **Con-Agg 2** as evidenced by the identical absorption spectra of **Con-Agg 2** and **(*R,R*)-Agg 2** (Figure 25b). Compared to **Con-Agg 1**, the absorption maximum of **Con-Agg 2** is further hypsochromically shifted to $\lambda = 464$ nm. Additional absorption bands appear at $\lambda = 489$ nm and 536 nm. The latter can be ascribed to the characteristic J-type excitonic coupling upon rotational displacement of the PBI dyes.[43, 252] As expected, **Con-Agg 2** does also not show any CD signal (Figure 25c). Conglomerate formation becomes directly visible by investigating the morphology of **Con-Agg 2** by AFM (Figure 26b and *Chapter 7.2*, Figure 55 for enlarged AFM images). While **(*R,R*)-Agg 2** and **(*S,S*)-Agg 2** show homochiral *P*- and *M*-helical 1D nanofibers (Figure 26e,h), respectively, **Con-Agg 2** reveals a 1:1 mixture of exactly these 1D supramolecular polymorphs. The *P*- and *M*-helices of **Con-Agg 2** both have a helical pitch of 5.7 ± 0.2 nm and a diameter of 4.5 ± 0.2 nm which are the same characteristics as observed for enantiopure **(*R,R*)-Agg 2** and **(*S,S*)-Agg 2** within the given error range (for details, see *Chapter 7.2*, Table 3). Hence, it can be concluded that upon ultrasonication at 293 – 298 K, **(*R,R*)-** and **(*S,S*)-Agg 1** individually transform into the homochiral nanofibers **(*R,R*)-** and **(*S,S*)-Agg 2** resulting in **Con-Agg 2**.

Next, it was attempted to transform **Con-Agg 1** into its thermodynamically stable state. In previous studies on **(*R,R*)-PBI**, it was shown that ultrasonication of a **(*R,R*)-Agg 1** solution in MCH/Tol 5:4 ($c_T = 3.0 \times 10^{-4}$ M) at 308 K for 180 min resulted in the formation of the thermodynamically stable **(*R,R*)-Agg 3** (Figure 25b and *Chapter 3.2.2*) and that this transformation process was faster the higher the concentration, thereby indicating an on-pathway self-assembly process from the original dimer species (*Chapter 3.2* and *3.3*).[77] While

at a concentration of $c_T = 3.0 \times 10^{-4}$ M **Con-Agg 1** did not transform into any new supramolecular polymorph within 180 min, ultrasonication of **Con-Agg 1** at an increased concentration of $c_T \geq 4.0 \times 10^{-4}$ M at 308 K led to the formation of a new supramolecular polymorph (Figure 25a). Unexpectedly, **Con-Agg 1** was not transformed into the conglomerate **Con-Agg 3** but rather into a new racemic supramolecular polymer termed as **Rac-Agg 4**.

In contrast to the conglomerates, **Rac-Agg 4** shows a broad and unstructured absorption spectrum with three absorption maxima that resembles those of **(*R*,*R*)-** or **(*S*,*S*)-Agg 3** (Figure 25b). In contrast to **(*R*,*R*)-** or **(*S*,*S*)-Agg 3**, however, the absorption maximum of **Rac-Agg 4** ($\lambda = 472$ nm) is blueshifted by 13 nm. The characteristic bathochromically shifted absorption band of **Rac-Agg 4** which results according to our theoretical calculations (*Chapter 3.2.3*) from longitudinally and transversally shifted PBI chromophores also appears at lower wavelengths ($\lambda = 569$ nm) and shows an about of 1500 M^{-1} cm^{-1} increased extinction coefficient of $\varepsilon = 13500$ M^{-1} cm^{-1} compared to **(*R*,*R*)-** or **(*S*,*S*)-Agg 3**. Recent theoretical studies by Spano and coworkers demonstrated that for such a slipped packing arrangement of PBIs, the large exciton band width of the absorption band might result from a rather strong coupling between Frenkel and charge transfer mediated excitons.[63] In contrast to **Con-Agg 1** and **Con-Agg 2**, **Rac-Agg 4** showed a negative monosignate CD signal with two minima at $\lambda = 478$ nm and 568 nm (Figure 25c) which was rather unexpected since racemic mixtures should not exhibit any CD signal. Notably, the same CD signal can be reproduced at different concentrations and is not a result of small enantiomeric excesses of **(*R*,*R*)-** or **(*S*,*S*)-PBI** within the **Rac-Agg 4** solution (*Chapter 7.2*, Figure 57). Instead, in accordance with previous reports,[297-298] we noted a (partial) alignment of supramolecular nanofibers in the cuvette, leading to the contamination of the CD spectra by artifacts from linear dichroism (LD) due to the optical imperfections of our setup[299] (further discussed in *Chapter 7.2*, Figure 58). By careful CD and LD studies in solution and aligned thin films we found that the observed monosignate CD signal stems from LD artifacts due to an alignment of **Rac-Agg 4** in the cuvette with preferentially vertically oriented PBIs. AFM studies reveal that **Rac-Agg 4** consists of short 1D nanorods (Figure 26c) with average lengths between 40 and 55 nm and a diameter of 4.1 ± 0.2 (*Chapter 7.2*, Table 3) that further agglomerate into sheet-like structures (*Chapter 7.2*, Figure 56) which is in line with the observed LD effect. Most notably, the non-helical nanorods of **Rac-Agg 4** constitute a unique structure which has never been observed during the supramolecular polymerization of enantiopure **(*R*,*R*)-** and **(*S*,*S*)-PBI** (Figure 26d–i). Hence, it can be concluded that those non-helical nanorods result from the formation of hetero-contacts between **(*R*,*R*)-** and **(*S*,*S*)-PBI** molecules within **Rac-Agg 4**.

For the elucidation of the hydrogen-bonding pattern within the new racemic supramolecular polymorph **Rac-Agg 4**, Fourier-transform infrared (FT-IR) spectroscopy was conducted which revealed N−H stretching frequencies at 3415, 3397 and 3306 cm^{-1} (Figure 27).

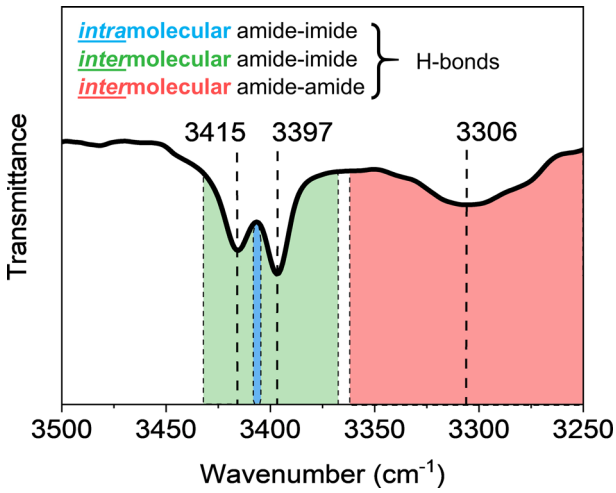

Figure 27. FT-IR spectrum of the N−H stretching region of **Rac-Agg 4** in MCH/Tol (5:4, v/v) at 298 K ($c_T = 5.0 \times 10^{-4}$ M). The approximate spectral regions corresponding to the N−H stretching vibrations of intramolecularly amide-imide (blue), intermolecularly amide-imide (green) and intermolecularly amide-amide (red) hydrogen-bonded N−H groups are indicated based on previous results on the supramolecular polymorphs of **(*R,R*)-PBI** under the same experimental conditions (*Chapter 3.2.2*, Figure 17b).[77]

According to our previous studies on **(*R,R*)-PBI** (*Chapter 3.2.2*, Figure 17b), the peaks at 3415 and 3397 cm^{-1} may be attributed to stretching vibrations of N−H groups incorporated into intermolecular hydrogen bonds between amide protons and imide oxygens of adjacent PBI molecules which have only been observed for **(*R,R*)-Agg 1**.[77] The fact, that two distinct frequencies are observed may be explained by two different arrangements within the hydrogen-bonded supramolecular polymer strand, i.e. between the same enantiomers and between different enantiomers. The broad peak at 3306 cm^{-1} and is characteristic for intermolecular amide-amide hydrogen bonds and has also been observed for **(*R,R*)-Agg 3** (*Chapter 3.2.2*, Figure 17b). Due to the broadness of this signal, the two types of intermolecular amide-amide hydrogen bonds between homo and heterochiral contacts presumably overlap. Since two different types of intermolecular amide-imide hydrogen bonds are observed for **Rac-Agg 4**, a structure with alternating monomers [•*R*••*S*••*R*••*S*•] (*R* and *S* denote **(*R,R*)-** and **(*S,S*)-PBI**, respectively) can be ruled out since in such a structure only one type of intermolecular amide-imide hydrogen bond should be observable. Instead, the present data in combination with mechanistic insights from kinetic studies (*Chapter 4.2.4*) indicate a structure of **Rac-Agg 4** in

which **(*R*,*R*)-** and **(*S*,*S*)-PBI** dimers are connected in an alternate fashion ([•*R*••*R*••*S*••*S*•]$_n$) with intermolecular amide-amide hydrogen bonds on one side and intermolecular amide-imide hydrogen bonds on the other side.

It is noteworthy that all three polymorphs of the racemic mixture can also be prepared at the same concentration of $c_T = 5.0 \times 10^{-4}$ M by the above mentioned ultrasonication procedure (Figure 25a and *Chapter 7.2*, Figure 59). They are kinetically stable and can be isolated in the solid state, which justifies the designation of **Con-Agg 1** and **Con-Agg 2** as supramolecular polymer conglomerates and **Rac-Agg 4** as a racemic supramolecular polymer (Figure 59).

4.2.3 Theoretical Calculations

To get further insight into the structure of **Rac-Agg 4**, quantum chemical calculations were performed for an octameric structural model of **Rac-Agg 4**, consisting of **(*R*,*R*)-** and **(*S*,*S*)-PBI** dimers organized in alternating order.* The subsequent optimization using PM6-D3H4[273-275] correction as implemented in the MOPAC software package[276] gives rise to a relaxed octameric structure (*Chapter 7.2*, Figure 60) from which for better clarity a tetramer section is extracted and shown in Figure 28.

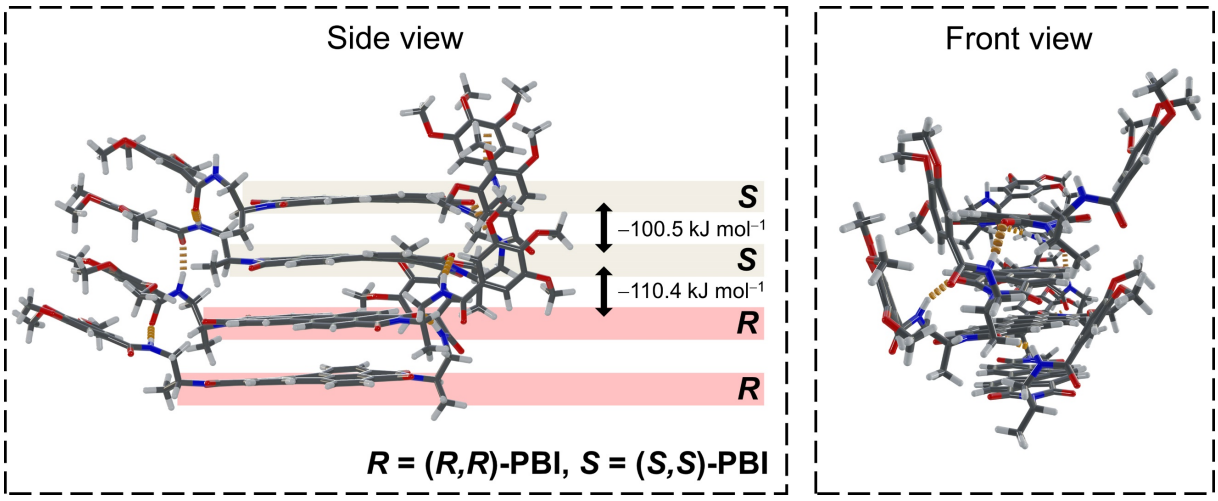

Figure 28. Side and front view of a geometry-optimized tetramer structure extracted from an octameric stack of **Rac-Agg 4** (*Chapter 7.2*, Figure 60).* Hydrogen bonds are indicated by orange dashes und dodecyloxy chains have been replaced by methoxy groups.

* Quantum chemical calculations were performed by M. I. S. Röhr.

Within **Rac-Agg 4** the PBI molecules show a π–π stacking distance of 3.4 Å, average longitudinal displacements of 0.7 Å and 2.1 Å within the homo- and hetero-contacts, respectively, and no transversal displacement. The respective PBI molecules within the homo- and heterodimers show average rotational displacements of 30° and 24°, respectively. Notably, the PBI molecules within the *RR*- and the *SS*-dimers as well as those within the *RS*- and *SR*-dimers are rotated in opposite directions (enantiomeric dimers within the **Rac-Agg 4** stack). Hence, the rotational displacements "cancel out" over the whole octameric stack resulting in a non-helical strand which is in accordance with the AFM results (Figure 26c). The geometry-optimized structure of **Rac-Agg 4** shows intermolecular amide-amide hydrogen bonds on one side and intermolecular amide-imide hydrogen bonds on the other side (Figure 28).

In order to estimate the "stabilization energy" upon packing of **(*R*,*R*)-** and **(*S*,*S*)-PBI** into a racemic supramolecular polymorph, we employed single point calculations on the isolated monomer and the homochiral (*RR* or *SS*) and heterochiral (*RS* or *SR*) dimers within the stack. Subtracting the gas phase energy of the isolated monomers from the respective dimer energies gives rise to the stabilization energy upon aggregation, which is on average −100.5 kJ mol^{-1} for the homochiral **(*R*,*R*)-** and **(*S*,*S*)-PBI** dimers and −110.4 kJ mol^{-1} for the heterochiral dimers. The greater energy gain upon hetero-contact formation might result from additional dispersion interactions between the peripheral phenyl rings[300-301] that are in close proximity to each other (middle *RS*-dimer in the front view, Figure 28 right). Such additional interactions are not observed within the homodimers in which the respective phenyl rings point to opposite sides (lower *RR*-dimer in the front view, Figure 28 right). In summary, our calculations indicate that heterochiral aggregation is significantly more favorable and the main driving force for the generation of the thermodynamically stable state **Rac-Agg 4** (*Chapter 4.2.5*).

4.2.4 Kinetic Analyses

In order to gain further insights into conglomerate and racemic supramolecular polymer formation, we performed time- and concentration-dependent UV/vis spectroscopic studies of the ultrasound-induced transformation of **Con-Agg 1** into **Con-Agg 2** or **Rac-Agg 4** (Figure 29).

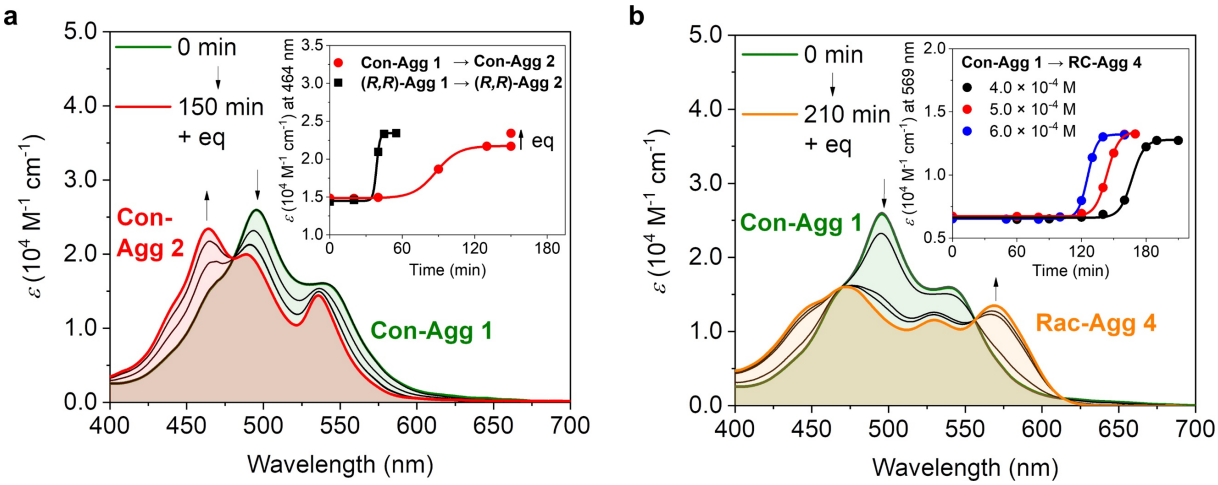

Figure 29. (**a**) UV/vis-absorption spectra for the transformations of **Con-Agg 1** → **Con-Agg 2** ($c_T = 3.0 \times 10^{-4}$ M, sonication at 293 − 298 K) (**a**) and **Con-Agg 1** → **Rac-Agg 4** ($c_T = 4.0 \times 10^{-4}$ M, sonication at 308 K) (**b**) in MCH/Tol (5:4, v/v) depending on the sonication period. Inset (**a**): Comparison of the ε values at $\lambda = 464$ nm of the ultrasound-induced transformations **Con-Agg 1** → **Con-Agg 2** with those of the transformation of **(*R*,*R*)-Agg 1** → **(*R*,*R*)-Agg 2** ($c_T = 3.0 \times 10^{-4}$ M). Inset (**b**): Plot of the time-dependent ε values at $\lambda = 569$ nm at different concentrations for the ultrasound-induced transformation of **Con-Agg 1** → **Rac-Agg 4**. "Eq" denotes equilibration achieved by letting the solution stand at room temperature after complete transformation. Lines are set to guide the eye.

The UV/vis spectra (Figure 29a) and plot of ε values (inset Figure 29a) at the absorption maximum of **Con-Agg 2** ($\lambda = 464$ nm) show a gradual transformation of **Con-Agg 1** into **Con-Agg 2** upon ultrasonication at 293 – 298 K. While at a concentration of $c_T = 3.0 \times 10^{-4}$ M this process is completed within 120 min it takes only 70 min at $c_T = 6.0 \times 10^{-4}$ M (*Chapter 7.2*, Figure 61) which indicates that **Con-Agg 2** is formed in an on-pathway fashion, i.e. **Con-Agg 1** directly transforms into **Con-Agg 2** without the dissociation into monomers as intermediates.[29, 160] The same behavior has also been observed for the self-assembly of enantiomerically pure **(*R*,*R*)-Agg 1** into **(*R*,*R*)-Agg 2** (*Chapter 3.2.5*).[77] Notably, clear isosbestic points can be observed in the UV/vis spectra indicating that only **Con-Agg 1** and **Con-Agg 2** are present during the transformation process and no **Rac-Agg 4** is formed under these "kinetic" ultrasonication conditions. The transformation of **Con-Agg 1** into **Con-Agg 2** is more than 60 min slower compared to the transformation of enantiopure **(*R*,*R*)-Agg 1** into **(*R*,*R*)-Agg 2** under the same experimental conditions (inset Figure 29a) which fits well with conglomerate formation because in a **Con-Agg 1** solution with a concentration of $c_T = 3.0 \times 10^{-4}$ M, the individual concentrations of **(*R*,*R*)-** and **(*S*,*S*)-PBI** are 1.5×10^{-4} M and, hence, the on-pathway transformation – a process that becomes slower upon lowering the

concentration − of **Con-Agg 1** into **Con-Agg 2** is slower compared to the transformation of **(*R,R*)-Agg 1** into **(*R,R*)-Agg 2** at the same concentration of $c_T = 3.0 \times 10^{-4}$ M.

Ultrasonication of **Con-Agg 1** at $c_T \geq 4.0 \times 10^{-4}$ M at 308 K leads to the transformation into **Rac-Agg 4** (Figure 29b). Again, isosbestic points in the UV/vis spectra prove the existence of only two species, i.e. **Con-Agg 1** and **Rac-Agg 4**, in equilibrium. A plot of the concentration and time-dependent ε values at $\lambda = 569$ nm reveals that the transformation of **Con-Agg 1** into **Rac-Agg 4** is faster the higher the concentration of **Con-Agg 1** (inset Figure 29b), indicating again that **Con-Agg 1** dimer units are on-pathway intermediates to **Rac-Agg 4**. Notably, this implies that no disassembly into monomers takes place prior further aggregation into **Rac-Agg 4** and, hence, this also precludes an alternating $[\bullet R \bullet\bullet S \bullet\bullet R \bullet\bullet S \bullet]_n$-structure of **Rac-Agg 4**. Together with the fact that all transformations within the supramolecular polymorphs of enantiopure **(*R,R*)-PBI** occur on the dimer level (*Chapter 3.2.3* and *3.3*)[77] this result further supports the calculated $[\bullet R \bullet\bullet R \bullet\bullet S \bullet\bullet S \bullet]_n$-structure of **Rac-Agg 4** with alternating dimers. Furthermore, the non-linear sigmoidal kinetics of **Rac-Agg 4** formation is characteristic for an autocatalytic process following the cooperative aggregation mechanism[25, 41, 43, 77] which is proven in the next section.

4.2.5 Thermodynamic Analyses

While the thermodynamic characteristics of **Con-Agg 1** and **Con-Agg 2** can be deduced from previous studies on **(*R,R*)-Agg 1** and **(*R,R*)-Agg 2** (*Chapter 3.2.4*, Table 1),[77] temperature-dependent UV/vis spectroscopic studies were conducted to elucidate the aggregation mechanism and the thermodynamic parameters of the new racemic supramolecular polymer **Rac-Agg 4** (Figure 30). Since **Rac-Agg 4** is only accessible at higher concentration under ultrasound irradiation, the thermodynamics of **Rac-Agg 4** formation cannot be monitored. However, the dissociation process of **Rac-Agg 4** can be analyzed by temperature-dependent UV/vis spectroscopy. Upon heating of **Rac-Agg 4** from 293 K to 340 K (Figure 30a), the characteristic lowest energy absorption band of **Rac-Agg 4** at $\lambda = 569$ nm and the broad absorption spectrum of **Rac-Agg 4** converts into an absorption spectrum resembling a mixture of **Con-Agg 1** and monomers (Figure 25b and *Chapter 7.2*, Figure 53). The lack of defined isosbestic points further supports the involvement of these three species.

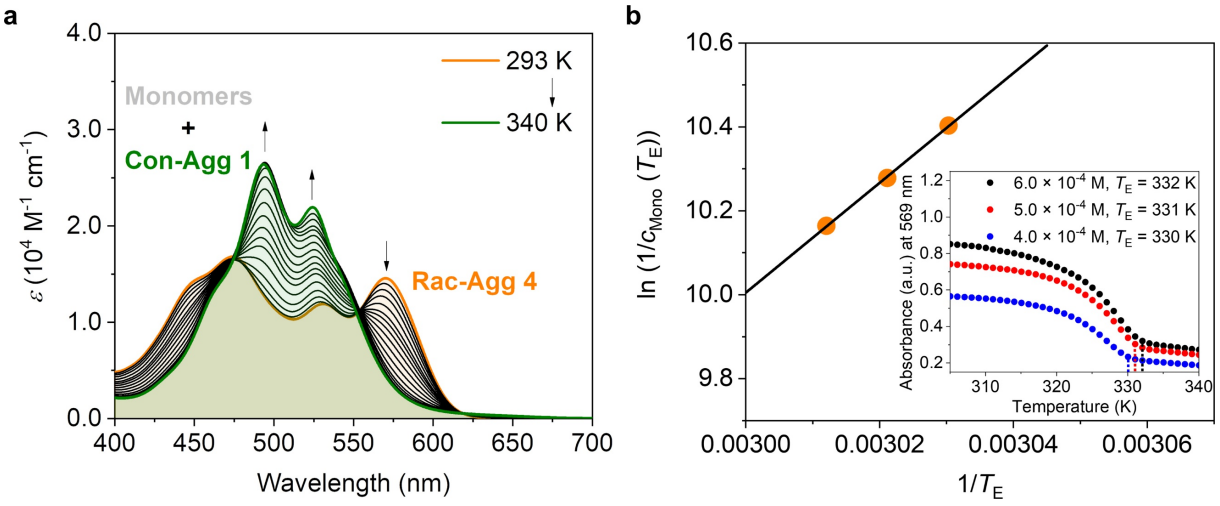

Figure 30. (**a**) Temperature-dependent UV/vis-absorption spectra of **Rac-Agg 4** upon heating ($c_T = 4.0 \times 10^{-4}$ M, T = 293 K ⟶ 340 K, heating rate: 1 K min^{-1}). (**b**) Van`t Hoff analysis of the thermodynamic parameters of the elongation of **Rac-Agg 4**. Inset (**b**): Plot of the absorbances at $\lambda = 569$ nm as a function of temperature and concentration. The dotted lines indicate the respective elongation temperatures.

A plot of absorbance at $\lambda = 569$ nm (inset Figure 30b) reveals a characteristic shape for a cooperative aggregation mechanism for **Rac-Agg 4** (*Chapter 2.2*)[25-26, 30] with critical temperatures T_E that increase from 330 K to 332 K upon increasing concentration from $c_T = 4.0 \times 10^{-4}$ M to 6.0×10^{-4} M. According to a previously reported procedure,[77] we determined the overall monomer concentrations c_{Mono} at the respective critical temperatures T_E for different concentration of **Rac-Agg 4** from which we prepared a van't Hoff plot giving a standard enthalpy release of $\Delta H° = -109$ kJ mol^{-1} and standard entropy of $\Delta S° = -243$ J mol^{-1} K^{-1} upon elongation as well as an association constant of $K_E = 2.6 \times 10^6$ M^{-1}, and a standard Gibbs free energy of $\Delta G° = -36.6$ kJ mol^{-1} at 298 K (for details, see *Chapter 7.2*). The thermodynamic parameters of the supramolecular polymorphs of the racemic mixture as well as those of the enantiopure compounds are summarized in Table 2. The thermodynamic parameters of **Con-Agg 1**, **Con-Agg 2** and hypothetic **Con-Agg 3** can be derived from those of **(*R*,*R*)-Agg 1**–**3** by taking the following considerations into account: since **(*R*,*R*)-Agg 1**–**3** and **(*S*,*S*)-Agg 1**–**3** are enantiomers with the same absorption characteristics (Figure 25b and *Chapter 7.2*, Figure 51) the thermodynamic parameters of **(*S*,*S*)-Agg 1**–**3** are identical to those of **(*R*,*R*)-Agg 1**–**3** (*Chapter 3.2.4*, Table 1).[77] **Con-Agg 1**, **Con-Agg 2** and hypothetic **Con-Agg 3** are conglomerates consisting of equal amounts of either **(*R*,*R*)-** and **(*S*,*S*)-Agg 1**, **(*R*,*R*)-** and **(*S*,*S*)-Agg 2** or equal amounts of **(*R*,*R*)-** and **(*S*,*S*)-Agg 3**, respectively.

Table 2. Thermodynamic parameters K_2, K_E, $\Delta H°$, $\Delta S°$ and $\Delta G°$ obtained for the supramolecular polymerization processes of **Con-Agg 1**, **Con-Agg 2**, **Rac-Agg 4** and of **(*R*,*R*)-** and **(*S*,*S*)-Agg 1**–**3** in MCH/Tol (5:4, v/v).

	Con-Agg 1 **(*R*,*R*)-Agg 1** **(*S*,*S*)-Agg 1**		**Con-Agg 2** **(*R*,*R*)-Agg 2** **(*S*,*S*)-Agg 2**	**(Con-Agg 3)** **(*R*,*R*)-Agg 3** **(*S*,*S*)-Agg 3**	**Rac-Agg 4**
	Dimerization	**Elongation**			
K_2 (298 K) (M^{-1})	2.0×10^6				
K_E (298 K) (M^{-1})		1.8×10^5	7.5×10^5	1.0×10^6	2.6×10^6
$\Delta H°$ (kJ mol^{-1})	−86.0	−86.0	−80.3	−96.3	−109
$\Delta S°$ (J mol^{-1} K^{-1})	−168	−188	−157	−208	−243
$\Delta G°$ (298 K) (kJ mol^{-1})	−35.9	−30.0	−33.5	−34.3	−36.6

Therefore, the thermodynamic parameters of **Con-Agg 1**–**3** are approximately identical to those of **(*R*,*R*)-Agg 1**–**3** under the assumption that no hetero-contacts are formed which is suggested by VT-^{1}H NMR spectroscopy (*Chapter 7.2*, Figure 54). We note that **Con-Agg 3** is not formed from the racemic mixture of **(*R*,*R*)-** and **(*S*,*S*)-PBI** and, hence, it is written in parenthesis in Table 2. The standard Gibbs free energies $\Delta G°$ at 298 K of **Con-Agg 1**–**3** and **Rac-Agg 4** were used to calculate the racemic polymorph stabilities upon increasing aggregate size (Figure 31).

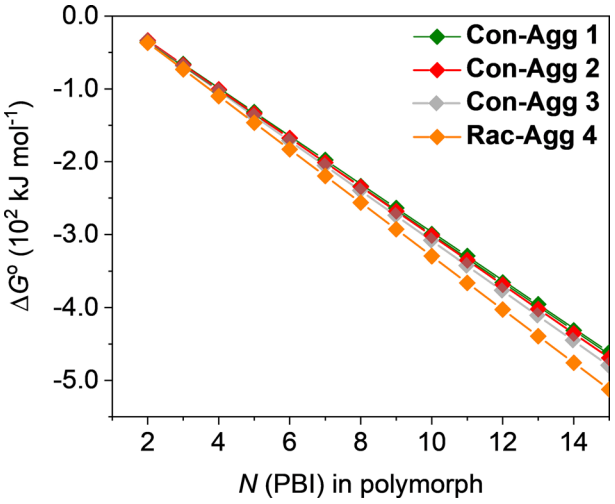

Figure 31. Change in the standard Gibbs free energy $\Delta G°$ of sections of stacks of the racemic mixture of **(*R*,*R*)-** and **(*S*,*S*)-PBI** consisting of *N* PBI molecules at 298 K. For comparison, the hypothetic $\Delta G°$ values of **Con-Agg 3** are also plotted although this species is not formed within the racemic mixture due to the formation of thermodynamically stable **Rac-Agg 4** (see *Chapter 4.3*).

4.3 Discussion

To construct a qualitative potential energy surface of the supramolecular conglomerate and racemic supramolecular polymer formation, the polymer structures and thermodynamic features of **Con-Agg 1** and **Con-Agg 2** will first be summarized (Figure 32 and Table 2).

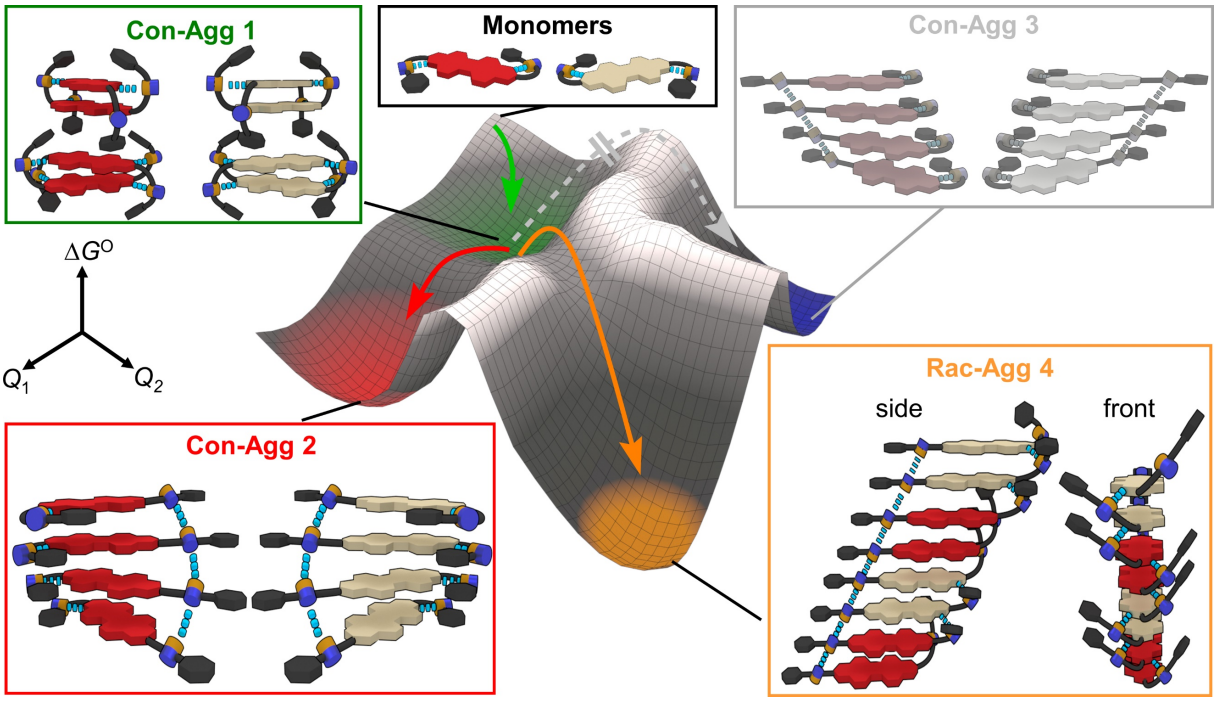

Figure 32. Qualitative energy landscape for the supramolecular conglomerate and the racemic supramolecular polymer formation from the racemic mixture of **(*R*,*R*)-** and **(*S*,*S*)-PBI**. The aggregate structures corresponding to "accessible" supramolecular pathways (**Con-Agg 1**, **Con-Agg 2** and **Rac-Agg 4**) are schematically illustrated in colour while the structure of the "inaccessible" polymorph **Con-Agg 3** is shown in grey. The colour code of the respective PBIs is adjusted to Figure 25a, hydrogen-bonding is indicated with blue dashes. Q_1 and Q_2 denote coordinates for the lowest-energy reaction pathway between the different polymorphs.

Since these two conglomerates are composed of equal mixtures of homochiral **(*R*,*R*)-** and **(*S*,*S*)-Agg 1** or **(*R*,*R*)-** and **(*S*,*S*)-Agg 2**, the aforementioned characteristics are known from previous extensive studies on **(*R*,*R*)-PBI** (*Chapter 3.2* and *3.3*).[77] Thus, **Con-Agg 1** consists of tightly bound homochiral *M*- and *P*-helical **(*R*,*R*)-** and **(*S*,*S*)-Agg 1** dimers (Figure 32 and *Chapter 7.2*, Figure 52) which are only loosely connected to each other by small elongation constants in an anticooperative aggregation mechanism.[28] Within those dimers the respective PBI dyes are connected by a combination of π–π interactions and intermolecular amide-imide hydrogen bonds that show N–H stretching frequencies of 3406 and 3377 cm^{-1} (*Chapter 3.2.2*, Figure 17b) while only weak van-der-Waals interactions are given between the respective dimers.

In contrast to **Con-Agg 1**, **Con-Agg 2** is formed by a cooperative supramolecular polymerization and shows helical structures in which the respective PBI monomers within the homochiral *P*- and *M*-helical **(*R,R*)-** and **(*S,S*)-Agg 2** are connected by a combination of π–π interactions and intermolecular amide-amide hydrogen bonds on one side (N−H stretching frequency at 3336 cm^{-1}). On the other side, however, intramolecular amide-imide hydrogen bonds with N−H stretching frequencies at 3406 cm^{-1} are formed (*Chapter 3.2.2*, Figure 17b). From the thermodynamic studies it becomes obvious that the racemic supramolecular polymer **Rac-Agg 4** is the thermodynamically stable state showing the highest Gibbs free energy release upon elongation of $\Delta G° = -36.6$ kJ mol^{-1} while **Con-Agg 1** shows $\Delta G°$ values of −35.9 kJ mol^{-1} for its dimerization and −30.0 kJ mol^{-1} for further elongation of these dimers and **Con-Agg 2** a value of $\Delta G°$ (298 K) = −33.5 kJ mol^{-1}. Thus, upon increasing aggregate size the thermodynamic stabilities follow the trend $\Delta G°$ (**Con-Agg 1**) > $\Delta G°$ (**Con-Agg 2**) > $\Delta G°$ (**Rac-Agg 4**) meaning that **Rac-Agg 4** is the most stable and **Con-Agg 1** the least stable species as indicated in Figure 31 and in the qualitative potential energy surface (Figure 32). This can on the one hand be explained by the formation of energetically favorable heterochiral contacts between **(*R,R*)-** and **(*S,S*)-PBI** dimers (Figure 28) but is also a result of stronger hydrogen-bonding within **Rac-Agg 4** (Figure 27) compared to that of **Con-Agg 1** and **Con-Agg 2**.[77] Especially the intermolecular amide-amide hydrogen bonds within **Rac-Agg 4** with a N−H stretching frequency of 3306 cm^{-1} are significantly stronger (indicated by a lower wavenumber) than the respective amide-amide hydrogen bonds in **Con-Agg 2** (3336 cm^{-1}). Furthermore, within **Rac-Agg 4** two additional intermolecular amide-imide hydrogen bonds with N−H stretching frequencies of 3415 and 3397 cm^{-1} are observed (Figure 27 and Figure 32) while **Con-Agg 2** shows beside intermolecular amide-amide H-bonds only intramolecular amide-imide H-bonds (N−H stretching frequency of 3406 cm^{-1}). **Con-Agg 1** shows slightly stronger intermolecular amide-imide hydrogen bonds with N−H stretching frequencies of 3406 and 3377 cm^{-1} than **Rac-Agg 4** but additional strong intermolecular amide-amide hydrogen bonds are missing within **Con-Agg 1**. Thus, the hydrogen-bonding pattern of **Rac-Agg 4** results in the energetically most favourable and most ordered structure with the highest standard enthalpy release and the lowest (most unfavourable) standard entropy upon aggregation (Table 2).

Based on these data, the potential energy surface shown in Figure 32 was constructed that reflects all the thermodynamic features of the supramolecular polymerization of the racemic mixture of **(*R,R*)-** and **(*S,S*)-PBI** into the supramolecular conglomerates **Con-Agg 1** and **Con-Agg 2** and the racemic supramolecular polymer **Rac-Agg 4**, respectively. Furthermore the

energy surface includes the hypothetic polymerization pathway to **Con-Agg 3** – a 1:1 mixture of **(*R,R*)-** and **(*S,S*)-Agg 3** – which is not formed by the racemic mixture. In contrast, **(*R,R*)-** and **(*S,S*)-Agg 3** have been observed for the pure enantiomers in our previous study (*Chapter 3.2* and *3.3*).[77] On a qualitative level, Figure 32 also includes the transition energies of the self-assembly pathways deduced from our kinetic data. Thus, upon cooling of a concentrated ($c_T \geq 3.0 \times 10^{-4}$ M) racemic mixture of **(*R,R*)-** and **(*S,S*)-PBI**, instantaneously **Con-Agg 1** is formed (green arrow, Figure 32) which is a kinetic conglomerate consisting of equal amounts of small **(*R,R*)-** and **(*S,S*)-Agg 1** oligomers containing strongly bound dimeric species (*Chapter 7.2*, Figure 54). **Con-Agg 1** is the central intermediate towards the formation of conglomerate **Con-Agg 2** and racemic compound **Rac-Agg 4**. Under kinetic conditions, i.e. ultrasonication at 293 – 298 K, **Con-Agg 1** is transformed into the more stable **Con-Agg 2** (red arrow, Figure 32) which is a kinetic polymorph. The kinetic barrier between **Con-Agg 1** and **Con-Agg 2** that has to be overcome is lower compared to that between **Con-Agg 1** and **Rac-Agg 4** and, hence, **Con-Agg 2** forms at lower temperatures of 293 – 298 K upon ultrasonication although it is less thermodynamically stable than **Rac-Agg 4**. In contrast, the kinetic barrier between **Con-Agg 2** and **Rac-Agg 4** is too high to be overcome spontaneously at 298 K. Hence, it can be summarized that conglomerates **Con-Agg 1** and **Con-Agg 2** are formed under kinetic control.

Transformation of **Con-Agg 1** under thermodynamic conditions, i.e. ultrasonication at a higher temperature of 308 K, allows the system to transform into its thermodynamically most stable state, that is **Rac-Agg 4** (orange arrow, Figure 32). This reveals the most striking difference to the supramolecular polymerization of the single enantiomer systems, **(*R,R*)-** or **(*S,S*)-PBI**, leading to **(*R,R*)-** or **(*S,S*)-Agg 3**, respectively. The inaccessibility of **Con-Agg 3** was rather unexpected since **(*R,R*)-Agg 3** was reported to be the thermodynamically stable state of the supramolecular polymerization of **(*R,R*)-PBI** under the same experimental conditions. The most obvious explanation is that **Rac-Agg 4** with the $[\bullet R \bullet\bullet R \bullet\bullet S \bullet\bullet S \bullet]_n$ sequence is by 2.3 kJ mol^{-1} more stable than **Con-Agg 3** consisting of $[\bullet S \bullet\bullet S \bullet\bullet S \bullet\bullet S \bullet]_n$ and $[\bullet R \bullet\bullet R \bullet\bullet R \bullet\bullet R \bullet]_n$ sequences (Table 2). Further experiments to produce **Con-Agg 3** by ultrasonication at intermediate temperatures of 303 K also failed and led to the formation **Rac-Agg 4** suggesting that the inaccessibility of **Con-Agg 3** has not only thermodynamic but also kinetic reasons, that is, the kinetic barrier between **Con-Agg 1** and **Rac-Agg 4** must be lower compared to the kinetic barrier between **Con-Agg 1** and **Con-Agg 3** (grey arrow, Figure 32). Therefore, the formation of **Rac-Agg 4** is favored over the formation of the hypothetic **Con-Agg 3**.

4.4 Conclusion

Understanding self-assembly pathways leading either towards conglomerates or racemic compounds by homo- and heterochiral aggregation of organic molecules is of major importance not only from an academic but also from an industrial point of view where conglomerate formation is a central requirement for certain sophisticated purification techniques for racemates. Herein, we describe the first in-depth mechanistic study of such homo- and heterochiral aggregation in 1D self-assembly by investigating the supramolecular polymerization of the racemic mixture of **(*R,R*)-** and **(*S,S*)-PBI**. Precise control of the self-assembly pathways by ultrasonication led to the production of three different polymorphs, namely two kinetically formed conglomerates **Con-Agg 1** and **Con-Agg 2** and the thermodynamically most stable racemic supramolecular polymer **Rac-Agg 4**, in the same solvent mixture at the same concentration. While the conglomerates **Con-Agg 1** and **Con-Agg 2** are 1:1 mixtures of homochiral **(*R,R*)-** and **(*S,S*)-Agg 1** and -**Agg 2**, respectively, that are also accessible from the single enantiomers, a new supramolecular polymerization pathway was launched for the racemic mixture to afford the thermodynamically most stable racemic supramolecular polymer **Rac-Agg 4** with a unique structure of alternating (*R,R*)- and (*S,S*)-homochiral dye pairs.

With our study we provide a first demonstration of kinetic and thermodynamic pathway control towards conglomerate and racemic supramolecular polymers, thereby elucidating an important process of chiral discrimination at its origin. As obvious from our study, the in-depth elaboration of energy landscapes in self-assembly processes as provided in Figure 32 can guide research towards the construction of sophisticated supramolecular materials. Such studies may ultimately also improve our understanding of symmetry breaking events in self-assembly processes that are not only vital for the synthesis and enantiomeric resolution of industry-relevant compounds but also explain the origin of homochirality in nature.

Chapter 5

–

Summary

After the synthesis of the first main chain supramolecular polymers in the 1990s, the research field of supramolecular polymer chemistry witnessed a rapid development in the last 30 years (*Chapter 2.1*) which led to the generation of functional supramolecular architectures with tailored mechanical, electronic or biological material properties. Firstly, researchers dealt with the thermodynamic description of supramolecular polymerization processes and developed a variety of mathematical models to elucidate the polymerization mechanism as well as the thermodynamic parameters (*Chapter 2.2*). Afterwards, the academic interest shifted towards the kinetic control of supramolecular polymerization pathways utilizing metastable species (*Chapter 2.3*). It was demonstrated that the pathway complexity of self-assembly processes can be precisely controlled by experimental parameters such as concentration, temperature or proper choice of solvents which enabled the establishment of the first seed-induced living supramolecular polymerization (*Chapter 2.4*). The beauty of seed-induced supramolecular polymerizations lies in the generation of highly ordered nanostructures with small polydispersity indices analogously to seed-induced crystal growth from a supersaturated solution. Recently, it was shown that similar to conventional crystallization processes, different supramolecular polymorphs can be produced for a given compound either by seeding or by proper choice of experimental parameters (*Chapter 2.5*). In addition to supramolecular polymorph formation of a single compound by self-association, the pool of accessible supramolecular architectures can be further increased by utilizing heterochiral aggregation. In this regard, several research groups studied the assembly of racemic mixtures which can afford − in analogy to racemate crystallization − either supramolecular conglomerates or racemic supramolecular polymers due to homochiral or heterochiral aggregation, respectively (*Chapter 2.6*).

Based on this knowledge, the aim of the present thesis was to investigate the solid-state phenomena of polymorphism and conglomerate *vs*. racemic crystal formation at their origin by

a supramolecular approach. Although the initial stages of nucleation and subsequent elongation of 3D crystallizations are decisive for the generation of a certain polymorph, conglomerate or racemic crystal, those processes are experimentally difficult to access. In contrast, nucleation and elongation can be mechanistically studied for one-dimensional supramolecular polymerization processes since thermodynamic and kinetic models to analyze them are well-established and supramolecular polymerization pathways can be precisely controlled by the choice of experimental parameters. For this purpose, PBI model compounds **(*R*,*R*)-** and **(*S*,*S*)-PBI** were synthesized (Figure 33a) which bear structural moieties that favor different supramolecular nanostructures. While small oligomers are favored by an α-CH_3 group next to each imide nitrogen atom, nanofiber formation is facilitated by the amide-appended side chains.

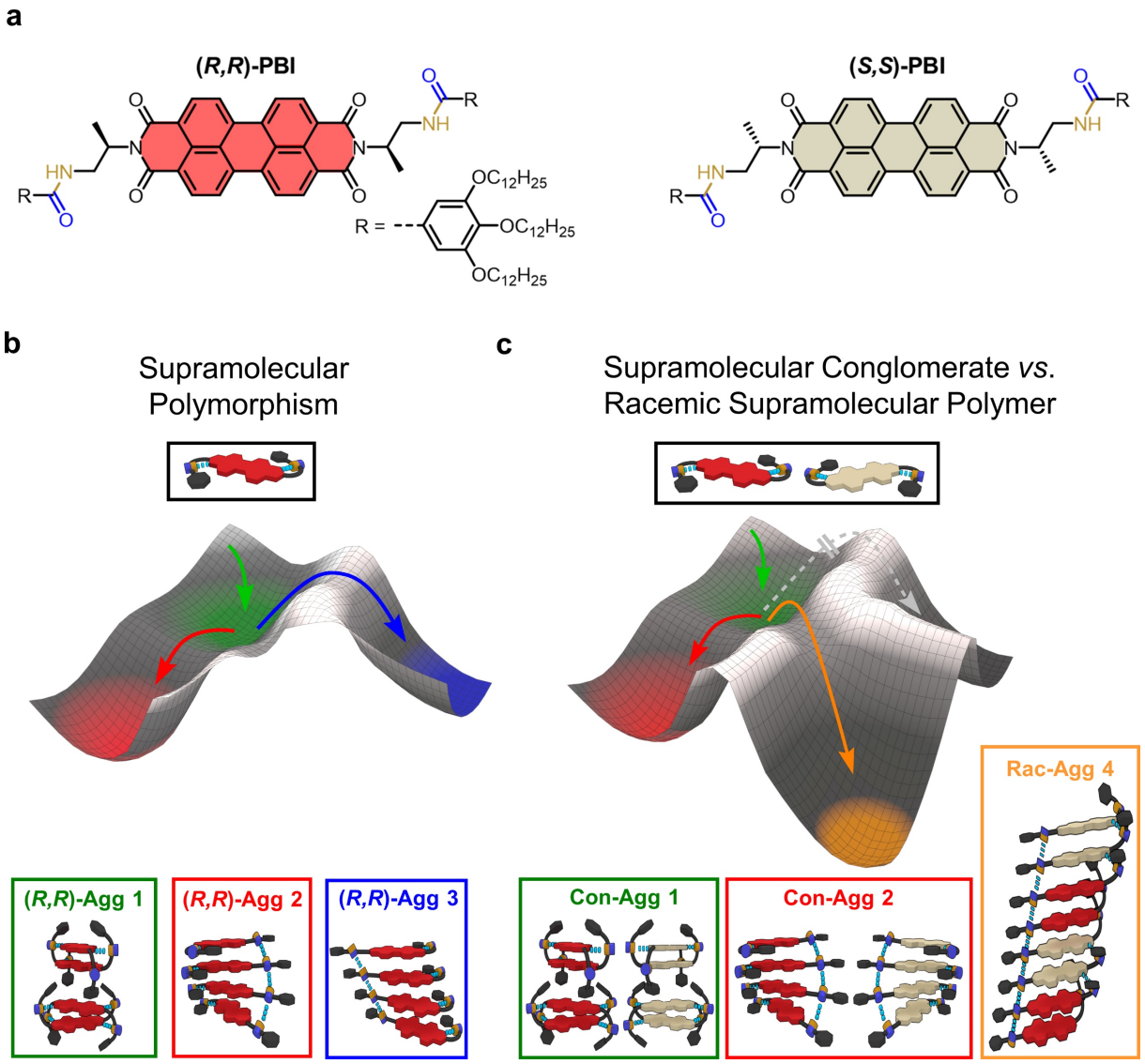

Figure 33. (**a**) Chemical structures of **(*R*,*R*)-** and **(*S*,*S*)-PBI.** Qualitative energy landscape of the supramolecular polymorphism of **(*R*,*R*)-PBI** (**b**) and supramolecular conglomerate *vs*. racemic supramolecular polymer formation in a racemic mixture of **(*R*,*R*)-** and **(*S*,*S*)-PBI** (**c**). The accessible polymerization pathways are indicated in color and schematic illustrations of the corresponding supramolecular polymorphs are depicted below.

As expected, those structural features led to a rather complex supramolecular polymerization behavior which was elucidated in detail for **(*R*,*R*)-PBI** by spectroscopic and microscopic techniques as well as quantum chemical calculations (*Chapter 3*). **(*R*,*R*)-PBI** forms three different polymorphic supramolecular polymers termed as **(*R*,*R*)-Agg 1**−**3** in a solvent mixture of methylcyclohexane and toluene (5:4, v/v). At a concentration of $c_T = 3.0 \times 10^{-4}$ M, monomeric **(*R*,*R*)-PBI** self-assembles into **(*R*,*R*)-Agg 1** which can be transformed into **(*R*,*R*)-Agg 2** or **(*R*,*R*)-Agg 3** upon ultrasonication at 293 – 298 K or 308 K, respectively (Figure 33b). The packing arrangement of the PBI molecules within the different polymorphs was elucidated by a combination of UV/vis, CD, NMR and fluorescence spectroscopy, AFM microscopy and quantum chemical calculations. **(*R*,*R*)-Agg 1** are nanoparticles built from **(*R*,*R*)-Agg 1** dimers which are interlocked by four intermolecular hydrogen bonds between amide protons and imide oxygens of the adjacent PBI molecules and π–π interactions. Between the respective dimers only weak van-der-Waals interactions are formed. **(*R*,*R*)-Agg 2** and **-Agg 3** are nanofibrous π stacks that both show a unique hydrogen-bonding pattern with intramolecular amide-imide hydrogen bonds on one side and intermolecular amide-amide hydrogen bonds on the opposite side. In **(*R*,*R*)-Agg 2** the PBI molecules are arranged in a helical fashion while they have a longitudinally slipped packing arrangement in **(*R*,*R*)-Agg 3** (Figure 33b). Temperature-, time- and concentration-dependent UV/vis studies revealed that **(*R*,*R*)-Agg 3** is the thermodynamically stable state at room temperature and high concentrations, **(*R*,*R*)-Agg 1** is the least stable polymorph and **(*R*,*R*)-Agg 2** is ranked in between. Furthermore, **(*R*,*R*)-Agg 1** serves as the central kinetically trapped state from which **(*R*,*R*)-Agg 2** and **-Agg 3** can be formed in an on-pathway fashion by seeding with the respective seeds. Therefore, the pathway complexity and supramolecular polymorphism are physically controllable by ultrasonication and chemically by seeding. Moreover, nudged elastic band calculations indicated that the nucleation of **(*R*,*R*)-Agg 1** into **(*R*,*R*)-Agg 2** or **-Agg 3** occurs on the dimer level and involves a reorganization of the α-CH_3 groups, the π-stacking mode as well as of the hydrogen bonding pattern rather than disassembly into monomers and successive supramolecular polymerization.

In summary, **(*R*,*R*)-PBI** provided the first molecule for which three different supramolecular polymorphs were produced under the same experimental conditions and structurally characterized. Hence, **(*R*,*R*)-PBI** provides an ideal model system to gain insights into the initial stages of polymorphism in an 1D self-assembly process. It was not only possible to determine the thermodynamic and kinetic features of the supramolecular polymorphism of **(*R*,*R*)-PBI** but also to simulate structural rearrangements on a molecular level that might occur during nucleation in the initial stage of polymorph formation.

The second goal of the present thesis was to acquire better knowledge on conglomerate *vs.* racemic crystal formation at its origin. Since three different supramolecular polymorphs with distinct arrangements of the chromophores were accessible for **(*R*,*R*)-PBI**, this might offer the possibility of investigating conglomerate and racemic supramolecular polymer formation in a racemic mixture of **(*R*,*R*)-** and **(*S*,*S*)-PBI** (*Chapter 4*). As expected for enantiomers, enantiopure **(*S*,*S*)-PBI** forms the same type of supramolecular polymorphs as **(*R*,*R*)-PBI** in MCH/Tol (5:4, v/v) but with opposite helicities as evidenced by UV/Vis and CD spectroscopy as well as AFM. The racemic mixture of **(*R*,*R*)-** and **(*S*,*S*)-PBI** was studied under the same experimental conditions where **(*R*,*R*)-PBI** showed its rich polymorphism (Figure 33c). Upon cooling of a hot solution of the racemic mixture to room temperature, the formation of conglomerate **Con-Agg 1** was observed which is a 1:1 mixture of **(*R*,*R*)-** and **(*S*,*S*)-Agg 1** as evidenced by VT-^{1}H NMR spectroscopy and UV/vis studies. Similar to **(*R*,*R*)-Agg 1**, **Con-Agg 1** serves as the central kinetically trapped state of the racemic mixture, from which other polymorphs can be prepared. Upon ultrasonication at 293 – 298 K, **Con-Agg 1** transforms into **Con-Agg 2**, which is a mixture of equal amounts of **(*R*,*R*)-** and **(*S*,*S*)-Agg 2** as proven by UV/vis spectroscopy. AFM measurements revealed an equal mixture of *P*- and *M*-helical nanofibers corresponding to homochiral **(*R*,*R*)-Agg 2** and **(*S*,*S*)-Agg 2**, respectively. In contrast to enantiopure **(*R*,*R*)-PBI** which transformed into **(*R*,*R*)-Agg 3** upon ultrasonication at 308 K, the PBI molecules within the racemic mixture did not transform into **(*R*,*R*)-** or **(*S*,*S*)-Agg 3** and, hence, no **Con-Agg 3** was observed. However, when performing the same experiment at an increased concentration, **Con-Agg 1** was transformed into the racemic supramolecular polymer **Rac-Agg 4** with an unprecedented packing arrangement of the molecules within the supramolecular polymers due to heterochiral aggregation. A combination of UV/vis and FT-IR spectroscopic studies as well as quantum chemical calculations revealed that **Rac-Agg 4** is a longitudinally displaced π stack consisting of alternating **(*R*,*R*)-** and **(*S*,*S*)-PBI** dimers with a novel hydrogen-bonding pattern. On one side intermolecular amide-amide hydrogen bonds are observed while on the opposite side intermolecular hydrogen bonds between an amide proton and an imide oxygen of the adjacent PBI molecule are found. While the thermodynamic characteristics of **Con-Agg 1** and **Con-Agg 2** are identical to those of **(*R*,*R*)-Agg 1** and **(*R*,*R*)-Agg 2**, respectively, concentration- and temperature-dependent UV/vis studies showed that **Rac-Agg 4** is the thermodynamically stable state of the racemic mixture. **Rac-Agg 4** is more stable and has probably a lower nucleation barrier than hypothetical **Con-Agg 3** which is the reason why **Con-Agg 3** is not observed in the racemic mixtures (Figure 33c). Moreover, kinetic experiments demonstrated that **Rac-Agg 4** is formed from **Con-Agg 1** in an on-pathway fashion, i.e. by rearrangement

processes within homochiral **(*R*,*R*)-** and **(*S*,*S*)-Agg 1** and not by intermediate dissociation into monomers, which is in accordance with the postulated packing arrangement of **Rac-Agg 4**. Furthermore, both supramolecular conglomerates and the racemic supramolecular polymer were prepared at the same concentration in solution and they were sufficiently kinetically stable to be isolated in the solid-state. In summary, this racemic mixture provides the first supramolecular model system for which the kinetic pathway control enabled the isolation of two conglomerates and one racemic supramolecular polymer within the same supramolecular system.

With these supramolecular systems, the solid-state phenomena of polymorphism and conglomerate *vs*. racemic crystal formation have been studied at their origin in the present thesis by reducing the complexity from 3D crystallization to 1D supramolecular polymerization. In order to generate three different supramolecular polymorphs for **(*R*,*R*)-PBI** or two conglomerates and one racemic supramolecular polymer for the racemic mixture of **(*R*,*R*)-** and **(*S*,*S*)-PBI**, it was crucial to precisely control the aggregation pathways. Therefore, it can be assumed that a plethora of tailored functional supramolecular materials might be generated via complex supramolecular polymerization pathways in near future. Moreover, studies on the supramolecular polymerization of racemic mixtures might be vital for a better understanding of symmetry breaking in self-assembly processes. The latter is not only important for the synthesis and enantiomeric resolution of industry-relevant compounds but has also been discussed in the context of the origin of homochirality in nature.

Chapter 6

–

Zusammenfassung

Nach der Synthese der ersten supramolekularen Hauptketten-Polymere in den 1990er Jahren erlebte das Forschungsgebiet der supramolekularen Polymerchemie in den letzten 30 Jahren eine rasche Entwicklung (*Kapitel 2.1*) hin zu funktionellen supramolekularen Architekturen mit maßgeschneiderten mechanischen, elektronischen oder biologischen Materialeigenschaften. Wissenschaftler befassten sich dabei zuerst mit der thermodynamischen Charakterisierung supramolekularer Polymerisationsprozesse und entwickelten eine Vielzahl an mathematischen Modellen, um die zugrunde liegenden Polymerisationsmechanismen sowie die thermodynamischen Parameter zu bestimmen (*Kapitel 2.2*). Anschließend verschob sich das akademische Interesse dahingehend, mittels metastabiler Spezies eine kinetische Kontrolle der supramolekularen Polymerisationspfade zu realisieren (*Kapitel 2.3*). Es konnte gezeigt werden, dass sich letztere durch experimentelle Parameter wie Konzentration, Temperatur oder durch die Wahl eines geeigneten Solvens gezielt steuern lassen. Im Zuge dessen wurde das Konzept der Saat-induzierten lebenden supramolekularen Polymerisation entwickelt (*Kapitel 2.4*), welches das supramolekulare Analogon zu Saat-induziertem Kristallwachstum aus übersättigten Lösungen darstellt und die Generierung hochgeordneter supramolekularer Nanostrukturen mit geringen Polydispersitäten ermöglicht. Kürzlich wurde außerdem gezeigt, dass analog zu konventionellen Kristallisationsprozessen verschiedene supramolekulare Polymorphe der gleichen chemischen Verbindung durch die Wahl geeigneter experimenteller Bedingungen sowie durch Saatzugabe dargestellt werden können (*Kapitel 2.5*). Darüber hinaus kann neben der Polymorph-Bildung durch Selbstassoziation auch eine heterochirale Aggregation ausgenutzt werden, um den Fundus an zugänglichen supramolekularen Architekturen zu vergrößern. Im Zuge dessen untersuchten einige Forschungsgruppen die Assemblierung von racemischen Mischungen, welche analog zu Kristallisationsprozessen

entweder über homochirale Aggregation zu supramolekularen Konglomeraten führt oder über heterochirale Aggregation zu racemischen supramolekularen Polymeren (*Kapitel 2.6*).

Basierend auf diesen Erkenntnissen war das Ziel der vorliegenden Doktorarbeit, die Festkörper-Phänomene Polymorphismus und Konglomerat- *vs.* racemische Kristallbildung mit Hilfe eines supramolekularen Ansatzes an ihrem Ursprung zu untersuchen. Obwohl die Anfangsphase einer dreidimensionalen Kristallisation (Nukleation und darauffolgende Elongation) für die Bildung eines bestimmten Polymorphs, Konglomerates oder racemischen Kristalls ausschlaggebend ist, kann diese nur schwer analysiert werden. Im Gegensatz dazu, können die Nukleation und Elongation in eindimensionalen supramolekularen Polymerisationen eingehend untersucht werden, da thermodynamische und kinetische Modelle zu deren Beschreibung bekannt sind und supramolekulare Polymerisationspfade durch die Wahl der experimentellen Bedingungen präzise steuerbar sind. Hierfür wurden die Perylenbisimid (PBI)-Derivate **(*R,R*)-** und **(*S,S*)-PBI** synthetisiert, welche strukturelle Merkmale aufweisen, die verschiedene supramolekulare Nanostrukturen begünstigen (Abbildung 1a). So fördert eine Methylgruppe in α-Position zu den jeweiligen Imid-Stickstoffatomen die Ausbildung kleiner Oligomere, während die Amidgruppen-enthaltenden Seitenketten die Bildung von Nanofasern bevorzugen.

Erwartungsgemäß führte dies zu einem komplexen supramolekularen Polymerisations-verhalten, welches anhand von **(*R,R*)-PBI** mit Hilfe spektroskopischer und mikroskopischer Methoden sowie quantenchemischen Berechnungen eingehend untersucht werden konnte (*Kapitel 3*). **(*R,R*)-PBI** bildet die drei verschiedenen polymorphen supramolekularen Polymere **(*R,R*)-Agg 1**−**3** in einer Solvensmischung aus Methylcyclohexan und Toluol (5:4, v/v). **(*R,R*)-PBI**-Monomere assemblieren bei einer Konzentration von $c_T = 3.0 \times 10^{-4}$ M zu **(*R,R*)-Agg 1**, welches sich durch Ultraschallbehandlung bei 293 – 298 K in **(*R,R*)-Agg 2** und bei 308 K in **(*R,R*)-Agg 3** umwandelt (Abbildung 1b). Die Packung der PBI-Moleküle innerhalb der verschiedenen Polymorphe wurde mit Hilfe von UV/Vis-, CD-, NMR- und Fluoreszenz-Spektroskopie, Rasterkraftmikroskopie sowie quantenchemischen Berechnungen charakterisiert. Es stellte sich heraus, dass es sich bei **(*R,R*)-Agg 1** um Nanopartikel handelt, welche aus **(*R,R*)-Agg 1**-Dimeren aufgebaut sind, die durch vier intermolekulare Wasserstoffbrückenbindungen zwischen den Amidprotonen und Imidsauerstoffatomen des benachbarten PBI-Moleküls und durch π–π-Wechselwirkungen miteinander verbunden sind. Zwischen den einzelnen Dimeren werden ausschließlich schwache van-der-Waals-Wechselwirkungen ausgebildet. **(*R,R*)-Agg 2** und **-Agg 3** sind π-Stapel mit einer Nanofasermorphologie, welche einzigartige, asymmetrische Wasserstoffbrückenbindungs-muster aufweisen.

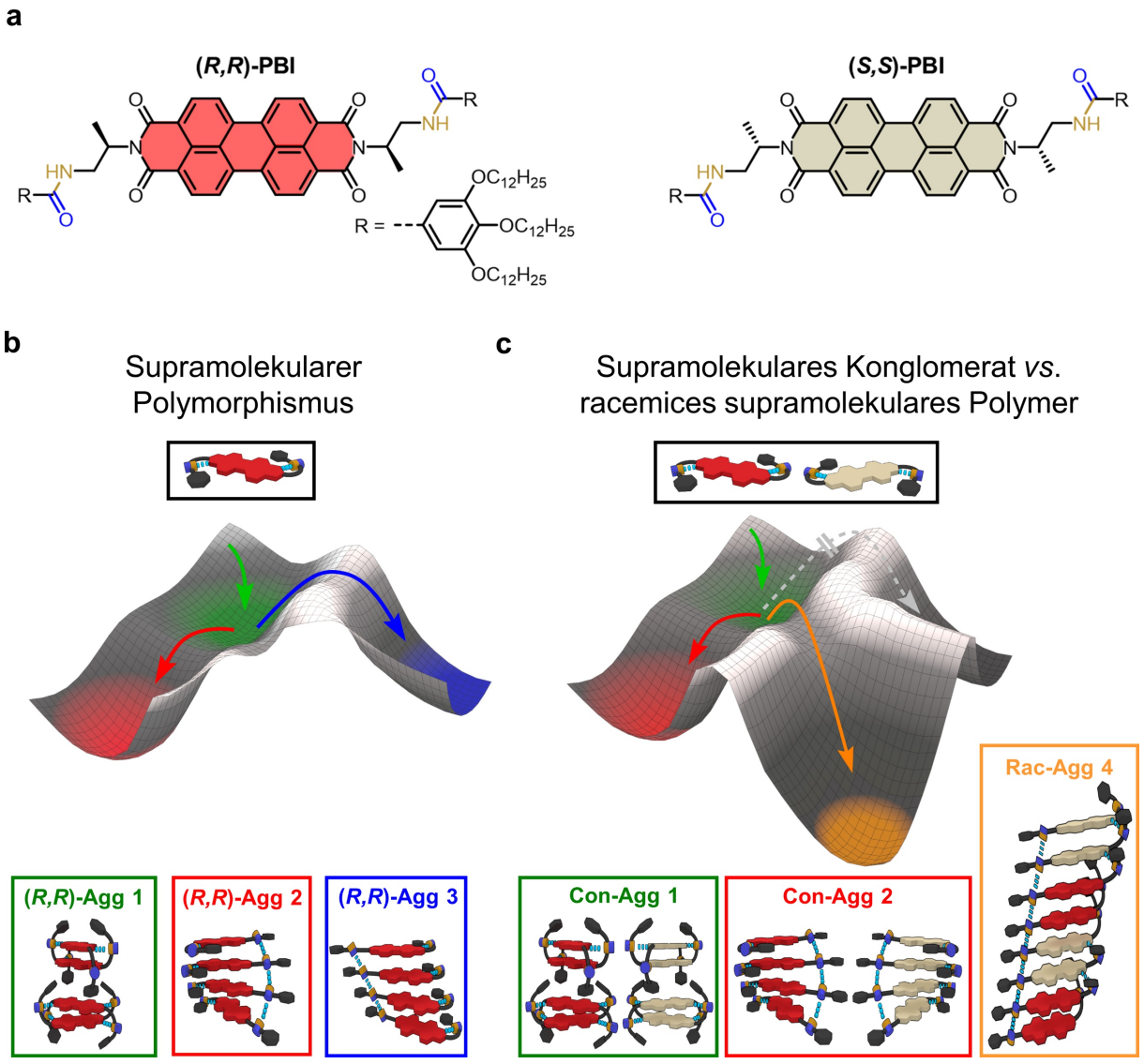

Abbildung 1. (**a**) Chemische Strukturen von **(*R*,*R*)-** und **(*S*,*S*)-PBI**. Qualitative Potenzialhyperfläche des supramolekularen Polymorphismus von **(*R*,*R*)-PBI** (**b**) und der supramolekularen Konglomerat- *vs.* racemischen supramolekularen Polymerbildung in einer racemischen Mischung aus **(*R*,*R*)-** und **(*S*,*S*)-PBI** (**c**). Die zugänglichen Polymerisationspfade sind in Farbe gekennzeichnet und die entsprechenden supramolekularen Polymorphe sind unterhalb der Potentialhyperfläche schematisch illustriert.

In beiden Aggregaten werden auf einer Seite intramolekulare Wasserstoffbrückenbindungen zwischen Amidprotonen und Imidsauerstoffatomen ausgebildet, wohingegen auf der gegenüberliegenden Seite intermolekulare Amid-Amid-Wasserstoffbrückenbindungen beobachtet werden. In **(*R*,*R*)-Agg 2** sind die PBI-Chromophore helikal aufgewunden während sie in **(*R*,*R*)-Agg 3** longitudinal versetzt angeordnet sind (Figure 33b). Weiterhin zeigten temperatur-, zeit- und konzentrationsabhängige UV/Vis-Experimente, dass bei Raumtemperatur und bei hoher Konzentration **(*R*,*R*)-Agg 3** der thermodynamisch stabile Zustand ist, gefolgt von **(*R*,*R*)-Agg 2** und **(*R*,*R*)-Agg 1**, welches das Polymorph mit der

geringsten thermodynamischen Stabilität ist. **(*R,R*)-Agg 1** stellt den zentralen, kinetisch gefangenen Zustand dar, aus welchem **(*R,R*)-Agg 2** oder **(*R,R*)-Agg 3** mit Hilfe der entsprechenden Saat in einem sogenannten „on-pathway"-Mechanismus erzeugt werden können. Somit werden die Polymerisationspfade und der supramolekulare Polymorphismus nicht nur physikalisch durch Ultraschallbehandlung, sondern auch chemisch durch Saatzugabe kontrollierbar. Darüber hinaus belegten „nudged elastic band"-Rechnungen, dass die Umwandlung von **(*R,R*)-Agg 1** in **(*R,R*)-Agg 2** oder **-Agg 3** auf dem Dimerlevel über eine Reorganisation der α-CH_3-Gruppen, der π-Flächen und der Wasserstoffbrückenbindungen verläuft und keine zwischenzeitliche Disassemblierung in Monomere beinhaltet.

Zusammenfassend kann gesagt werden, dass **(*R,R*)-PBI** das erste Molekül darstellt, für welches drei verschiedene supramolekulare Polymorphe unter den gleichen experimentellen Bedingungen generiert und strukturell charakterisiert werden konnten. Daher ist es ein ideales Modellsystem, um Einblicke in das Anfangsstadium von Polymorphismus in einem eindimensionalen Selbstassemblierungsprozess zu erhalten. Es konnten nicht nur die kinetischen und thermodynamischen Eigenschaften des Polymorphismus von **(*R,R*)-PBI** bestimmt werden, sondern auch Umorganisationsprozesse auf molekularem Level simuliert werden, wie sie während der Nukleation in der Anfangsphase der Polymorphbildung auftreten können.

Das zweite Ziel dieser Arbeit war es, tiefere Einblicke in die Anfangsphase der Konglomerat- bzw. racemischen Kristallbildung zu gewinnen. Da **(*R,R*)-PBI** drei verschiedene supramolekulare Polymorphe mit unterschiedlichen Anordnungen der Chromophore bildet, könnte sich die Möglichkeit zur Untersuchung von supramolekularer Konglomerat- vs. racemischer supramolekularer Polymerbildung in der racemischen Mischung aus **(*R,R*)-** und **(*S,S*)-PBI** ergeben (*Kapitel 4*). Wie für Enantiomere erwartet, bildete **(*S,S*)-PBI** in MCH/Tol (5:4, v/v) die gleichen supramolekularen Polymorphe wie **(*R,R*)-PBI**, allerdings mit spiegelbildlicher Helizität, was mittels UV/Vis- und CD-Spektroskopie sowie Rasterkraftmikroskopie belegt werden konnte. Die racemische Mischung aus **(*R,R*)-** und **(*S,S*)-PBI** wurde anschließend unter den gleichen experimentellen Bedingungen wie der supramolekulare Polymorphismus von **(*R,R*)-PBI** untersucht (Abbildung 1c). Nach Abkühlen einer heißen Racematlösung auf Raumtemperatur, wurde mittels temperaturabhängiger ^{1}H-NMR-Spektroskopie und UV/Vis-Spektroskopie die Bildung des Konglomerats **Con-Agg 1** nachgewiesen, welches eine 1:1-Mischung aus **(*R,R*)-** und **(*S,S*)-Agg 1** ist. **Con-Agg 1** stellt ähnlich wie **(*R,R*)-Agg 1** den zentralen, kinetisch gefangenen Zustand dar, aus welchem die anderen Polymorphe hergestellt werden können. Dabei führt die Ultraschallbehandlung einer

Con-Agg 1-Lösung bei 293 – 298 K zu der Bildung von **Con-Agg 2**, was unter anderem mittels UV/Vis-Experimenten belegt wurde. Rasterkraftmikroskopie-Messungen zeigten eine Mischung gleicher Anteile *P*- und *M*-Helizes, welche **(*R*,*R*)-** bzw. **(*S*,*S*)-Agg 2** zugeordnet werden konnten. Während enantiomerenreines **(*R*,*R*)-PBI** durch Ultraschallbehandlung bei 308 K in **(*R*,*R*)-Agg 3** umgewandelt wurde, konnte innerhalb der racemischen Mischung keine Transformation der PBI-Moleküle zu **(*R*,*R*)-** oder **(*S*,*S*)-Agg 3** und damit auch kein **Con-Agg 3** beobachtet werden. Allerdings führte das gleiche Experiment bei höherer Konzentration zur Umwandlung von **Con-Agg 1** in das racemische supramolekulare Polymer **Rac-Agg 4**, welches aufgrund einer heterochiralen Aggregation eine neuartige Anordnung der Moleküle innerhalb des supramolekularen Polymers aufweist. UV/Vis- und FT-IR-Untersuchungen sowie quantenchemische Rechnungen belegten für **Rac-Agg 4** eine Struktur bestehend aus alternierenden, longitudinal zueinander verschobenen **(*R*,*R*)-** und **(*S*,*S*)-PBI**-Dimeren mit einem neuartigen Wasserstoffbrückenbindungsmuster. Auf einer Seite des π-Stapels werden intermolekulare Wasserstoffbrückenbindungen zwischen den Amidgruppen beobachtet, wohingegen auf der gegenüberliegenden Seite intermolekulare Wasserstoffbrückenbindungen zwischen einem Amidproton und einem Imidsauerstoffatom des benachbarten PBI-Moleküls vorliegen. Während die thermodynamischen Charakteristika von **Con-Agg 1** und **(*R*,*R*)-Agg 1** bzw. **Con-Agg 2** und **(*R*,*R*)-Agg 2** jeweils identisch sind, belegten konzentrations- und temperaturabhängige Studien, dass **Rac-Agg 4** der thermodynamisch stabile Zustand der racemischen Mischung ist. Darüber hinaus ist **Rac-Agg 4** stabiler und weißt höchstwahrscheinlich eine geringere Nukleationsbarriere als das hypothetische **Con-Agg 3** auf, weshalb dieses für racemische Mischungen nicht beobachtet wird (Abbildung 1c). Kinetische Experimente zeigten weiterhin, dass **Rac-Agg 4** aus **Con-Agg 1** nach einem „on-pathway"-Mechanismus gebildet wird, d.h. durch Reorganisationsprozesse innerhalb der homochiralen **(*R*,*R*)-** bzw. **(*S*,*S*)-Agg 1**-Oligomere und nicht durch intermediäre Dissoziation in Monomere. Dieser „on-pathway"-Mechanismus steht im Einklang mit der postulierten Aggregatstruktur von **Rac-Agg 4**. Außerdem wurden beide supramolekularen Konglomerate und das racemische supramolekulare Polymer bei der gleichen Konzentration in Lösung hergestellt und diese zeigten eine hohe kinetische Stabilität, sodass eine Isolierung im Festkörper möglich war. Zusammenfassend stellt diese racemische Mischung das erste supramolekulare Modellsystem dar, bei welchem die kinetische Kontrolle der Reaktionspfade die Isolierung zweier Konglomerate und eines racemischen supramolekularen Polymers innerhalb desselben supramolekularen Systems ermöglichte.

Mit diesen supramolekularen Systemen wurden in der vorliegenden Doktorarbeit die Anfangsstadien der Festkörper-Phänomene Polymorphismus und Konglomerat- *vs.* racemische Kristallbildung untersucht, indem die Komplexität von dreidimensionaler Kristallisation auf eindimensionale supramolekulare Polymerisation reduziert wurde. Dabei war eine präzise Kontrolle der Reaktionspfade unerlässlich, um drei verschiedene supramolekulare Polymorphe für **(*R,R*)-PBI** bzw. zwei Konglomerate und ein racemisches supramolekulares Polymer für die racemische Mischung aus **(*R,R*)-** und **(*S,S*)-PBI** zu generieren. Folglich kann angenommen werden, dass zukünftig eine Vielzahl an funktionellen supramolekularen Polymeren über komplexe Polymerisationspfade maßgeschneidert werden können. Weiterhin sind Studien zur supramolekularen Polymerisation racemischer Mischungen bedeutend für ein besseres Verständnis der Symmetriebrechung in Selbstassemblierungsprozessen. Letztere spielt nicht nur eine große Rolle für die Synthese und Enantiomerentrennung von industriellen, chemischen Verbindungen, sondern wird auch im Kontext des Ursprungs der Homochiralität in der Natur diskutiert.

Chapter 7

–

Appendix

7.1 Supporting Information for *Chapter 3*: Supramolecular Polymorphism in One-Dimensional Self-Assembly by Kinetic Pathway Control[77]

In *Chapter 7.1* **(*R*,*R*)-Agg 1−3** are abbreviated as **Agg 1−3** for simplicity. The synthetic details and related characterization data of the herein described compounds have also been reported in reference[253].

Materials and methods

General: All chemicals and solvents were purchased from commercial suppliers and used without further purification. The ^{1}H and ^{13}C NMR spectra were recorded with a Bruker Avance III HD 400 or 600 MHz spectrometer and calibrated against the residual proton signal or natural abundance carbon resonance of the used deuterated solvent from tetramethylsilane (TMS) as the internal standard. The chemical shifts δ are indicated in ppm and the coupling constants J in Hz. The multiplicities are given at center of the respective signal as s (singlet), d (doublet), dd (doublet of doublets), t (triplet), q (quartet) and m (multiplet). The MALDI-TOF mass spectra were measured with a Bruker Daltonics autoflex II LRF by using *trans*-2-[3-(4-*tert*-butylphenyl)-2-methyl-2-propenylidene]malononitrile (DCTB) as a matrix. The high-resolution mass spectra (HRMS) were measured by electrospray ionization (ESI) with a microTOF Focus spectrometer from Bruker Daltonics.

Optical UV/vis-Absorption Spectroscopy: The spectroscopic measurements were conducted under ambient conditions using dry solvents of spectroscopic grade. The UV/vis spectra of the

samples were measured with Jasco V-670 and Jasco V-770 spectrophotometers equipped with a PAC-743R Auto Peltier 6/8-cell changer for temperature control. The temperature-dependent absorption spectra were density corrected for the different temperatures. Solid state UV/vis spectra were recorded with a Jasco V-770 spectrophotometer equipped with an ILN-925 150 mm integrating sphere.

Circular Dichroism (CD) Spectroscopy: CD spectra were measured with a Jasco J-810 spectropolarimeter equipped with a Jasco CDF-426S Peltier temperature controller. All CD spectra were density corrected for different temperatures.

Steady-State Fluorescence Spectroscopy: Fluorescence and excitation spectra were either recorded on a PTI QM4/2003 fluorescence spectrometer equipped with a R928 photomultiplier-detector and a GL302 dye laser or on an Edinburgh Instruments FLS980 fluorescence spectrometer. The fluorescence quantum yield of monomeric **(*R*,*R*)-PBI** was determined by the optical dilution method (OD $\leq$ 0.05) as the average value of 4 different excitation wavelengths with Lumogen Red (BASF) as reference (in $CHCl_3$, Φ_{fl} = 0.96).[302] The fluorescence and excitation spectra for the different aggregates (OD $\leq$ 0.05) were determined using a front-face setup (22.5°) under magic angle.

Fourier Transform Infrared Spectroscopy: The FT-IR spectroscopic analyses were performed on a Jasco FT/IR-4600 spectrometer. For measurements in solution the spectrometer was equipped with a Falcon Mid-IR transmission accessory (temperature control module, liquid recirculator) with a fixed path cuvette with CaF_2 windows and path length of 1 mm (PIKE technologies). Solid state FT-IR spectra were recorded on the same spectrometer using an ATR Pro ONE accessory (Jasco).

Atomic Force Microscopy (AFM): AFM measurements were performed under ambient conditions using a Bruker Multimode 8 SPM system operating in tapping mode in air. Silica cantilevers (OMCL-AC160TS, Olympus) with a resonance frequency of ~ 300 kHz and a spring constant of ~ 40 Nm^{-1} were used. The samples were spin-coated from solution onto highly ordered pyrolytic graphite (HOPG) with 10000 rpm.*

* AFM measurements were performed by V. Stepanenko.

Ultrasonication: Ultrasonication was performed with an ultrasonic processor UP50H (30 kHz, 50 Watt, 100% amplitude) from Hielscher. A portion of 3.1 mL of **Agg 1** solution in a mixture of methylcyclohexane (MCH) and toluene (Tol) in a volume ratio of 5:4 was placed in a vial and heated. The ultrasonic finger was dipped about half-way in the hot solution and the vial was sealed with a cap and parafilm. The temperature, at which ultrasonication was conducted, was controlled by a water bath in which the vial was placed.

Seed Preparation: A vial containing 3.1 mL of the respective aggregate solution in MCH/Tol (5:4, v/v) was placed in a BANDELIN SONOREX RK 102 H sonication bath and sonicated at 20 – 25 °C for 10 min (**Agg 2**) or 5 min (**Agg 3**) to obtain seeds that are comparable in length.

Computational Details:* The optimized dimer structures of the three polymorphs were calculated in the framework of the semi-empirical PM6[273] method along with the D3H4[274-275] correction for an adequate description of hydrogen bonds and dispersion by using the MOPAC2016 program suite[276] and additionally, employing density functional theory (DFT), using the B3LYP[277] functional and the def2-SVP basis set[278] as implemented in the Gaussian 16 quantum chemical software package.[303] In order to decrease the computational demand, we replaced the long alkyl chains by methyl groups.

The automated nudged elastic band (NEB) method[282-283] has been employed for obtaining the rearrangement pathways between the optimized structures of **Agg 1** dimer and **Agg 2** or **Agg 3** dimers, respectively. Linear interpolation cannot be used for the generation of initial pathways for NEB calculations of such complex transitions, since the rearrangement does not proceed via a linear displacement of atoms. Therefore, we have used an advanced interpolation scheme based on root-mean-square deviation (RMSD)-driven molecular dynamics for the generation of initial pathways as implemented in the metaFALCON program package that works as follows:[284] The optimized starting structure is propagated in a molecular dynamics simulation while an artificial bias potential is used to drive the conformational transition. The bias is chosen to be proportional to the difference of the RMSD value with respect to the optimized end structure. The proportionality factor is rescaled dynamically to achieve a nearly linearly decreasing RMSD value along the pathway. Furthermore, an additional quadratic bias potential is employed to constrain the RMSD value between the two PBI planes resulting in a reasonable small distance between the two planes.

* Quantum chemical calculations were performed by M. I. S. Röhr and M. Bühler.

Subsequently, structures can be sampled and further optimized using the NEB method. The optimized NEB pathways give rise to the "minimal (electronic) energy pathway" of the rearrangement of the dimer structures. In order to decrease the computational demand, we replaced the long alkyl chains by methyl groups.

Synthesis and Characterization

(*R*)-*tert*-Butyl (1-(3,4,5-tris(dodecyloxy)benzamido)propan-2-yl)carbamate ((*R*)-18):

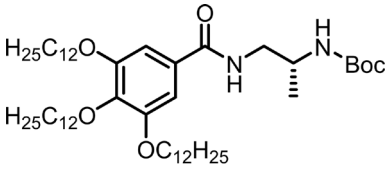

(*R*)-18

A mixture of 3,4,5-tris(dodecyloxy)benzoic acid (1.39 g, 2.06 mmol) (**16**)[254] and thionyl chloride (5 mL) was stirred at 80 °C for 3 h under nitrogen atmosphere. Excess thionyl chloride was removed at 50 °C under reduced pressure and the colorless solid was redissolved in 30 mL dry DCM. Subsequently, the solution was added dropwise to a solution of (*R*)-*tert*-butyl (1-aminopropan-2-yl)carbamate (**(*R*)-17**)[255-256] (300 mg, 1.72 mmol) and NEt_3 (3 mL) in 40 mL dry DCM. After stirring the reaction mixture at room temperature for 30 min the solvent was removed under reduced pressure. The crude product was purified by column chromatography (silica gel; DCM/MeOH 10:1 and 99.75:0.25) and precipitation by addition of MeOH to a solution in DCM to give **(*R*)-18** (1.07 g, 1.25 mmol, 75%) as a colorless solid. Mp. 92 – 93 °C. ^{1}H NMR (400 MHz, $CDCl_3$): δ = 7.41 (br, 1 H), 7.05 (s, 2 H), 4.67 (br, 1 H), 4.02 (t, ^3J = 6.5 Hz, 4 H), 3.98 (t, ^3J = 6.6 Hz, 2 H), 3.94–3.86 (m, 1 H), 3.55–3.48 (m, 1 H), 3.41–3.32 (m, 1 H), 1.84–1.69 (m, 6 H), 1.50–1.42 (m, 6 H), 1.40 (s, 9 H), 1.37–1.20 (m, 51 H), 0.90–0.85 (m, 9 H). ^{13}C NMR (101 MHz, $CDCl_3$): δ = 167.4, 157.2, 153.1, 141.0, 129.2, 105.7, 80.1, 77.4, 73.6, 69.3, 48.5, 46.8, 32.1, 30.5, 29.9, 29.8, 29.7, 29.6, 29.5, 28.5, 26.2, 22.8, 19.0, 14.3. MS (MALDI-TOF, positive mode, DCTB in $CHCl_3$): *m/z* calculated for $C_{51}H_{94}N_2O_6$ $[M]^+$: 830.711, found: 830.625.

(*R*)-*N*-(2-Aminopropyl)-3,4,5-tris(dodecyloxy)benzamide ((*R*)-19)

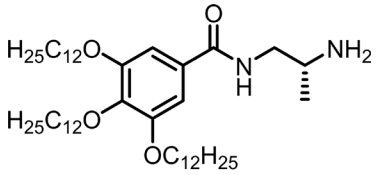

(*R*)-19

To a solution of **(*R*)-18** (600 mg, 720 µmol) in 10 mL $CHCl_3$, trifluoroacetic acid (0.7 mL) was added dropwise. The reaction mixture was stirred at room temperature for 21 h and subsequently heated to reflux for 1 min. After washing with aqueous $NaHCO_3$ (3 × 30 mL), the solvent was evaporated under reduced pressure and the crude product was purified by column chromatography (silica gel; DCM / MeOH 94:6) to give **(*R*)-19** (443 mg, 600 µmol, 84%) as a slightly rose solid. Mp. 58 – 60 °C. ^{1}H NMR (400 MHz, $CDCl_3$): δ = 7.22 (br, 1 H), 7.04 (s, 2 H), 4.09–3.84 (m, 8 H), 3.58–3.47 (m, 1 H), 3.38–3.27 (m, 2 H), 1.79–1.69 (m, 6 H), 1.49–1.18 (m, 57 H), 0.89–0.85 (m, 9 H). ^{13}C NMR (101 MHz, $CDCl_3$): δ = 168.3, 153.1, 141.2, 128.9, 106.0, 73.6, 69.4, 47.8, 45.5, 32.1, 30.5, 29.9, 29.8, 29.6, 29.5, 26.3, 26.2, 22.8, 19.3, 14.3. MS (MALDI-TOF, positive mode, DCTB in $CHCl_3$): *m/z* calculated for $C_{46}H_{87}N_2O_4$ $[M+H]^+$: 731.666 found: 731.623.

(*R,R*)-*N,N*'-Di(3,4,5-tris(dodecyloxy)benzoylamino-1-methylethyl)-perylene-3,4:9,10-tetracarboxylic acid bisimide ((*R,R*)-PBI)

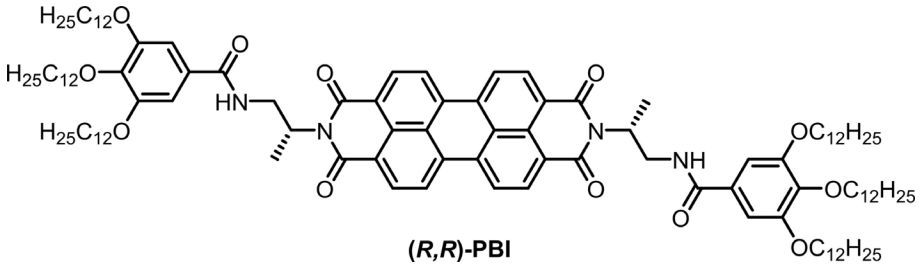

(*R,R*)-PBI

Perylene-3,4:9,10-tetracarboxylic acid bisanhydride (**20**) (66.7 mg, 170 µmol) and benzamide **(*R*)-19** (285 mg, 390 µmol) were mixed in 3 g of imidazole. The reaction mixture was stirred under nitrogen atmosphere at 100 °C for 5 h. After being cooled down to room temperature, the mixture was dissolved in $CHCl_3$ (80 mL) and washed successively with 1N HCl (3 × 80 mL) and aqueous $NaHCO_3$ (1 × 80 mL). After evaporation of the solvent under reduced pressure, the crude product was purified by column chromatography (silica gel; $CHCl_3$) followed by preparative TLC (silica gel; $CHCl_3$/MeOH 99:1) and precipitation by addition of MeOH to a solution in *n*-hexane to give **(*R,R*)-PBI** (190 mg, 104 µmol, 61%) as a red solid. Mp.

182 – 183 °C. ^{1}H NMR (400 MHz, toluene-d_8, 365 K): δ = 8.36 (d, ^{3}J = 8.0 Hz, 4 H), 7.64 (d, ^{3}J = 8.0 Hz, 4 H), 7.34 (s, 4 H), 6.96 (br, 2 H), 5.81 (br, 2 H), 4.59–4.50 (m, 2 H), 4.13 (t, ^{3}J = 6.5 Hz, 4 H), 3.96–3.86 (m, 8 H), 3.85–3.77 (m, 2 H), 1.88–1.80 (m, 4 H), 1.76–1.68 (m, 8 H), 1.67 (d, ^{3}J = 7.1 Hz, 6 H), 1.62–1.09 (m, 108 H), 0.96–0.84 (m, 18 H). ^{13}C NMR (151 MHz, toluene-d_8, 365 K): δ = 167.0, 164.2, 153.8, 142.9, 134.3, 131.1, 130.8, 129.6, 126.4, 124.1, 122.9, 107.9, 73.6, 70.1, 50.3, 43.7, 32.2, 31.0, 30.1, 30.0, 29.8, 29.7, 26.6, 22.9, 20.7, 16.0, 14.0. MS (MALDI-TOF, positive mode, DCTB in $CHCl_3$): *m/z* calculated for $C_{116}H_{177}N_4O_{12}$ $[M+H]^+$: 1818.336, found: 1818.391. HRMS (ESI-TOF, positive mode, MeCN/$CHCl_3$ 1:1): *m/z* calculated for $C_{116}H_{176}N_4NaO_{12}$ $[M+Na]^+$: 1840.31770, found: 1840.31770. UV/vis ($CHCl_3$, nm): λ_{max} (ε_{max} M^{-1} cm^{-1}) = 528 (78000).

Characterization of the (*R*,*R*)-PBI Polymorphs

AFM Studies

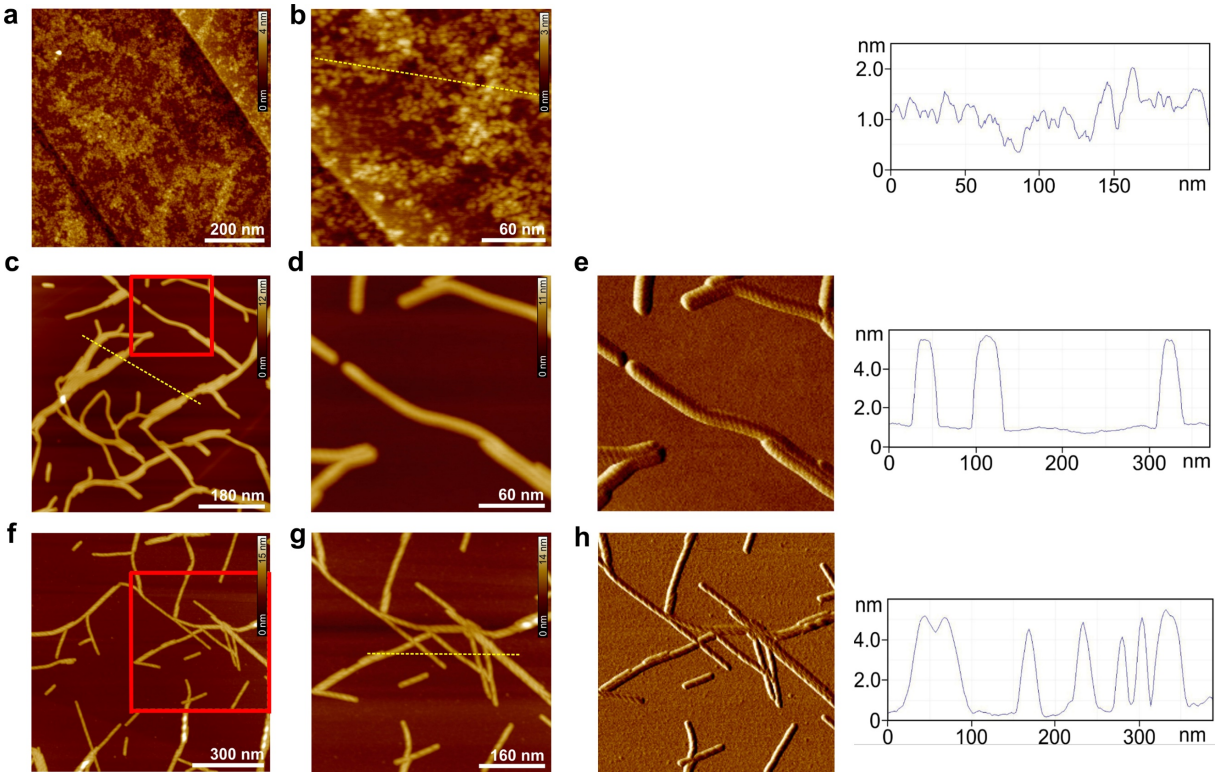

Figure 34. AFM height images of **Agg 1** (**a**, **b**), **Agg 2** (**c**, **d**) and **Agg 3** (**f**, **g**) and phase images of **Agg 2** (**e**) and **Agg 3** (**h**) spin-coated (10000 rpm) on HOPG from MCH/Tol (5:4, v/v).* For **Agg 2** and **Agg 3** the zoomed height images shown in (**d**) and (**g**) are extracted from the regions enclosed with the red box in (**c**) or (**f**), respectively. *Z* scale is 4 nm (**a**), 3 nm (**b**), 12 nm (**c**), 11 nm (**d** and **e**), 15 nm (**f**) or 14 nm (**g** and **h**). The respective cross section analyses along the yellow dashed lines are depicted next to the images of the respective polymorphs.

* AFM measurements were performed by V. Stepanenko.

UV/vis and FT-IR Spectroscopy of **(*R*,*R*)-PBI** in $CHCl_3$

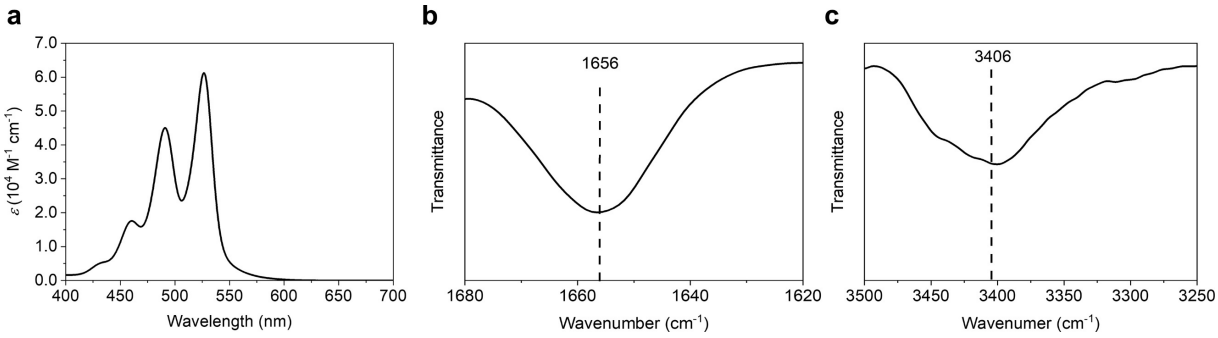

Figure 35. UV/vis-absorption spectrum (**a**) and enlarged C=O (**b**) and N–H (**c**) stretching regions of the FT-IR spectra of ~ 85% monomeric **(*R*,*R*)-PBI** in $CHCl_3$ ($c_T = 4.0 \times 10^{-4}$ M, 323 K).

Asymmetric Hydrogen Bonding Pattern in **Agg 2** and **Agg 3**

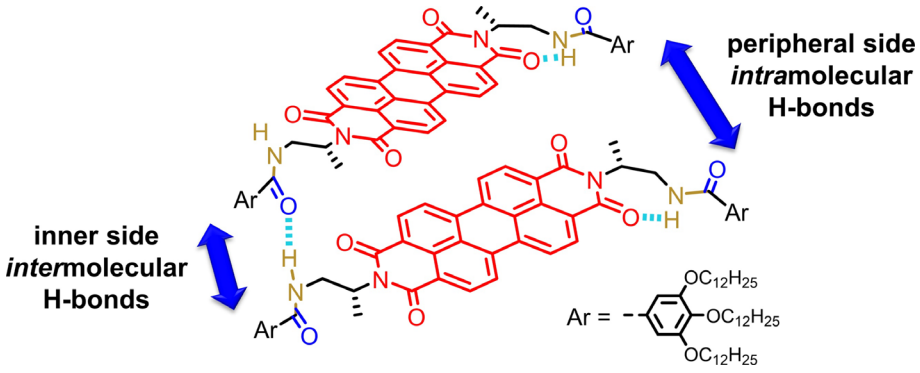

Figure 36. Schematic representation of longitudinally, transversally and rotationally displaced PBI molecules as found within **Agg 2** and **Agg 3**, creating a "inner" side with an intermolecular amide-to-amide hydrogen bond and a "peripheral" side with intramolecular hydrogen bonds between amide protons and imide oxygens. For the exact packing arrangements of the chromophores within **Agg 2** and **Agg 3** see *Chapter 3.1* and *Chapter 3.2*.

Thin Film UV/vis and FT-IR Spectroscopy of the Three Polymorphs of **(*R*,*R*)-PBI**

Agg 1, **Agg 2** and **Agg 3** were prepared in MCH/Tol (5:4, v/v) solution at a concentration of $c_T = 4.0 \times 10^{-4}$ M as described in *Chapter 3.2.2*. For UV/vis measurements (Figure 37a) the solutions of the different aggregates were spin-coated (1 min at 1000 rpm followed by 1 min at 4000 rpm) on quarz plates to give thin films. The UV/vis absorption spectra of the thin film

polymorphs resemble those in solution with absorption maxima in the same range (*Chapter 3.2.2*, Figure 16a). For solid state FT-IR measurements (Figure 37b,c), the solvent of the respective polymorph solution was evaporated by flushing nitrogen over the solution followed by drying *in vacuo* for several days.

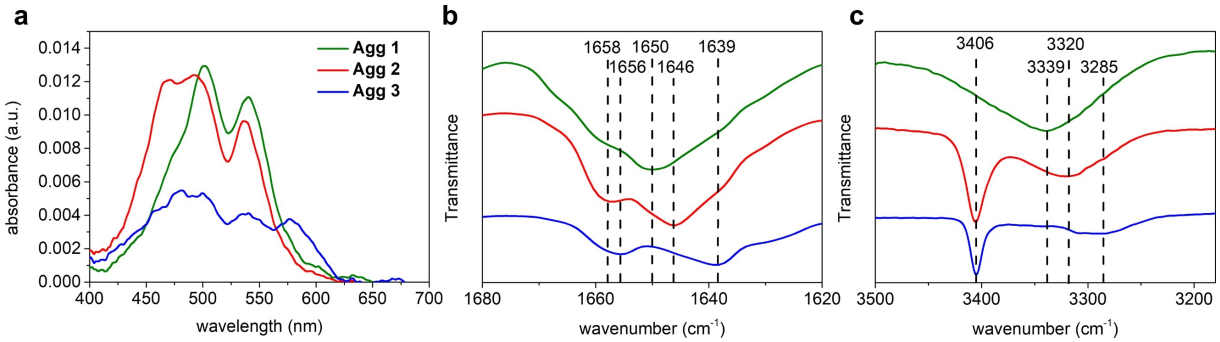

Figure 37. UV/vis-absorption (**a**) and FT-IR spectra of the C=O (**b**) and N–H (**c**) stretching region of the **(*R*,*R*)-PBI** polymorphs in the solid state.

Agg 1 shows a C=O stretching vibration 1650 cm^{-1} and a N–H stretching vibration at 3339 cm^{-1} corresponding to the formation of intermolecular hydrogen bonds between amide protons and imide oxygens of the adjacent chromophore within a **(*R*,*R*)-PBI Agg 1** dimer (*Chapter 3.2.2*, Figure 17).[28] We note that the characteristic peaks for intramolecular hydrogen bonds at around 1656 $cm^{-1}$and 3406 cm^{-1} are missing for **Agg 1** which is in accordance to the FT-IR data obtained in solution (*Chapter 3.2.2*, Figure 17).

Agg 2 and **Agg 3** show a C=O stretching vibration at 1658 cm^{-1} and 1656 cm^{-1}, respectively, and an N–H stretching vibration at 3406 cm^{-1} attributable to intramolecular hydrogen bonds between an amide proton and imide oxygen. Additionally, C=O and N–H stretching frequencies at 1646 cm^{-1} and 3320 cm^{-1} (**Agg 2**) and 1639 cm^{-1} and 3285 cm^{-1} (**Agg 3**), respectively, can be observed, which can be attributed to the formation of intermolecular amide-to-amide hydrogen bonds (*Chapter 3.2.2*, Figure 17 and *Chapter 3.2.3*, Figure 18). As in solution, the intermolecular hydrogen bonds within **Agg 3** are stronger compared to those of **Agg 2**. The intramolecular hydrogen bonds are preserved in **Agg 2** and **Agg 3** in the solid state and their N–H stretching frequencies appear exactly at the same energy (3406 cm^{-1}) as in MCH/Tol (5:4, v/v) solution (*Chapter 3.2.2*, Figure 17b). In sharp contrast, all N–H stretching vibrations corresponding to intermolecular hydrogen bonds are shifted to lower energy in the solid state, indicative for stronger intermolecular hydrogen bonds in the solid state than in solution. From the UV/vis and FT-IR data it can be concluded that in the solid state the same supramolecular

polymorphs as in MCH/Tol (5:4, v/v) solution are formed. This means that the polymorphs show sufficient kinetic stability upon spin-coating or slowly increasing the concentration while evaporating the solvent by nitrogen flushing and, hence, they do not convert into e.g. the thermodynamically most stable state.

Simulated Transformation of Dimeric Agg 1 into Agg 3

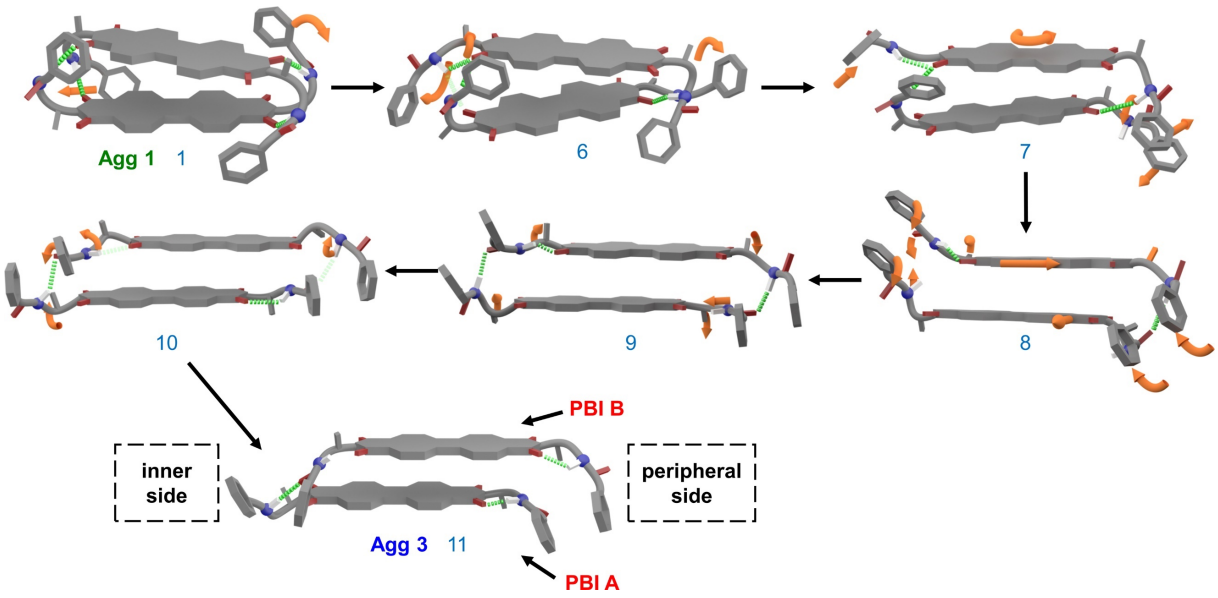

Figure 38. Simulated transformation of dimeric **Agg 1** into **Agg 3**.* The numbered structures correspond to the respective transition states in *Chapter 3.2.3*, Figure 19a. PBI A and PBI B denote the lower and upper PBI molecule within the dimer, respectively, and orange arrows indicate the molecular rearrangement processes. The inner and peripheral side always refer to the left and right side of the dimer, respectively.

During the transformation of **Agg 1 → Agg 3** the intermolecular hydrogen bond between the amide proton of PBI A and the imide oxygen of PBI B breaks on the peripheral side followed by the formation of a transient three-centered (bifurcated) hydrogen bond between the amide protons of PBI A and B and the imide oxygen and PBI B on the inner side (**#6**). The remaining intermolecular hydrogen bond between the amide proton of PBI B and the imide oxygen of PBI A on the peripheral side elongates (**#7**).

* Quantum chemical calculations were performed by M. I. S. Röhr and M. Bühler.

A rotation around the N_{amide}–C=O bond of PBI B on the inner side together with a rotational displacement of the PBI molecules relative to each other leads to a breakage of the intermolecular hydrogen bond between the amide proton of PBI A and the imide oxygen of PBI B on the inner side. On the peripheral side, the intermolecular hydrogen bond between the amide proton of PBI B and the imide oxygen of PBI A breaks in favor of the formation of a transient intermolecular amide-amide hydrogen bond (**#8**). Upon longitudinal displacement of the PBIs molecules relative to each other, an intermolecular amide-to-amide hydrogen bond between PBI A and B and a transient intramolecular $N–H_{amide} \cdots O=C_{imide}$ hydrogen bond of PBI B form on the inner side (**#9**). Next, an intramolecular $N–H_{amide} \cdots O=C_{imide}$ hydrogen bond forms on the peripheral side of PBI A concomitant with an elongation of the transient intermolecular amide-amide hydrogen bond on the same side caused by a rotation around the $N_{imide}–C_{spacer}$ bond of PBI B orienting the α-CH_3 from outwards to inwards. On the inner side of PBI B the intramolecular $N–H_{amide} \cdots O=C_{imide}$ hydrogen bond of PBI B elongates (**#10**). In the last step, rotations around the bonds of the C2-spacer units on both sides of PBI B occur leading to the breakage of the transient intramolecular $N–H_{amide} \cdots O=C_{imide}$ hydrogen bond on its inner side and the formation of an intramolecular $N–H_{amide} \cdots O=C_{imide}$ hydrogen bond on its peripheral side leading to **Agg 3** with both α-CH_3 groups pointing upwards on the inner and downwards on the peripheral side.

Thermodynamic Characterization of the Polymorphism of (*R*,*R*)-PBI

Proof for Dimers as the Main Species in the Anticooperative Aggregation of **Agg 1**

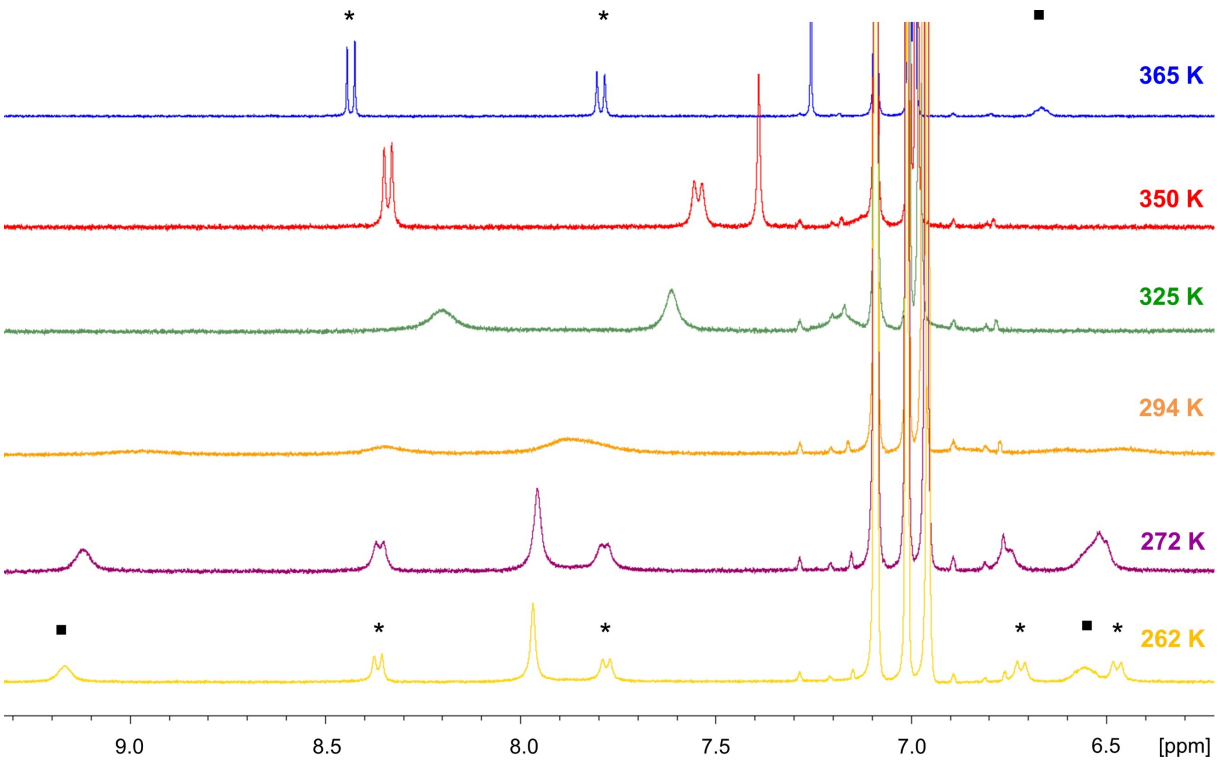

Figure 39. Partial VT-^{1}H NMR spectra of **(*R*,*R*)-PBI** in toluene-d^8 ($c_T = 4.0 \times 10^{-4}$ M). Upon decreasing temperature from 365 K to 262 K monomeric **(*R*,*R*)-PBI** self-assembles into **Agg 1** dimers, leading to a splitting of the perylene (*) and N–H (■) protons at low temperatures.

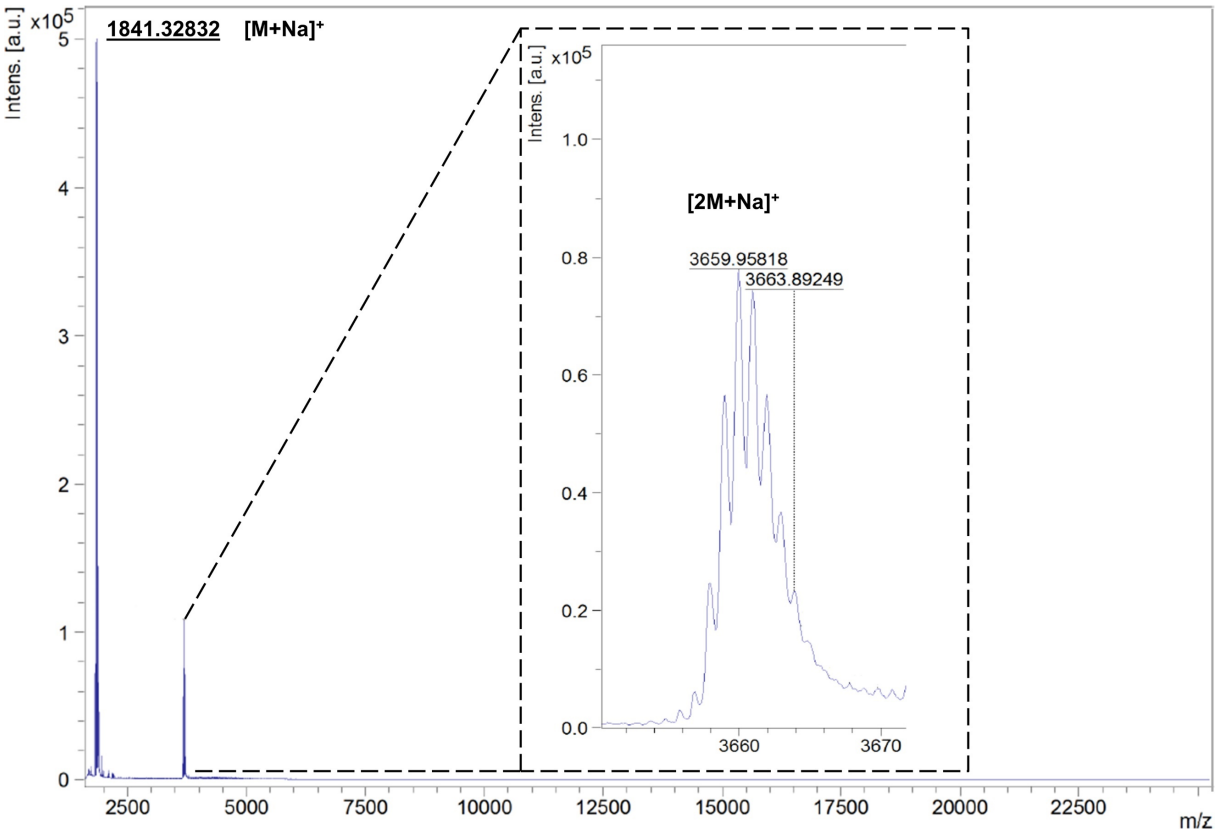

Figure 40. MALDI-TOF spectrum of **(*R*,*R*)-PBI**. Inset: Expanded region showing the molecular peak corresponding to the Na^+ adduct of the dimer.

Disassembly Process of **Agg 2**

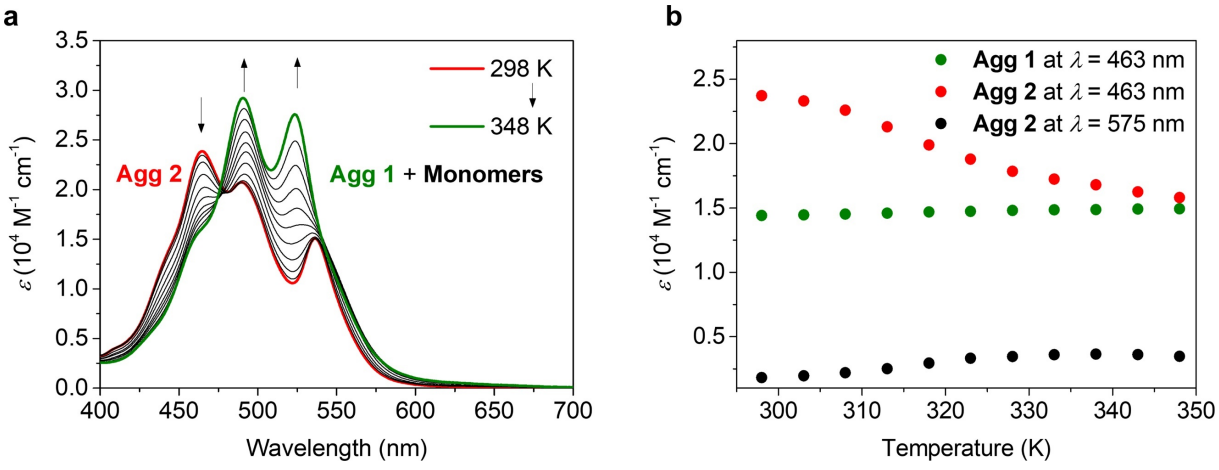

Figure 41. Temperature-dependent UV/vis-absorption spectra of **Agg 2** (**a**) and plot of the extinction coefficients ε at different wavelengths as a function of temperature (**b**) for **Agg 1** and **Agg 2** in MCH/Tol (5:4, v/v) ($c_T = 2.0 \times 10^{-4}$ M, $T = 298$ K → 363 K, heating rate: 5 K min^{-1}).

During the disassembly of **Agg 2** upon heating no pronounced changes at $\lambda = 575$ nm (characteristic J-type absorption band of **Agg 3**) are observed meaning that **Agg 3** is not involved in the disassembly process. Furthermore, at the absorption maximum of **Agg 2** at $\lambda = 463$ nm, **Agg 1** does not show pronounced changes during the heating experiment. Thus, the changes in the absorption spectrum at $\lambda = 463$ nm upon heating are solely caused by the disassembly of **Agg 2**.

Disassembly Process of **Agg 3**

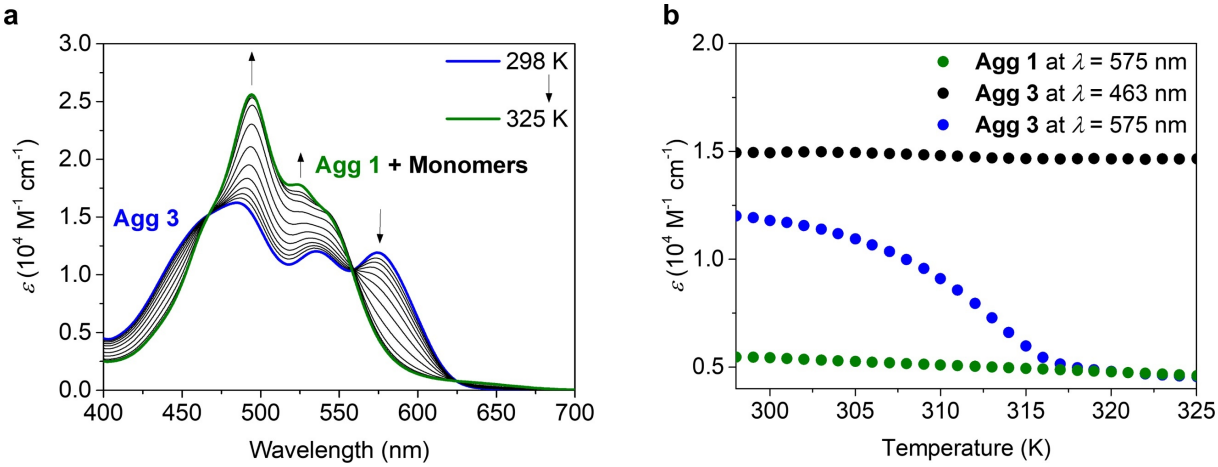

Figure 42. Temperature-dependent UV/vis-absorption spectra of **Agg 3** (**a**) and plot of the molar extinction coefficient ε at different wavelengths as a function of temperature (**b**) for **Agg 1** and **Agg 3** in MCH/Tol (5:4, v/v) ($c_T = 4.0 \times 10^{-4}$ M, $T = 293$ K $\rightarrow$ 325 K, heating rate: 1 K min^{-1}).

During the disassembly of **Agg 3** upon heating no changes at $\lambda = 463$ nm (absorption maximum of **Agg 2**) are observed meaning that **Agg 2** is not involved in the disassembly process. Furthermore, at the J-type absorption band of **Agg 3** at $\lambda = 575$ nm, **Agg 1** does not show pronounced changes during the heating experiment. Thus, the changes in the absorption spectrum at $\lambda = 575$ nm are solely caused by the disassembly of **Agg 3**.

Determination of the Thermodynamic Parameters of **Agg 2** and **Agg 3**

During the disassembly of **Agg 2** and **Agg 3** upon heating the resultant monomers reassemble into **Agg 1** through an anticooperative process with preferential formation of even-sized aggregates due to the higher dimerization constant K_2 of **Agg 1** compared to the association constant K_E for further elongation (*Chapter 3.2.4*, Table 1). Thus, the monomer concentrations

c_{Mono} at the critical temperatures of the disassembly processes of **Agg 2** (*Chapter 3.2.4*, Figure 20e) or **Agg 3** (*Chapter 3.2.4*, Figure 20f) were determined based on an anticooperative model that accounts for the preferential formation of even-numbered aggregates.[28] According to the aforementioned model, the known total concentration of molecules c_T can be expressed by the sum of the concentration of monomers c_{Mono}, molecules in even-numbered and odd-numbered aggregates at a certain temperature (equation (8), *Chapter 2.2*). For the determination of c_{Mono} at the respective critical temperature T_E (c_{Mono} (T_E)), the dimerization constant K_2 and the association constant for further elongation K_E of **Agg 1** at the critical temperatures T_E were put into equation (8).

After numerical determination of c_{Mono} (T_E), a van't Hoff plot (*Chapter 3.2.4*, Figure 20b,c) was prepared according to equation (13)[288-289] from which the standard enthalpy change $\Delta H°$ and the standard entropy change $\Delta S°$ upon aggregation were estimated:

$$\ln K(T_E) = \ln\left[\frac{1}{c_{Mono}(T_E)}\right] = \frac{-\Delta H^0}{RT_E} + \frac{\Delta S^0}{R} \qquad (13)$$

The Gibbs free energy changes ΔG^O at 298 K were determined according to the Gibbs-Helmholtz equation (14):[288-289]

$$\Delta G^O = \Delta H^0 - T\Delta S^0 \qquad (14)$$

Kinetic Characterization of the Polymorphism of (*R*,*R*)-PBI

Ultrasound-induced Transformation of **Agg 1** into **Agg 2**

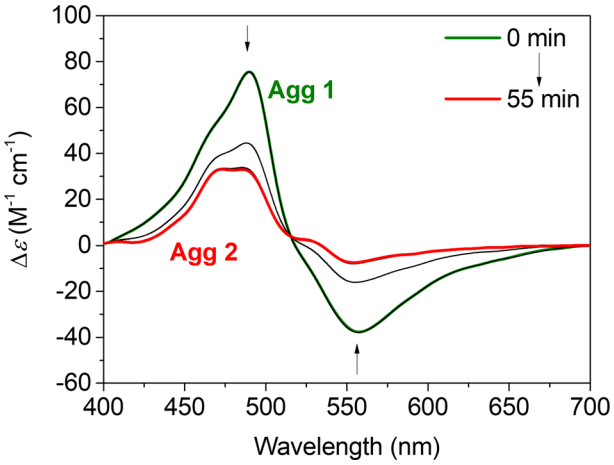

Figure 43. CD spectra for the transformation **Agg 1** → **Agg 2** in MCH/Tol (5:4, v/v) depending on the sonication period (c_T = 3.0 × 10^{-4} M, 298 K).

Ultrasound-induced Transformation of **Agg 1** into **Agg 3**

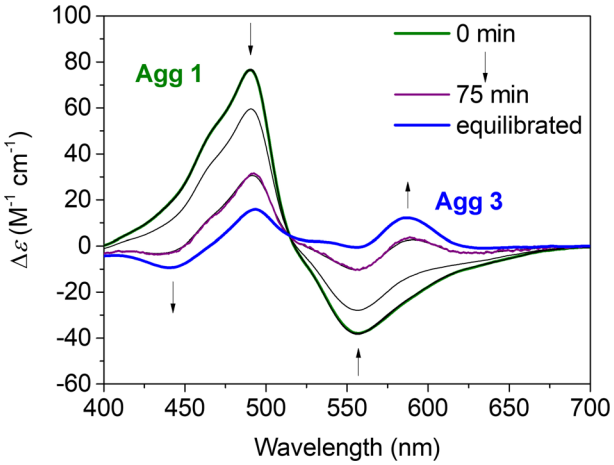

Figure 44. CD spectra for the transformation **Agg 1** → **Agg 3** in MCH/Tol (5:4, v/v) depending on the sonication period (c_T = 5.0 ×10^{-4} M, 308 K). A fully equilibrated solution of **Agg 3** (dark blue line) was obtained after cooling of the solution from 308 K (purple line) to 298 K (blue line) after complete transformation.

NMR Spectra of Synthetic Intermediates and (*R,R*)-PBI

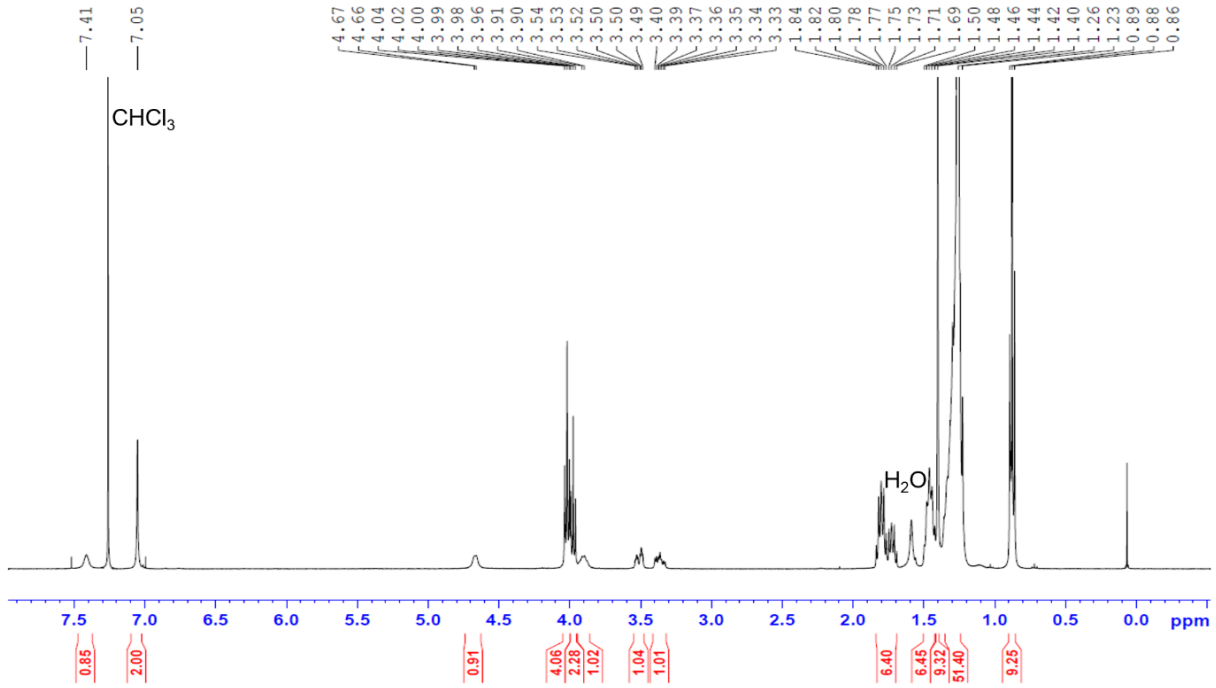

Figure 45. ^{1}H NMR (400 MHz) spectrum of (*R*)-*tert*-butyl (1-(3,4,5-tris(dodecyloxy)benzamido)propan-2-yl)carbamate (**(*R*)-18**) in $CDCl_3$ at 295 K.

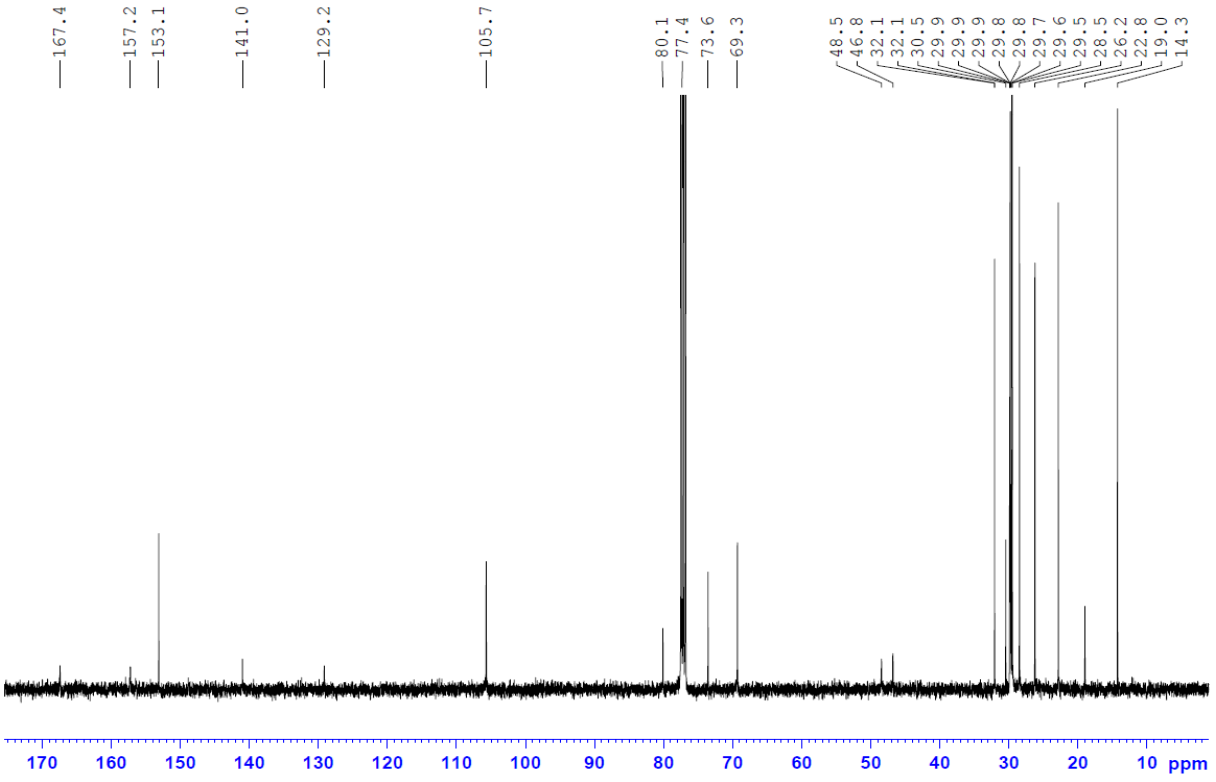

Figure 46. ^{13}C NMR (101 MHz) spectrum of (*R*)-*tert*-butyl (1-(3,4,5-tris(dodecyloxy)benzamido)propan-2-yl)carbamate (**(*R*)-18**) in $CDCl_3$ at 295 K.

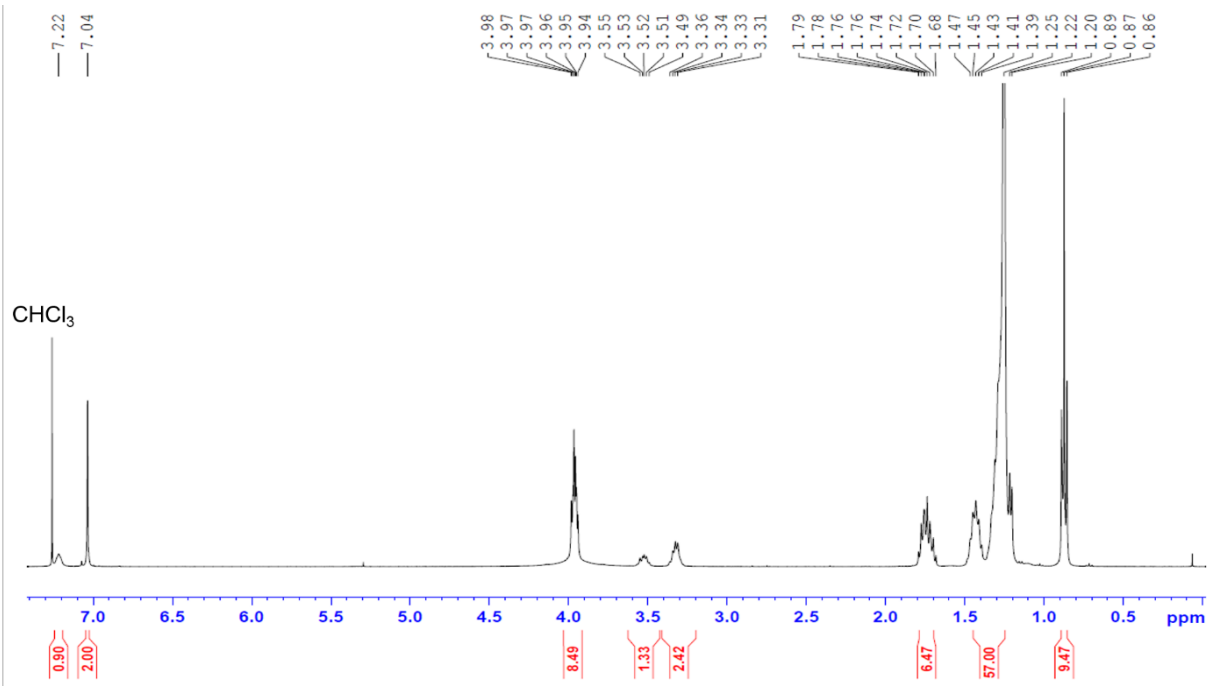

Figure 47. ^{1}H NMR (400 MHz) spectrum of (*R*)-*N*-(2-aminopropyl)-3,4,5-tris(dodecyloxy)benzamide (**(*R*)-19**) in $CDCl_3$ at 295 K.

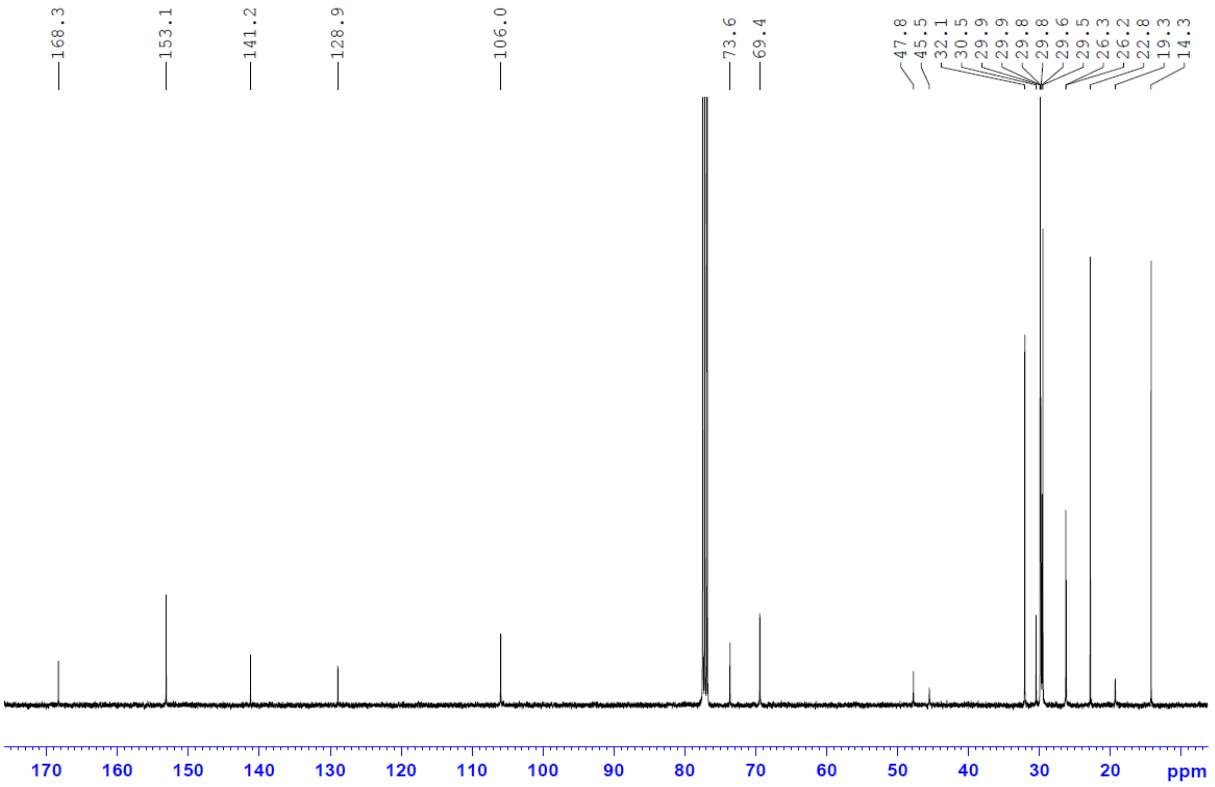

Figure 48. ^{13}C NMR (101 MHz) spectrum of (*R*)-*N*-(2-aminopropyl)-3,4,5-tris(dodecyloxy)benzamide (**(*R*)-19**) in $CDCl_3$ 295 K.

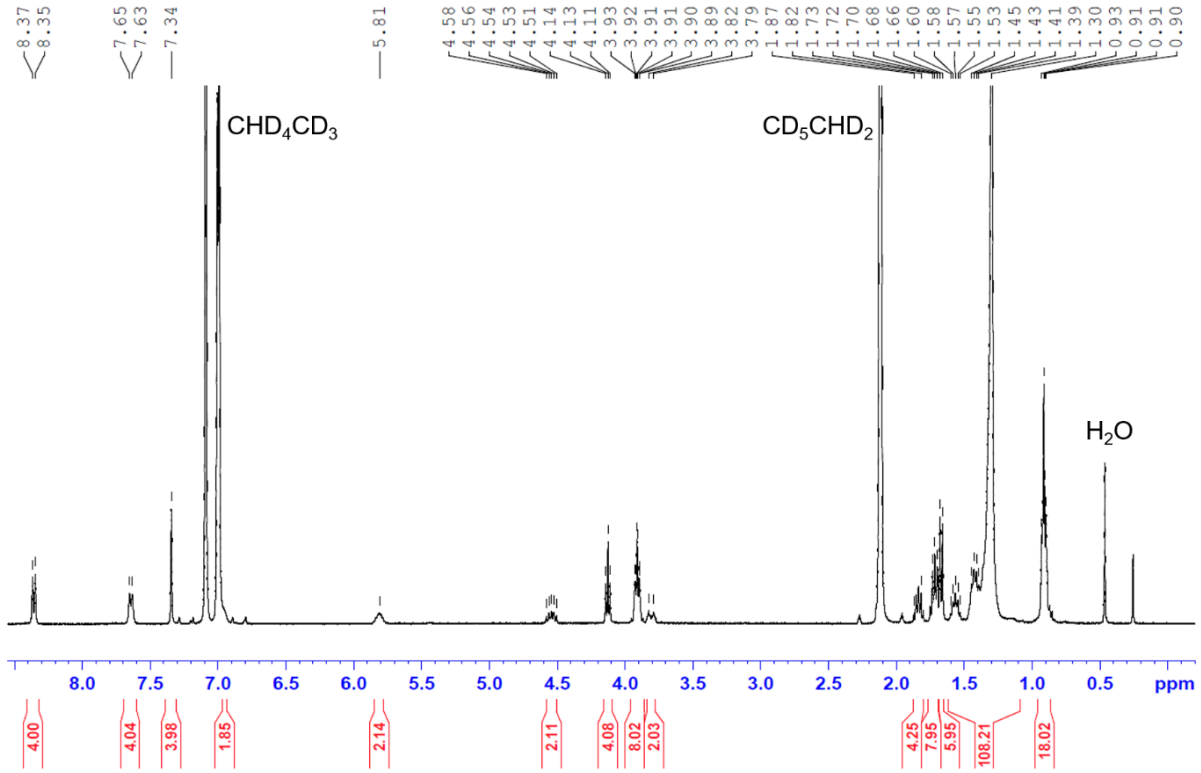

Figure 49. ^{1}H NMR (400 MHz) spectrum of (*R,R*)-*N,N*'-di(3,4,5-tris(dodecyloxy)benzoylamino-1-methylethyl)-perylene-3,4:9,10-tetracarboxylic acid bisimide (**(*R,R*)-PBI**) in toluene-d_8 at 365 K.

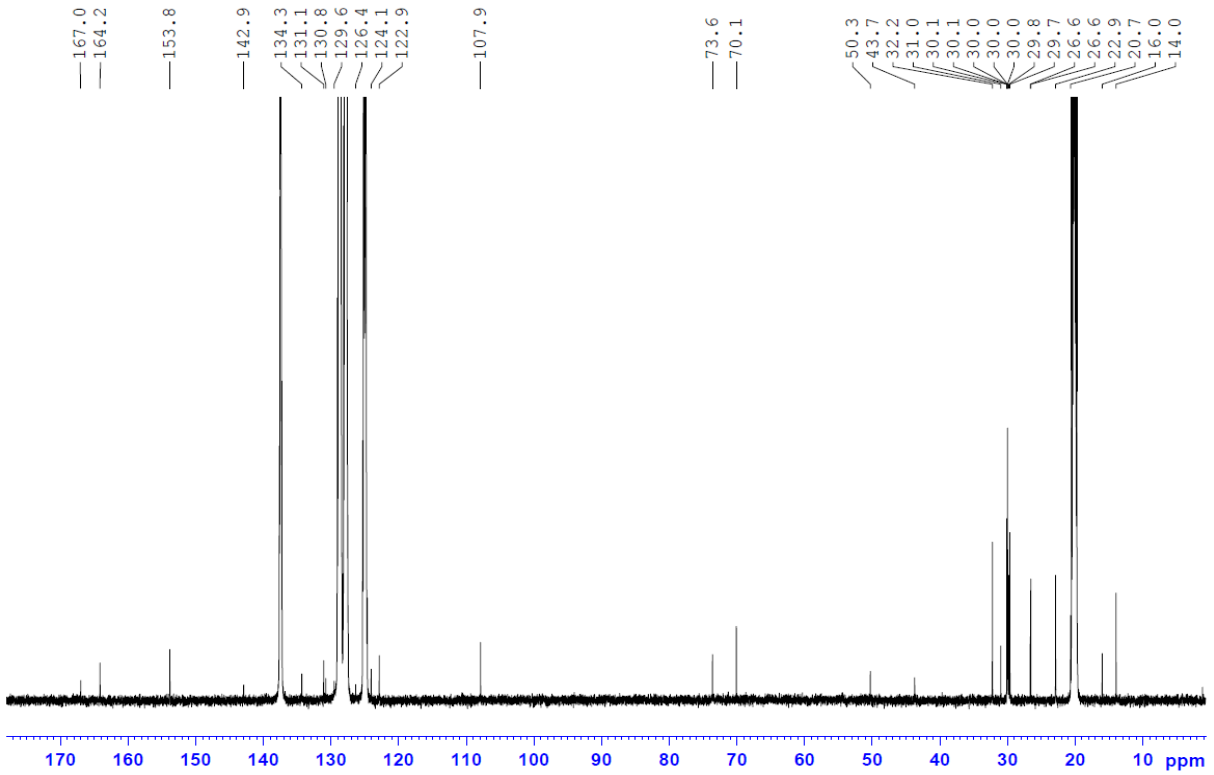

Figure 50. ^{13}C NMR (151 MHz) spectrum of (*R,R*)-*N,N*'-di(3,4,5-tris(dodecyloxy)benzoylamino-1-methylethyl)-perylene-3,4:9,10-tetracarboxylic acid bisimide (**(*R,R*)-PBI**) in toluene-d_8 at 365 K.

7.2 Supporting Information for *Chapter 4*: Control of Self-Assembly Pathways toward Conglomerate and Racemic Supramolecular Polymers

In *Chapter 7.2* the supramolecular polymorphs of **(*R,R*)-** and **(*S,S*)-PBI** are abbreviated as **(*R,R*)-Agg 1−3** and **(*S,S*)-Agg 1−3**, respectively. The synthetic details and related characterization data of the herein described compounds have also been reported in reference[253].

Materials and methods

General: All chemicals and solvents were purchased from commercial suppliers and used without further purification. The ^{1}H and ^{13}C NMR spectra were recorded with a Bruker Avance III HD 400 or 600 MHz spectrometer and calibrated against the residual proton signal or natural abundance carbon resonance of the used deuterated solvent from tetramethylsilane (TMS) as the internal standard. The chemical shifts δ are indicated in ppm and the coupling constants J in Hz. The multiplicities are given at center of the respective signal as s (singlet), d (doublet), dd (doublet of doublets), t (triplet), q (quartet) and m (multiplet). The MALDI-TOF mass spectra were measured with a Bruker Daltonics autoflex II LRF by using *trans*-2-[3-(4-*tert*-butylphenyl)-2-methyl-2-propenylidene]malononitrile (DCTB) as a matrix. The high-resolution mass spectra (HRMS) were measured by electrospray ionization (ESI) with a microTOF Focus spectrometer from Bruker Daltonics.

Optical UV/vis-Absorption Spectroscopy: The spectroscopic measurements were conducted under ambient conditions using dry solvents of spectroscopic grade. The UV/vis spectra of the samples were measured with Jasco V-670 and Jasco V-770 spectrophotometers equipped with a PAC-743R Auto Peltier 6/8-cell changer for temperature control. The temperature-dependent absorption spectra were density corrected for the different temperatures. Solid state UV/vis spectra were recorded with a Jasco J-810 spectropolarimeter.

Circular Dichroism (CD) and linear dichroism (LD) Spectroscopy: CD and LD spectra were measured with a Jasco J-810 spectropolarimeter equipped with a Jasco CDF-426S Peltier temperature controller. All CD and LD spectra were density corrected for different temperatures.

Fourier Transform Infrared (FT-IR) Spectroscopy: The FT-IR spectroscopic analyses were performed on a Jasco FT/IR-4600 spectrometer. For measurements in solution the spectrometer was equipped with a Falcon Mid-IR transmission accessory (temperature control module, liquid recirculator) with a fixed path cuvette with CaF_2 windows and path length of 1 mm (PIKE technologies).

Atomic Force Microscopy (AFM): AFM measurements were performed under ambient conditions using a Bruker Multimode 8 SPM system operating in tapping mode in air. Silica cantilevers (OMCL-AC160TS, Olympus) with a resonance frequency of ~ 300 kHz and a spring constant of ~ 40 Nm^{-1} were used. The samples were spin-coated from solution onto highly ordered pyrolytic graphite (HOPG) with 4000 or 10000 rpm.*

Preparation of the Racemic Mixture (Yielding Con-Agg 1): In order to prepare a racemic mixture of **(*R,R*)-** and **(*S,S*)-PBI** ([**(*R,R*)-PBI**] / [**(*S,S*)-PBI**] = 1:1), stock solutions with the same concentrations were prepared for both compounds individually. Therefore, a weighed amount of a methylcyclohexane (MCH) and toluene (Tol) mixture with a volume ratio of v/v = 5:4 was added to the solid sample of the respective enantiomer in a screw cap vial. After preparation of the stock solution of each enantiomer, equal volumes of **(*R,R*)-** and **(*S,S*)-PBI** solution were added to a new vial with a glass pipette (solution were weighed). After heating to > 363 K and cooling to 298 K, the racemic nature of the solution was double checked by careful CD measurements (and potentially adjusted by addition of tiny amounts of the "minor" enantiomer solution) to ensure that equal amounts of both enantiomers are present in the racemic mixture resulting in no observable CD signal. Prior further experiments, heating and cooling was repeated for the racemic mixture in a sealed vial.

Ultrasonication: Ultrasonication was performed with an ultrasonic processor UP50H (30 kHz, 50 Watt, 100% amplitude) from Hielscher. A portion of 3.1 mL of **Con-Agg 1** solution in a mixture of MCH/Tol in a volume ratio of v/v = 5:4 was placed in a vial and heated. The ultrasonic finger was dipped about half-way in the hot solution and the vial sealed with a cap and parafilm. The temperature, at which ultrasonication was conducted, was controlled by a water bath in which the vial was placed.

* AFM measurements were performed by V. Stepanenko.

Computational Details: The optimized octameric structure of **Rac-Agg 4** was calculated in the framework of the semi-empirical PM6 method[273] along with the D3H4[274-275] correction for an adequate description of hydrogen bonds and dispersion by using the MOPAC2016 program suite.[276] In order to decrease the computational demand, the long alkyl chains were replaced by methyl groups.*

* Quantum chemical calculations were performed by M. I. S. Röhr.

Synthesis and Characterization

(*S*)-*tert*-Butyl (1-(3,4,5-tris(dodecyloxy)benzamido)propan-2-yl)carbamate ((*S*)-18)

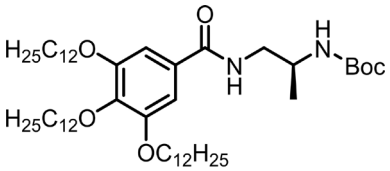

(*S*)-18

Compound **(*S*)-18** was synthesized according to the reported procedure for its enantiomer (for details, see *Chapter 7.1*)[77, 253] using 3,4,5-tris(dodecyloxy)benzoic acid (**16**) (697 mg, 1.03 mmol), thionyl chloride (1.5 mL), **(*S*)-17** (150 mg, 860 µmol), NEt_3 (1 mL) and 25 mL dry dichloromethane (DCM). Rose solid (602 mg, 720 µmol, 84%). Mp. 93 – 94 °C. ^{1}H NMR (400 MHz, $CDCl_3$): δ = 7.41 (br, 1 H), 7.05 (s, 2 H), 4.67 (br, 1 H), 4.02 (t, ^3J = 6.6 Hz, 4 H), 3.98 (t, ^3J = 6.6 Hz, 2 H), 3.95−3.86 (m, 1 H), 3.55−3.47 (m, 1 H), 3.42−3.32 (m, 1 H), 1.84−1.69 (m, 6 H), 1.50−1.42 (m, 6 H), 1.40 (s, 9 H), 1.36−1.21 (m, 51 H), 0.90−0.85 (m, 9 H). ^{13}C NMR (100 MHz, $CDCl_3$): δ = 167.4, 157.2, 153.1, 141.0, 129.1, 105.6, 80.1, 77.3, 73.5, 69.3, 48.4, 46.8, 32.0, 30.4, 29.9, 29.8, 29.7, 29.5, 28.4, 26.2, 22.8, 18.9, 14.2. MS (MALDI, positive mode, DCTB in $CHCl_3$): *m/z* calculated for $C_{51}H_{94}N_2O_6$ $[M]^+$: 830.711, found: 830.700.

(*S*,*S*)-*N*,*N*'-di[3,4,5-tris(dodecyloxy)benzoylamino-1-methylethyl]-perylene-3,4:9,10-tetracarboxylic acid bisimide ((*S*,*S*)-PBI)

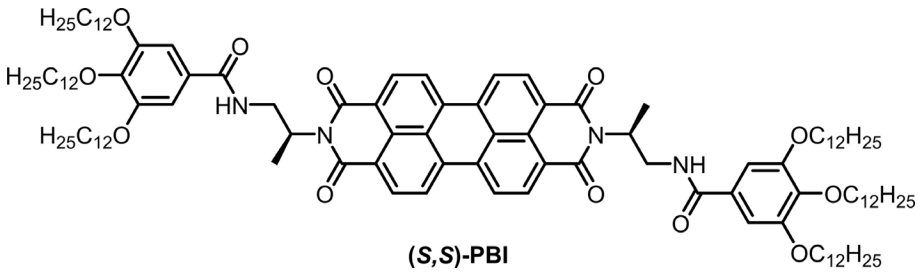

(*S*,*S*)-PBI

(*S*,*S*)-PBI was synthesized in a two-step procedure according to the reported procedure for **(*R*,*R*)-PBI** (for details, see *Chapter 7.1*)[77, 253] from **(*S*)-18** (250 mg, 300 µmol), trifluoroacetic acid (0.1 mL), 5 mL $CHCl_3$, perylene-3,4:9,10-tetracarboxylic acid bisanhydride (**20**) (49.0 mg, 120 µmol) and imidazole (3 g). Red solid (149 mg, 81.9 µmol, 68% over 2 steps). Mp. 183 – 184 °C. ^{1}H NMR (400 MHz, toluene-d_8, 365 K): δ = 8.43 (d, ^3J = 8.0 Hz, 4 H), 7.80 (d, ^3J = 8.0 Hz, 4 H), 7.25 (s, 4 H), 6.66 (br, 2 H), 5.71 (br, 2 H), 4.62−4.49 (m, 2 H), 4.12 (t, ^3J = 6.5 Hz, 4 H), 3.94−3.83 (m, 8 H), 3.74−3.63 (m, 2 H), 1.87−1.80 (m, 4 H), 1.76−1.67 (m, 8 H), 1.65 (d, ^3J = 7.1 Hz, 6 H), 1.61−1.21 (m, 108 H), 0.94−0.87 (m, 18 H). ^{13}C-NMR (150 MHz, toluene-d_8, 365 K): δ = 167.0, 164.2, 153.8, 142.9, 134.3, 131.1, 130.8, 129.6, 126.4, 124.7, 124.1, 122.9, 107.9, 73.6, 70.1, 50.3, 43.7, 32.2, 31.0, 30.1, 30.0, 29.8, 29.7, 26.6, 22.9, 20.7, 16.0, 14.0. MS (MALDI-TOF, positive mode, DCTB in $CHCl_3$): *m/z* calculated for $C_{116}H_{177}N_4O_{12}$ $[M+H]^+$: 1818.336, found: 1818.350. HRMS (ESI-TOF, positive mode, MeCN/$CHCl_3$ 1:1): *m/z* calculated for $C_{116}H_{177}N_4O_{12}$ $[M+H]^+$: 1818.33575, found: 1818.33575.

Characterization of the Polymorphs of (*R,R*)- and (*S,S*)-PBI

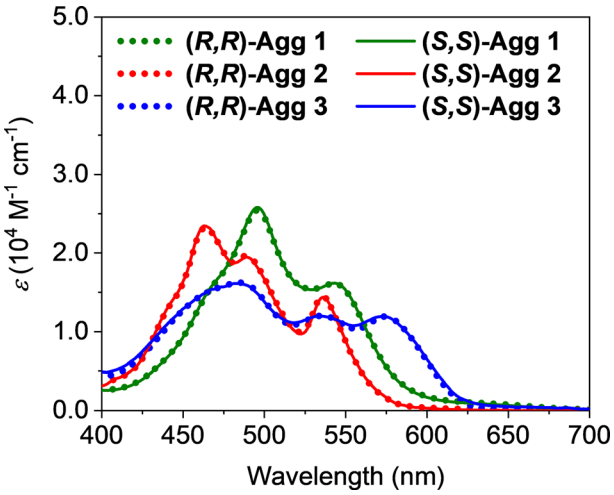

Figure 51. UV/vis-absorption spectra of the three polymorphs of **(*R,R*)-** or **(*S,S*)-PBI** (c_T = 4.0 × 10^{-4} M, 298 K) in MCH/Tol (5:4, v/v) which are denoted as **(*R,R*)-Agg 1–3** or **(*S,S*)-Agg 1–3**, respectively.

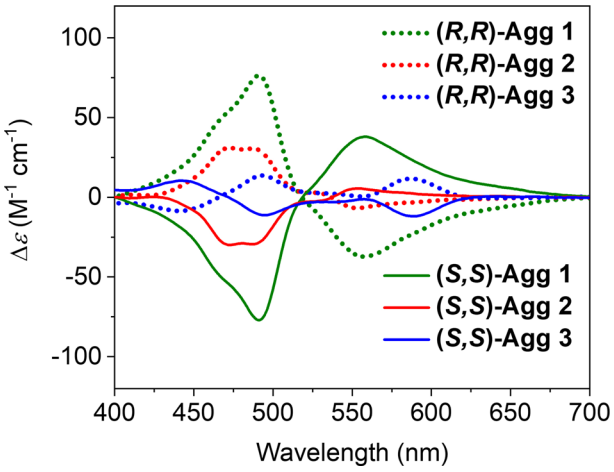

Figure 52. CD spectra of **(*R,R*)-Agg 1−3** and **(*S,S*)-Agg 1−3** (c_T = 4.0 × 10^{-4} M, 298 K) in MCH/Tol (5:4, v/v). The clear bisignate Cotton effects observed for **(*R,R*)-** and **(*S,S*)-Agg 1** correspond to *M*- and *P*-helical oligomers according to the exciton chirality method.[263] Notably, the CD spectra of the respective enantiomeric polymorphs **(*R,R*)-Agg 1−3** and **(*S,S*)-Agg 1−3** show mirror image behavior, i.e. **(*R,R*)-** and **(*S,S*)-PBI** form the same type of supramolecular polymorphs but with opposite helicities.

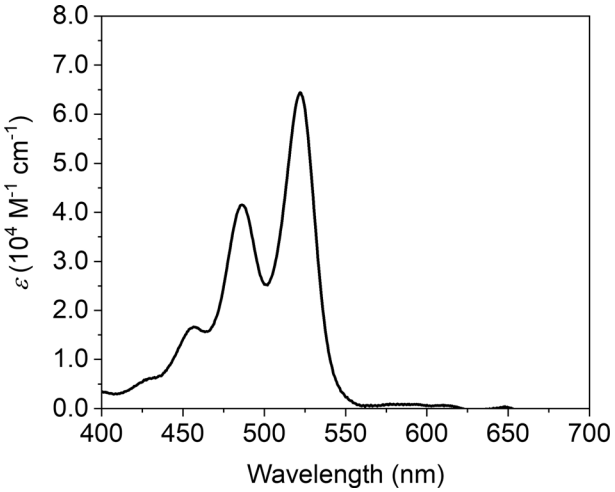

Figure 53. UV/vis-absorption spectrum of monomeric **(*R*,*R*)-PBI** (c_T = 2.0 × 10^{-6} M, 357 K) in MCH/Tol (5:4, v/v).

Characterization of the Supramolecular Conglomerates Con-Agg 1 and Con-Agg 2 and the Racemic Supramolecular Polymer Rac-Agg 4

VT-^{1}H NMR Studies of the Dimerization Process of **Con-Agg 1** and **(*R*,*R*)-Agg 1**

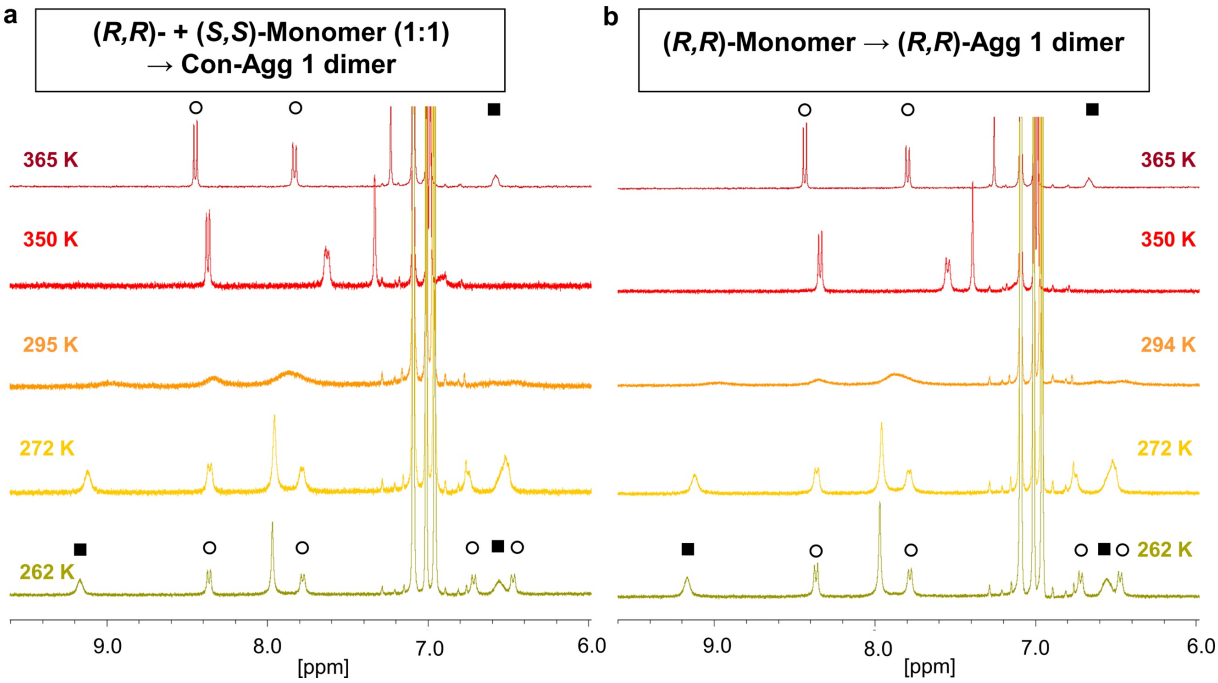

Figure 54. Partial VT-^{1}H NMR spectra of the dimerization process of **Con-Agg 1** (**a**) and **(*R*,*R*)-Agg 1** (compare *Chapter 7.1*, Figure 39)[77] (**b**) in toluene-d^8 ($c_T = 4.0 \times 10^{-4}$ M). Upon decreasing temperature from 365 K to 262 K the racemic mixture of monomeric **(*R*,*R*)-** and **(*S*,*S*)-PBI** self-assembles into **Con-Agg 1** dimers (**a**) while monomeric **(*R*,*R*)-PBI** self-assembles into **(*R*,*R*)-Agg 1** (**b**). Since both dimerization processes show the same VT-^{1}H NMR spectra, it can be concluded that **Con-Agg 1** consists of equal amounts of **(*R*,*R*)-** and **(*S*,*S*)-Agg 1** which show the same ^{1}H NMR spectra as **(*R*,*R*)-Agg 1** at the respective temperatures. Upon dimerization a splitting of the perylene (○) and N–H (■) protons is observed at low temperatures.

Additional AFM Studies of **Con-Agg 2**

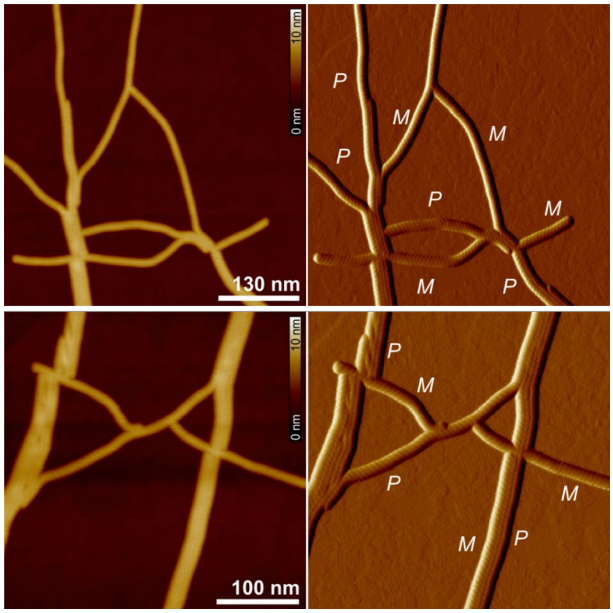

Figure 55. AFM height and phase images of **Con-Agg 2** spin-coated on HOPG from MCH/Tol (5:4, v/v). *Z* scale is 10 nm. The helicities of the nanofibers of **Con-Agg 2** are indicated in the phase images.*

Additional AFM Studies of **Rac-Agg 4**

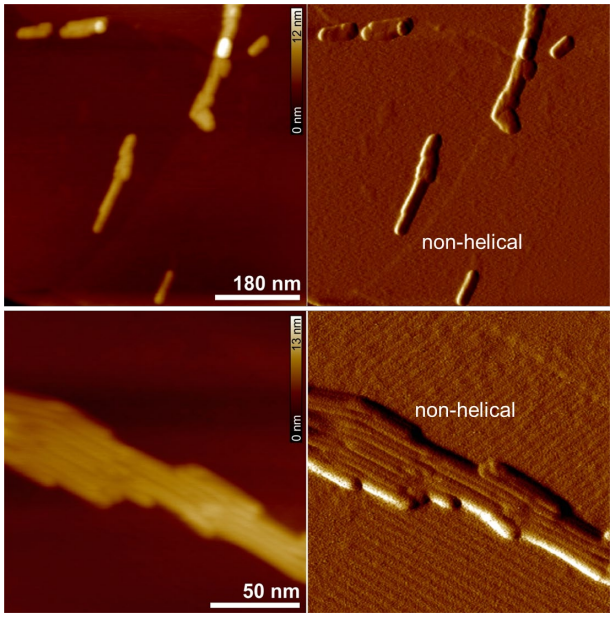

Figure 56. AFM height and phase images of **Rac-Agg 4** spin-coated on HOPG from MCH/Tol (5:4, v/v). *Z* scales are 12 and 13 nm, respectively. For **Rac-Agg 4** only non-helical nanorods were observed that further bundle into sheet-like structures.*

---

* AFM measurements were performed by V. Stepanenko.

Summary of the AFM Data

Table 3. Summary of morphology data for **Con-Agg 1**, **Con-Agg 2** and **Rac-Agg 4** obtained by AFM. Additionally, the respective data for **(*R*,*R*)-** and **(*S*,*S*)-Agg 1–3** is listed for comparison.

	Morphology	**Helical pitch / nm**	**Diameter / nm**	**Length / nm**
Con-Agg 1	Nanoparticles	–	3.8 ± 0.3	–
Con-Agg 2	Nanofibers	5.7 ± 0.2	4.5 ± 0.2	40 − 750
Rac-Agg 4	Nanorods	non-helical	4.1 ± 0.2	40 − 55
(*R*,*R*)-Agg 1	Nanoparticles	–	3.8 ± 0.3	–
(*R*,*R*)-Agg 2	Nanofibers	5.5 ± 0.3	4.7 ± 0.2	50 – 600
(*R*,*R*)-Agg 3	Nanofibers	16 ± 2	4.6 ± 0.2	45 – 450
(*S*,*S*)-Agg 1	Nanoparticles	–	3.8 ± 0.2	–
(*S*,*S*)-Agg 2	Nanofibers	5.4 ± 0.3	4.6 ± 0.2	60 – 800
(*S*,*S*)-Agg 3	Nanofibers	16 ± 2	4.5 ± 0.3	40 – 350

CD and LD Studies of **Rac-Agg 4**

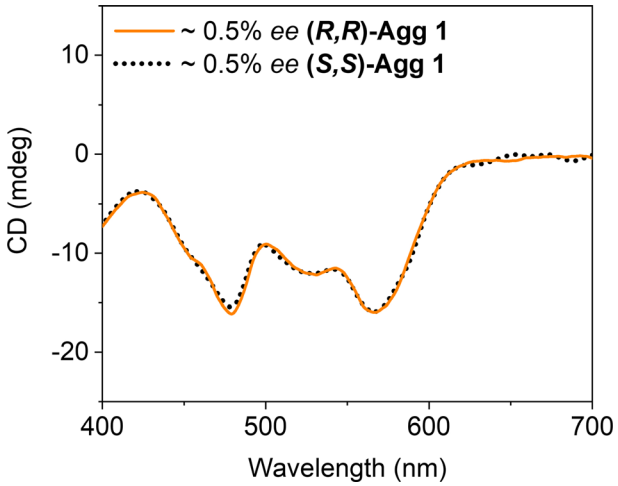

Figure 57. CD spectra of "**Rac-Agg 4**" obtained after transformation of mixtures of **(*R*,*R*)-** and **(*S*,*S*)-Agg 1** with approximate enantiomeric excesses (*ee*) of **(*R*,*R*)-** or **(*S*,*S*)-PBI** of 0.5% in MCH/Tol (5:4, v/v) at 298 K (c_T = 5.0 ×10^{-4} M, ultrasonication at 308 K). The shape and CD signal intensities are independent of small *ee*'s.

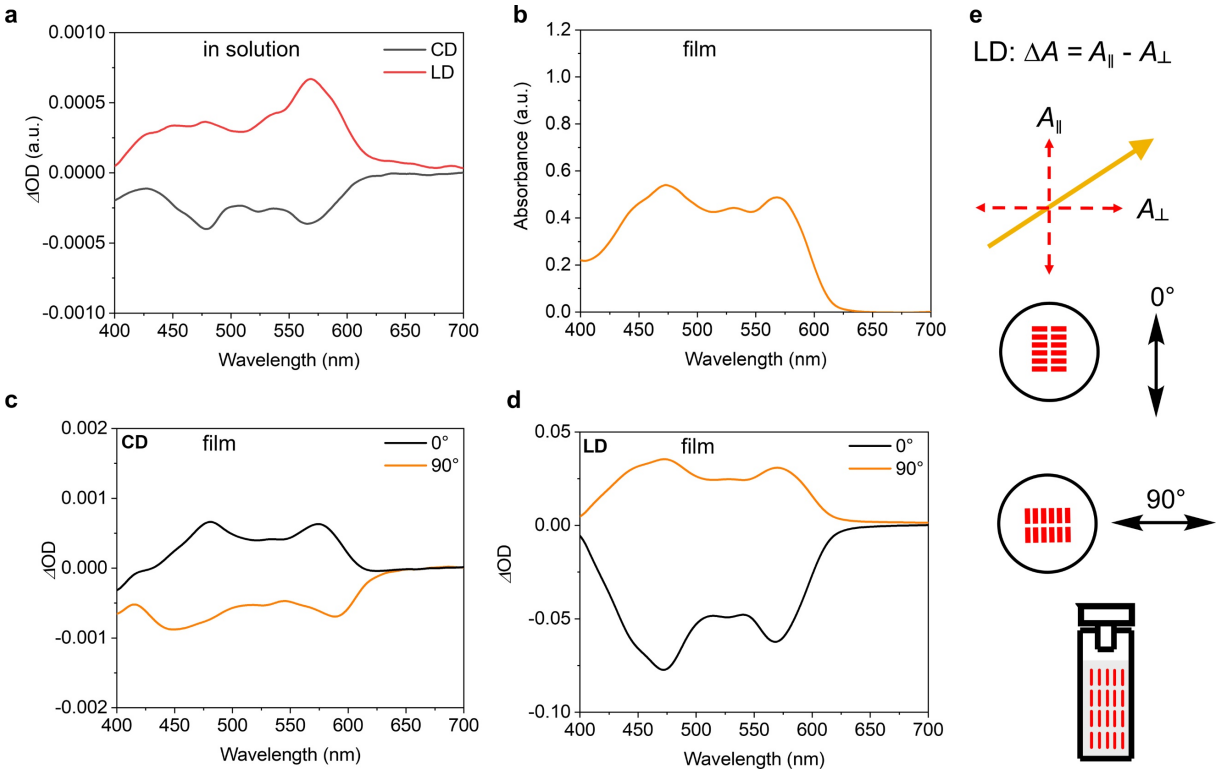

Figure 58. (**a**) CD and LD spectra of **Rac-Agg 4** in MCH/Tol (5:4, v/v) at 298 K ($c_T = 4.0 \times 10^{-4}$ M). (**b**) UV/vis-absorption spectrum of an aligned film (alignment as described in reference[297]) of **Rac-Agg 4**. CD (**c**) and LD (**d**) spectra of the aligned film of **Rac-Agg 4** measured at 0° and 90°. (**e**) Schematic depiction of the LD effect which is defined as the difference in absorption of linearly polarized light parallel ($A_{||}$) and perpendicular ($A_{\perp}$) to an orientation axis.[304] Furthermore, the orientation of the perylene bisimide (PBI) molecules within the aligned film and cuvette is indicated (red bars represent the PBIs' long and short axis).

The apparent CD signal of **Rac-Agg 4** (*Chapter 4.2.2*, Figure 25c and Figure 58a) can be interpreted as a LD artefact (all CD instruments bear inherent optical imperfections leading to a contamination of circularly polarized light with linearly polarized light[297, 299, 305]) which results from the (partial) orientation of the molecules within the cuvette. In solution the observed LD signal is more intense than the CD signal (Figure 58a). In an aligned thin film no structural change of **Rac-Agg 4** upon alignment is observed (compare absorption spectra in solution (*Chapter 4.2.2*, Figure 25b) and Figure 58b). The LD signal of the film is more than 20 times larger than the respective CD signal of the aligned film (Figure 58c,d). The CD and LD results observed in solution can be qualitatively reproduced by measuring the aligned film in a 90° angle with respect to the alignment direction (Figure 58e) which proves that the respective PBI molecules are oriented vertically with respect to their long molecular axis in the cuvette (Figure 58e, the measured $S_0 \rightarrow S_1$ electronic transition is polarized along the long molecular axis of the PBI molecules).[64]

UV/vis Studies of **Con-Agg 1**, **Con-Agg 2** and **Rac-Agg 4** in Solution and Thin Films

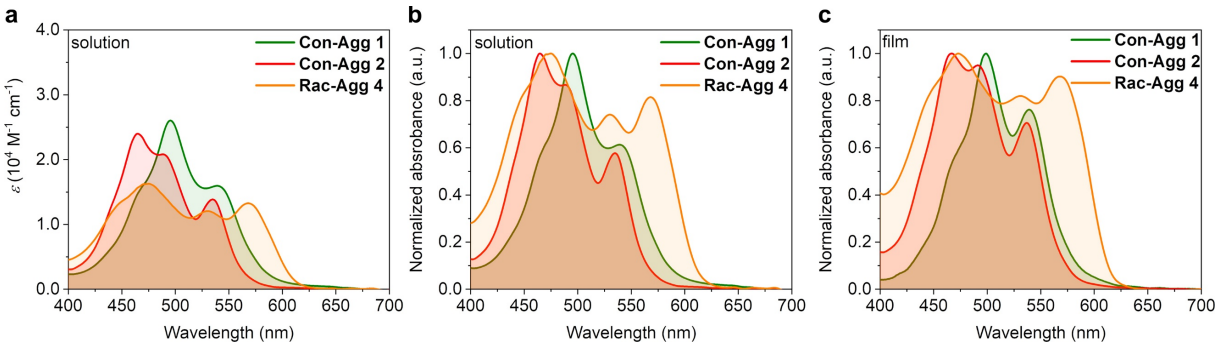

Figure 59. UV/vis-absorption spectra (**a**) and normalized UV/Vis-absorption spectra (**b**) of **Con-Agg 1**, **Con-Agg 2** and **Rac-Agg 4** (c_T = 5.0 × 10^{-4} M) in MCH/Tol (5:4, v/v) at 298 K. (**c**) UV/vis-absorption spectra of thin films prepared by drop casting solutions of **Con-Agg 1**, **Con-Agg 2** or **Rac-Agg 4** on quarz plates. Notably, the thin-film absorption spectra resemble those obtained in solution.

Quantum Chemical Calculations for Rac-Agg 4

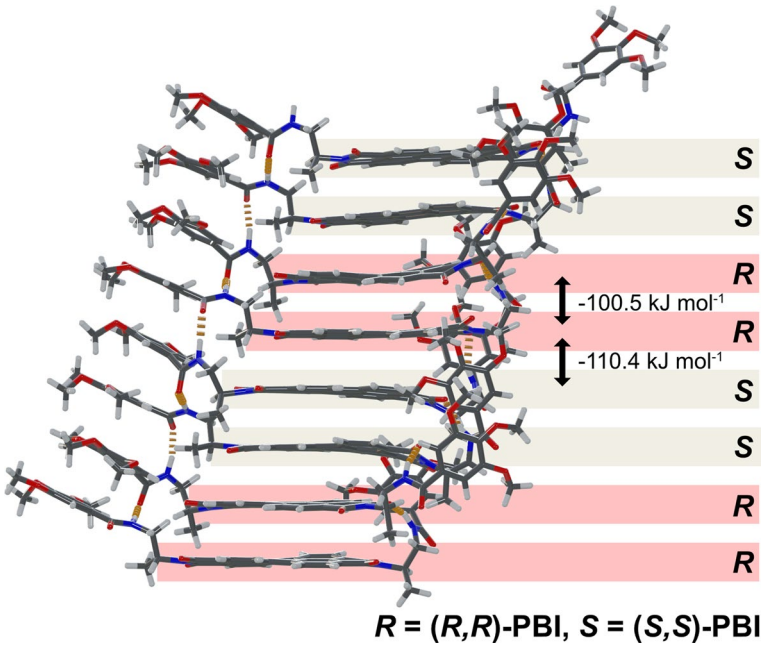

Figure 60. Geometry-optimized octamer structure of **Rac-Agg 4** using PM6-D3H4[273-275] correction as implemented in the MOPAC software package.[276]* *R* and *S* denote **(*R*,*R*)-** and **(*S*,*S*)-PBI**, respectively. The lower *RRSS*-tetramer stack is shown in *Chapter 4.2.3*. The calculated average gas-phase stabilization energies between the homochiral *RR* and heterochiral *RS* contacts are shown.

* Quantum chemical calculations were performed by M. I. S. Röhr.

Kinetic Analysis

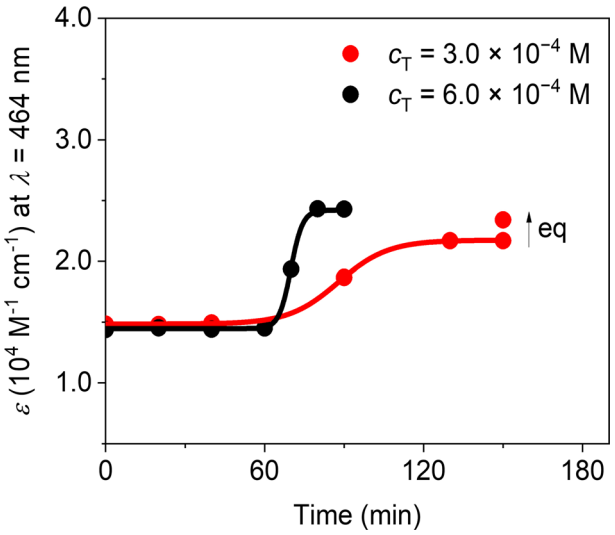

Figure 61. Plot of the time-dependent ε values at $\lambda = 464$ nm derived from the respective absorption spectra at different concentrations for the ultrasound-induced transformation of **Con-Agg 1** → **Con-Agg 2**. Lines are set to guide the eye.

Thermodynamic Analysis

Elucidation of the Thermodynamic Parameters of **Rac-Agg 4**

The analysis of the thermodynamic parameters was conducted as described in *Chapter 7.1*.[77] For the analysis of the thermodynamic parameters the following considerations were made:

1) **Con-Agg 1** is a racemic mixture consisting of exclusively **(*R*,*R*)-** and **(*S*,*S*)-Agg 1** and virtually no hetero aggregates which was proven by UV/vis and NMR spectroscopy (*Chapter 4.2.2*, Figure 25b and Figure 54).

2) The thermodynamic parameters of **(*S*,*S*)-Agg 1** are by definition the same as those of **(*R*,*R*)-Agg 1**[77] (*Chapter 3.2.4*, Table 1 and *Chapter 4.2.5*, Table 2) due to their enantiomeric relation.

3) Since **Con-Agg 1** consists exclusively of **(*R*,*R*)-** and **(*S*,*S*)-Agg 1** and the thermodynamic parameters of **(*R*,*R*)-** and **(*S*,*S*)-Agg 1** are identical, the thermodynamic parameters of **Con-Agg 1** are accurately described by those determined for **(*R*,*R*)-Agg 1**[77] (*Chapter 4.2.5*, Table 2). In other words, **Con-Agg 1** can be treated as **(*R*,*R*)-Agg 1** with regard to its thermodynamics.

During the disassembly of **Rac-Agg 4** upon heating, the resultant monomers of **(*R*,*R*)-** and **(*S*,*S*)-PBI** reassemble into conglomerate **Con-Agg 1**. As reported for **(*R*,*R*)-Agg 1** (*Chapter 3.2.4* and *Chapter 3.3*),[77] also **Con-Agg 1** is formed through an anticooperative process with preferential formation of even-sized aggregates due to the formation of tightly bound dimeric units within **(*R*,*R*)-** and **(*S*,*S*)-Agg 1** with a higher dimerization constant K_2 compared to the association constant K_E for further elongation (*Chapter 4.2.5*, Table 2).[28, 77] Thus, the overall monomer concentrations c_{Mono} at the critical temperatures of the disassembly processes of **Rac-Agg 4** (*Chapter 4.2.5*, inset Figure 30b) were determined based on an anticooperative model that accounts for the preferential formation of even-numbered aggregates.[28] According to the aforementioned model, the known total concentration of molecules c_T can be expressed by the sum of the concentration of monomers c_{Mono}, molecules in even-numbered and odd-numbered aggregates at a certain temperature (equation (8), *Chapter 2.2*). For the determination of c_{Mono} at the respective critical temperature T_E (c_{Mono} (T_E)), the dimerization constant K_2 and the association constant for further elongation K_E of **Con-Agg 1** (which are the same as those of **(*R*,*R*)-Agg 1**) at the critical temperature T_E[77] were put into equation (8).

After numerical determination of c_{Mono} (T_E), a van't Hoff plot (*Chapter 4.2.5*, Figure 30b) was prepared according to equation (13) (*Chapter 7.1*) from which the standard enthalpy change $\Delta H°$ and the standard entropy change $\Delta S°$ upon aggregation were estimated.[288-289] The Gibbs free energy change $\Delta G°$ at 298 K was determined according to the Gibbs-Helmholtz equation (14) (*Chapter 7.1*).[288-289]

NMR spectra of synthetic intermediates and (*S*,*S*)-PBI

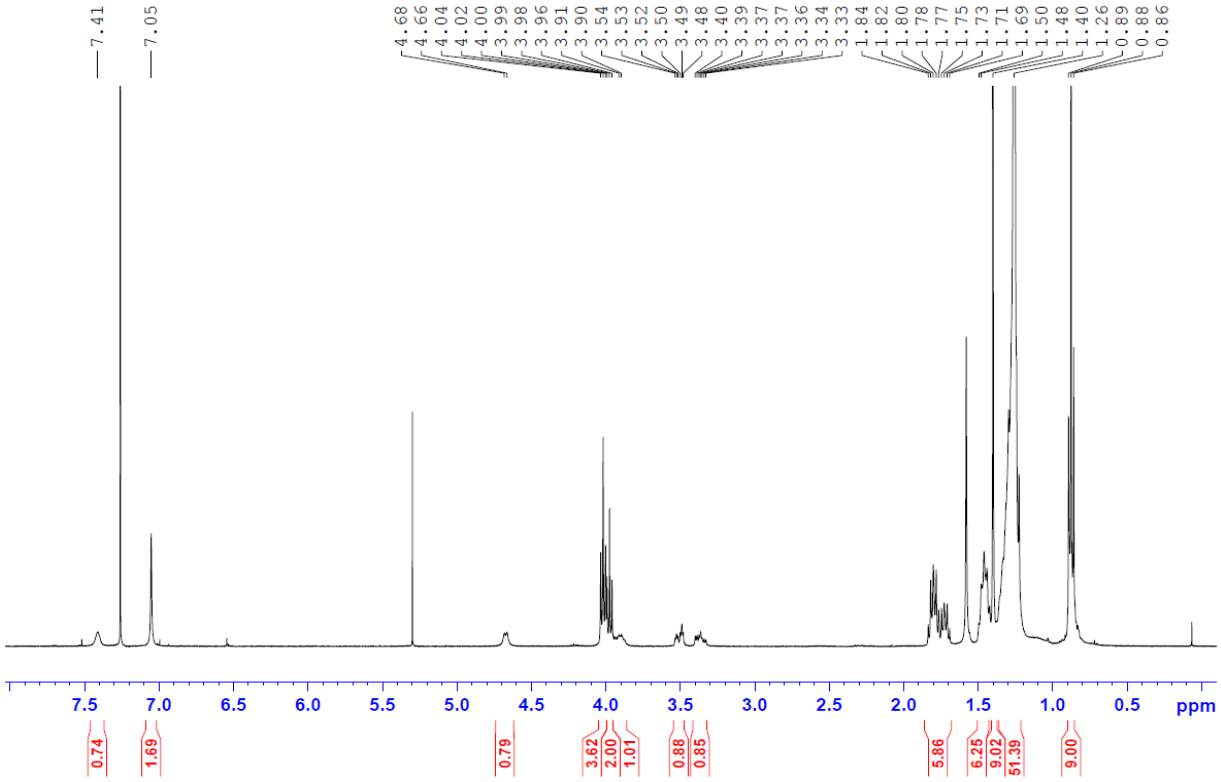

Figure 62. ^{1}H NMR (400 MHz) spectrum of (*S*)-*tert*-butyl (1-(3,4,5-tris(dodecyloxy)benzamido)propan-2-yl)carbamate (**(*S*)-18**) in $CDCl_3$ at 295 K.

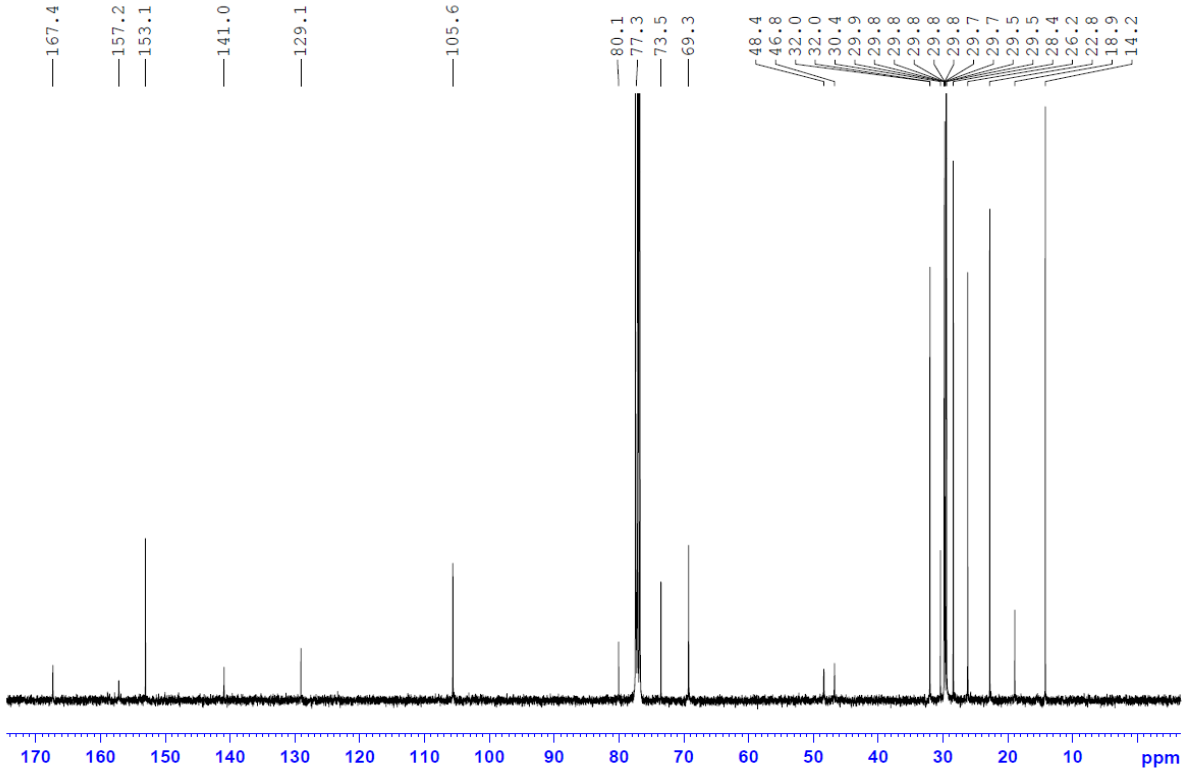

Figure 63. ^{13}C NMR (101 MHz) spectrum of (*S*)-*tert*-butyl (1-(3,4,5-tris(dodecyloxy)benzamido)propan-2-yl)carbamate (**(*S*)-18**) in $CDCl_3$ at 295 K.

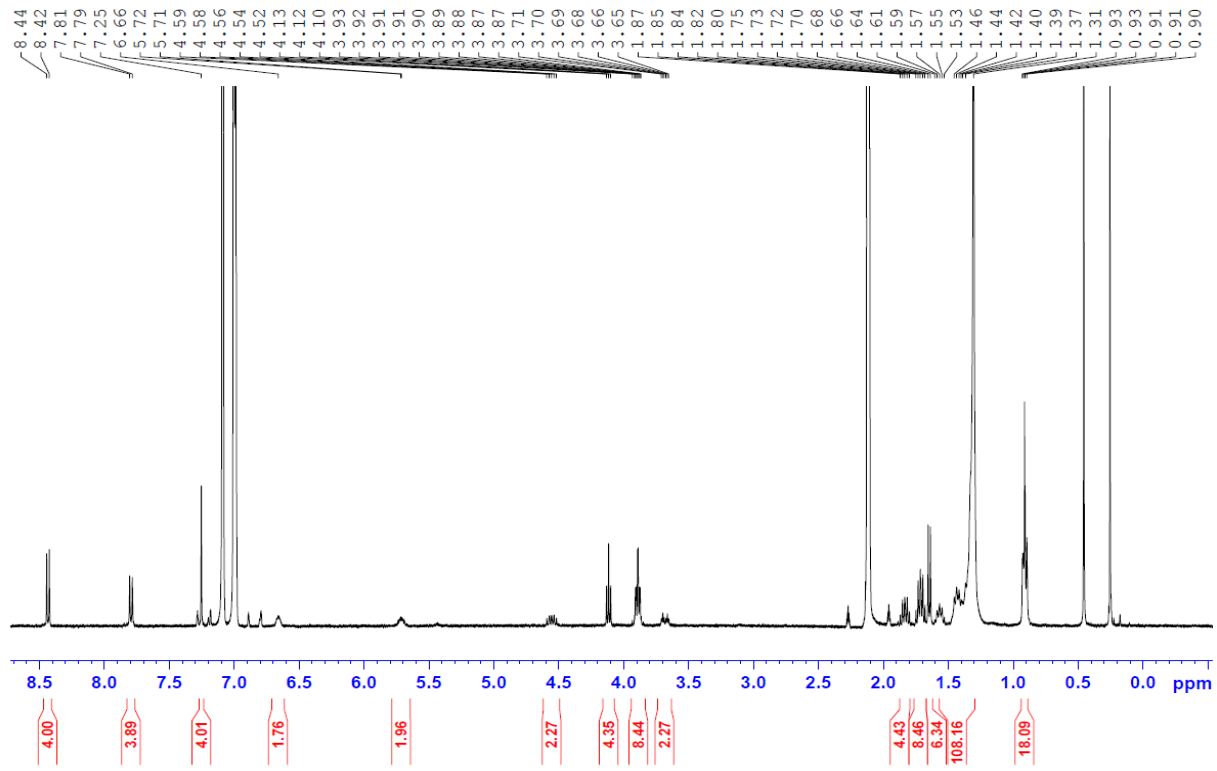

Figure 64. ^{1}H NMR spectrum (400 MHz) of (*S,S*)-*N,N*'-di[3,4,5-tris(dodecyloxy)benzoylamino-1-methylethyl]-perylene-3,4:9,10-tetracarboxylic acid bisimide (**(*S,S*)-PBI**) in toluene-d_8 at 365 K.

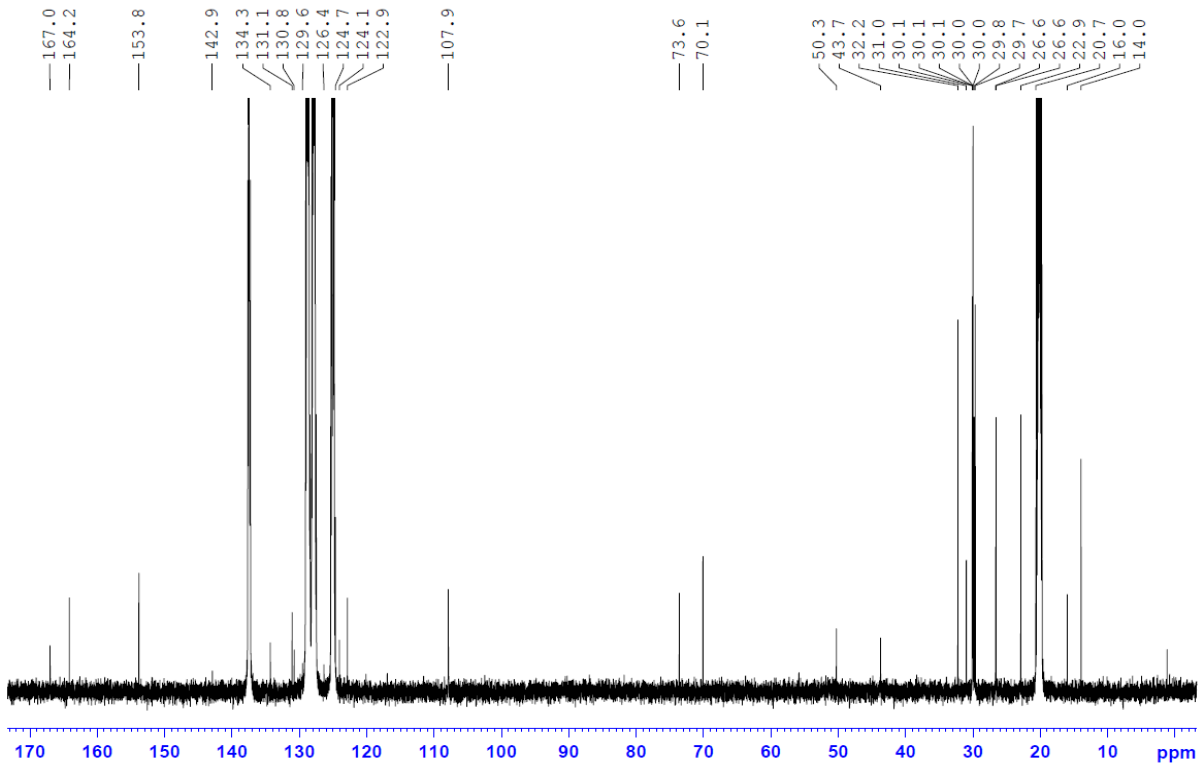

Figure 65. ^{13}C NMR spectrum (151 MHz) of (*S,S*)-*N,N*'-di[3,4,5-tris(dodecyloxy)benzoylamino-1-methylethyl]-perylene-3,4:9,10-tetracarboxylic acid bisimide (**(*S,S*)-PBI**) in toluene-d_8 at 365 K.

References

[1] H. Staudinger, *Ber. Dtsch. Chem. Ges. A/B* **1920**, *53*, 1073-1085.

[2] T. Aida, E. W. Meijer, *Isr. J. Chem.* **2020**, *60*, 33-47.

[3] J.-F. Lutz, J.-M. Lehn, E. W. Meijer, K. Matyjaszewski, *Nat. Rev. Mater.* **2016**, *1*, 16024.

[4] K. Matyjaszewski, N. V. Tsarevsky, *Nat. Chem.* **2009**, *1*, 276-288.

[5] K. Matyjaszewski, *Science* **2011**, *333*, 1104-1105.

[6] T. Aida, *Adv. Mater.* **2019**, 1905445.

[7] T. F. A. de Greef, E. W. Meijer, *Nature* **2008**, *453*, 171-173.

[8] T. Aida, E. W. Meijer, S. I. Stupp, *Science* **2012**, *335*, 813-817.

[9] L. Yang, X. Tan, Z. Wang, X. Zhang, *Chem. Rev.* **2015**, *115*, 7196-7239.

[10] E. Krieg, M. M. C. Bastings, P. Besenius, B. Rybtchinski, *Chem. Rev.* **2016**, *116*, 2414-2477.

[11] L. Brunsveld, B. J. B. Folmer, E. W. Meijer, R. P. Sijbesma, *Chem. Rev.* **2001**, *101*, 4071-4097.

[12] M. Wehner, F. Würthner, *Nat. Rev. Chem.* **2020**, *4*, 38-53.

[13] X. Yan, F. Wang, B. Zheng, F. Huang, *Chem. Soc. Rev.* **2012**, *41*, 6042-6065.

[14] J. B. Beck, S. J. Rowan, *J. Am. Chem. Soc.* **2003**, *125*, 13922-13923.

[15] X. Ma, H. Tian, *Acc. Chem. Res.* **2014**, *47*, 1971-1981.

[16] A. Campanella, D. Döhler, W. H. Binder, *Macromol. Rapid Commun.* **2018**, *39*, 1700739.

[17] P. Cordier, F. Tournilhac, C. Soulié-Ziakovic, L. Leibler, *Nature* **2008**, *451*, 977-980.

[18] L. R. Hart, J. L. Harries, B. W. Greenland, H. M. Colquhoun, W. Hayes, *Polym. Chem.* **2013**, *4*, 4860-4870.

[19] R. J. Wojtecki, M. A. Meador, S. J. Rowan, *Nat. Mater.* **2011**, *10*, 14-27.

[20] S.-L. Li, T. Xiao, C. Lin, L. Wang, *Chem. Soc. Rev.* **2012**, *41*, 5950-5968.

[21] R. Dong, Y. Zhou, X. Huang, X. Zhu, Y. Lu, J. Shen, *Adv. Mater.* **2015**, *27*, 498-526.

[22] Y. Yanagisawa, Y. Nan, K. Okuro, T. Aida, *Science* **2018**, *359*, 72-76.

[23] M. A. C. Stuart, W. T. S. Huck, J. Genzer, M. Müller, C. Ober, M. Stamm, G. B. Sukhorukov, I. Szleifer, V. V. Tsukruk, M. Urban, F. Winnik, S. Zauscher, I. Luzinov, S. Minko, *Nat. Mater.* **2010**, *9*, 101-113.

[24] R. B. Martin, *Chem. Rev.* **1996**, *96*, 3043-3064.

[25] T. F. A. De Greef, M. M. J. Smulders, M. Wolffs, A. P. H. J. Schenning, R. P. Sijbesma, E. W. Meijer, *Chem. Rev.* **2009**, *109*, 5687-5754.

[26] D. Zhao, J. S. Moore, *Org. Biomol. Chem.* **2003**, *1*, 3471-3491.

[27] Z. Chen, A. Lohr, C. R. Saha-Möller, F. Würthner, *Chem. Soc. Rev.* **2009**, *38*, 564-584.

[28] J. Gershberg, F. Fennel, T. H. Rehm, S. Lochbrunner, F. Würthner, *Chem. Sci.* **2016**, *7*, 1729-1737.

[29] P. A. Korevaar, S. J. George, A. J. Markvoort, M. M. J. Smulders, P. A. J. Hilbers, A. P. H. J. Schenning, T. F. A. De Greef, E. W. Meijer, *Nature* **2012**, *481*, 492-496.

[30] M. M. J. Smulders, M. M. L. Nieuwenhuizen, T. F. A. de Greef, P. van der Schoot, A. P. H. J. Schenning, E. W. Meijer, *Chem. Eur. J.* **2010**, *16*, 362-367.

[31] G. Fernández, M. Stolte, V. Stepanenko, F. Würthner, *Chem. Eur. J.* **2013**, *19*, 206-217.

[32] A. Sorrenti, J. Leira-Iglesias, A. J. Markvoort, T. F. A. de Greef, T. M. Hermans, *Chem. Soc. Rev.* **2017**, *46*, 5476-5490

[33] C. Kulkarni, S. Balasubramanian, S. J. George, *ChemPhysChem* **2013**, *14*, 661-673.

[34] S. A. P. van Rossum, M. Tena-Solsona, J. H. van Esch, R. Eelkema, J. Boekhoven, *Chem. Soc. Rev.* **2017**, *46*, 5519-5535.

[35] E. Mattia, S. Otto, *Nat. Nanotechnol.* **2015**, *10*, 111-119.

[36] G. Ashkenasy, T. M. Hermans, S. Otto, A. F. Taylor, *Chem. Soc. Rev.* **2017**, *46*, 2543-2554.

[37] J. Matern, Y. Dorca, L. Sánchez, G. Fernández, *Angew. Chem. Int. Ed.* **2019**, *58*, 16730-16740.

[38] Y. Okamoto, T. Nakano, E. Ono, K. Hatada, *Chem. Lett.* **1991**, *20*, 525-528.

[39] M. M. Bouman, E. W. Meijer, *Adv. Mater.* **1995**, *7*, 385-387.

[40] P. A. Korevaar, T. F. A. de Greef, E. W. Meijer, *Chem. Mater.* **2014**, *26*, 576-586.

[41] S. Ogi, K. Sugiyasu, S. Manna, S. Samitsu, M. Takeuchi, *Nat. Chem.* **2014**, *6*, 188-195.

[42] T. Fukui, S. Kawai, S. Fujinuma, Y. Matsushita, T. Yasuda, T. Sakurai, S. Seki, M. Takeuchi, K. Sugiyasu, *Nat. Chem.* **2017**, *9*, 493-499.

[43] S. Ogi, V. Stepanenko, K. Sugiyasu, M. Takeuchi, F. Würthner, *J. Am. Chem. Soc.* **2015**, *137*, 3300-3307.

[44] J. Kang, D. Miyajima, T. Mori, Y. Inoue, Y. Itoh, T. Aida, *Science* **2015**, *347*, 646-651.

[45] J. D. Dunitz, in *The Crystal as a Supramolecular Entity, Vol. 2* (Ed.: G. R. Desiraju), Wiley, Chichester, U.K., **1996**, pp. 1-30.

[46] J. Bernstein, *Polymorphism in Molecular Crystals*, Oxford University Press, Oxford, **2002**.

[47] B. Moulton, M. J. Zaworotko, *Chem. Rev.* **2001**, *101*, 1629-1658.

[48] G. R. Desiraju, J. J. Vittal, A. Ramanan, *Crystal Engineering: A Textbook*, World Scientific, Singapore, **2011**.

[49] M. R. Caira, in *Design of Organic Solids* (Eds.: E. Weber, Y. Aoyama, M. R. Caira, G. R. Desiraju, J. P. Glusker, A. D. Hamilton, R. E. Meléndez, A. Nangia), Springer Berlin Heidelberg, Berlin, Heidelberg, **1998**, pp. 163-208.

[50] A. R. Oganov, *Faraday Discuss.* **2018**, *211*, 643-660.

[51] A. R. A. Palmans, *Mol. Syst. Des. Eng.* **2017**, *2*, 34-46.

[52] R. Tamura, H. Takahashi, D. Fujimoto, T. Ushio, in *Novel Optical Resolution Technologies* (Eds.: K. Sakai, N. Hirayama, R. Tamura), Springer Berlin Heidelberg, Berlin, Heidelberg, **2007**, pp. 53-82.

[53] L. Pérez-García, D. B. Amabilino, *Chem. Soc. Rev.* **2002**, *31*, 342-356.

[54] G. R. Desiraju, *Angew. Chem. Int. Ed.* **2007**, *46*, 8342-8356.

[55] P. G. Vekilov, *Cryst. Growth Des.* **2010**, *10*, 5007-5019.

[56] R. E. Schreiber, L. Houben, S. G. Wolf, G. Leitus, Z.-L. Lang, J. J. Carbó, J. M. Poblet, R. Neumann, *Nat. Chem.* **2017**, *9*, 369-373.

[57] J. M. Gibson, *Science* **2009**, *326*, 942-943.

[58] B.-S. Lee, G. W. Burr, R. M. Shelby, S. Raoux, C. T. Rettner, S. N. Bogle, K. Darmawikarta, S. G. Bishop, J. R. Abelson, *Science* **2009**, *326*, 980-984.

[59] G. C. Sosso, J. Chen, S. J. Cox, M. Fitzner, P. Pedevilla, A. Zen, A. Michaelides, *Chem. Rev.* **2016**, *116*, 7078-7116.

[60] W. J. E. M. Habraken, J. Tao, L. J. Brylka, H. Friedrich, L. Bertinetti, A. S. Schenk, A. Verch, V. Dmitrovic, P. H. H. Bomans, P. M. Frederik, J. Laven, P. van der Schoot, B. Aichmayer, G. de With, J. J. DeYoreo, N. A. J. M. Sommerdijk, *Nat. Commun.* **2013**, *4*, 1507.

[61] L.-C. Sögütoglu, R. R. E. Steendam, H. Meekes, E. Vlieg, F. P. J. T. Rutjes, *Chem. Soc. Rev.* **2015**, *44*, 6723-6732.

[62] N. J. Hestand, F. C. Spano, *Acc. Chem. Res.* **2017**, *50*, 341-350.

[63] N. J. Hestand, F. C. Spano, *Chem. Rev.* **2018**, *118*, 7069-7163.

[64] F. Würthner, C. R. Saha-Möller, B. Fimmel, S. Ogi, P. Leowanawat, D. Schmidt, *Chem. Rev.* **2016**, *116*, 962-1052.

[65] M. Sadrai, G. R. Bird, *Opt. Commun.* **1984**, *51*, 62-64.

[66] M. G. Ramírez, S. Pla, P. G. Boj, J. M. Villalvilla, J. A. Quintana, M. A. Díaz-García, F. Fernández-Lázaro, Á. Sastre-Santos, *Adv. Opt. Mater.* **2013**, *1*, 933-938.

[67] R. Reisfeld, G. Seybold, *Chimia* **1990**, *44*, 295-297.

[68] X. Feng, Y. An, Z. Yao, C. Li, G. Shi, *ACS Appl. Mater. Interfaces* **2012**, *4*, 614-618.

[69] J. R. Siekierzycka, C. Hippius, F. Würthner, R. M. Williams, A. M. Brouwer, *J. Am. Chem. Soc.* **2010**, *132*, 1240-1242.

[70] L. Zang, R. Liu, M. W. Holman, K. T. Nguyen, D. M. Adams, *J. Am. Chem. Soc.* **2002**, *124*, 10640-10641.

[71] L. Rossetti, M. Franceschin, A. Bianco, G. Ortaggi, M. Savino, *Bioorg. Med. Chem. Lett.* **2002**, *12*, 2527-2533.

[72] V. L. Malinovskii, D. Wenger, R. Häner, *Chem. Soc. Rev.* **2010**, *39*, 410-422.

[73] E. Hädicke, F. Graser, *Acta Cryst. C* **1986**, *42*, 189-195.

[74] G. Klebe, F. Graser, E. Hädicke, J. Berndt, *Acta Cryst. B* **1989**, *45*, 69-77.

[75] S. Ogi, V. Stepanenko, J. Thein, F. Würthner, *J. Am. Chem. Soc.* **2016**, *138*, 670-678.

[76] W. Wagner, M. Wehner, V. Stepanenko, S. Ogi, F. Würthner, *Angew. Chem. Int. Ed.* **2017**, *56*, 16008-16012.

[77] M. Wehner, M. I. S. Röhr, M. Bühler, V. Stepanenko, W. Wagner, F. Würthner, *J. Am. Chem. Soc.* **2019**, *141*, 6092-6107.

[78] W. Wagner, M. Wehner, V. Stepanenko, F. Würthner, *J. Am. Chem. Soc.* **2019**, *141*, 12044-12054.

[79] W. Wagner, M. Wehner, V. Stepanenko, F. Würthner, *CCS Chem.* **2019**, *1*, 598-613.

[80] X.-Q. Li, V. Stepanenko, Z. Chen, P. Prins, L. D. A. Siebbeles, F. Würthner, *Chem. Commun.* **2006**, 3871-3873.

[81] J. W. Steed, J. L. Atwood, *Supramolecular Chemistry*, 2nd ed., Wiley, **2013**.

[82] C. J. Pedersen, *Angew. Chem. Int. Ed. Engl.* **1988**, *27*, 1021-1027.

[83] D. J. Cram, *Angew. Chem. Int. Ed. Engl.* **1988**, *27*, 1009-1020.

[84] J.-M. Lehn, *Angew. Chem. Int. Ed. Engl.* **1988**, *27*, 89-112.

[85] J.-M. Lehn, *Angew. Chem. Int. Ed. Engl.* **1990**, *29*, 1304-1319.

[86] H. Furukawa, K. E. Cordova, M. O'Keeffe, O. M. Yaghi, *Science* **2013**, *341*, 1230444.

[87] C. Fouquey, J. M. Lehn, A.-M. Levelut, *Adv. Mater.* **1990**, *2*, 254-257.

[88] G. Scheibe, *Angew. Chem.* **1937**, *50*, 212-219.

[89] G. Scheibe, L. Kandler, H. Ecker, *Naturwissenschaften* **1937**, *25*, 75.

[90] E. E. Jelley, *Nature* **1936**, *138*, 1009-1010.

[91] E. E. Jelley, *Nature* **1937**, *139*, 631-632.

[92] Y. Hong, J. W. Y. Lam, B. Z. Tang, *Chem. Soc. Rev.* **2011**, *40*, 5361-5388.

[93] E. Daltrozzo, G. Scheibe, K. Gschwind, F. Haimerl, *Photogr. Sci. Eng.* **1974**, *18*, 441-450.

[94] H. von Berlepsch, C. Böttcher, L. Dähne, *J. Phys. Chem. B* **2000**, *104*, 8792-8799.

[95] A. Klug, *Philos. Trans. R. Soc. Lond., B, Biol. Sci.* **1999**, *354*, 531-535.

[96] A. Klug, *Annu. Rev. Biochem.* **2010**, *79*, 1-35.

[97] B. Rybtchinski, *ACS Nano* **2011**, *5*, 6791-6818.

[98] E. Busseron, Y. Ruff, E. Moulin, N. Giuseppone, *Nanoscale* **2013**, *5*, 7098-7140.

[99] S. K. Yang, S. C. Zimmerman, *Isr. J. Chem.* **2013**, *53*, 511-520.

[100] A. Winter, U. S. Schubert, *Chem. Soc. Rev.* **2016**, *45*, 5311-5357.

[101] F. Würthner, *Acc. Chem. Res.* **2016**, *49*, 868-876.

[102] S. Dong, B. Zheng, F. Wang, F. Huang, *Acc. Chem. Res.* **2014**, *47*, 1982-1994.

[103] M. Xue, Y. Yang, X. Chi, X. Yan, F. Huang, *Chem. Rev.* **2015**, *115*, 7398-7501.

[104] J. Zhou, G. Yu, F. Huang, *Chem. Soc. Rev.* **2017**, *46*, 7021-7053.

[105] R. P. Sijbesma, F. H. Beijer, L. Brundsveld, B. J. B. Folmer, J. H. K. K. Hirschberg, R. F. M. Lange, J. K. L. Lowe, E. W. Meijer, *Science* **1997**, *278*, 1601-1604.

[106] R. K. Castellano, D. M. Rudkevich, J. Rebek, *Proc. Natl. Acad. Sci. U. S. A.* **1997**, *94*, 7132-7137.

[107] R. K. Castellano, C. Nuckolls, S. H. Eichhorn, M. R. Wood, A. J. Lovinger, J. Rebek, *Angew. Chem. Int. Ed.* **1999**, *38*, 2603-2606.

[108] R. K. Castellano, R. Clark, S. L. Craig, C. Nuckolls, J. Rebek, *Proc. Natl. Acad. Sci. U. S. A.* **2000**, *97*, 12418-12421.

[109] U. Velten, M. Rehahn, *Chem. Commun.* **1996**, 2639-2640.

[110] C. Rest, R. Kandanelli, G. Fernández, *Chem. Soc. Rev.* **2015**, *44*, 2543-2572.

[111] R. F. Pasternack, C. Fleming, S. Herring, P. J. Collings, J. dePaula, G. DeCastro, E. J. Gibbs, *Biophys. J.* **2000**, *79*, 550-560.

[112] S. Ogi, T. Fukui, M. L. Jue, M. Takeuchi, K. Sugiyasu, *Angew. Chem. Int. Ed.* **2014**, *53*, 14363-14367.

[113] K. Venkata Rao, D. Miyajima, A. Nihonyanagi, T. Aida, *Nat. Chem.* **2017**, *9*, 1133-1139.

[114] M. F. J. Mabesoone, A. J. Markvoort, M. Banno, T. Yamaguchi, F. Helmich, Y. Naito, E. Yashima, A. R. A. Palmans, E. W. Meijer, *J. Am. Chem. Soc.* **2018**, *140*, 7810-7819.

[115] N. Micali, H. Engelkamp, P. G. van Rhee, P. C. M. Christianen, L. M. Scolaro, J. C. Maan, *Nat. Chem.* **2012**, *4*, 201-207.

[116] F. Helmich, C. C. Lee, M. M. L. Nieuwenhuizen, J. C. Gielen, P. C. M. Christianen, A. Larsen, G. Fytas, P. E. L. G. Leclère, A. P. H. J. Schenning, E. W. Meijer, *Angew. Chem. Int. Ed.* **2010**, *49*, 3939-3942.

[117] F. Würthner, S. Yao, U. Beginn, *Angew. Chem. Int. Ed.* **2003**, *42*, 3247-3250.

[118] S. Yao, U. Beginn, T. Gress, M. Lysetska, F. Würthner, *J. Am. Chem. Soc.* **2004**, *126*, 8336-8348.

[119] A. Lohr, M. Lysetska, F. Würthner, *Angew. Chem. Int. Ed.* **2005**, *44*, 5071-5074.

[120] A. Lohr, F. Würthner, *Angew. Chem. Int. Ed.* **2008**, *47*, 1232-1236.

[121] A. P. H. J. Schenning, P. Jonkheijm, E. Peeters, E. W. Meijer, *J. Am. Chem. Soc.* **2001**, *123*, 409-416.

[122] P. Jonkheijm, P. van der Schoot, A. P. H. J. Schenning, E. W. Meijer, *Science* **2006**, *313*, 80-83.

[123] P. A. Korevaar, C. Schaefer, T. F. A. de Greef, E. W. Meijer, *J. Am. Chem. Soc.* **2012**, *134*, 13482-13491.

[124] T. E. Kaiser, V. Stepanenko, F. Würthner, *J. Am. Chem. Soc.* **2009**, *131*, 6719-6732.

[125] E. Krieg, H. Weissman, E. Shimoni, A. Bar On, B. Rybtchinski, *J. Am. Chem. Soc.* **2014**, *136*, 9443-9452.

[126] C. Kulkarni, K. K. Bejagam, S. P. Senanayak, K. S. Narayan, S. Balasubramanian, S. J. George, *J. Am. Chem. Soc.* **2015**, *137*, 3924-3932.

[127] M. M. J. Smulders, A. P. H. J. Schenning, E. W. Meijer, *J. Am. Chem. Soc.* **2008**, *130*, 606-611.

[128] N. M. Matsumoto, R. P. M. Lafleur, X. Lou, K.-C. Shih, S. P. W. Wijnands, C. Guibert, J. W. A. M. van Rosendaal, I. K. Voets, A. R. A. Palmans, Y. Lin, E. W. Meijer, *J. Am. Chem. Soc.* **2018**, *140*, 13308-13316.

[129] L. Albertazzi, D. van der Zwaag, C. M. A. Leenders, R. Fitzner, R. W. van der Hofstad, E. W. Meijer, *Science* **2014**, *344*, 491-495.

[130] T. Brixner, R. Hildner, J. Köhler, C. Lambert, F. Würthner, *Adv. Energy Mater.* **2017**, *7*, 1700236.

[131] F. Würthner, S. Yao, T. Debaerdemaeker, R. Wortmann, *J. Am. Chem. Soc.* **2002**, *124*, 9431-9447.

[132] W. J. Schutte, M. Sluyters-Rehbach, J. H. Sluyters, *J. Phys. Chem.* **1993**, *97*, 6069-6073.

[133] R. Wortmann, U. Rösch, M. Redi-Abshiro, F. Würthner, *Angew. Chem. Int. Ed.* **2003**, *42*, 2080-2083.

[134] P. J. Camp, A. C. Jones, R. K. Neely, N. M. Speirs, *J. Phys. Chem. A* **2002**, *106*, 10725-10732.

[135] R. F. Goldstein, L. Stryer, *Biophys. J.* **1986**, *50*, 583-599.

[136] F. Würthner, C. Thalacker, S. Diele, C. Tschierske, *Chem. Eur. J.* **2001**, *7*, 2245-2253.

[137] T. Heek, C. Fasting, C. Rest, X. Zhang, F. Würthner, R. Haag, *Chem. Commun.* **2010**, *46*, 1884-1886.

[138] T. E. Kaiser, H. Wang, V. Stepanenko, F. Würthner, *Angew. Chem. Int. Ed.* **2007**, *46*, 5541-5544.

[139] S. S. Babu, V. K. Praveen, A. Ajayaghosh, *Chem. Rev.* **2014**, *114*, 1973-2129.

[140] F. Oosawa, M. Kasai, *J. Mol. Biol.* **1962**, *4*, 10-21.

[141] E. T. Powers, D. L. Powers, *Biophys. J.* **2006**, *91*, 122-132.

[142] P. Besenius, *J. Polym. Sci., Part A: Polym. Chem.* **2017**, *55*, 34-78.

[143] A. T. Haedler, S. C. J. Meskers, R. H. Zha, M. Kivala, H.-W. Schmidt, E. W. Meijer, *J. Am. Chem. Soc.* **2016**, *138*, 10539-10545.

[144] T. Yamamoto, T. Fukushima, Y. Yamamoto, A. Kosaka, W. Jin, N. Ishii, T. Aida, *J. Am. Chem. Soc.* **2006**, *128*, 14337-14340.

[145] Z. Chen, Y. Liu, W. Wagner, V. Stepanenko, X. Ren, S. Ogi, F. Würthner, *Angew. Chem. Int. Ed.* **2017**, *56*, 5729-5733.

[146] Y. Tidhar, H. Weissman, S. G. Wolf, A. Gulino, B. Rybtchinski, *Chem. Eur. J.* **2011**, *17*, 6068-6075.

[147] P. A. Korevaar, C. J. Newcomb, E. W. Meijer, S. I. Stupp, *J. Am. Chem. Soc.* **2014**, *136*, 8540-8543.

[148] H. Cui, Z. Chen, S. Zhong, K. L. Wooley, D. J. Pochan, *Science* **2007**, *317*, 647-650.

[149] J. P. Hill, W. Jin, A. Kosaka, T. Fukushima, H. Ichihara, T. Shimomura, K. Ito, T. Hashizume, N. Ishii, T. Aida, *Science* **2004**, *304*, 1481-1483.

[150] L. Zang, Y. Che, J. S. Moore, *Acc. Chem. Res.* **2008**, *41*, 1596-1608.

[151] S. Yagai, S. Okamura, Y. Nakano, M. Yamauchi, K. Kishikawa, T. Karatsu, A. Kitamura, A. Ueno, D. Kuzuhara, H. Yamada, T. Seki, H. Ito, *Nat. Commun.* **2014**, *5*, 4013.

[152] N. Komiya, T. Muraoka, M. Iida, M. Miyanaga, K. Takahashi, T. Naota, *J. Am. Chem. Soc.* **2011**, *133*, 16054-16061.

[153] A. Aliprandi, M. Mauro, L. De Cola, *Nat. Chem.* **2016**, *8*, 10-15.

[154] J. Boekhoven, W. E. Hendriksen, G. J. M. Koper, R. Eelkema, J. H. van Esch, *Science* **2015**, *349*, 1075-1079.

[155] J. Boekhoven, J. M. Poolman, C. Maity, F. Li, L. van der Mee, C. B. Minkenberg, E. Mendes, J. H. van Esch, R. Eelkema, *Nat. Chem.* **2013**, *5*, 433-437.

[156] J. Leira-Iglesias, A. Sorrenti, A. Sato, P. A. Dunne, T. M. Hermans, *Chem. Commun.* **2016**, *52*, 9009-9012.

[157] J. Leira-Iglesias, A. Tassoni, T. Adachi, M. Stich, T. M. Hermans, *Nat. Nanotechnol.* **2018**, *13*, 1021-1027.

[158] M. Kumar, P. Brocorens, C. Tonnelé, D. Beljonne, M. Surin, S. J. George, *Nat. Commun.* **2014**, *5*, 5793.

[159] A. Lohr, F. Würthner, *Isr. J. Chem.* **2011**, *51*, 1052-1066.

[160] D. van der Zwaag, P. A. Pieters, P. A. Korevaar, A. J. Markvoort, A. J. H. Spiering, T. F. A. de Greef, E. W. Meijer, *J. Am. Chem. Soc.* **2015**, *137*, 12677-12688.

[161] F. Tantakitti, J. Boekhoven, X. Wang, R. V. Kazantsev, T. Yu, J. Li, E. Zhuang, R. Zandi, J. H. Ortony, C. J. Newcomb, L. C. Palmer, G. S. Shekhawat, M. O. de la Cruz, G. C. Schatz, S. I. Stupp, *Nat. Mater.* **2016**, *15*, 469-476.

[162] S. Sevim, A. Sorrenti, C. Franco, S. Furukawa, S. Pané, A. J. deMello, J. Puigmartí-Luis, *Chem. Soc. Rev.* **2018**, *47*, 3788-3803.

[163] Y. Olivier, D. Niedzialek, V. Lemaur, W. Pisula, K. Müllen, U. Koldemir, J. R. Reynolds, R. Lazzaroni, J. Cornil, D. Beljonne, *Adv. Mater.* **2014**, *26*, 2119-2136.

[164] S. Zhang, M. A. Greenfield, A. Mata, L. C. Palmer, R. Bitton, J. R. Mantei, C. Aparicio, M. O. de la Cruz, S. I. Stupp, *Nat. Mater.* **2010**, *9*, 594-601.

[165] S. Ogi, C. Grzeszkiewicz, F. Würthner, *Chem. Sci.* **2018**, *9*, 2768-2773.

[166] K. Cai, J. Xie, D. Zhang, W. Shi, Q. Yan, D. Zhao, *J. Am. Chem. Soc.* **2018**, *140*, 5764-5773.

[167] A. Langenstroer, K. K. Kartha, Y. Dorca, J. Droste, V. Stepanenko, R. Q. Albuquerque, M. R. Hansen, L. Sánchez, G. Fernández, *J. Am. Chem. Soc.* **2019**, *141*, 5192-5200.

[168] B. Kemper, L. Zengerling, D. Spitzer, R. Otter, T. Bauer, P. Besenius, *J. Am. Chem. Soc.* **2018**, *140*, 534-537.

[169] S. M. Doyle, O. Genest, S. Wickner, *Nat. Rev. Mol. Cell Biol.* **2013**, *14*, 617-629.

[170] H. Saibil, *Nat. Rev. Mol. Cell Biol.* **2013**, *14*, 630-642.

[171] J. Adamcik, R. Mezzenga, *Angew. Chem. Int. Ed.* **2018**, *57*, 8370-8382.

[172] N. J. Van Zee, B. Adelizzi, M. F. J. Mabesoone, X. Meng, A. Aloi, R. H. Zha, M. Lutz, I. A. W. Filot, A. R. A. Palmans, E. W. Meijer, *Nature* **2018**, *558*, 100-103.

[173] J. M. Ribó, J. Crusats, F. Sagués, J. Claret, R. Rubires, *Science* **2001**, *292*, 2063-2066.

[174] M. Endo, T. Fukui, S. H. Jung, S. Yagai, M. Takeuchi, K. Sugiyasu, *J. Am. Chem. Soc.* **2016**, *138*, 14347-14353.

[175] G. Odian, *Principles of Polymerization*, 4 ed., Wiley, Hoboken, **2004**.

[176] M. Szwarc, M. Levy, R. Milkovich, *J. Am. Chem. Soc.* **1956**, *78*, 2656-2657.

[177] O. W. Webster, *Science* **1991**, *251*, 887-893.

[178] T. Fukui, T. Uchihashi, N. Sasaki, H. Watanabe, M. Takeuchi, K. Sugiyasu, *Angew. Chem. Int. Ed.* **2018**, *57*, 15465-15470.

[179] J. S. Valera, R. Gómez, L. Sánchez, *Small* **2018**, *14*, 1702437.

[180] S. Ogi, K. Matsumoto, S. Yamaguchi, *Angew. Chem. Int. Ed.* **2018**, *57*, 2339-2343.

[181] E. E. Greciano, B. Matarranz, L. Sánchez, *Angew. Chem. Int. Ed.* **2018**, *57*, 4697-4701.

[182] E. E. Greciano, L. Sánchez, *Chem. Eur. J.* **2016**, *22*, 13724-13730.

[183] H. Kar, G. Ghosh, S. Ghosh, *Chem. Eur. J.* **2017**, *23*, 10536-10542.

[184] G. Ghosh, S. Ghosh, *Chem. Commun.* **2018**, *54*, 5720-5723.

[185] X. Wang, G. Guerin, H. Wang, Y. Wang, I. Manners, M. A. Winnik, *Science* **2007**, *317*, 644-647.

[186] T. Gädt, N. S. Ieong, G. Cambridge, M. A. Winnik, I. Manners, *Nat. Mater.* **2009**, *8*, 144-150.

[187] W. Zhang, W. Jin, T. Fukushima, A. Saeki, S. Seki, T. Aida, *Science* **2011**, *334*, 340-343.

[188] E. T. Powers, D. L. Powers, *Biophys. J.* **2008**, *94*, 379-391.

[189] A. Aguzzi, A. M. Calella, *Physiol. Rev.* **2009**, *89*, 1105-1152.

[190] M. E. Robinson, D. J. Lunn, A. Nazemi, G. R. Whittell, L. De Cola, I. Manners, *Chem. Commun.* **2015**, *51*, 15921-15924.

[191] Q. Wan, W.-P. To, C. Yang, C.-M. Che, *Angew. Chem. Int. Ed.* **2018**, *57*, 3089-3093.

[192] J. Kang, D. Miyajima, Y. Itoh, T. Mori, H. Tanaka, M. Yamauchi, Y. Inoue, S. Harada, T. Aida, *J. Am. Chem. Soc.* **2014**, *136*, 10640-10644.

[193] D. S. Pal, H. Kar, S. Ghosh, *Chem. Commun.* **2018**, *54*, 928-931.

[194] S. Ogi, N. Fukaya, Arifin, B. B. Skjelstad, Y. Hijikata, S. Yamaguchi, *Chem. Eur. J.* **2019**, *25*, 7303-7307.

[195] M. E. Robinson, A. Nazemi, D. J. Lunn, D. W. Hayward, C. E. Boott, M.-S. Hsiao, R. L. Harniman, S. A. Davis, G. R. Whittell, R. M. Richardson, L. De Cola, I. Manners, *ACS Nano* **2017**, *11*, 9162-9175.

[196] H. Frisch, E.-C. Fritz, F. Stricker, L. Schmüser, D. Spitzer, T. Weidner, B. J. Ravoo, P. Besenius, *Angew. Chem. Int. Ed.* **2016**, *55*, 7242-7246.

[197] D. Spitzer, V. Marichez, G. J. M. Formon, P. Besenius, T. M. Hermans, *Angew. Chem. Int. Ed.* **2018**, *57*, 11349-11353.

[198] A. Mishra, D. B. Korlepara, M. Kumar, A. Jain, N. Jonnalagadda, K. K. Bejagam, S. Balasubramanian, S. J. George, *Nat. Commun.* **2018**, *9*, 1295.

[199] A. Jain, S. Dhiman, A. Dhayani, P. K. Vemula, S. J. George, *Nat. Commun.* **2019**, *10*, 450.

[200] E. Mitscherlich, *Ann. Chim. Phys.* **1822**, *19*, 350-419.

[201] A. J. Cruz-Cabeza, S. M. Reutzel-Edens, J. Bernstein, *Chem. Soc. Rev.* **2015**, *44*, 8619-8635.

[202] F. Wöhler, J. von Liebig, *Ann. Pharm.* **1832**, *3*, 249-282.

[203] K. E. Johansson, J. van de Streek, *Cryst. Growth Des.* **2016**, *16*, 1366-1370.

[204] A. J. Cruz-Cabeza, J. Bernstein, *Chem. Rev.* **2014**, *114*, 2170-2191.

[205] D.-K. Bučar, R. W. Lancaster, J. Bernstein, *Angew. Chem. Int. Ed.* **2015**, *54*, 6972-6993.

[206] J. Bernstein, R. J. Davey, J.-O. Henck, *Angew. Chem. Int. Ed.* **1999**, *38*, 3440-3461.

[207] J.-P. Brog, C.-L. Chanez, A. Crochet, K. M. Fromm, *RSC Adv.* **2013**, *3*, 16905-16931.

[208] P. Kulkarni, T. L. Solomon, Y. He, Y. Chen, P. N. Bryan, J. Orban, *Protein Sci.* **2018**, *27*, 1557-1567.

[209] F. Chiti, C. M. Dobson, *Nat. Chem. Biol.* **2009**, *5*, 15-22.

[210] F. Chiti, C. M. Dobson, *Annu. Rev. Biochem.* **2017**, *86*, 27-68.

[211] C. Lara, J. Adamcik, S. Jordens, R. Mezzenga, *Biomacromolecules* **2011**, *12*, 1868-1875.

[212] C. Lara, S. Handschin, R. Mezzenga, *Nanoscale* **2013**, *5*, 7197-7201.

[213] E. Unger, K. J. Böhm, W. Vater, *Electron Microsc. Rev.* **1990**, *3*, 355-395.

[214] A. C. H. Durham, A. Klug, *Nat. New Biol.* **1971**, *229*, 42-46.

[215] A. C. H. Durham, J. T. Finch, A. Klug, *Nat. New Biol.* **1971**, *229*, 37-42.

[216] Y. Liu, Z. Wang, X. Zhang, *Chem. Soc. Rev.* **2012**, *41*, 5922-5932.

[217] D. G. Blackmond, *Cold Spring Harb. Perspect. Biol.* **2019**, *11*, a032540.

[218] S. Dutta, A. J. Gellman, *Chem. Soc. Rev.* **2017**, *46*, 7787-7839.

[219] G. P. Moss, *Pure Appl. Chem.* **1996**, *68*, 2193-2222.

[220] M. M. Safont-Sempere, G. Fernández, F. Würthner, *Chem. Rev.* **2011**, *111*, 5784-5814.

[221] H. Jędrzejewska, A. Szumna, *Chem. Rev.* **2017**, *117*, 4863-4899.

[222] B. Y. Shekunov, P. York, *J. Cryst. Growth* **2000**, *211*, 122-136.

[223] A. A. Bredikhin, Z. A. Bredikhina, *Chem. Eng. Technol.* **2017**, *40*, 1211-1220.

[224] S. Mane, *Anal. Methods* **2016**, *8*, 7567-7586.

[225] H. Lorenz, A. Seidel-Morgenstern, *Angew. Chem. Int. Ed.* **2014**, *53*, 1218-1250.

[226] G. Coquerel, *Top. Curr. Chem.* **2007**, *269*, 1-51.

[227] R. K. Hylton, G. J. Tizzard, T. L. Threlfall, A. L. Ellis, S. J. Coles, C. C. Seaton, E. Schulze, H. Lorenz, A. Seidel-Morgenstern, M. Stein, S. L. Price, *J. Am. Chem. Soc.* **2015**, *137*, 11095-11104.

[228] A. Gavezzotti, S. Rizzato, *J. Org. Chem.* **2014**, *79*, 4809-4816.

[229] L. Pérez-García, D. B. Amabilino, *Chem. Soc. Rev.* **2007**, *36*, 941-967.

[230] G. An, P. Yan, J. Sun, Y. Li, X. Yao, G. Li, *CrystEngComm* **2015**, *17*, 4421-4433.

[231] S. De Feyter, F. C. De Schryver, *Chem. Soc. Rev.* **2003**, *32*, 139-150.

[232] A. Kühnle, T. R. Linderoth, B. Hammer, F. Besenbacher, *Nature* **2002**, *415*, 891-893.

[233] R. Fasel, M. Parschau, K.-H. Ernst, *Nature* **2006**, *439*, 449-452.

[234] J. Seibel, M. Parschau, K.-H. Ernst, *J. Am. Chem. Soc.* **2015**, *137*, 7970-7973.

[235] J. Lin, Z. Guo, J. Plas, D. B. Amabilino, S. De Feyter, A. P. H. J. Schenning, *Chem. Commun.* **2013**, *49*, 9320-9322.

[236] M. Liu, L. Zhang, T. Wang, *Chem. Rev.* **2015**, *115*, 7304-7397.

[237] C. Roche, H.-J. Sun, M. E. Prendergast, P. Leowanawat, B. E. Partridge, P. A. Heiney, F. Araoka, R. Graf, H. W. Spiess, X. Zeng, G. Ungar, V. Percec, *J. Am. Chem. Soc.* **2014**, *136*, 7169-7185.

[238] A. R. A. Palmans, E. W. Meijer, *Angew. Chem. Int. Ed.* **2007**, *46*, 8948-8968.

[239] W. Herbst, K. Hunger, *Industrial Organic Pigments: Production, Properties, Applications*, 3rd ed., Wiley-VCH, Weinheim, **2004**.

[240] T. L. Threlfall, *Analyst* **1995**, *120*, 2435-2460.

[241] P. Erk, H. Hengelsberg, in *The Porphyrin Handbook, Vol. 19* (Eds.: K. M. Kadish, K. M. Smith, R. Guilard), Academic Press, San Diego, **2003**, pp. 105-149.

[242] H.-J. Sun, S. Zhang, V. Percec, *Chem. Soc. Rev.* **2015**, *44*, 3900-3923.

[243] J. H. van Esch, R. Klajn, S. Otto, *Chem. Soc. Rev.* **2017**, *46*, 5474-5475.

[244] J. Baram, H. Weissman, B. Rybtchinski, *J. Phys. Chem. B* **2014**, *118*, 12068-12073.

[245] P. A. Rupar, L. Chabanne, M. A. Winnik, I. Manners, *Science* **2012**, *337*, 559-562.

[246] J. Hu, W. Kuang, K. Deng, W. Zou, Y. Huang, Z. Wei, C. F. J. Faul, *Adv. Funct. Mater* **2012**, *22*, 4149-4158.

[247] M. T. Fenske, W. Meyer-Zaika, H.-G. Korth, H. Vieker, A. Turchanin, C. Schmuck, *J. Am. Chem. Soc.* **2013**, *135*, 8342-8349.

[248] X. Zhang, D. Görl, V. Stepanenko, F. Würthner, *Angew. Chem. Int. Ed.* **2014**, *53*, 1270-1274.

[249] M. Hifsudheen, R. K. Mishra, B. Vedhanarayanan, V. K. Praveen, A. Ajayaghosh, *Angew. Chem. Int. Ed.* **2017**, *56*, 12634-12638.

[250] T. M. Hermans, M. A. C. Broeren, N. Gomopoulos, P. van der Schoot, M. H. P. van Genderen, N. A. J. M. Sommerdijk, G. Fytas, E. W. Meijer, *Nat. Nanotechnol.* **2009**, *4*, 721-726.

[251] F. Würthner, C. Bauer, V. Stepanenko, S. Yagai, *Adv. Mater.* **2008**, *20*, 1695-1698.

[252] S. Ghosh, X.-Q. Li, V. Stepanenko, F. Würthner, *Chem. Eur. J.* **2008**, *14*, 11343-11357.

[253] M. Wehner, Master's thesis, Julius-Maximilians-Universität Würzburg (Würzburg), **2016**.

[254] Y. Tang, L. Zhou, J. Li, Q. Luo, X. Huang, P. Wu, Y. Wang, J. Xu, J. Shen, J. Liu, *Angew. Chem. Int. Ed.* **2010**, *49*, 3920-3924.

[255] M. Gobbini, S. Armaroli, L. Banfi, A. Benicchio, G. Carzana, G. Fedrizzi, P. Ferrari, G. Giacalone, M. Giubileo, G. Marazzi, R. Micheletti, B. Moro, M. Pozzi, P. E. Scotti, M. Torri, A. Cerri, *J. Med. Chem.* **2008**, *51*, 4601-4608.

[256] H. Nishiwaki, H. Nagaoka, M. Kuriyama, S. Yamauchi, Y. Shuto, *Biosci. Biotechnol. Biochem.* **2011**, *75*, 780-782.

[257] J. M. Malicka, A. Sandeep, F. Monti, E. Bandini, M. Gazzano, C. Ranjith, V. K. Praveen, A. Ajayaghosh, N. Armaroli, *Chem. Eur. J.* **2013**, *19*, 12991-13001.

[258] G. Ruecroft, D. Hipkiss, T. Ly, N. Maxted, P. W. Cains, *Org. Process Res. Dev.* **2005**, *9*, 923-932.

[259] R. Chow, R. Blindt, R. Chivers, M. Povey, *Ultrasonics* **2005**, *43*, 227-230.

[260] P. W. Cains, P. D. Martin, C. J. Price, *Org. Process Res. Dev.* **1998**, *2*, 34-48.

[261] J. R. G. Sander, B. W. Zeiger, K. S. Suslick, *Ultrason. Sonochem.* **2014**, *21*, 1908-1915.

[262] T. Y. Wu, N. Guo, C. Y. Teh, J. X. W. Hay, *Advances in Ultrasound Technology for Environmental Remediation*, Springer Netherlands, **2013**.

[263] N. Harada, K. Nakanishi, *Acc. Chem. Res.* **1972**, *5*, 257-263.

[264] Z. Chen, V. Stepanenko, V. Dehm, P. Prins, L. D. A. Siebbeles, J. Seibt, P. Marquetand, V. Engel, F. Würthner, *Chem. Eur. J.* **2007**, *13*, 436-449.

[265] M. Son, K. H. Park, C. Shao, F. Würthner, D. Kim, *J. Phys. Chem. Lett.* **2014**, *5*, 3601-3607.

[266] J. Sung, P. Kim, B. Fimmel, F. Würthner, D. Kim, *Nat. Commun.* **2015**, *6*, 8646.

[267] E. G. McRae, M. Kasha, *J. Chem. Phys.* **1958**, *28*, 721-722.

[268] M. Kasha, H. R. Rawls, M. A. El-Bayoumi, *Pure Appl. Chem.* **1965**, *11*, 371-392.

[269] F. Würthner, Z. Chen, V. Dehm, V. Stepanenko, *Chem. Commun.* **2006**, 1188-1190.

[270] F. Graser, E. Hädike, *Liebigs Ann. Chem.* **1984**, *1984*, 483-494.

[271] B. C. Smith, *Infrared Spectral Interpretation: A Systematic Approach*, CRC Press, Boca Raton, **1998**.

[272] R. Marty, R. Szilluweit, A. Sánchez-Ferrer, S. Bolisetty, J. Adamcik, R. Mezzenga, E.-C. Spitzner, M. Feifer, S. N. Steinmann, C. Corminboeuf, H. Frauenrath, *ACS Nano* **2013**, *7*, 8498-8508.

[273] J. J. P. Stewart, *J. Mol. Model.* **2007**, *13*, 1173-1213.

[274] J. Řezáč, P. Hobza, *J. Chem. Theory Comput.* **2012**, *8*, 141-151.

[275] S. Grimme, J. Antony, S. Ehrlich, H. Krieg, *J. Chem. Phys.* **2010**, *132*, 154104.

[276] J. J. P. Stewart, *MOPAC2016*, Stewart Computational Chemistry, Colorado Springs, CO, USA, HTTP://OpenMOPAC.net/, **2016**.

[277] A. D. Becke, *J. Chem. Phys.* **1993**, *98*, 5648-5652.

[278] F. Weigend, R. Ahlrichs, *Phys. Chem. Chem. Phys.* **2005**, *7*, 3297-3305.

[279] R. F. Fink, J. Seibt, V. Engel, M. Renz, M. Kaupp, S. Lochbrunner, H.-M. Zhao, J. Pfister, F. Würthner, B. Engels, *J. Am. Chem. Soc.* **2008**, *130*, 12858-12859.

[280] C. M. Dobson, *Nature* **2003**, *426*, 884-890.

[281] S. I. A. Cohen, R. Cukalevski, T. C. T. Michaels, A. Šarić, M. Törnquist, M. Vendruscolo, C. M. Dobson, A. K. Buell, T. P. J. Knowles, S. Linse, *Nat. Chem.* **2018**, *10*, 523-531.

[282] H. Jónsson, G. Mills, K. W. Jacobsen, in *Classical and Quantum Dynamics in Condensed Phase Simulations* (Eds.: B. J. Berne, G. Ciccotti, D. F. Coker), World Scientific, Singapore, **1998**, pp. 385-404.

[283] E. L. Kolsbjerg, M. N. Groves, B. Hammer, *J. Chem. Phys.* **2016**, *145*, 094107.

[284] J. O. Lindner, K. Sultangaleeva, M. I. S. Röhr, R. Mitrić, *J. Chem. Theory Comput.* **2019**, *15*, 3450-3460.

[285] A. Hjorth Larsen, J. Jørgen Mortensen, J. Blomqvist, I. E. Castelli, R. Christensen, M. Dułak, J. Friis, M. N. Groves, B. Hammer, C. Hargus, E. D. Hermes, P. C. Jennings, P. Bjerre Jensen, J. Kermode, J. R. Kitchin, E. Leonhard Kolsbjerg, J. Kubal, K. Kaasbjerg, S. Lysgaard, J. Bergmann Maronsson, T. Maxson, T. Olsen, L. Pastewka, A. Peterson, C. Rostgaard, J. Schiøtz, O. Schütt, M. Strange, K. S. Thygesen, T. Vegge, L. Vilhelmsen, M. Walter, Z. Zeng, K. W. Jacobsen, *J. Phys. Condens. Matter* **2017**, *29*, 273002.

[286] *Computational Thermochemistry, Vol. 677* (Eds.: K. K. Irikura, D. J. Frurip), American Chemical Society, Washington, DC, **1998**.

[287] J. W. Ochterski, *Thermochemistry in Gaussian*, Gaussian, Inc., https://gaussian.com/thermo/ and https://gaussian.com/wp-content/uploads/dl/thermo.pdf, **2000**.

[288] G. Wedler, *Lehrbuch der Physikalischen Chemie, Vol. 5*, WILEY-VCH, Weinheim, **2004**.

[289] P. W. Atkins, J. de Paula, *Physikalische Chemie, Vol. 4*, WILEY-VCH, Weinheim, **2006**.

[290] F. Würthner, C. Thalacker, A. Sautter, *Adv. Mater.* **1999**, *11*, 754-758.

[291] V. Percec, H.-J. Sun, P. Leowanawat, M. Peterca, R. Graf, H. W. Spiess, X. Zeng, G. Ungar, P. A. Heiney, *J. Am. Chem. Soc.* **2013**, *135*, 4129-4148.

[292] W. C. McCrone, in *Physics and Chemisty of the Organic Solid-State, Vol. 2* (Eds.: D. Fox, M. M. Labes, A. Weissberger), Wiley-Interscience, New York, pp. 725-767.

[293] L. Pasteur, *Ann. Chim. Phys.* **1848**, *24*, 442-459.

[294] T. Kudernac, S. Lei, J. A. A. W. Elemans, S. De Feyter, *Chem. Soc. Rev.* **2009**, *38*, 402-421.

[295] L. Herkert, J. Droste, K. K. Kartha, P. A. Korevaar, T. F. A. de Greef, M. R. Hansen, G. Fernández, *Angew. Chem. Int. Ed.* **2019**, *58*, 11344-11349.

[296] T. Hunt, H. C. Atherton-Watson, S. P. Collingwood, K. J. Coote, S. Czarnecki, H. Danahay, C. Howsham, P. Hunt, D. Paisley, A. Young, *Bioorg. Med. Chem. Lett.* **2012**, *22*, 2877-2879.

[297] M. Wolffs, S. J. George, Ž. Tomović, S. C. J. Meskers, A. P. H. J. Schenning, E. W. Meijer, *Angew. Chem. Int. Ed.* **2007**, *46*, 8203-8205.

[298] A. Tsuda, M. A. Alam, T. Harada, T. Yamaguchi, N. Ishii, T. Aida, *Angew. Chem. Int. Ed.* **2007**, *46*, 8198-8202.

[299] Y. Shindo, Y. Ohmi, *J. Am. Chem. Soc.* **1985**, *107*, 91-97.

[300] S. Grimme, *Angew. Chem. Int. Ed.* **2008**, *47*, 3430-3434.

[301] M. Pitoňák, P. Neogrády, J. Řezáč, P. Jurečka, M. Urban, P. Hobza, *J. Chem. Theory Comput.* **2008**, *4*, 1829-1834.

[302] A. M. Brouwer, *Pure Appl. Chem.* **2011**, *83*, 2213-2228.

[303] M. J. Frisch, G. W. Trucks, H. B. Schlegel, G. E. Scuseria, M. A. Robb, J. R. Cheeseman, G. Scalmani, V. Barone, G. A. Petersson, H. Nakatsuji, X. Li, M. Caricato, A. V. Marenich, J. Bloino, B. G. Janesko, R. Gomperts, B. Mennucci, H. P. Hratchian, J. V. Ortiz, A. F. Izmaylov, J. L. Sonnenberg, Williams, F. Ding, F. Lipparini, F. Egidi, J. Goings, B. Peng, A. Petrone, T. Henderson, D. Ranasinghe, V. G. Zakrzewski, J. Gao,

N. Rega, G. Zheng, W. Liang, M. Hada, M. Ehara, K. Toyota, R. Fukuda, J. Hasegawa, M. Ishida, T. Nakajima, Y. Honda, O. Kitao, H. Nakai, T. Vreven, K. Throssell, J. A. Montgomery Jr., J. E. Peralta, F. Ogliaro, M. J. Bearpark, J. J. Heyd, E. N. Brothers, K. N. Kudin, V. N. Staroverov, T. A. Keith, R. Kobayashi, J. Normand, K. Raghavachari, A. P. Rendell, J. C. Burant, S. S. Iyengar, J. Tomasi, M. Cossi, J. M. Millam, M. Klene, C. Adamo, R. Cammi, J. W. Ochterski, R. L. Martin, K. Morokuma, O. Farkas, J. B. Foresman, D. J. Fox, *Gaussian 16 Rev. C.01*, Wallingford, CT, **2016**.

[304] A. Rodger, G. Dorrington, D. L. Ang, *Analyst* **2016**, *141*, 6490-6498.

[305] Y. Shindo, M. Nishio, *Biopolymers* **1990**, *30*, 25-31.

Individual Contribution

The coauthors of the manuscripts included in this partially cumulative thesis are informed and agree with the reprint and the respective individual contributions as stated below.

Supramolecular Polymorphism in One-Dimensional Self-Assembly by Kinetic Pathway Control

M. Wehner, M. I. S. Röhr, M. Bühler, V. Stepanenko, W. Wagner, F. Würthner, *J. Am. Chem. Soc.* **2019**, *141*, 6092−6107.

Author	M.W.	M.I.S.R.	M.B.	V.S.	W.W.	F.W.
Design of research	50%	–	–	–	–	50%
Synthesis and characterization	100%	–	–	–	–	–
UV/vis spectroscopy	100%	–	–	–	–	–
CD spectroscopy	100%	–	–	–	–	–
FT-IR spectroscopy	100%	–	–	–	–	–
Atomic force microscopy	–	–	–	100%	–	–
Quantum chemical calculations	–	60%	40%	–	–	–
Publication writing	80%	10%	10%	–	–	–
Publication correction	–	10%	–	–	10%	80%
Publication coordination	30%	10%	–	–	–	60%
Total	56%	9%	5%	10%	1%	19%

Supramolecular polymerization through kinetic pathway control and living chain growth

M. Wehner, F. Würthner, *Nat. Rev. Chem.* **2020**, *4*, 38−53.

Author	M.W.	F.W.
Literature survey	60%	40%
Design of graphics	90%	10%
Publication writing	70%	30%
Publication correction	20%	80%
Publication coordination	20%	80%
Total	52%	48%

Acknowledgement / Danksagung

Mein besonderer Dank gilt meinem Doktorvater Prof. Dr. Frank Würthner für das Überlassen des sehr interessanten Forschungsthemas, für die vielen hilfreichen Diskussionen und seine immerwährende Unterstützung während meiner Doktorarbeit. Außerdem möchte ich mich für die hervorragenden Arbeitsbedingungen in seiner Arbeitsgruppe sowie für das entgegengebrachte Vertrauen und die damit verbundenen wissenschaftlichen Freiheiten bedanken. All diese Faktoren haben wesentlich zu dem Gelingen dieser Arbeit beigetragen. Außerdem möchte ich mich für seine Unterstützung bei der Bewerbung für ein Chemiefonds-Stipendium bedanken und für die Ermöglichung der Teilnahme an einigen wissenschaftlichen Konferenzen.

Mein weiter Dank gilt Prof. Dr. Frank Würthner, Dr. Chantu Saha-Möller, Dr. Soichiro Ogi, Dr. Matthias Stolte, Dr. David Bialas und Dr. Bartolome Soberats Reus für die anregenden wissenschaftlichen Diskussionen im Rahmen unserer Subgroup-Meetings. Besonders möchte ich mich hierbei bei Prof. Dr. Frank Würthner und Dr. Chantu Saha-Möller für die große Unterstützung beim Verfassen und Überarbeiten von Manuskripten sowie für sonstige Korrekturarbeiten bedanken.

Darüber hinaus möchte ich mich bei dem Verband der Chemischen Industrie e.V. für die finanzielle Unterstützung der Doktorarbeit im Rahmen eines Chemiefonds-Stipendium bedanken.

Weiterhin möchte ich mich bei Dr. Soichiro Ogi für die exzellente Betreuung in meinem dreimonatigem Forschungspraktikum und die kompetente Einführung in das Forschungsgebiet der supramolekularen Polymerchemie bedanken, was den Grundstein für meine weiteren Forschungsarbeiten gelegt hat.

Besonders möchte ich mich bei Dr. Matthias Stolte bedanken, der immer ein offenes Ohr für wissenschaftliche Diskussionen hatte und für seine immerwährende Hilfe bei spektroskopischen Fragestellungen und Messungen sowie bei der Auswertung von Daten.

Bei Dr. Merle Röhr, Michael Bühler, Joscha Hoche und Dr. Joachim Lindner möchte ich mich für die Durchführung von quantenchemischen Rechnungen bedanken. Ebenfalls bedanke ich mich bei Dr. Vladimir Stepanenko für die Durchführung der zahlreichen AFM-Messungen und Auswertung der erhaltenen Daten. Bei Dr. Matthias Grüne, Patricia Altenberger und Marvin Grüne bedanke ich mich für die Durchführung bzw. Hilfe bei der Durchführung von zahlreichen

NMR-Experimenten. Außerdem bedanke ich mich bei Dr. Michael Büchner und Juliane Adelmann für die Aufnahme von Massenspektren.

Weiterhin möchte ich mich besonders bei Dr. David Bialas für die kompetente und freundschaftliche Betreuung in meinem ersten Forschungspraktikum im Arbeitskreis Würthner bedanken und für die perfekte Eingliederung in das Sozialleben des Arbeitskreises. Außerdem möchte ich mich bei ihm für die Hilfe bei der Bewerbung für ein Chemiefonds-Stipendium bedanken und dafür, dass er immer Zeit und ein offenes Ohr für sämtliche Fragestellungen bzw. Diskussionen hatte.

Bei Dr. Franziska Fennel möchte ich mich für die Hilfe bei der Auswertung von supramolekularen Polymerisationsprozessen sowie für die Bereitstellung entsprechender mathematischer Modelle bedanken.

Bei Joachiam Bialas, Johannes Thein, Anja Rausch, Julius Albert, Maximilian Roth und Petra Seufert-Baumbach bedanke ich mich für ihre Hilfsbereitschaft im Laboralltag.

Ich bedanke mich darüber hinaus bei Christiana Toussaint, Eleonore Klaus und Sarah Bullnheimer für die Vorbereitungen für nationale und internationale Dienstreisen sowie für die Hilfe bei organisatorischen Angelegenheiten.

Ein besonderer Dank gilt meinem langjährigen Laborpartner Dr. Wolfgang Wagner, alias „der Captain“, für die exzellente wissenschaftliche Zusammenarbeit, für die harmonische Arbeitsatmosphäre und die unzähligen lustigen Momente, die wir im Laboralltag und außerhalb des Labors hatten.

Außerdem möchte ich mich bei Dr. Wolfgang Wagner, Kevin Bold, Kaan Menekse, Tim Schlossarek, Markus Hecht, Julian Götz, Lara Kleine-Kleffmann, Oliver Nagler, Natalie Schäfer, Viktoria Leonhardt, Christina Kaufmann, Julius Albert, Manuel Weh, Rebecca Renner, Alexander Schulz, Meike Sapotta, Daniel Volland und Benedikt Herbert für die super Stimmung im Labor, während der Pausen und außerhalb des Labors bedanken. Wir hatten so eine klasse Zeit zusammen, dass es den Rahmen dieser Danksagung sprengen würde, alle Momente aufzuzählen. Eine Sache wäre allerdings wichtig zu nennen: Ich hoffe, dass die einst eingeführten „Schlagerfreitage“ weiterhin beibehalten werden.

Weiterhin möchte ich mich bei Emely Freytag (Bachelorarbeit) und Stefan Hagspiel, Tabea Gerlach und Lara Kleine-Kleffmann (OC Masterpraktika) für ihre Unterstützung bei der Synthesearbeit bedanken.

Ein ganz besonderer Dank gilt außerdem noch allen Mitgliedern der Arbeitskreise Würthner, Beuerle und Nowak-Król für die freundliche und hilfsbereite Arbeitsatmosphäre und die vielen legendären Abende und „Stammtische“, welche die Zeit der Promotion bereichert haben. Es hat mir sehr viel Spaß bereitet, in solch einem tollen Arbeitsumfeld zu arbeiten.

Ein ganz besonderer Dank gilt meiner Freundin Jennifer Zablocki für ihr Verständnis und ihre bedingungslose Unterstützung während meiner Promotion. Ich möchte mich herzlich für die Liebe, den starken Rückhalt, die Harmonie und für die schöne gemeinsame Zeit bedanken.

Von ganzem Herzen möchte ich mich zuletzt bei meiner Familie und ganz besonders bei meinen Eltern bedanken, welche mich auf meinem gesamten Lebensweg mit Liebe begleitet haben, mich immer bindungslos unterstützt haben und mir in allen Lebenssituationen ein starker Rückhalt waren. Ich bin unfassbar glücklich, eine so tolle, harmonische und liebenswerte Familie zu haben!

List of Publications

Taming the beast: fluoromesityl groups induce a dramatic stability enhancement in boroles

Z. Zhang, R. M. Edkins, M. Haehnel, M. Wehner, A. Eichhorn, L. Mailänder, M. Meier, J. Brand, F. Brede, K. Müller-Buschbaum, H. Braunschweig, T. B. Marder, *Chem. Sci.* **2015**, *6*, 5922−5927.

Regioselective Catalytic and Stepwise Routes to Bulky, Functional-Group-Appended, and Luminescent 1,2-Azaborinines

M. Schäfer, J. Schäfer, R. D. Dewhurst, W. C. Ewing, M. Krahfuß, M. W. Kuntze-Fechner, M. Wehner, C. Lambert, H. Braunschweig, *Chem. Eur. J.* **2016**, *22*, 8603−8609.

Living Supramolecular Polymerization of a Perylene Bisimide Dye into Fluorescent J-Aggregates

W. Wagner, M. Wehner, V. Stepanenko, S. Ogi, F. Würthner, *Angew. Chem. Int. Ed.* **2017**, *56*, 16008−16012.

Supramolecular Polymorphism in One-Dimensional Self-Assembly by Kinetic Pathway Control

M. Wehner, M. I. S. Röhr, M. Bühler, V. Stepanenko, W. Wagner, F. Würthner, *J. Am. Chem. Soc.* **2019**, *141*, 6092−6107.

Bis(merocyanine) Homo-Folda-Dimers: Evaluation of Electronic and Spectral Changes in Well-Defined Dye Aggregate Geometries

E. Kirchner, D. Bialas, M. Wehner, D. Schmidt, F. Würthner, *Chem. Eur. J.* **2019**, *25*, 11285−11293.

Supramolecular Block Copolymers by Seeded Living Polymerization of Perylene Bisimides

W. Wagner, M. Wehner, V. Stepanenko, F. Würthner, *J. Am. Chem. Soc.* **2019**, 141, 12044−12054.

Impact of Molecular Shape on Supramolecular Copolymer Synthesis in Seeded Living Polymerization of Perylene Bisimides

W. Wagner, M. Wehner, V. Stepanenko, F. Würthner, *CCS Chem.* **2019**, *1*, 598−613.

Supramolecular polymerization through kinetic pathway control and living chain growth

M. Wehner, F. Würthner, *Nat. Rev. Chem.* **2020**, *4*, 38−53.